ABSTRACT

Title of Dissertation: CONTRIBUTIONS TOWARDS THE UNDERSTANDING OF ROTOR-INDUCED DUST PARTICLE MOBILIZATION AND TRANSPORT

Anish Joshua Sydney, Doctor of Philosophy, 2014

Dissertation directed by: Minta Martin Professor J. Gordon Leishman
Department of Aerospace Engineering

To better understand the problem of rotor-induced particle motion and rotorcraft brownout, time-resolved, dual-phase particle image velocimetry and particle tracking velocimetry measurements were made in the flow produced by a small laboratory rotor that was hovering over a ground plane covered with a mobile sediment bed. To investigate the three-dimensionality of the wake and resultant particle field, flow measurements were made in vertical and horizontal planes around the rotor and near the ground. The primary goals of the work were to: 1. Characterize the fundamental flow physics of a rotor wake interacting with a sediment bed; 2. Investigate how rotor operating parameters, such as the disk loading, blade loading coefficient, and wake shedding frequency affected the mobilization, uplift and overall development of the particle field; 3. Examine the effects of placing a body between the rotor and the ground to understand how the interactions of the rotor wake with the body affected the transport of particles from the bed. The results showed that the rotor wake was very three-dimensional, with highly non-uniform velocities near the ground that resulted in the radially asymmetric mobiliza-

tion, uplift and suspension of particles. The tip vortices were found to be the primary contributor to the uplift of particles, with the aperiodic variations in their trajectories near the ground causing intermittent particle mobilization events. These effects were caused, in part, by wave-like displacements that developed along the lengths of the tip vortices, which caused some parts of the filaments to convect closer to the ground than other parts and so uplift discrete bursts or plumes of particles. The quantity and distribution of uplifted particles were shown to be affected by the operating condition of the rotor, with the overall complexity of the rotor wake generally resulting in the formation of a highly three-dimensional and time-varying particle field. The rotor operating parameters were shown to interdependently alter the characteristics of the groundwash flow and the tip vortices produced by the rotor. Stronger wake vortices that impinged on the bed generally uplifted more particles, however, higher near-wall flow velocities over the bed also convected particles further downstream before they could be suspended. The near-wall flow developments were further complicated by the interaction of the rotor wake with a body, which significantly distorted the development of the rotor wake at the ground, the resulting near-wall flow velocities generally being lower in magnitude. The degree of wake distortion, however, was found to be sensitive to the cross-sectional shape of the body. In cases where there was direct impingement of the tip vortices on the body surfaces, the distortions to the wake caused lower near-wall flow velocities but still contained vortices that were able to suspend sediment particles radially closer to the rotor compared to the isolated rotor case.

CONTRIBUTIONS TOWARDS THE UNDERSTANDING OF ROTOR-INDUCED DUST PARTICLE MOBILIZATION AND TRANSPORT

by

Anish Joshua Sydney

Dissertation submitted to the Faculty of the Graduate School of the
University of Maryland, College Park in partial fulfillment
of the requirements for the degree of
Doctor of Philosophy
2014

Advisory Committee:
Minta Martin Professor J. Gordon Leishman, Chair/Advisor
Professor Inderjit Chopra
Associate Professor James Baeder
Assistant Professor Anya Jones
Professor Kenneth Kiger

Acknowledgments

First and foremost, I'd like to thank my advisor and dissertation committee chair, Professor J. Gordon Leishman, for providing me the opportunity to work under his tutelage on this interesting and challenging project. Dr. Leishman has been an excellent guide from my beginnings as an undergraduate student through becoming a doctoral candidate. I am very grateful for all that he has taught me.

I would like to thank Professors Inderjit Chopra, James Baeder, Anya Jones, and Kenneth Kiger for their contributions as members of my dissertation committee.

I want to thank all of the guys in the lab, Joe Milluzzo, Dave Mayo, Joe Ramsey, Jaime Reel, Ajay Baharani, Ben Hance, Bharath Govindarajan, Bradley Johnson, and Tim Lee, who have been a constant source of help and guidance over the years. More importantly, these guys have been a family to me and have shown me that no matter the situation, there is always time to have some fun. I could not ask for a better group of people to work with.

A very special thanks goes to Joe Milluzzo, Bharath Govindarajan, and Dave Mayo, who have been with me since the beginning. These three have been like brothers to me, always willing to provide support when I needed it. It was a privilege and an honor to work with these gentlemen.

I must express my deepest appreciation for my family, specifically my twin brother Nitin. He has always been my strength and motivation. His unwavering support throughout our undergraduate and graduate careers has kept me going. I might be finishing my dissertation before he is, but he will always be the better twin. A warm thank you to my

parents, Mukesh and Rekha as well. They have given me so many opportunities, opened so many doors, and showered me with unconditional love. Without them, this work would have been impossible. I hope that I have made them proud.

Last, but certainly not least, I would like to thank my girlfriend, Kelsey Shields. If anyone has sacrificed as much as I have towards the completion of this work, it is Kelsey. For three years she has put up with all the late nights in the lab and the long hours of writing. Throughout it all, she encouraged me and stayed by my side, helping me in any way she could. Her steadfast love has been a source of strength for me.

Even though this work has my name on it, it has really been a group effort. Words cannot express my gratitude to all the people, even those not mentioned here, who have made sacrifices to carry me from Anish to Dr. Sydney. I could not have done this without you. Thank you all so much!

I would like to acknowledge the support of the Air Force Office of Scientific Research (AFOSR) under Multidisciplinary University Research Initiative Grant No. W9.

Table of Contents

List of Tables

List of Figures

Nomenclature

A	Rotor area, $= \pi R^2$, m^2
c	Blade chord, m
C_T	Rotor thrust coefficient, $= T/\rho\pi\Omega^2 R^4$
C_T	Rotor thrust coefficient, $= T/\rho\pi\Omega^2 R^4$
C_T/σ	Blade loading coefficient
DL	Disk loading, $= T/A$, Nm^{-2}
M	Camera magnification factor
N_b	Number of rotor blades
R	Rotor radius, m
Re_{tip}	Blade tip Reynolds number, $= \rho V_{\mathrm{tip}} c/\mu$
Re_ν	Vortex Reynolds number, $= \Gamma/\nu$
r_c	Vortex core radius, m
r, ψ, z	Polar coordinate system centered at the rotor shaft, (m, deg, m)
r_p, θ_p	Polar coordinate system centered at a reference point in the x-z plane, (m, deg)
T	Rotor thrust, N
V_r	Velocity in the r direction, ms^{-1}
V_ψ	Velocity in the ψ direction, ms^{-1}
V_{tip}	Blade tip speed, $= \Omega R$, ms^{-1}
V_{xz}	Total velocity in the x-z plane, ms^{-1}
V_{xy}	Total velocity in the x-y plane, ms^{-1}
V_θ	Vortex swirl velocity, ms^{-1}

v_h	Hover induced velocity, ms^{-1}
σ	Rotor solidity, $= N_b c/\pi R$
u, v, w	Velocities in x , y, and z directions, respectively, ms^{-1}
x_i, x_j	nodes of interrogation window grid
x, y, z	Cartesian coordinate system, m
ζ	Wake age, deg
ρ	Air density, kg m^{-3}
ρ_p	Particle density, kg m^{-3}
ψ_b	Blade azimuth angle, deg
Ω	Rotational frequency of the rotor, rad s^{-1}
μ	Dynamic viscosity of air, kg $\mathrm{m}^{-1}\mathrm{s}^{-1}$
$\widehat{\Gamma}_v$	Non-dimensional tip vortex circulation, $= \Gamma_v/\Omega R c$
Γ_v	Tip vortex circulation, $= k(C_T/\sigma)\Omega R c$, $\mathrm{m}^2\mathrm{s}$
Δt	Pulse separation time, μs
Δx, Δy	Grid spacing in the x and y directions, respectively, m
Φ_{fg}	Cross-correlation function
ε	uncertainty value, m

Abbreviations

CFD	Computational fluid dynamics
CMOS	Complementary metal oxide semiconductor
fps	frames-per-second
FV	Flow visualization
PIV	Particle image velocimetry
PTV	Particle tracking velocimetry
PSD	Particle size distribution
ROI	Region of interest
TPP	Rotor tip path plane
TR-PIV	Time-resolved particle image velocimetry

Chapter 1

Introduction

1.1 The Problem of Brownout

"Brownout" is a phenomenon that occurs when rotorcraft operate in arid environments near a ground surface covered with loose sediment, such as desert sand. The problem of brownout generally occurs when the rotorcraft is taking off, landing, hovering, or otherwise operating near the ground. The intense wake produced by the rotor interacts with the ground in a way that mobilizes the sediment and lifts it up into the air, often creating a dust cloud of sufficient size to engulf the entire rotorcraft. An example of a helicopter encountering brownout conditions during a landing is shown in Fig. 1.1, where a large dust cloud is formed. For this to happen, the aerodynamic forces produced by the rotor wake must become sufficient to mobilize and uplift the sediment particles, which then causes the rapid development of a brownout dust cloud that quickly engulfs the entire helicopter.

The main practical concern of brownout is the formation of a degraded visual environment (DVE). During landing and take-off, pilots use certain visual cues (such as the horizon, items on the ground, nearby structures, etc.) to determine the orientation and movement of the rotorcraft. The suspended dust particles can quickly obscure the pilot's vision, eliminating visual cues that are needed to safely operate the rotorcraft. The swirling flow produced by the rotor wake within the dust cloud can also cause the pilot

Figure 1.1: A landing helicopter experiencing brownout conditions in a desert environment. Image courtesy of Optical Air Data Systems.

to experience vection illusions, in which the pilot perceives an apparent, but false, sense of relative motion. In extreme cases, the DVE conditions can cause pilot disorientation, which can lead to incorrect pilot control inputs that may cause the vehicle to drift into the ground or nearby obstacles. Accidents from brownout occurrences have continued to grow in both military and civilian rotorcraft operations [1, 2].

Besides the loss of visibility, the suspended dust particles within the cloud can cause serious maintenance issues such as rapid erosion of the rotor blades. Most blades are made of composite materials, with a metallic erosion strip that is placed along the leading edge. Flight in brownout conditions has been known to wear through this erosion strip within tens of flight hours; see Fig. 1.2. The dust particles also cause engine wear and permeate into critical components and systems of the aircraft, resulting in serious and costly maintenance issues. The constant need for in-field maintenance after brownout occurrences leads to reduced flight readiness times and an overall reduced service life for

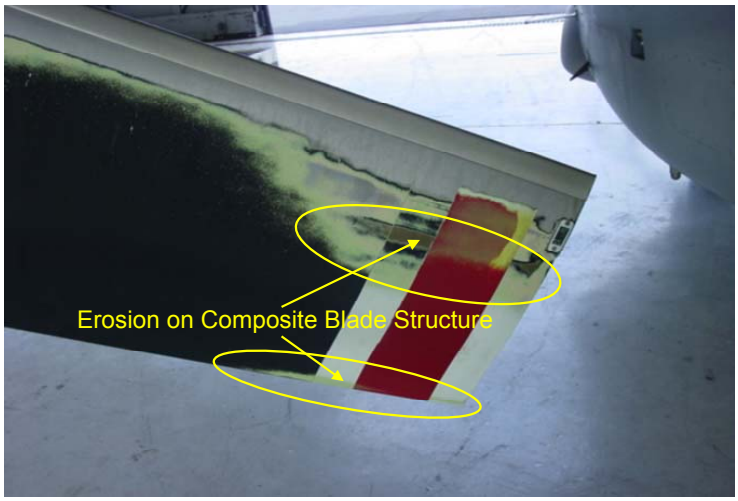

Figure 1.2: Erosion damage on a rotor blade from operation in brownout conditions.

the rotorcraft. Other brownout related safety issues include a dangerous working environment for ground personnel (such as during sling load operations) and complications for formation landings or takeoffs, where the brownout dust cloud produced by one rotorcraft can interfere with the operation of another rotorcraft.

In an effort to reduce the number of mishaps associated with the problem of brownout, pilots have adopted various operational strategies. One such strategy is to fly with a relatively higher airspeed near the ground, essentially "out running" or "out pacing" the dust cloud, which now develops just behind the rotorcraft. Pilots have also been known to perform more rapid descents toward the ground such that the dust cloud does not fully develop before the actual landing. Another strategy pilots implement is to minimize the amount of time in the landing flare in an attempt to reduce the amount of airborne dust in the required field of view. While these operational tactics have somewhat reduced the number of brownout mishaps, they also introduce other safety of flight risks, i.e., flying faster near the ground or approaching the ground at a higher rate of descent generally

increases risk. Furthermore, the development of brownout clouds is heavily dependent on environmental factors such as the prevailing wind, the sediment characteristics, humidity, etc. and so the effectiveness of piloting mitigation strategies are not always consistent.

Initial attempts at brownout mitigation have been directed toward the development of so-called "see-through" technologies [3–5]. These technologies focus on giving the pilots the ability to "see" through the dust cloud rather that trying to minimize the severity of its development. With the use of advanced avionics and heads-up displays, software can be used to replace certain types of missing visual information that the pilot needs to safely operate the rotorcraft. When combined with operational tactics and flight path management, these systems have been reasonably effective. However, brownout mishaps and overall maintenance costs still remain unacceptably high. Therefore, the foregoing issues demonstrate a need to mitigate brownout at its source, i.e., recognizing brownout as a fluid dynamics problem produced by the rotor wake with, potentially, a fluid dynamics solution. Understanding the mechanisms and factors involved in the generation and evolution of a brownout cloud is paramount toward developing a viable overall brownout mitigation strategy, which is at least one practical motivation behind the present research.

In terms of mitigation, anecdotal evidence suggests that different rotorcraft platforms produce unique brownout signatures, some more favorable than others. The differences in these clouds fundamentally arise from the different design aspects of each rotorcraft, including but not limited to: number of blades, blade shape, disk loading, blade loading, fuselage shape, etc. These factors ultimately effect the geometry, concentration, and rate of development of the dust clouds, with some configurations producing less dense and more optically favorable clouds than others. For example, Fig. 1.3 shows a photo-

Figure 1.3: A landing helicopter with the formation of a more favorable ring or toroidal shaped dust cloud away from the immediate landing zone.

graph of a helicopter during landing. Notice that, in this particular case, the brownout cloud has taken the shape of a toroidal ring. While the interaction with the ground has entrained a significant amount of dust, it is being blown further away from the rotorcraft, providing a relatively clear field of view for the pilot to safely operate the vehicle. Other rotorcraft create more dome shaped clouds in which the vehicle is completely engulfed by the dust; see Fig. 1.4. In this case, the suspended dust particles are reingested by the rotor system and bombarded back onto the ground, a phenomenon that appears to significantly increase the overall quantity of dust in the surrounding flow.

Of particular interest in the present research is that these dust clouds are generally highly three-dimensional in nature. They often show discrete structures such as localized columns of dust, which are sometimes seen to form around the periphery of the cloud. These columnar dust structures or "plumes" can cause local, time-varying obscurations of the visual cues that can affect the pilot's vision of the ground. However, the reasons

Figure 1.4: A landing helicopter with the formation of a less favorable dome shaped dust cloud that engulfs the aircraft.

for the overall shape and the formation of the plume-like three-dimensionality of the dust cloud remain unclear. Understanding the rotor wake/sediment bed interactions and how they are affected by different factors will provide valuable insight into how brownout clouds are formed. To this end, the objective of the present research was to investigate the physics of rotor-induced sediment particle transport through a series of laboratory experiments, and to examine how the resulting particle clouds were affected by different rotor operating conditions.

1.2 Flow Physics Associated with Brownout

It is essential to better understand the dual-phase fluid mechanics associated with the formation of the brownout dust clouds. Fundamentally, the problem of brownout consists of two fluid phases that interact with each other: 1. The *carrier-phase*, which is the complex, unsteady, three-dimensional rotor wake produced by the rotor, and 2. The

dispersed-phase, which consists of the sediment particles that are subsequently mobilized, entrained, and uplifted from the sediment bed below the rotor. While the dust is not a fluid, per se, it behaves in many ways as a fluid as it is convected by the carrier flow, and so the details of how the brownout dust cloud forms also lies in the underlying interaction between the carrier and dispersed phases of the flow. However, studying this multiphase flow is challenging because of the difficulties that are associated with the separation and discrimination of the two phases. Furthermore, these phases are inherently coupled, in that the carrier-phase not only mobilizes and transports the dispersed-phase, but the dispersed phase will, in turn, affect the characteristics of the carrier-phase. However, for a rotor-induced particle field, the degree to which this coupling affects the overall development of the flow remains largely unknown.

The flow environment induced by the rotor wake at the ground (synonymously referred to as the "wall") is responsible for initiating the various fluid dynamic forces that mobilize and uplift the particles. Such forces have their origin in viscous shear, unsteady pressures, and turbulence effects. A schematic of a helicopter performing a landing and encountering brownout conditions is shown in Fig. 1.5, which identifies at least some of the particle mobilization and uplift mechanisms that may be involved. The rotor wake causes loose particles in the sediment bed to be mobilized and ultimately uplifted (sometimes as discrete plumes). Once suspended, these particles have the tendency to be reingested through the rotor system and are quickly convected downward and impact the ground, a process called bombardment, by which many more particles are ejected into the near-wall flow that are also eligible to be uplifted into suspension.

Measurements made with landing helicopters [4,5] have shown that brownout clouds

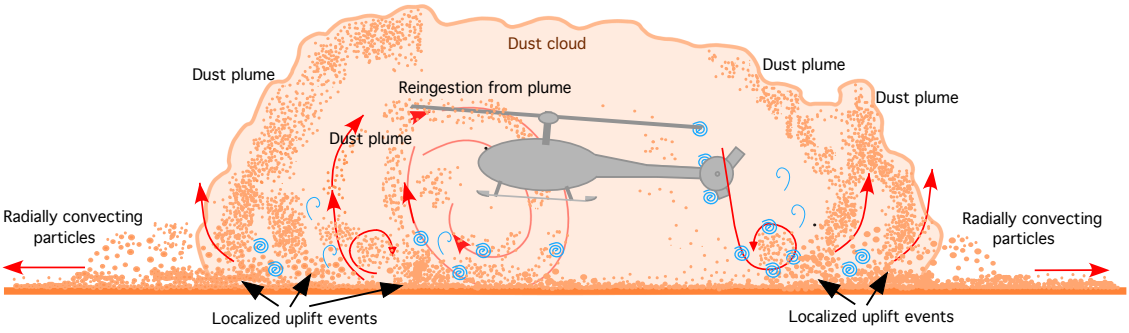

Figure 1.5: A schematic of the dual-phase flow induced by a helicopter during approach.

are actually composed of a wide range of dust particle sizes (1–1000 μm in diameter), although the particles that are actually suspended in the cloud tend to be in the smaller ($<$10 μm in diameter) size range; see Fig. 1.6a and Fig. 1.6b for the particle concentrations and densities that have been measured in brownout dust clouds. The smaller particles have relatively higher inter-particle forces and are not as easily mobilized by the shear stresses induced below a rotor, which indicates that the local action of the rotor blade tip vortices and the bombardment of particles back onto the underlying bed is more likely to dominate the creation of the brownout dust clouds [6–8]. Compounding the brownout problem is that different levels of brownout severity can be expected based solely on the nature of the sediment bed over which the rotorcraft is operating, such as the size and mineralogy of the particles, as well as their compactness, inter-particle forces, moisture content, etc., all of which can all effect the initial uplift of sediment particles.

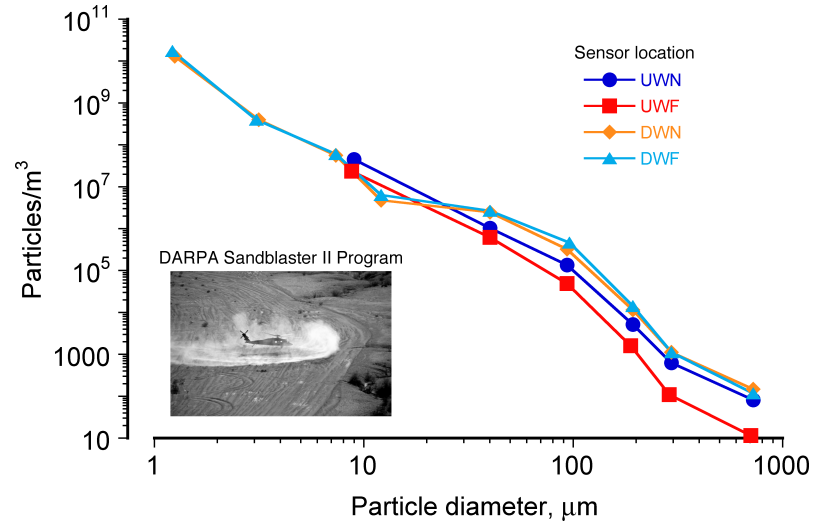

(a) Particle concentration

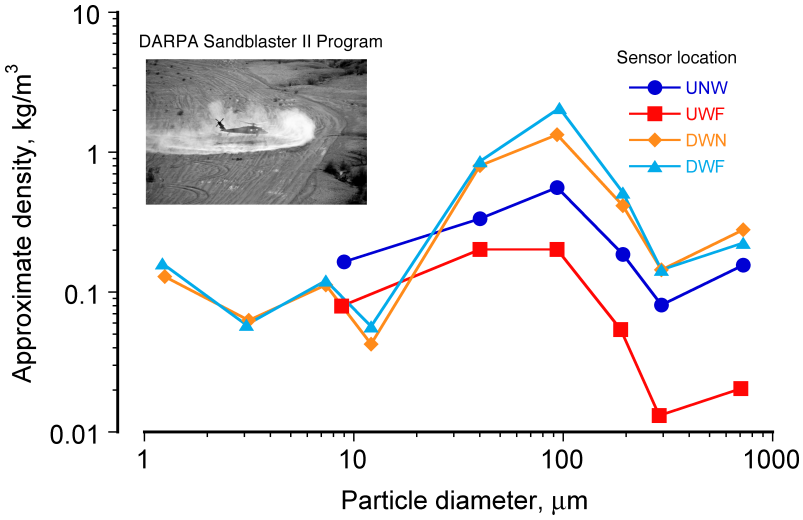

(b) Particle densities

Figure 1.6: Field test results showing (a) the concentration of particles and (b) the density of particles within a brownout dust cloud as a function of particle diameters.

1.3 Rotor Wake Flows

The problem of brownout is dependent on the flow physics of rotor wakes that develop in ground effect (so-called "IGE"), and so understanding the flow of the rotor near the ground in the absence of sediment is a necessary prerequisite to understanding the complex phenomenon of brownout. The rotor wake contains vortical flows, turbulence and other secondary flow structures that interact not only with the ground plane, but also with each other. In terms of performance (i.e., thrust and power), rotors operating IGE have been well studied [9–16]. It has been established that when a rotor is operating IGE (within approximately two rotor radii away from the ground), then it experiences a performance benefit that becomes more significant the closer the rotor plane comes to the ground, i.e., the rotor requires less power to produce a given thrust compared to out of ground effect (so-called "OGE") operation. This main reason for this power reduction compared to OGE operation is the reduced inflow at the rotor during IGE operation, causing the rotor blades operate at a lower angle of attack that will manifest as lower profile power requirement to produce a given amount of thrust.

However, the problem of brownout is not one of performance, but of the fluid dynamic interactions of the rotor wake with the ground plane and mobile sediment bed. In fact, the rotor flow produced when operating IGE differs greatly from a rotor flow that develops in OGE conditions. For example, Fig. 1.7 shows a representative flow visualization of a rotor wake for OGE conditions, which can be used to convey the general complexity of the wake system produced by a helicopter rotor. The wake, in this case, was visualized using seed particles (smoke), which was illuminated in a vertical plane by using a laser

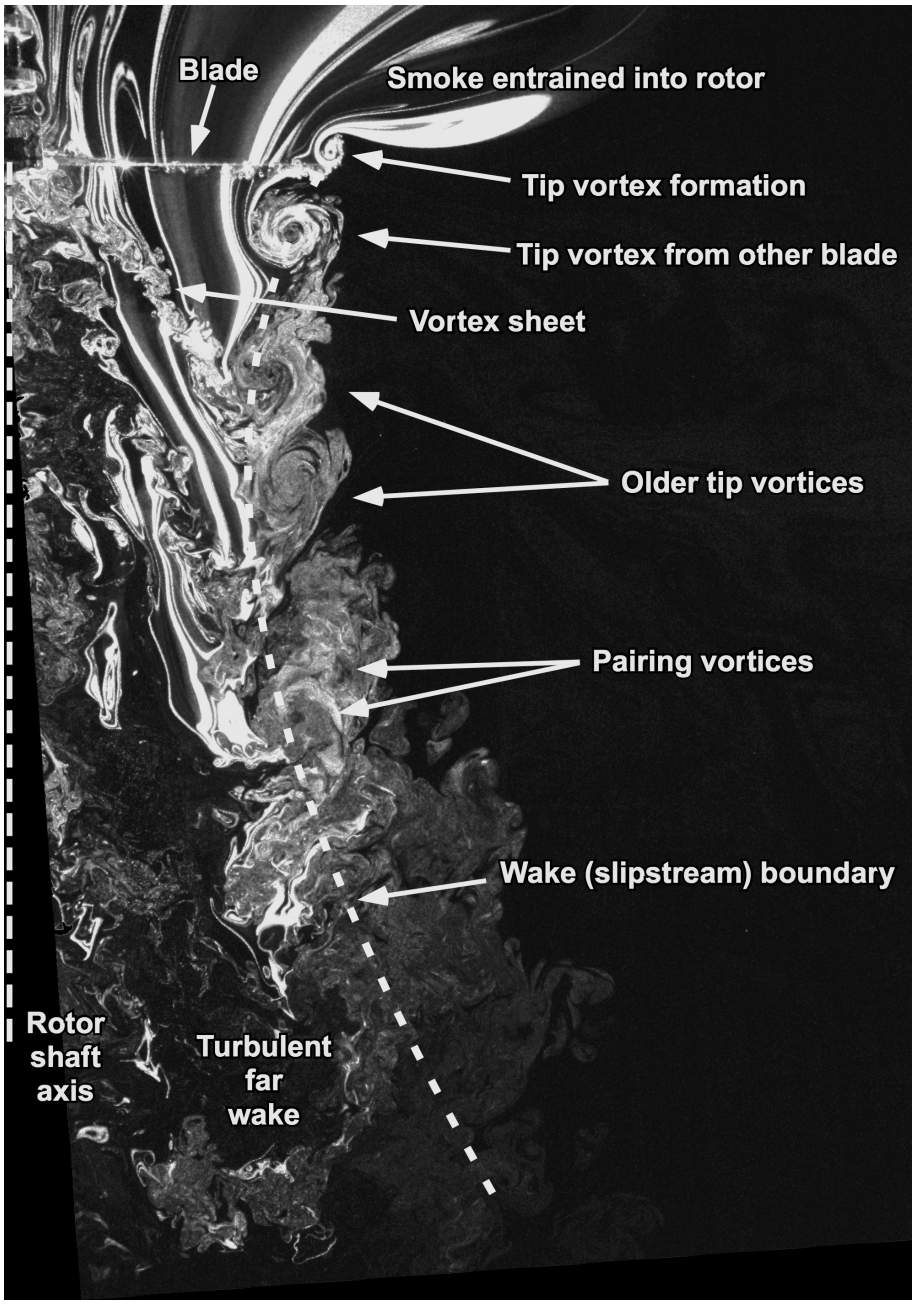

Figure 1.7: Flow visualization of a two-bladed rotor out of ground effect.

light sheet. The seeded flow enters the plane of the rotor disk and immediately begins to contract as it is accelerated through the rotor disk. Under the influence of diffusion and turbulence, however, the flow then begin to slow down and the wake expands. A dominant feature of the wake flow are the vortex filaments that are individually trailed off the tip of each blade, which can be identified as the darker "circular" regions in the images. It is important to note that these vortices are actually trailed as continuous helicoidal filaments, and the dark circular regions here are representative of the cross-sections of these filaments. The vortices can be seen to convect along the slipstream boundary of the rotor wake, occasionally merging with adjacent vortices. These vortices, also under the influence of viscosity and turbulence, normally diffuse under OGE conditions within a few rotor revolutions (nominally 2 to 3 revolutions).

Notice from Fig. 1.8 that the flow of the rotor when operating IGE is very different compared to that found in OGE conditions. In IGE conditions, the rotor wake is constrained by the presence of the ground plane and is forced to radially expand in a direction that is more parallel to the ground, a process that is discussed in much greater detail later in this dissertation. The radial expansion of the flow over the ground creates a turbulent wall-jet like flow that initially thins and then thickens as it develops further downstream. The tip vortices still follow the slipstream boundary of the rotor wake, but in this case they can be seen to come in close proximity to the ground and interact with the developing flow there. The rotor wake is still laden with concentrated vorticity but, in contrast to the OGE case, it persists to much older wake ages (i.e., 4 to 5 rotor revolutions, sometimes longer), which is a result of the stretching effects produced on the vortex filaments [17, 18]. Stretching produces the reintensification of vorticity and creates rela-

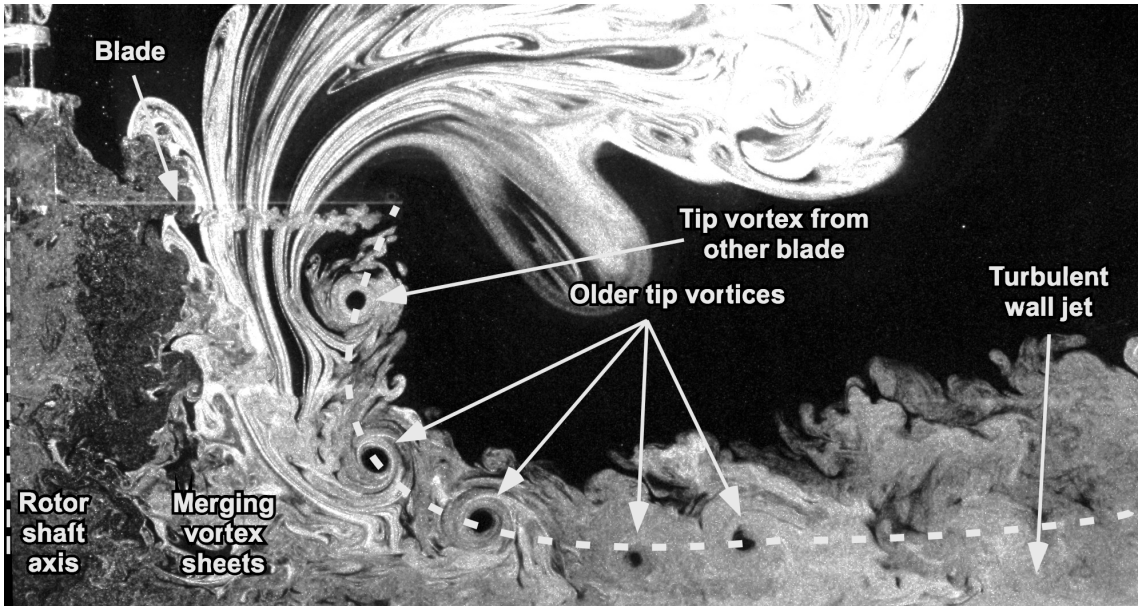

Figure 1.8: Flow visualization of a two-bladed rotor in ground effect.

tively high local velocities in the near-wall region, rather strongly influencing the initial mobilization and uplift of sediment [6, 7].

Further complicating the development of the rotor wake near the ground is the presence of an airframe (or body) that may be in the wake. Figure 1.9 shows a schematic of the nominal flow produced by a rotor in the presence of a body. It seems obvious that the body under the rotor can potentially distort the development of the rotor wake. However, because the body is generally not centered under the rotor, the resulting flow will be less axisymmetric than an isolated rotor in hover. In the nose region, the rotor blade tips pass far away from the body and so the trailed vortices will likely be unaffected by the presence of the body. In the tail region, however, the rotor blade tips pass directly over the body and the tip vortices will convect downward interact with its upper surface. The downwash of the rotor will also create a flow about the body and wake below the body. It is known that turbulence and vortical flows affect the mobilization and transport of sediment [19, 20]

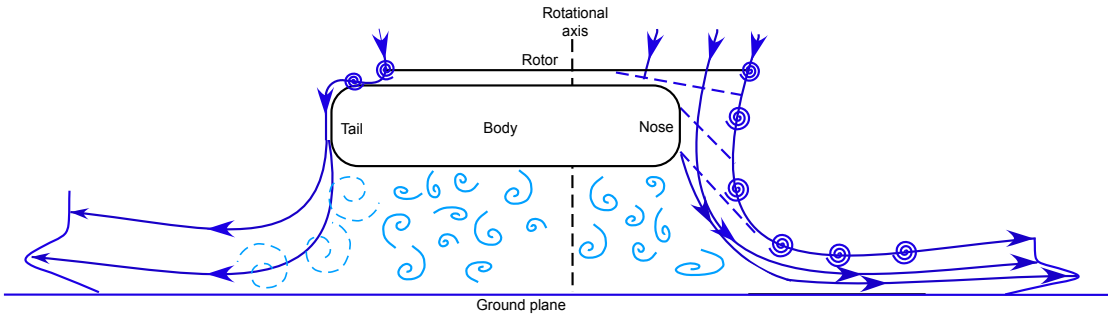

Figure 1.9: A schematic of the wake distortions caused by the presence of a body under the rotor.

and so it is likely that the bluff nature of typical airframe body shapes may also alter the formation of the resulting dust clouds. The interaction between the vortical wake and the body, and how such interactions effect the mobilization and transport of sediment, was also investigated in the present work.

1.4 Particle Dynamics

Understanding the formation of a brownout dust clouds necessitates the basic understanding of the detailed particle physics that are involved in the processes of their mobilization and uplift. Previous work in the field of aeolian sciences to study sediment transport are also useful, but are somewhat limited in their applicability to the brownout problem. Such studies have dealt with wind-blown sands, riverine sediment flows, and simple jet-type flows [21–25].

Of particular interest, is that the field of aeolian sciences has formed a basis on which to begin characterizing particle motion for the problem of brownout. Particle motion can be categorized into three processes: 1. *Mobilization*, a process by which particles

initially begin to move under the action of an external flow, 2. *Entrainment*, in which particles are rapidly lifted from the bed and drawn into the external flow, and 3. *Transport*, a process that involves the movement of particles under the influence of the aerodynamic, inertial and gravitational forces.

When on the ground, a typical sediment particle is subject to a number of forces including aerodynamic forces (from the wall shear stress caused by the boundary layer), pressure forces (such as induced by passing tip vortices), the force of gravity (which depends on the mass of the particles), and inter-particle forces (which are influenced by the particle composition and environmental characteristics). Once the shear stress on the sediment bed exceeds a certain threshold and/or the aerodynamic forces exceed the gravitational and inter-particle forces, the sediment particles will become mobilized. If a particle is then subsequently uplifted into the external flow, then particle will experience additional aerodynamic and inertial forces as it is convected. The particles also extract energy from the surrounding flow, and their subsequent motion is primarily effected by the lift, drag, and inertia of each particle; see Fig. 1.10.

These sedimentology studies, however, have been performed for conditions are not representative of the flow conditions found below rotors, which, as previously described, are generally more three-dimensional and unsteady, and are dominated by the presence of discrete vorticity, i.e., by vortices and larger turbulent eddies. Therefore, it is essential to better characterize the particle mobilization, entrainment and transport as observed under the action of a rotor wake. To this end, Fig. 1.11 shows a schematic of the previously observed near-wall dual-phase flow mechanisms that are induced by a rotor flow. Identified in red are the sediment transport mechanisms that have been observed in prior

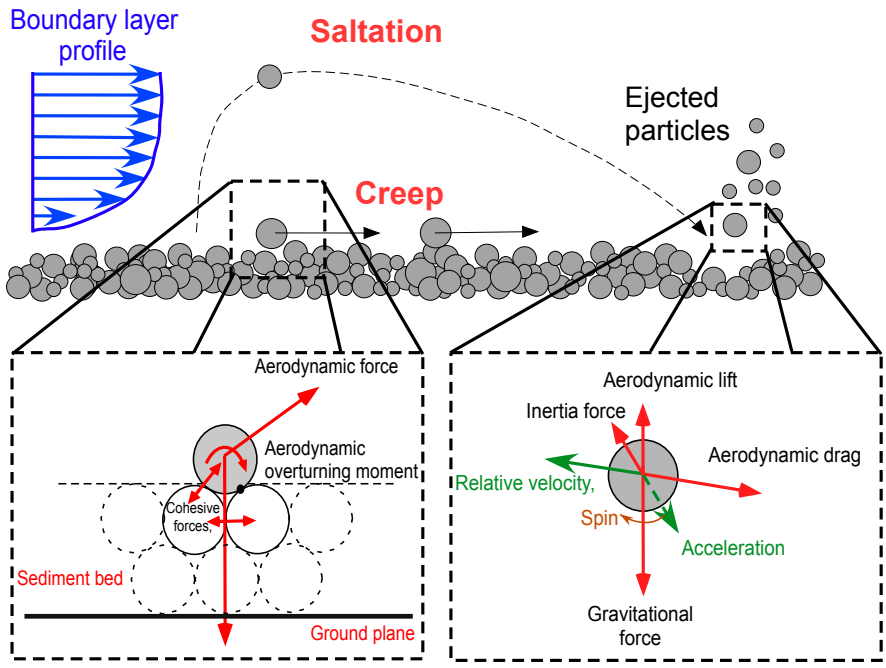

Figure 1.10: A schematic of the classic aeolian creep and saltation sediment transport mechanisms and the particle forces involved in mobilization and suspension.

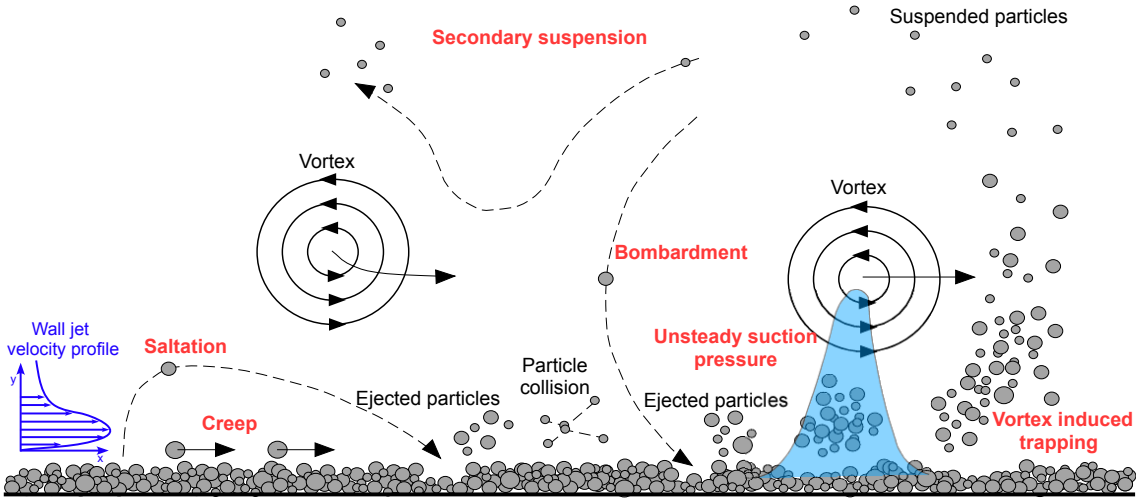

Figure 1.11: Schematic showing the different modes of sediment particle motion and the fundamental uplift mechanisms as observed in the near-wall region.

work [7,26] to contribute most significantly to the processes of sediment mobilization, entrainment and transport. These mechanisms are: creep, modified saltation, bombardment, unsteady pressure effects, vortex-induced particle trapping, and secondary suspension.

The process of creep and saltation have been well-studied in the field of aeolian sciences [21–25]. Below a rotor, these mechanisms clearly appear in the near-wall region, but in modified forms. Creep is a process by which loose particles on the ground roll along the surface of the bed, disturbing other particles in their paths. These creeping particles move under the action of the non-uniform flow at the ground, which produces forces that are sufficient to mobilize them while the wall-normal velocities or external pressure forces are too low to uplift them into the main flow. Saltation occurs when mobilized particles on the bed obtain sufficient vertical components of velocity, such as through a collision or from a wall-normal excursion in the external flow velocity. The saltating particles gain velocity from the flow and usually follow ballistic-like trajectories back to impact the bed, causing the ejection of more particles at each impact (i.e., saltation bombardment).

Saltation occurs in a modified form on the bed below a rotor because the velocities and trajectories of the particles are also influenced by vortical flow and turbulent eddies produced by the rotor wake. Such effects can either slow or accelerate the local velocities of the saltating particles, changing their trajectories from the otherwise more parabolic or ballistic-like trajectories that would be obtained in a uniform flow. The process of saltation bombardment is a self-sustaining phenomenon that manifests as a significant increase in the airborne particle count at further downstream distances. The mobile layer of particles near the ground created by the creeping and saltating particles is referred to as a saltation layer. The particles in the saltation layer are generally susceptible to uplift from

the surrounding turbulence and fluctuating flow velocities (e.g., from a passing near-wall tip vortex).

More unique to the problem of brownout are the characteristic bursts of uplifted sediment that occur throughout the dust cloud. Besides the effects of pressure forces, for particles to move in the wall normal direction above the saltation layer they must entrained by an upwash region in the flow field, such as the upwash induced by an impinging vortex on the bed. As the upwash region induced by a vortex passes within proximity to the bed, particles within the saltation layer in this region are uplifted, i.e., through the mechanism of vortex-induced trapping. This latter phenomenon of particle uplift is a form of transport that is not generally observed in wind and riverine driven flows.

The bigger and heavier particles uplifted by the vortex flow are spun out by centrifugal forces unless they are captured by another vortical flow structure (i.e., a process termed secondary trapping), in which case they follow nominally ballistic trajectories back toward the bed. For the smaller particles, the flow velocities are sufficiently large to keep them in suspension in the particle field; particle suspension will occur when the balance of forces on the particle from the vertical flow and turbulent fluctuations in the surrounding flow is greater than the settling velocity caused by gravity. This process can continue as long as upwash regions remain present, and as more particles are suspended the probability of particles encountering these vortex-induced upwash regions becomes more likely. The result is swirling particle flows and a rapid overall accumulation of suspended particles near the rotor, with intense upward bursts of particles occurring as the vortices sweep over the bed.

Downwash regions present in the flow can also be responsible for mobilizing parti-

cles by means of bombardment of previously suspended particles back onto the bed. Such effects can be produced by the downwash from the rotor (e.g., a larger, global region of downwash directly below the rotor) or by the downwash from the passing vortices (e.g., a locally produced downwash). The particles can orbit around the vortex flow and then impact the bed, and the resulting impact is then responsible for dislodging and ejecting more particles into the saltation layer. Particles that are suspended much higher off the bed near the rotor plane can be reingested through the rotor, which causes the particles to be convected rapidly downward and produce particle bombardment on the bed. This process is similar in principal to saltation bombardment, but the generally higher velocities and momentum of the particles in this case ejects more new particles into suspension. Notice also that the point that a given particle impacts the bed is not necessarily limited to the regions in which particle mobilization and entrainment have been previously observed.

Reingestion bombardment can also occur at points directly below the rotor, ejecting particles in a region that would have otherwise seen relatively few particles being mobilized from the bed by the blade tip vortices. Interpretations of field observations [4, 5] suggest that helicopters that experience the reingestion of suspended dust through the rotor disk can produce some of the most intense and optically dense brownout dust clouds.

1.5 Literature Review

Brownout is clearly a complex, dual-phase fluid dynamics problem that requires a multidisciplinary approach to fully understand it. The fields that are relevant to the problem of brownout can be comprised into four main categories:

1. *Fluid dynamics*: The study of the flow produced by the rotor and how it is altered by the presence of the ground. The forces produced by the rotor wake are ultimately responsible for the mobilization and uplift of the sediment particles, and so a thorough understanding of the fluid dynamics of the rotor wake is it interacts with the ground and sediment bed is critical to the understanding of the resultant dual-phase flow.

2. *Particle physics*: The particles are susceptible to the surrounding flow environment, be it wind-driven, riverine, or rotor-induced flows. Understanding the resultant transport and deposition of these particles is a large research field in the aeolian sciences, although it is less understood in the context of a rotor flow, which is a much more three-dimensional and unsteady type of flow.

3. *Flight dynamics*: Rotorcraft are generally performing take-off and landing maneuvers when they are operating near the ground. As such, an understanding of how the flight path affects the formation of development of brownout clouds will be relevant to understanding how to mitigate brownout. As previously discussed, it is known that pilots may adopt certain tactics to manage the flight path of the rotorcraft relative to the ground to help reduce the probability of a brownout-related mishap.

4. *Human factors*: Pilots require certain visual cues and sensory inputs to safely operate the rotorcraft near the ground. Brownout clouds can reduce or eliminate these cues and also lead to false sensory inputs (such as relative motion) that can cause the pilot to lose situational awareness, which can jeopardize the safety of flight.

The first two categories (fluid dynamics and particle physics) involve studies of rotors operating near the ground and the processes that induce brownout dust cloud formation, and so a literature review was performed to thoroughly examine these areas of work. Prior work has been performed using various approaches, including overall brownout severity characterization, field tests, computational studies, and laboratory experiments. The present work investigates the dual-phase, rotor-induced flow from an experimental fluid mechanics standpoint, however, the multidisciplinary nature of the problem means that all approaches must be used to provide a full understanding to the problem of brownout. As such, the following literature review has examined four topics: (1) Brownout characterization, (2) Field tests, (3) Computational studies (including attempts at mitigation), (4) Laboratory experiments of rotors operating in single-phase and dual-phase flow environments.

1.5.1 Brownout Characterization

Despite the overall fluid dynamic and other complexity of brownout, the severity of the dust cloud and its rate of development can, at least to a first-order level of approximation, be correlated to certain geometric and operational parameters of the rotorcraft. Mulluzzo and Leishman [27] have used photographs and videography of brownout events combined with historical data for different rotorcraft to characterize the severity of brownout. As such, the study was partially subjective, but nevertheless it provided valuable insight into the brownout problem that could be used to guide more detailed experimental and computational studies. They showed that parameters such as disk loading,

blade loading coefficient, tip speed, rotational frequency, number of blades, and number of rotors could all affect the severity and rate of development of the dust clouds. In general, rotorcraft with higher average disk loadings and blade loading coefficients appeared to form the most severe dust clouds, while rotorcraft with more rotors and/or more blades and higher rotational frequencies tended to increase the rate at which the dust clouds were formed. The results ultimately showed that the primary factors that appear to correlate to the severity of brownout dust clouds, and also the rate at which they develop, are the average downwash velocities in the rotor wake, the blade tip vortex strengths, the total strength of the vortical wake, and the frequency at which tip vortices impinge on the ground (i.e., the wake shedding frequency). Ultimately, however, understanding how the geometric and operational parameters of the rotor affect the rotor wake developments and the interaction of the rotor wake with the sediment particles will provide a solution into how brownout clouds are generated. One of the goals of the current work was to perform a detailed examination of this rotor wake-ground interaction problem, and to characterize in detail how at least some of these rotor operating parameters can affect the processes of sediment particle mobilization and transport away from the bed.

1.5.2 Brownout Field Tests

One approach for characterizing brownout clouds is to perform tests on rotorcraft operating in brownout conditions. To this end, a number of flight tests have been conducted [4,5,28]. Full-scale brownout flight tests, however, are difficult to perform because of the many challenges associated in obtaining the needed measurements. A practical con-

cern also is that such flight tests can also be very expensive to conduct. Furthermore, the standard measurement techniques used to survey flow fields are generally more difficult to apply at full-scale. Also, the measurement techniques that can be used can be limited by pilot safety concerns (e.g., to use the lasers, sensor deployment, view obstruction, etc.). Because of these challenges, only limited measurements have been performed thus far, and so they do not provide the detailed quantitative information needed to truly expose the fundamental flow physics of rotor wake-induced particle motion. Nevertheless, field tests with rotorcraft in brownout conditions have provided valuable insight into the problem of brownout and have been used, to some extent, to validate computational models of the problem.

One of the first brownout flight test campaigns was performed by Rodgers [29] using a tandem configuration helicopter undergoing takeoff and landing maneuvers at various "dusty" locations. A total of 98 flight tests were performed that examined the effects of soil composition, hover height, and disk loading on the characteristics of brownout clouds. The dust was sampled by placing solenoid-operated samplers on the sides of the fuselage. It was found that the highest concentrations of particles were in the overlap region of the rotors, and takeoff and landing maneuvers significantly increased the concentration of dust. Furthermore, if multiple rotorcraft were operating in close proximity to each other then the resultant brownout cloud contained higher concentrations of dust particles. This study also showed that the dust cloud was comprised of relatively small particles, with no particles greater than 500 μm in diameter.

The DARPA "Sandblaster" program performed flight tests of helicopters performing various maneuvers in the desert [4, 5]. The primary goal here was to quantify the dust

cloud composition and densities for different rotorcraft platforms. A number of aircraft configurations and flight maneuvers were performed, including landing, takeoff, and taxi. Measurements of the cloud were performed by placing dust collectors (primarily bins and density samplers) a significant distance away to avoid any potential collisions with the aircraft. The collection of dust samples from the cloud, however, were biased by the effects of the ambient wind, which pushed the dust cloud towards the sensor locations. One issue that arose during testing was that such concentrated dust clouds were produced such that they exceeded the maximum capacity of a few of the collectors. A primary result of the study was the characterization of the particle sizes in dust cloud, which were, again, found to be relatively small. The study also indicated that rotorcraft with higher disk loadings tended to produce more concentrated dust clouds, but no detailed examination or quantification of the affects of rotor operating condition on the dust cloud development was performed.

Gilles et al. [30] performed a study to examine rotorcraft performing low level passes over a pre-prepared dust field. The dust field was equipped with three towers that each had several real-time dust monitors that collected data on dust emissions. They also placed sensors on the field that could measure pressure differentials on the ground, which they converted to a measure of the effective shear stress acting on the sediment bed. The main result from the study was that increasing vehicle forward flight speed decreased the quantity of dust emissions, resulting in less severe brownout clouds, though the rotor wake characteristics that was likely to have caused this decrease in severity were not exposed.

The flight test experiments performed by Wong and Tanner [28] used an imaging technique called photogrammetry to quantify the geometric shape and surface velocities

of the outside envelope of a brownout dust cloud generated by a helicopter during various maneuvers. Photogrammetry uses an array of cameras to simultaneously capture images of the location of objects in three-dimensional space, the different viewing axes of the camera are then used to triangulate the positions of these objects. The brownout experiments were conducted in two phases. Phase-one utilized two cameras, but they did not provide sufficient resolution to resolve the cloud geometry. Therefore, in phase-two, the experiments were conducted using six high-resolution cameras that were more also more carefully aligned. Identification of key reference points on the dust cloud were needed for the post-processing of the photogrammetry images, introducing some subjectivity into in the determination of the cloud shape. Tanner [31] further analyzed the data to measure velocities throughout the cloud. However, these images were taken with a relatively low temporal resolution, introducing significant uncertainties into the velocity estimates. While this latter study furthered the scope of brownout field tests, the detailed measurements that are required to quantify the fluid dynamic mechanisms that affected the development of the particle field were not practical.

1.5.3 Computational Studies of Brownout

A majority of brownout related research has focused on creating relatively sophisticated computational models that simulate the formation of rotor-induced dust clouds [8, 32–45]. The advantage of performing computational studies is that the resulting simulations (if they are to be believed) can provide insight into the various causes and effects of brownout, including the three-dimensionality of the dust cloud. But of course, these mod-

els contain many assumptions and modeling approximations (such as one-way coupling between the rotor wake and the particles), and thorough validation is still lacking. One difficulty in simulating brownout dust clouds is that the mathematical models must have the fidelity to resolve the detailed vortical structures and turbulent flow produced at the ground by the rotor wake, in addition to modeling the uplift and subsequent convection of billions of dust particles. Fluid modeling challenges also include the need to accurately represent the effects of unsteady boundary layers, wall-jets, shear layers, concentrated vorticity in the form of trailed tip vortices from the rotor, and also the effects of turbulence. The modeling of the sediment particles and their associated dynamics as they are convected in a highly three-dimensional unsteady flow further increases the complexity of these simulations, creating a very challenging computational problem.

Phillips and Brown [33] performed an Eulerian type of simulation of the fluid dynamics of helicopter brownout. The rotor wake was modeled using a vorticity transport model (based on a velocity-vorticity form of the Navier–Stokes equations) that calculated the evolution of the vorticity distribution over a structured mesh around the rotorcraft and near the ground. Most computational studies model particle transport in a Lagrangian sense, however, Phillips and Brown sought to simulate the dust cloud in an Eulerian reference frame that used the appropriate transport equations to estimate the particle densities within the cloud. The study examined single main rotor and tandem rotor configurations for simulated landings. They found that the single main rotor configuration produced an asymmetric dust cloud at moderate advance ratios, while the cloud produced by the tandem configuration was more symmetric. At lower advance ratios, the single main rotor configuration also generated a more symmetric dust cloud. The ground vortex formed by

both configurations caused the dust to be reingested by the rotor systems, which further accelerated the evolution of the dust cloud. This work, however, showed that some rotorcraft formed fairly symmetric dust clouds, which is not supported by brownout flight tests.

D'Andrea [34–36] used a surface singularity or panel method coupled to a form of free-vortex rotor wake model to simulate a rotor wake near the ground. The rotor wake simulation was then combined with a Lagrangian particle tracking method to simulate the evolving dust cloud. The particle simulation used a Bagnold-like threshold friction velocity criteria at the ground in which a certain threshold had to be met before any particles could be mobilized. This study examined the differences between a single main rotor configuration and a tiltrotor (side-by-side rotor) configuration. The results showed that the tiltrotor configuration produced higher concentrations of dust particles that were also reingested through the rotor systems, causing the rapid overall growth of the size and concentration of the dust cloud. Certain single main rotor configurations, however, were found to create a toroidal ground vortex that was convected radially outward, away from the rotorcraft, resulting in an area that was relatively free of dust in the pilot's immediate field of view. The results confirmed anecdotal evidence that suggests that different helicopters and rotorcraft produce different dust cloud particle concentrations and geometries.

Syal et al. [38, 46, 46, 47] coupled a free-vortex wake methodology with a Lagrangian based particle tracking algorithm to simulate brownout dust clouds for an isolated rotor. One of the goals of the work was to design an efficient architecture for a coupled rotor/particle method by using parallel programming, GPU processing, and particle clustering methods. The work aimed to simulate the dust cloud using fundamental particle

entrainment mechanisms that were seen from experimental work [7, 26] (discussed later), and also included effects such as particle bombardment on the bed. The particle entrainment model also included the effects of the unsteady pressures caused by the near-wall vortices. The study found that the inclusion of these fundamental physics were critical to the proper simulation of brownout dust clouds. However, like all the other brownout computational studies, the dual-phase flow was only one-way coupled in that the rotor wake caused the particle motion but the particles did not affect the development of the rotor wake; this simplifying assumption was made to significantly reduce the computational costs. The simulated brownout clouds were compared to the measurements obtained by Wong and Tanner [28], with reasonably good agreement. This study in particular showed the value of performing laboratory-scale experiments in that the overall agreement of the brownout clouds with field tests was significantly improved by incorporating the particle uplift mechanisms that were observed in controlled, smaller-scale experiments.

Other modeling studies have used computational fluid dynamics (CFD) simulations to model the rotor wake. Lakshminarayan et al. [40, 48] used a compressible Reynolds-Averaged Navier–Stokes (RANS) method with structural overset grids to compute the flow velocities produced by a small-scale rotor hovering over a ground plane. The overset meshes were used to better preserve the vorticity observed in experiments with the same rotor [16]. This work found that the vortices developed instabilities as they convected closer to the ground, creating a three-dimensional flow field that was not observed with a coarser mesh and also without an overset grid. This solver was then coupled by Thomas et al. [39] to a Lagrangian-based sediment tracking algorithm to examine the resultant dual-phase environment produced by the rotor when it was hovering over a sediment

bed. The results agreed well with the dual-phase experiments performed by Sydney and Leishman [7] (discussed in detail later). The representation of the dual-phase flow mechanisms observed in the experiments was critical in the validation of these computational models. These models will also benefit from further measurements that have examined the interdependent effects of rotor operating conditions, and also other complicating factors such as the presence of an airframe or body under the rotor.

Some simulations have also been used to investigate brownout mitigation strategies. Whitehouse et al. [41] used a free-vortex wake methodology to simulate a rotor wake and a Lagrangian method to simulate the transport of the sediment particles. This study considered a number of factors, including the scaling of brownout clouds and also the potential for mitigating these clouds. Their simulations showed that the bundling or pairing of vortices was primarily responsible for the vertical transport of sediment particles. These investigators also simulated the effects of blade devices that would alter the initial formation of the tip vortex, causing it to diffuse rapidly. These devices were shown to significantly reduce the vertical transport of sediment particles and, in doing so, potentially reduced the severity of brownout from the pilots perspective. This study used a threshold criteria to simulate particle mobilization but did not factor in the effects of particle bombardments or other important near-wall particle flow physics that experiments have shown to be critical to the formation and development of rotor wake-induced dust clouds.

Tritschler et al. [42, 43] performed a number of brownout mitigation studies using the model developed by Syal et al. [8, 38] where a free-vortex methodology to simulate the rotor wake was coupled to a Lagrangian-based particle tracking algorithm to simulate

the dust cloud. Tritchler et al. [42] developed a formal optimization approach that created a design space for the rotor (using various geometric parameters including blade radius, blade chord and twist rate) to minimize the severity of brownout clouds. A metric based on the number of particles in the pilot's field of view was used as a surrogate for the optical attenuation in the brownout cloud. The study showed that rotorcraft with higher downwash velocities generally produced less severe brownout signatures, an outcome contrary to initial expectations. While the higher downwash resulted in more particle entrainment into the rotor wake, the higher near-wall velocities convected the dust cloud rapidly away from the rotorcraft, resulting in a clearer field of view for the pilot. Tritschler et al. [49] also applied a similar methodology to optimize the flight path of the helicopter and found that the best approaches to reduce the severity of brownout were low /fast approaches (out pacing the developing cloud) and fast/steep approaches (landing quickly before the cloud could fully develop). This latter study showed that the higher downwash from the rotors convected the particles radially outward before they were uplifted, but this behavior has not yet been observed in experiments.

Syal et al. [50] also used the free-vortex/Lagrangian simulation methodology to study a potential blade design that would diffuse the vortices before they convected to the ground. In particular, a slotted tip design was examined, which uses internal channels to direct the air from the leading edge of the blade and out of the side edge of the blade [51,52], introducing turbulent mixing into the otherwise laminar core and so diffusing the vortices. The study used the measurements from Milluzzo et al. [52] to prescribe the core growth of the tip vortices, both from the baseline blade and from the slotted tip blade, as a function of time. The study found that the slotted tip design, or other device that could

diffuse the vortices, could potentially reduce the number of sediment particles that were vertically transported, resulting in fewer particles being reingested by the rotor disk.

1.5.4 Laboratory Experiments

While computational studies have provided insight to the problem of brownout, they require validation with experiments, which are lacking. Validation must include not only the details of the particle physics, but if they are to be confidently used for predictive purposes, then the near-wall aerodynamics produced by a rotor in ground effect must be faithfully reproduced. Most prior work to study rotors operating in ground effect have focused on the performance benefits that are gained when operating near the ground [9–16]. However, there have also been a number of studies performed to examine the single-phase and dual-phase flows produced by a rotor operating near the ground and over a sediment bed, respectively [7, 16, 17, 26, 52–57]. Most of these studies have been performed on an isolated rotor, though some of the studies have also examined the effect of an airframe or body that is placed in the rotor wake [58–61].

1.5.4.1 Rotors in Ground Effect

One of the earliest fluid dynamic studies of a rotor in ground effect was performed by Taylor [62] who recognized the need to visualize the airflow produced by a rotor operating near the ground if the performance benefits were to be understood. Taylor developed a flow visualization technique that involved using balsa dust that had a maximum settling rate of only 1 fts^{-1}. The method was used to visualize the wakes produced by a single

main rotor, a coaxial rotor system, and a side-by-side rotor system, however no quantitative measurements were obtained.

Fradenburgh [15] used smoke to visualize the wake of a small-scale rotor that was operating in ground effect. The smoke was introduced through nozzles that distributed the smoke just above the rotor system so that it was then entrained by the salient features of the rotor wake, namely the blade tip vortices. This study showed that in ground effect, each blade trailed a tip vortex filament that persisted to relatively old wake ages, and the vortices were convected radially outward when they reached the ground plane. A wake sheet was also observed to trail from the blades and convect axially downward within the slipstream boundary of the rotor wake. Again, no quantification of the flow was undertaken.

Light [53] performed a more quantitative flow field study of a rotor in ground effect that used a wide-field shadowgraph method to visualize the tip vortices. To perform the shadowgraphy, screens of retroreflective material were placed behind the rotor test stand. By marking the screens to determine the magnification factors, the shadowgraph images were used to obtain quantitative measurements of the tip vortex locations for various rotor thrusts, both out of ground effect and in ground effect operation. This study also found that the tip vortices initially contracted in the rotor wake but then rapidly expanded as the wake approached the ground. The measurements were also compared to a free-vortex wake rotor wake simulation, with reasonable correlation. While this study provided valuable information about the tip vortex trajectories, it did not provide the quantitative results needed to properly characterize the development of the tip vortices or the wake near the ground, which is critical to the problem of rotor-induced particle motion.

Curtiss et al. [63] examined the wake produced by a rotor operating in forward flight in ground effect at moderate advance ratios. These tests were performed by towing the rotor in an enclosed test track. As the rotor was moved over the ground plane, smoke was introduced below the rotor to visualize the flow, while simultaneous force and moment measurements were gathered. The study showed that the presence of the ground caused significant effects on rotor performance. The smoke flow visualization showed that the ground altered the rotor wake, from hover through low-speed forward flight. At lower advance ratios, a flow recirculation region was observed to form underneath the leading edge of the rotor disk. At higher advance ratios, the flow visualization revealed the formation of a stronger ground vortex just forward of the rotor disk, which was comprised of the bundling of the individual vortices trailed from the blade tips. A hot wire anemometer was used to measure the flow velocities within the ground vortex, showing that the ground vortex was almost order of magnitude stronger than the individual tip vortices. However, the flow measurements made in this study were somewhat limited.

Ramasamy et al. [17] conducted experiments using laser Doppler velocimetry (LDV) (a point measurement technique) to quantify the interdependence of viscous/turbulent diffusion and straining of rotor tip vortex filaments in the presence of a ground plane. The advantage of this laser-based technique is that it does not affect the development of the flow, and can measure all three components of velocity at a given point. The results showed that the presence of the ground caused the tip vortex filaments to strain and stretch along their axis. This process decreased the vortex core size and balanced the growth of the core resulting from turbulent diffusion. This study also showed that the vortices that developed with the rotor in ground effect operation could persist in the flow to much older

wake ages than for the equivalent out of ground effect flow, i.e, when the rotor operated at the same thrust but far away from the ground. The results were then used to develop a semi-empirical vortex model that combined the effects of turbulent diffusion as well as vortex stretching on the growth of the vortex core. While these measurements provided valuable information on the structure and development of tip vortices as they were affected by a ground plane, spatially and temporally resolved flow measurements are required to properly characterize the interaction of the vortices with the wall and, ultimately, with a sediment bed.

Ramasamy et al. [54] continued the study of rotor tip vortices by examining the formation and evolution of the tip vortices produced by a one-bladed rotor by using dual-plane stereoscopic particle image velocimetry (DP-SPIV). This technique uses two laser light sheets to illuminate closely spaced parallel planes in the flow, allowing for the measurement of all the components of velocity and also the nine components of the velocity gradient tensor. The study particularly focused on the turbulent flow features present during the roll-up of the vortices and how these features affected the final evolution of the vortices. The relatively high resolution of the measurements revealed a wake sheet that formed at the trailing edge of the blade, which consisted of counter-rotating Taylor-Görtler vortical pairs. The results also showed that the turbulence within the vortex was not isotropic and that stress cannot not be represented as a linear function of strain. The results showed good correlation with the LDV measurements, confirming that PIV is suitable for turbulence quantification. The relatively high spatial resolution of these measurements helped to characterize the detailed structure of the vortices, but time-resolved measurements are needed to fully understand the evolution of the vortices.

Lee et al. [16] explored the aerodynamic flow field generated by a small-scale rotor operating at several heights above a ground plane, quantifying the evolution of the wake as it interacted with the ground. The study used flow visualization to determine the overall structure of the wake and particle image velocimetry (PIV) to measure the flow velocities within the wake. While this study significantly advanced the knowledge of rotor wakes that develop near the ground, it was limited by the resolution and capture rate of the measurement equipment. It was found that when the rotor was relatively high above the ground ($\approx 2R$) the tip vortices diffused before they could reach the ground. However, when the rotor was at lower heights, the stretching of the vortices reintensified their vorticity and caused them to persist in the flow and also interact with each other at older wake ages. Of particular interest was that the tip vortex trajectories near the ground were found to follow aperiodic trajectories, never following the exactly same path from one rotor revolution to another. While this study focused on the interaction of the vortices with the ground and characterized the effects of different rotor heights (an important factor for rotor-induced particle motion), it did not examine the three-dimensional time-history of the flow.

Milluzzo et al. [52] used PIV to measure the evolution of tip vortices for different blade tip shapes that developed in ground effect in an effort to quantify how the blade tip shape may affect the flow at the ground. This study examined four different blade tips, a baseline rectangular tip, a swept tip, a BERP-like tip, and a slotted tip (mentioned previously). The goal of the research was to diffuse the vortex before it convected to the ground, and to examine whether the change in the flow structures might help to mitigate the problem of brownout. The velocity profiles in the boundary layer flow as it developed

along the ground plane were measured. The core size and velocity profile of the tip vortices for each blade tip shape was extracted from the measurements, as well as the resultant flow velocities in the near-wall region. The results showed that the rectangular and swept tips produced relatively strong vortices that persisted to older wake ages. The BERP-like tip trailed a more diffused vortex initially, but this vortex was reintensified as it expanded radially along the ground. The slotted tip injected turbulence into the vortex core as it formed in a way that fundamentally altered its evolution, to the point where the stretching of the filament could not counteract turbulent diffusion of vorticity, and so producing shallower velocity profiles at the ground. The measurements showed the importance of the tip vortex-induced flows on the development of the rotor wake near the ground, but did not to resolve the temporal evolution of the flow.

Geiser and Kiger [64] studied the evolution of vortices with a simplified version of a rotor flow over a ground plane by using an axisymmetric forced jet to create a downwash flow and a toroidal vortex ring. While this flow removes many of the complexities associated with the helicoidal nature of rotor wakes as they develop near the ground, it did give more controlled and repeatable vortex/wall interactions. Using PIV, this study found that the flow was much more periodic compared to a rotor flow. The measurements also showed that as the vortices impinged on the ground, they interacted with the boundary layer, causing it to momentarily detach from the ground and roll-up into a secondary counter-rotating vortex.

Later, Geiser and Kiger [65] used the same experimental set-up to examine the three-dimensionality of the flow in both horizontal and vertical cross-sections. This study focused on the breakdown of the vortex filaments and how the evolution of the filaments

was altered by a small radial fence placed on the ground plane; the purpose of the fence was to simulate natural protuberances that form in the sediment bed during rotor-induced particle motion. The study found that without the fence, the vortices spun down under the action of turbulent diffusion. However, the presence of the fence precipitated the formation of secondary and tertiary vorticity that caused the vortex filament to develop complex instabilities and radial asymmetries. These measurements show that even relatively simple flows, such as a toroidal vortex ring, can induce complicated, three-dimensional interactions near the ground.

1.5.4.2 Rotor/Body Interactions

In practice, rotorcraft will also have some form of airframe or body that is generally inside the boundaries of the rotor wake. As such, there have been many studies performed in the field of rotor/body aerodynamic interactions; a summary of this work can be found in Leishman [66]. Most of these studies have involved the use of pressure sensors to measure the unsteady loads that are produced on the surface of the fuselage in the presence of the rotor [66] with little work examining the actual fluid dynamic interactions of the rotor/body system [58, 60, 61]. However, there have been relatively few studies of rotor/body aerodynamic interactions in ground effect.

Measurements of the unsteady pressure fluctuations induced on a body by a rotor was performed by Bi et al. [59]. The rotor and body were tested in hover (away from the ground) and also in forward flight in a wind tunnel. The body was equipped with pressure sensors that could measure the unsteady pressures caused by the impingement of the tip

vortices on the body. The study found that the flow interaction was extremely unsteady and complex, with large amplitude variations from the mean surface pressure. As such, the study concluded that these unsteady pressure effects must be included in modeling of the rotor/body interaction problem.

Crouse et al. [58] used pressure sensors to measure the unsteady loads on a body surface, which was supported by the development of a theoretical model based on potential flow assumptions. It was found that unsteady effects needed to be incorporated in the model to predict the observed effects. Flow visualization using shadowgraphy indicated that the tip vortices convected at a fairly constant skew angle until they approached the body surface, at which point the skew angle gradually increased and the vortices were found to drape over and convect along the upper surface of the body. By prescribing the paths of the vortices, it was shown that the modeling gave very good agreement with the measured pressure signatures. It was concluded that the development of a better rotor wake model was key to the prediction of rotor/airframe aerodynamic interactions. While the flow visualization and shadowgraphy provided good insight into the interaction of the filaments with the body, there was no quantification of the actual flow velocities caused by the presence of the body in the rotor wake.

Bagai and Leishman [60] also used the shadowgraphy technique to perform a more comprehensive visualization of the rotor/body interactions. This work also obtained quantitative information on the tip vortex trajectories from the shadowgraphy results, which was performed with and without the presence of the body. The results showed that the body caused significant changes to the radial contraction and axial displacements of the tip vortices. In general, the interaction of the filaments with the body were found to sig-

nificantly distort the development of the wake. While the results did not conclusively show the three-dimensional displacements of the filaments, they suggested that the impingement of the filaments on the upper surface of the bodies caused the filaments to form hairpin-type loops around the body.

More recently, Hance [61] performed PIV measurements of the flow produced by hovering rotor in ground effect in the presence of a body. Three generic bodies were examined with cross-sections that were circular, elliptical, and quasi-rectangular, respectively. The results showed that the flow over the nose of the bodies developed relatively unimpeded by the presence of the body, however, because the wake directly impinged on the upper surface of the tail of the bodies it caused a severe distortion to the wake developments. The resulting flow velocities at the ground were found to be different for all three body shapes. This study, however, only made flow measurements along the centerline of the body, and the three-dimensional flow variations caused by the bodies were not examined.

1.5.4.3 Aeolian Flows

The fundamental mechanisms of particle mobilization and the resulting dusty flow produced under the action of the wind has been studied in detail in the aeolian sciences [21–25, 67–69]. Many of these studies have used experimental information to develop theories and models that can better predict the onset of particle mobilization and the subsequent transport of the particles downstream. Bagnold [21] identified that the flow must induce a threshold shear stress at the ground for particles to be mobilized, this

threshold being dependent on particle size. Greeley and Iverson [24] built on his work by incorporating inter-particle forces, recognizing that the aerodynamically generated forces must overcome both the weight and the inter-particle forces if they are to be entrained by the flow. Shao and Lu [68] simplified the Greeley and Iverson model to better represent the physical forces that are at play the processes of sediment mobilization and transport.

Shao [67] developed anther model that included the effects of saltation bombardment, the principles based conservation of energy and momentum during particle bombardment with the mobile bed. Particles bombarding the ground with a certain amount of energy and momentum that will eject a volume of particles from the sediment bed, creating a local crater in the bed. This model, however, was rather complicated and so Shao [69] introduced a simpler model that still captured the fundamental particle dynamics of saltation bombardment. These models were later used by Syal [8, 46, 47] in the study of rotorcraft brownout.

Haenel and Dade [70] measured the dual-phase flow environment produced by a jet flow impinging on a sediment bed consisting of so called "cohesionless" particles. They measured the flow velocities and entrainment flux of the particles. The results showed that the erosion of the bed could not be predicted based on the time-averaged flow velocities, but the erosion correlated well with the turbulent shear stress near the ground. The flow induced by a jet impinging on a sediment bed was found to significantly alter the rate at which particles were mobilized and entrained, in comparison to a wall-parallel, boundary layer type flow. The study also characterized certain unsteady turbulence quantities, such as the turbulent kinetic energy and Reynolds shear stress in an effort to examine how they affected the entrainment rate and threshold mobilization criteria of the particles. This

study, however is relatively simple compared to the flow produced by a rotor and does not include the complexities introduced by the presence of coherent vorticity near the sediment bed.

Mulinti and Kiger [71] performed dual-phase experiments using the same forced impinging jet as in earlier work [64]. The goal of the experiments was to characterize the mobilization of sediment particles under the action of a simpler and more repeatable flow, i.e., it was less complicated than a rotor wake. PIV was used to measure the velocities of the impinging jet and particle tracking velocimetry (PTV) was used to obtain the velocities of the particles in the dispersed-phase. The results showed the formation of deflation regions where the vortices impinged on the sediment bed and dune regions where the sediment was redeposited. The study also calculated the wall-parallel and wall-normal fluxes and showed that particles primarily convected radially outward, though there were local uplift events caused by the near-wall vortices that convected some particles into suspension. Near the ground, negative vertical flux values were caused by secondary counterrotating vorticity that was produced by the impingement of a primary vortex. The results showed that the near-wall vorticity played a strong role in the mobilization and transport of sediment.

Johnson et al. [26] used flow visualization and time-resolved PIV/PTV to examine the single-phase and dual-phase flow environments produced by a two-bladed, small-scale rotor system that was hovering over a ground plane and a sediment bed, respectively. For the dual-phase flow experiments, two different types of sediment were deposited below the rotor; both sets of particles were tetrahedral/granular in shape (similar to sand). The relatively high resolution results near the ground showed that the vortices aperiodically

interacted with each other by pairing and/or merging together. When the vortices convected close enough to the ground, they were observed to interact with the boundary layer, causing a local flow separation region just upstream of the vortex location. The dual-phase measurements showed that the vortices were primarily responsible for mobilizing and uplifting sediment through the mechanism of vortex-induced trapping. Other mechanisms that were observed were saltation, saltation bombardment, and reingestion bombardment, the latter being responsible for ejecting large quantities of particles into the near-wall flow. This study, however, used particles of non-uniform shape and provided mostly qualitative results of the rotor wake interaction with the sediment bed.

Sydney and Leishman [7] built on the work performed by Johnson et al. [26] by performing quantitative, dual-phase flow visualization, PIV, and PTV on the flows produced by one-bladed and two-bladed rotors hovering with the rotor plane at varying heights off the ground. The particle species included three size ranges of well-characterized glass microspheres. Time-histories of the rotor wake interactions with the bed were obtained, providing a better understanding of the transient processes and mechanisms that lead to the mobilization and uplift of particles from the bed. The flow measurements confirmed five mechanisms of particle uplift and transport: 1. Creep, 2. Modified saltation and saltation bombardment, 3. Vortex-induced trapping, 4. Reingestion bombardment, and 5. Secondary suspension. Greater levels of particle entrainment were found to occur near the wake impingement zone on the bed, mainly from the localized effects of the blade tip vortices. Once entrained, the PTV showed that significant numbers of particles were intermittently trapped in the vortex-induced upwash field. The pairing and merging of adjacent turns of the vortex wake was seen to affect particle mobilization and to enhance

secondary particle suspension. The bombardment of previously trapped particles back onto the bed by the flow was shown to be a primary mechanism responsible for liberating new particles into the flow.

This latter study significantly advanced the understanding of rotor wake interactions with a sediment bed, but only examined an isolated rotor (i.e., it did not include the effects of a airframe or body in the wake) and with the rotor at one operating condition. Furthermore, this study only investigated the dual-phase flow environment in one vertical measurement plane. Because rotor-induced particle motion is a three-dimensional problem, additional cross-sections of the wake will be required to better quantify the three-dimensional developments of the rotor wake and the induced particle field.

Reel [56] investigated the effect that the near-wall low pressure regions caused by convecting vortices had on the mobilization and transport of sediment particles. This study started off by noticing that Sydney and Leishman [7] had identified movement of particles directly towards the cores of passing vortices, i.e., their trajectories deviated significantly from surrounding flow velocities and were at times almost perpendicular to the local flow direction. To further investigate this observation, pressure sensors were installed on the surface of a ground plane that was placed below a hovering rotor and used to measure the time-history of the surface pressures caused by the impinging rotor wake. The study examined the effects of vortex strength and vortical shedding frequency on the unsteady pressure response, and found that the vortices induced a significant suction pressure on the ground. This work also included dual-phase experiments under the same operating conditions, and showed that certain particle movements could be correlated to the unsteady pressure field, i.e., the existence of a so-called Saffman pressure force that

acted on the particles, which could contribute to the plume-like formations observed in rotor-induced particle fields. Similarly to other dual-phase flow experiments using rotors, this study only examined a vertical cross-section of the rotor wake and, therefore, did not investigate the three-dimensional effects that are potentially induced by the near-wall tip vortex flows.

Recognizing the need for a scaling study for the problem of rotor-induced particle motion, Baharani [72] examined the effects of specific scaling parameters on the dual-phase flow environment produced by a hovering rotor. Five non-dimensional scaling parameters, often used in the field of aeolian sciences, were selected: 1. Particle diameter-to-rotor radius ratio, 2. Particle-to-fluid density ratio, 3. Ratio of characteristic flow (or wind) speed to particle terminal speed, 4. Densimetric Froude number, and 5. Threshold friction velocity ratio. The effects of these scaling parameters were examined by performing tests on a number of different particle species with varying compositions and sizes. This study showed that the quantity of particle entrainment and uplift was significantly affected by the particle-to-fluid density ratio, and the flow was also sensitive to changes in the particle diameter-to-rotor radius ratio. The present study has used the work performed by Baharani to carefully select the operating parameters of the rotor and also the characteristics of the particles that comprised the sediment bed.

Rauleder and Leishman [19, 20] performed a number of PIV and PTV analyses to examine the turbulence in the wake produced by a hovering rotor, and how turbulence affected the dual-phase flow environment. One of the goals of the study was to investigate the boundary conditions that might be required for the development of entrainment models for rotor-induced particle flows. They showed that the turbulence characteristics

of a rotor wake significantly differed from that of a wall-jet like flow. The presence of coherent tip vortices caused the production of turbulence and high levels of Reynolds shear stress near the ground. Furthermore, It was shown that the vortical flow below the rotor could be significantly altered by entrained sediment particles, suggesting a significant coupling between the carrier and dispersed phases.

Nathan and Green [57] performed measurements of the dusty flow produced by rotor operating in a wind tunnel. While the boundary conditions for this experiment were not representative of a rotor translating in forward flight over a stationary sediment bed, the results provided some insight into the particle fields that can be produced upstream of a rotor when operating in brownout conditions. As shown previously by others [63, 73, 74], the measurements showed that the vortices bundled together to create a larger "super vortex" upstream of the rotor, which contained the combined vorticity of all the individual vortices. This super vortex was shown to recirculate the particles back into the rotor disk. However, the measurements did not discriminate between the carrier and particle phases of the flow. This study only performed dual-phase flow visualization, and so it did not extract the quantitative information needed (i.e. simultaneous flow and particle velocities) to characterize the carrier-phase and dispersed-phase flows.

1.6 Objectives of the Present Work

The foregoing literature review has summarized prior research that is relevant to the problem of rotor-induced particle motion. Most of the previous work has been of a computational nature, and while these models are continually improving they still re-

quire much experimental validation to be confidently used as predictive tools. Furthermore, these models also tend to predict more regular, dome-shaped clouds, which are not observed in practice. The field tests that have been performed on full-scale rotorcraft encountering actual brownout conditions have been limited in scope because of the challenges associated with performing measurements at this scale. While the prior work performed at laboratory scale with smaller rotors operating over mobile sediment beds have been useful in identifying the potential mechanisms involved in brownout, a number of unanswered questions remain. For example, the effects of various changes to the rotor operating conditions, or the effects of a fuselage/body shape. Furthermore, rotor-induced particle clouds tend to be extremely three-dimensional, often with distinct columnar, plume-like structures, the formation of which have not yet been understood.

The primary objectives of the present work are to: 1. Quantify the underlying physics of rotor-induced particle motion in controlled single-phase and dual-phase flow environments, i.e., with and without sediment particles; 2. Investigate, in detail, the fluid dynamic flow mechanisms that cause the formation of three-dimensional, plume-like structures within rotor-induced particle fields; 3. Examine how rotor operating conditions affect the fluid dynamics of the rotor wake, as well as the development and evolution of the particle field; 4. Investigate the transient interactions between the rotor wake and an airframe/body, and how such interactions can affect the development of the particle field. Specific focus in this work was placed on quantifying the three-dimensional evolution of the tip vortex filaments as they interacted with each other, with the body, and also with the flow at the ground.

1.7 Organization of this Dissertation

This research work comprises a detailed investigation of a rotor wake interacting with a mobile sediment bed, leading to an overall better understanding of the mechanisms that underlie the formation of brownout dust clouds. The main problem of rotorcraft brownout has been introduced in the present chapter, which is the principle motivation behind this work. The basic fluid dynamics of rotors operating near and away from the ground were discussed, along with the physical mechanisms that are already known to be involved in rotor-induced particle mobilization. A literature review was conducted on brownout characterization, brownout field tests, computational studies (including attempts at mitigation), and laboratory experiments. The review showed that there were many aspects to the problem of rotor-induced particle motion that have not yet been studied, including the three-dimensional aspects of the problem and how this was affected by the rotor operating conditions and the presence of a body.

The remainder of the dissertation is divided into three chapters. Chapter 2, the next chapter, describes the experimental techniques used to examine the single-phase and dual-phase flow environments induced by a rotor operating near a ground plane and over a mobile sediment bed. The techniques of flow visualization (FV), particle image velocimetry (PIV), and particle tracking velocimetry (PTV) are explained. The chapter also reviews the operating conditions that were tested, and why. Finally, Chapter 2 gives a description of the technical challenges associated with performing flow measurements with a rotor operating near a solid boundary.

Chapter 3 discusses the results of the present work. This chapter is divided into

three sections; each section first discusses the single-phase flow results, which is then followed by a discussion of the corresponding dual-phase flow results. The first section discusses the primary fluid dynamics of a rotor operating near the ground, including the quantification of the vorticity in the flow and how this vorticity causes particle mobilization and uplift events. This section also describes results from the study of the three-dimensionality of the rotor-induced particle field. The second section in Chapter 3 discusses results from a comparative study on the flows produced by one-bladed and two-bladed rotors operating at different disk loadings and blade loading coefficients, the goal being to understand how the rotor operating condition may alter the flow environment near the ground. The third section in Chapter 3 describes results that compare the rotor wake of an isolated rotor to the flow produced by body between the rotor and the ground. Results for three-different body cross-sectional shapes were obtained to help characterize how, in practice, an airframe could potentially affect the problem of brownout.

Chapter 4 states the conclusions that were derived from the present work. While this work has improved the understanding of the fluid dynamics involved in the problem of rotor-induced particle motion, there remain several avenues of research that can further this understanding. Therefore, Chapter 4 provides a number of suggestions for potential future work.

Chapter 2

Description of the Experiments

This chapter provides a description of the experiments and the instrumentation used to better understand the problem of rotor-induced particle motion. A description of the experiment is given first, followed by an explanation of the particle image velocimetry (PIV) and particle tracking velocimetry (PTV) experiments that were performed. The chapter provides a detailed explanation of the testing procedures that were used in the present work, along with a description of the challenges that are associated with studying rotor-induced dual-phase flow fields.

2.1 General Description of the Experiments

The experiments were conducted using a laboratory-scale rotor that was operated in simulated hovering flight over a ground plane covered with a mobile sediment bed. The purpose of the experiments was to better understand the formation and development of rotor-induced flows and particle (dust) fields, and hence the physical mechanisms that are likely to underlie the problem of rotorcraft brownout.

Several types of experiments were performed in the single-phase flow environment (i.e., with no sediment or dust) as well as in the dual-phase flow environment (i.e., with suspended sediment particles). Another important goal of the study was to examine how the rotor configuration (to the degree to which this could be examined), the rotor oper-

ating state, and a body representing an airframe in the wake of the rotor all affected the mobilization and uplift of particles from the bed. To this end, a comparative study was performed that varied the rotor operating conditions in both the single-phase flow and the dual-phase flow environments.

In particular, the current work has examined the effects of one-bladed and two-bladed rotors, the effects of disk loading (DL), and blade loading coefficient (C_T/σ), and also the effects produced by different fuselage cross-sectional shapes in the wake below the rotor. These studies were performed by measuring the flow fields using PIV and PTV techniques. The PIV/PTV measurement planes were aligned in various vertical and horizontal orientations with respect to the rotor to obtain a better understanding of the three-dimensionality of the rotor wake developments and also of the rotor-induced particle fields.

2.2 Testing Facility

The experiments were performed inside a dust chamber. This chamber was specially designed to provide a controlled environment for the experiments. The chamber also protected the measurement equipment from contamination by airborne particles. A photograph of the dust chamber is shown in Fig. 2.1, with a corresponding schematic being shown in Fig. 2.2.

The chamber was a 2-by-2-by-2 meter cube, the frame of the chamber being constructed using slotted aluminum beams. Large Plexiglas sheets were seated inside the slots to provide optically clear walls, which gave minimal laser light attenuation and an

Figure 2.1: The specially built dust chamber in which both the single-phase and dual-phase flow experiments with the rotor were performed.

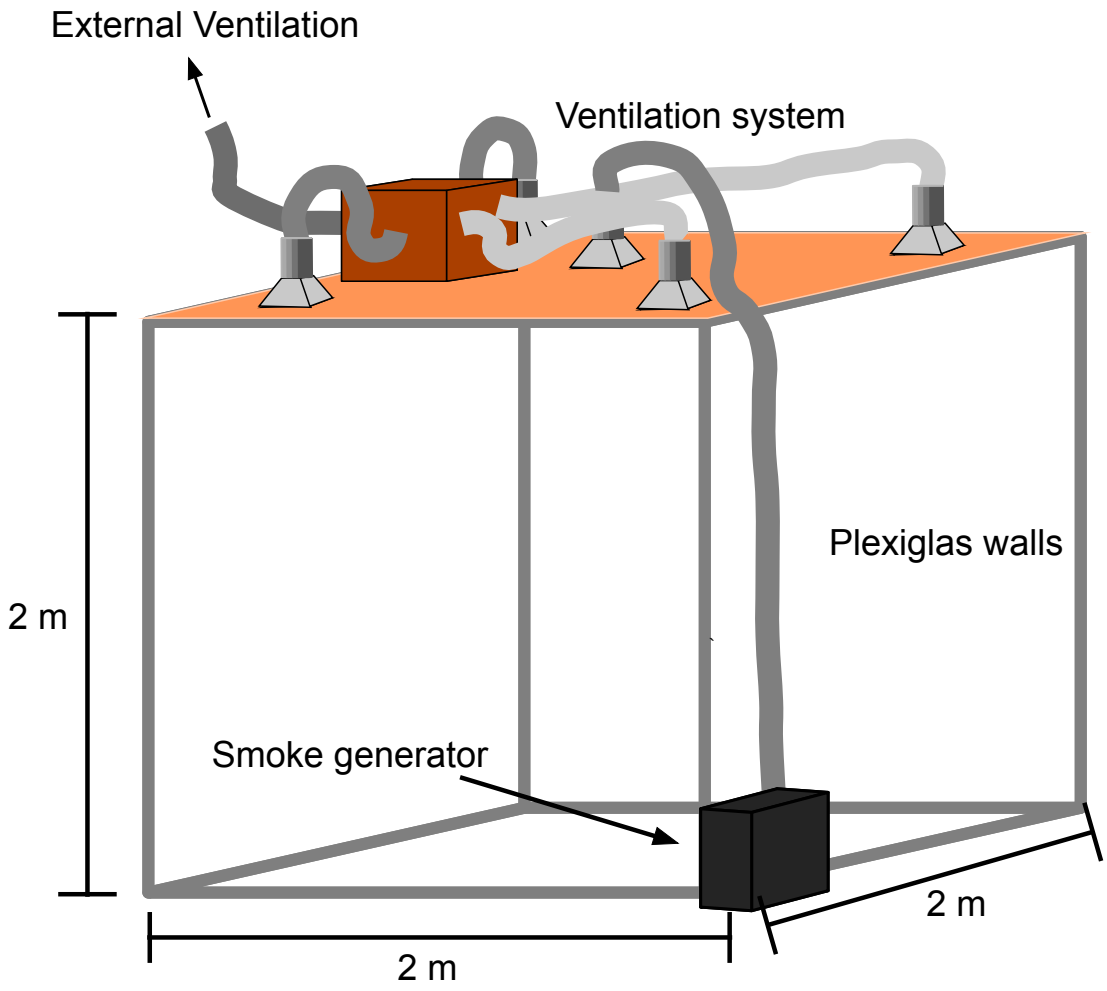

Figure 2.2: Schematic of the dust chamber.

unobstructed view of the test set-up. The chamber was sealed such that dust particles remained within the confines of the test cell. Specific portions of the dust chamber were also lined with a non-reflective black material to minimize background laser light reflections.

The dust chamber was equipped with a ventilation system that could control the concentration of seed particles within the chamber and also evacuate suspended dust particles between tests; see Fig. 2.3. A single vent was installed at the center of the ceiling to introduce smoke (or seed) particles into the test cell. Upon entering the chamber, the seed

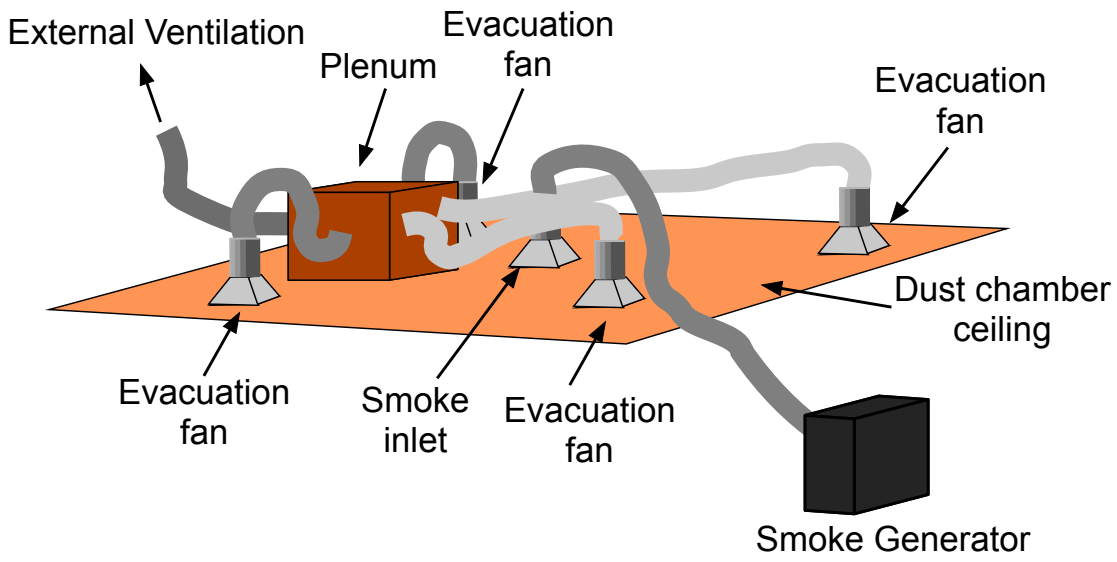

Figure 2.3: Schematic of the dust chamber ventilation system.

was passed through a honeycomb flow straightener to reduce the natural turbulence in the flow. For ventilation and evacuation of the smoke, four fans were attached to the ceiling of the chamber; all four fans were ducted to a single plenum that had a single exit vent. The exit vent was equipped with a fan to direct the air to an external ventilation system and so safely transport the seed and sediment particles outside of the test facility.

The 8 m^3 volume of the chamber was, by design, sufficiently large based on rotor radius to facility dimensions to minimize flow recirculation from the rotor during the duration of each test. The ratio of the length of the dust chamber to the rotor radius was approximately 24, allowing the rotor to be placed approximately $12R$ away from the nearest wall. Flow diverters where also placed along the periphery of the ground plane that directed the flow downward toward the floor of the dust chamber, effectively providing a longer travel distance to increase the time-scales for the onset of any possible flow recirculation in the chamber; see Fig. 2.4.

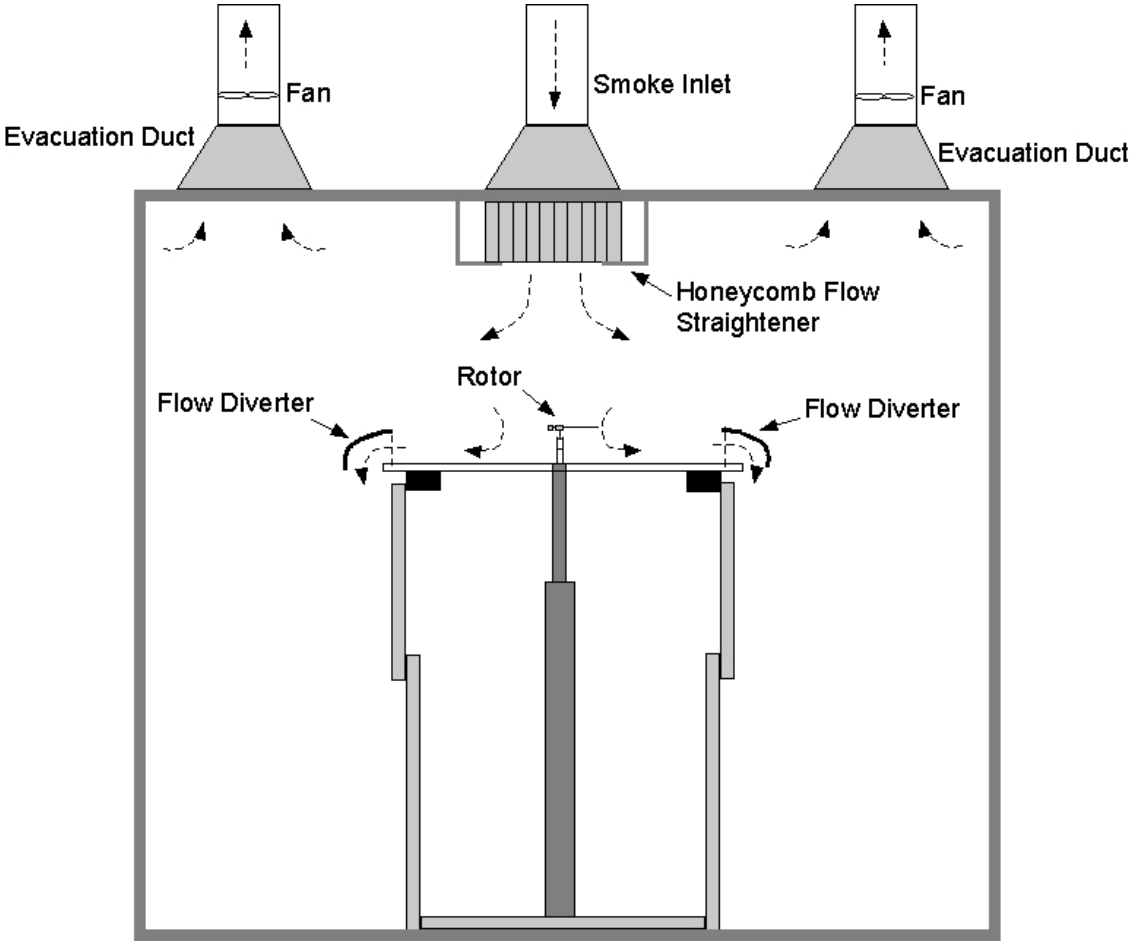

Figure 2.4: Schematic of the flow within the dust chamber.

2.3 Experimental Setup

A small rotor, with a radius of 85 mm (3.346 in) and a blade chord of 18 mm (0.71 in), was used to generate the rotor wake for the experiments. The blade cross-sectional shape was a thin, cambered plate airfoil with a thickness-to chord ratio of 3% with a sharpened leading edge. At the relatively lower chord Reynolds number of the current experiments (only 40,000 at the blade tip), these blade shapes have been found to be preferable in terms of aerodynamic performance [55]. The blades were attached to a teetering rotor hub that could be used in either a one-bladed or a two-bladed rotor

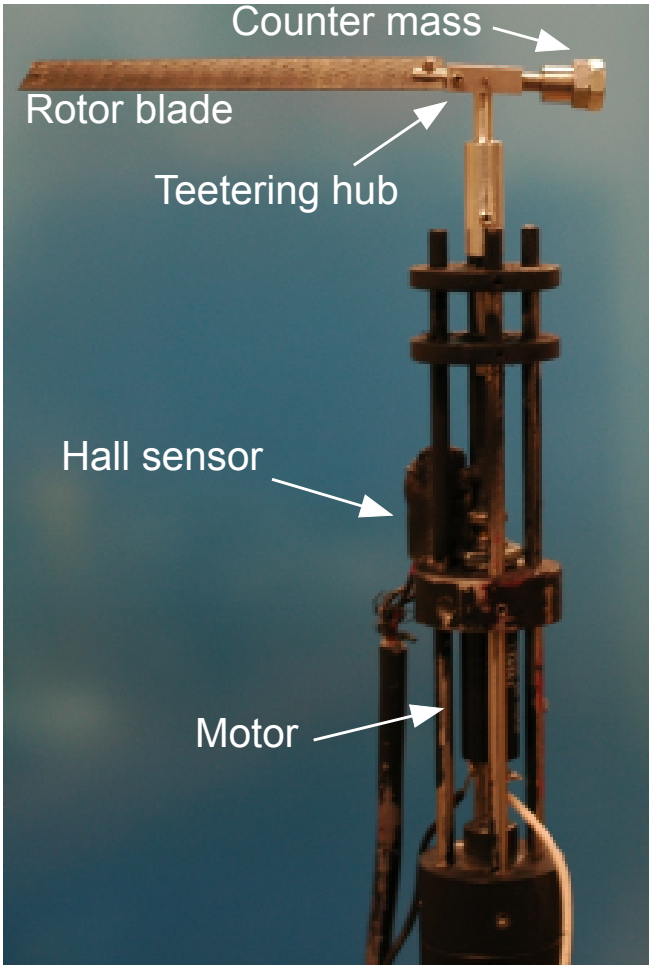

Figure 2.5: Photograph of the rotor system used for the experiments shown in a one-bladed configuration.

configuration; one of the blades could be exchanged for an equivalent counter-mass to produce a one-bladed rotor. A photograph of the rotor in its one-bladed configuration is shown in Fig. 2.5, with a corresponding schematic in Fig. 2.6. The rotor hub was designed such that each blade could be continuously varied in pitch to create the required thrust, the pitch being set manually. A schematic of the overall set-up used for the experiments is shown in Fig. 2.7. Notice that the rotor was mounted from the ceiling of the dust chamber so that a fuselage or body could be mounted in the wake of the rotor.

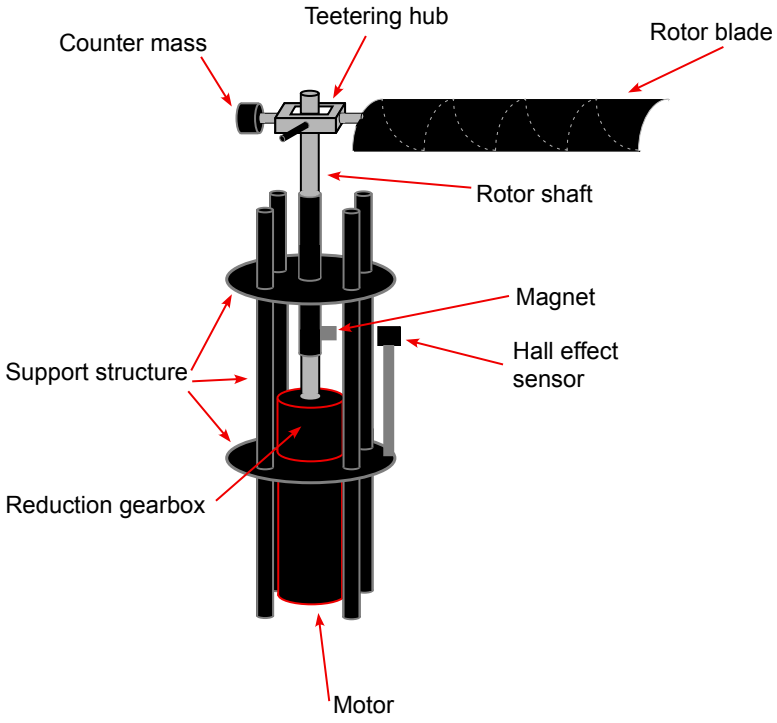

Figure 2.6: A schematic of the rotor system used for the experiments shown in a one-bladed configuration.

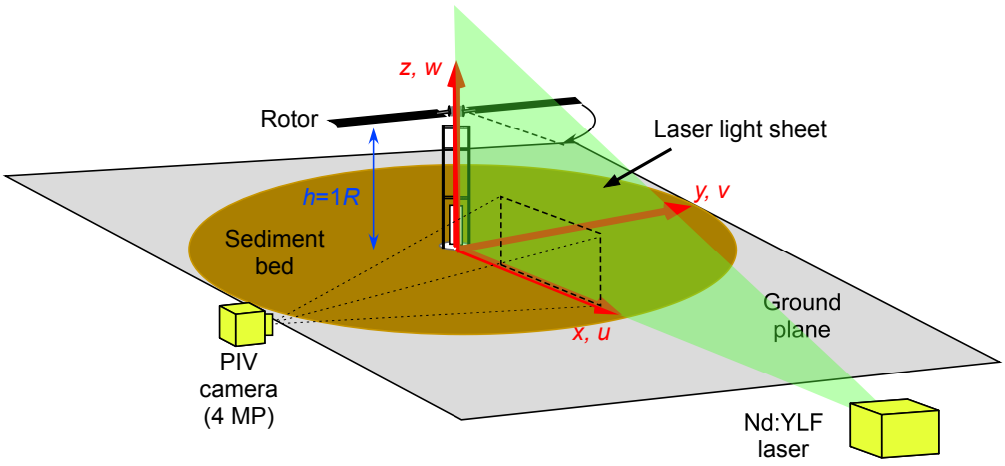

Figure 2.7: Schematic of the experimental setup with the laser illuminating a vertical plane in the flow.

The rotor hub was connected to a shaft adapter by using a steel pin. This hub was then directly attached to the rotor shaft. An adapter was also used between the rotor shaft and the motor shaft to transfer the torque from the motor to the rotor. The motor used was a precision brushless direct current motor that was operated using a speed controller. A small magnet was mounted to the rotor shaft and passed by a Hall-effect sensor, creating a one-per-rotor revolution signal that was used to control the rotor speed. A matte-black cowling was placed around the rotor and motor assembly to minimize laser reflections and to protect the various components from the heat of the laser light.

A ground plane that was $4R$ in diameter was supported from below. This ground plane was constructed from a flat, hardened thermoplastic resin in the shape of a circular plate and was then painted matte-black to reduce laser reflections. Both the rotor and the ground plane were adjustable relative to each other such that the height of the rotor plane from the ground could be varied. The present experiments were all performed with the rotor hovering at one rotor radius above the ground (i.e., at $z/R = 1.0$). For the dual-phase flow experiments, sediment particles were distributed on the ground plane in the shape of a circular bed. The particles used in the dual-phase experiments (discussed later) were loosely deposited to a thickness of 1 cm and leveled using a scraper prior to each test.

2.4 Seeding and Sediment Particles

Submicron smoke particles were used as seed for the carrier flow, i.e., for the rotor wake. These particles were produced by vaporizing mineral oil within a heat exchanger and mixing it with high-pressure nitrogen. This gaseous mixture was then ejected out of a

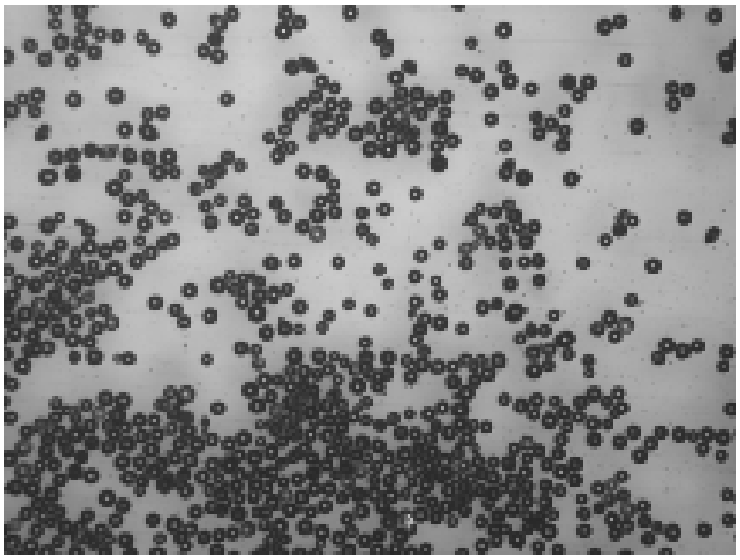

Figure 2.8: Microscope image of the glass microspheres.

nozzle into the ambient air, causing the oil to rapidly condense into submicron particles; 95% of these particles were 0.2 μm in diameter and they were small enough to follow the flow without significant tracking errors [75].

For the dual-phase flow experiments, sodaglass microspheres were used to represent the sediment particles. All the particles were nominally spherical in shape, and were carefully characterized in terms of their size and mass [72]. For the current experiments, the particles were 45–65 μm in diameter; see Fig. 2.8. Further details on these particles can be found in Appendix A. These particles gave good mobility, could be readily uplifted by the rotor flow, and were similar in size to particles found in actual brownout conditions [5, 7]. Furthermore, brownout specific scaling studies have been performed on these particles [72] and have found that the similarity parameters used to better represent full-scale particle dynamics, such as the ratio of the particle density to the fluid density (ρ_s/ρ), are matched relatively well using sodaglass microspheres of this diameter;

see [72] for more details on the scaling considerations for rotorcraft brownout.

An X-ray sedigraph method was used to characterize the particle size ranges [72]. This technique involved measuring the settling rates of different sized particles under the force of gravity in a liquid with known properties. The particle size could then be calculated from the measured settling velocity by using Stokes' law. The X-ray sedigraph was able to characterize both the size range of the particles and the mass frequency of each particle diameter, as documented in Appendix A.

For the PIV experiments, the 0.2 μm diameter seed particles were introduced in the dust chamber and uniformly mixed so as they could be used to obtain good cross-correlations between the PIV image pairs. The seed particles were also sufficiently small to allow good phase discrimination from the larger (about 50 μm in diameter) sediment particles used in the dual-phase experiments. A light intensity thresholding process was used to separate the carrier and dispersed phases (explained in detail later). This process was dependent on the differences in the Mie scattering signature produced by each particle, with the carrier-phase (the seed particles) giving a lower reflective intensity than the dispersed-phase (the sediment particles).

2.5 Instrumentation

A particle image velocimetry (PIV) system was used to measure the time-history of the rotor-induced flow in both the single-phase and dual-phase flow environments. The PIV system consisted of two primary components, namely a laser and a camera. A high-speed dual-laser system was used to illuminate a two-dimensional plane within the flow.

The laser chosen for the experiments was a diode-pumped Nd:YLF dual-laser system. This laser system consisted of three parts: 1. power unit, 2. laser head, and 3. chiller unit. The power unit was used to adjust the laser settings and to provide power to the laser head. Contained within the laser head was a dual cavity, with each cavity producing a separate laser beam. Upon exiting the cavities, the beams were directed toward a single exit aperture using heat resistant mirrors. Each beam was capable of producing light with energy levels up to 12 mJ per pulse at a maximum rate of 1,000 Hz. The dual-laser system allowed the beams to be individually fired within microseconds of each other, which is required for PIV applications. The chiller unit cooler and pumped distilled water through the laser head to dissipate the heat generated by the laser head.

The camera was equipped with a 2,560 x 1,600 CMOS sensor providing a spatial resolution of 4 Mp per image. At the full 4 Mp resolution, the camera was capable of capturing images at a rate of 1,450 frames-per-second. For PIV applications, however, the camera captured image pairs at a rate of 750 frames-per-second while maintaining a 4 Mp spatial resolution in each image. This capture rate and spatial resolution gave the ability to track individual flow structures in the rotor wake, such as the wake sheet and tip vortices, as well as the movement of individual sediment particles in the dual-phase flow experiments.

The PIV system was located outside the dust chamber; see Fig. 2.9. The laser system was used to illuminate the desired regions of interest (ROI). The laser beams were directed through a series of cylindrical and spherical lenses to diverge them into thin light sheets with a 2 mm thickness at the thinnest part of the sheet. The light sheets were slightly thicker in the imaging regions, and were measured to be 3 ± 0.5 mm. These

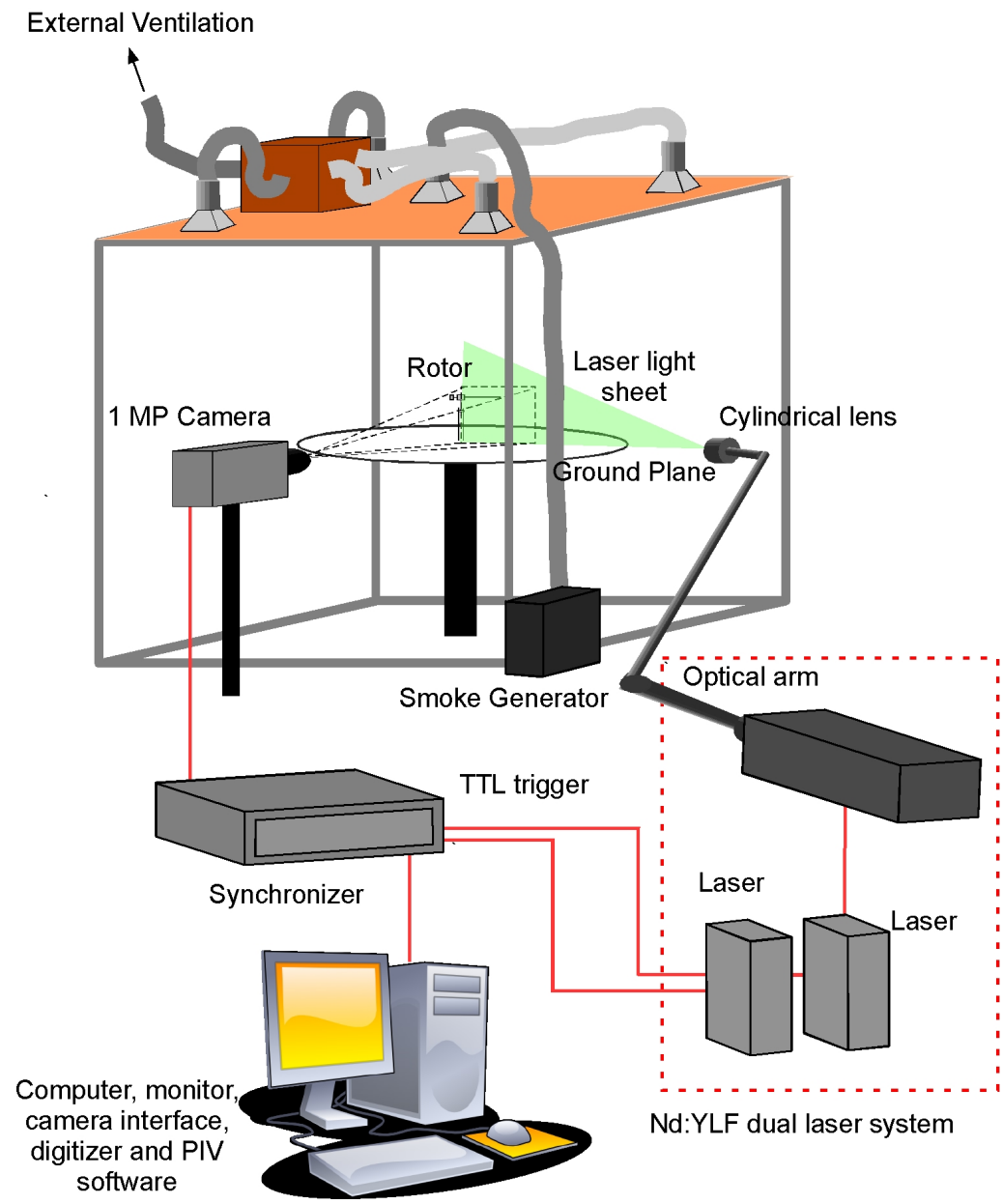

Figure 2.9: Schematic showing the instrumentation setup.

sheets were also judiciously aligned to minimize reflections from the ground plane and the sediment bed. The viewing axis of the camera was aligned so as to be orthogonal to the plane of the laser light sheet. The camera was then carefully focused on the desired ROI.

The laser and camera were both connected to a high-speed controller. This high-speed controller digitally synchronized the laser pulses to the camera frame rate such that the desired ROI was illuminated at the exact moment each camera image was captured. The controller was connected to a computer from which the entire PIV system could be operated.

2.6 Measurement Regions

One of the goals of this study was to understand the three-dimensional structure of the rotor wake as it developed over the ground plane and so to document its effect on the mobilization and uplift of sediment particles. Therefore, the regions of interest (ROI) studied included both vertical (x-z) and horizontal (x-y) interrogation planes (the coordinate system has been shown previously in Fig. 2.7). For the vertical planes, the laser light sheet was aligned so that it intersected the rotor shaft axis and was also perpendicular to the ground plane. For the experiments with the fuselages (bodies) in place below the rotor, the bodies were oriented so that their longitudinal centerlines intersected the laser sheets (details on the body shapes are given later in Section 2.7.2). A schematic of the ROIs used with the laser sheet in the vertical orientation is shown in Fig. 2.10.

ROI 1 was a larger region of the flow in which both single-phase and dual-phase

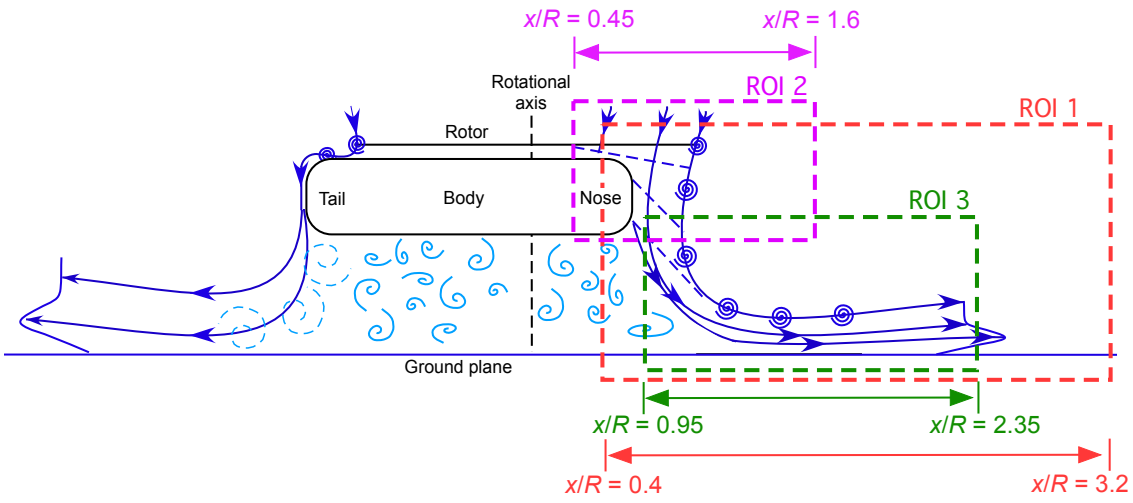

(a) ROI schematic at the nose

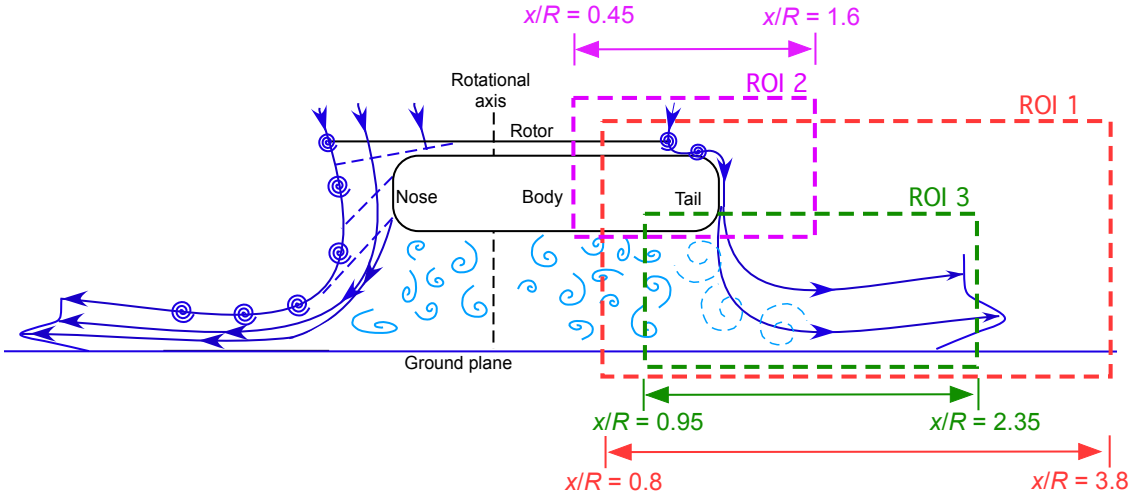

(b) ROI schematic at the tail

Figure 2.10: Schematics of the ROIs used in the vertical plane to study the nose and the tail regions.

flow experiments were performed. This ROI provided an overall view of the rotor flow field and was particularly useful in identifying the areas of the flow where more detailed measurements needed to be made. ROI 2 allowed for a more detailed examination of the initial formation of the blade tip vortices and also the interactions between the rotor wake and the body surfaces. ROI 3 was a near-wall region that was used to observe the interactions of the rotor wake with the ground plane, as well as the mobilization and entrainment of sediment particles.

A schematic of the ROIs used for the horizontal planes is shown in Fig. 2.11. For these ROIs, the laser light sheets were aligned to be parallel to the ground plane and perpendicular to the rotor shaft axis. These regions were used to examine the three-dimensional development of the rotor wake from the rotor disk plane down toward the ground plane. The flow field was dissected into ten individual ROIs starting from $z/R = 1.0$ (the rotor disk or tip-path-plane) down to $z/R = 0.1$ (just above the ground plane). Dual-phase flow experiments were also performed in these horizontal ROIs to expose the more three-dimensional aspects of the dual-phase flow environment.

2.7 Rotor and Body Setup

Experiments were performed with three goals in mind: 1. Obtain an understanding of how the rotor wake develops near the ground and interacts with the mobile sediment particles on the bed, and 2. Investigate the effects of disk loading, blade loading coefficient, and wake shedding frequency on the mobilization and transport of sediment particles as well as the overall severity of the particle field, and 3. Determine the effects

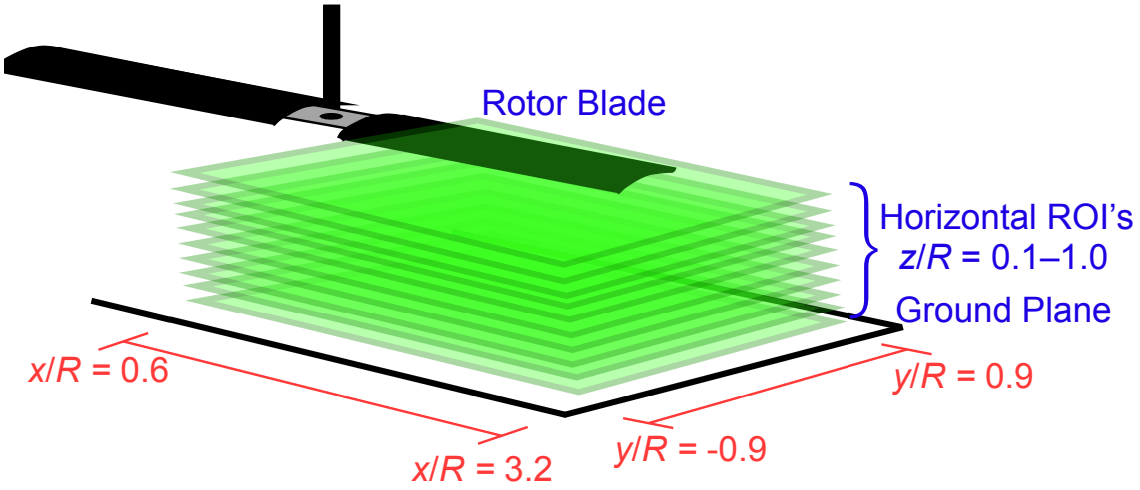

Figure 2.11: Schematic of the horizontal regions of interest.

that a airframe/body has on the development of the rotor wake and resultant particle field. To this end, the studies that were performed in the present work are discussed next.

2.7.1 Rotor System

One of the goals of the present work was to examine the effects that disk loading (DL), C_T/σ, and vortex impingement frequency had on the rotor wake near the ground as well as on the resultant particle field. This study was performed by investigating the effects produced by the wakes generated by the one-bladed and two-bladed rotors. To perform a meaningful comparison between these two rotors, it was important to have a metric that was held constant between the test cases. In the present work, experiments were first performed with the value of DL being held constant and then repeated with the value of C_T/σ being held constant. These parameters, however, are interdependent, i.e., changing one will also change the other. For the problem of brownout, it is useful to understand how these parameters affect the features of rotor wake, e.g., the groundwash

flow and tip vortices.

The value of DL of the rotor is the ratio of the rotor thrust, T, to the rotor area, A, i.e., $DL = T/A$. The value of DL can also be related to the average hover induced velocity, v_h, which can in turn be related to the downwash of the rotor, w, using

$$w = 2v_h = 2\sqrt{\frac{T}{2\rho A}} = 2\sqrt{\frac{DL}{2\rho}} \tag{2.1}$$

The rotor area is constant. Therefore, keeping the thrust constant for both rotors will result in the same disk loading and nominally in the same downwash and resulting groundwash velocities.

The value of C_T/σ is the ratio of the rotor thrust coefficient, C_T (where $C_T = T/\rho A(\Omega R)^2$), to the rotor solidity, σ. The rotor solidity is the ratio of the rotor area and the blade area, i.e., $\sigma = N_b c/\pi R$. In the present work, the rotor radius, chord, and rotational frequency were held constant for all experiments.

In previous experiments, the value of C_T/σ has generally been the metric that has been held constant, primarily because it can be related to the strength of the blade tip vortices, Γ_v, by using

$$\Gamma_v = k\left(\frac{C_T}{\sigma}\right)\Omega R c \tag{2.2}$$

where k = 2 for an ideal rotor. Notice that because the rotor solidity depends on the number of blades, if the one-bladed and two-bladed rotors are operated at a constant thrust (i.e., constant value of C_T), then the strength of the tip vortices will be different. Therefore, the value of DL and C_T/σ become interdependent. As such, independently characterizing the effects that the groundwash velocities and the tip vortex strength have on the rotor wake and resultant brownout cloud is not possible. Nevertheless, these pa-

rameters can still be varied in a controlled manner to investigate the combined effects of changing both the values of DL and C_T/σ.

Another consequence of testing both one-bladed and two-bladed rotors is that the number of blades will change the rate (frequency) at which vortices impinge on the ground. In the present work, the parameter that was used to examine the effect that vortex impingement rate was the wake shedding frequency, Ω_s, as defined by Milluzzo and Leishman [27], i.e.

$$\Omega_s = N_r N_b \Omega \tag{2.3}$$

where N_r is the number of rotors, which is one for present work. Therefore, Ω_s is simply the rotor operating frequency, Ω, multiplied by the number of blades. As such, the two-bladed rotor will produce vortices that impinge on the ground at twice the frequency of the one-bladed rotor.

In the first set of experiments, the value of DL was held constant, which was done by adjusting the pitch of the one-bladed rotor until it produced the same thrust as the two-bladed rotor. The thrust was measured using a balance. In this set of experiments, the value of DL was 0.039 lb ft^{-2}, C_T/σ for the one-bladed rotor was 0.21, C_T/σ for the two-bladed rotor was 0.105, Ω_s for the one-bladed rotor was 377 rads^{-1}, and Ω_s for the two-bladed rotor was 745 rads^{-1}. Notice that because these parameters are interdependent, the tip vortex strengths between the rotors was different (Eq. 2.2), while the groundwash velocities were nominally the same. A schematic explaining these operating conditions is shown in Fig. 2.12a.

In the next set of experiments, the value of C_T/σ was held constant between the

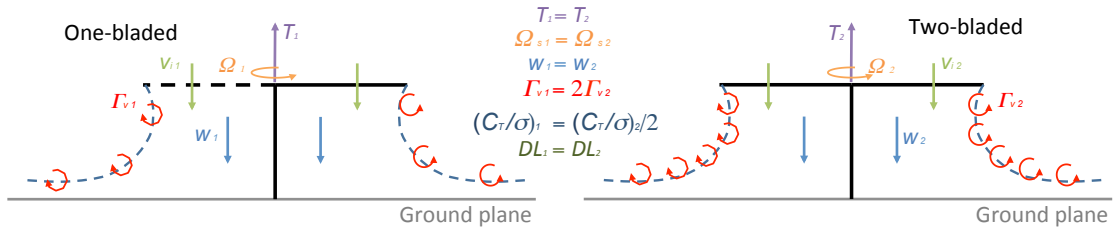

(a) Matched disk loading

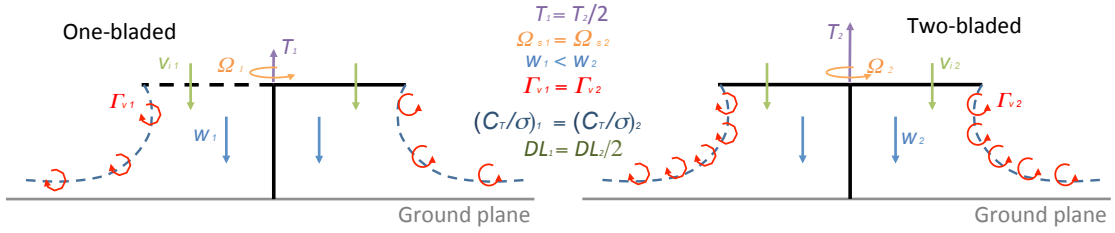

(b) Matched blade loading coefficient

Figure 2.12: Schematics showing the different operating conditions for the rotor systems, (a) matched disk loading and (b) matched blade loading coefficient.

one-bladed and two-bladed rotors. C_T/σ was held constant by setting the pitch of the one-bladed rotor such that it produced half the thrust of the two-bladed rotor, i.e., each individual blade generated the same thrust and had similar inflow distributions. In this set of experiments, the value of C_T/σ was 0.133, the value of DL for the one-bladed rotor was 0.024 ft^{-2}, DL for the two-bladed rotor was 0.049 lbft^{-2}, Ω_s for the one-bladed rotor was 377 rads^{-1}, and Ω_s for the two-bladed rotor was 745 rads^{-1}. The tip vortex strength was nominally the same, in this case, while the groundwash velocities were different. A schematic of the two rotors at these operating conditions is shown in Fig. 2.12b and the test matrix for all the experiments is given in Table 2.1.

Table 2.1: Test matrix for the one- and two-bladed rotor experiments examining the effect of disk loading, blade loading coefficient, and vortex shedding frequency for single-phase (SP) flows and dual-phase (DP) flows.

Number of Blades	**Disk Loading** (lbft^{-2})	C_T/σ	Ω_S (rads^{-1})	**SP/DP**	**Measurement Plane(s)**
1	0.039	0.21	377	SP	ROI 1
2	0 .039	0.105	745	SP	ROI 1
1	0 .024	0.133	377	SP	ROI 1
2	0 .049	0.133	745	SP	ROI 1
1	0 .039	0.21	377	DP	ROI 1
2	0 .039	0.105	745	DP	ROI 1
1	0 .024	0.133	377	DP	ROI 1
2	0 .049	0.133	745	DP	ROI 1

2.7.2 Body Shapes

A study was also performed to investigate the effect of a body placed below the rotor on the development of the rotor wake near the ground plane, and also to examine how the bodies affected the process of particle mobilization and transport. Three different bodies (representing helicopter fuselages) were individually placed in the wake below the rotor, as shown previously in Fig. 2.7.

The dimensions of the bodies used in the present studies were determined based on a statistical average of existing helicopters (see Appendix B). The bodies had cross-sectional shapes that were circular, elliptical, and quasi-rectangular (the latter being referred to as "rectangular" in the present work), respectively; the cross-sectional shape of each body is shown in Fig. 2.13. These cross-sectional body shapes were based on geometric definitions used by Hance [61], and are defined by a super-ellipsoid function given by

$$L(\theta) = \left[\left| \cos(\frac{1}{4}m\theta)/a \right|^{n_2} + \left| \sin(\frac{1}{4}m\theta)/b \right|^{n_3} \right]^{-1/n_1} \tag{2.4}$$

where L is the distance from the origin of the reference axis to the boundary of the cross-section, and θ is the subtended angle measured from the reference axis; see Fig. 2.13. The values of n_1, n_2 and n_3 are used to change the curvature of the vertices, while the value of m changes the number of vertices. The values of a and b are used to set the width and the height of the cross-section, respectively. The values of the variables used for the elliptical and rectangular bodies are given in Table 2.2.

The body shapes that were selected for the experiments were $1.8R$ in length and $0.38R$ in width. The width of the bodies was constant such that their projected horizontal

Table 2.2: Test matrix for the body shape parametric study.

Body Shape	m	n_1	n_2	n_3	a	b	**Height (in)**	**Width (in)**
Elliptical Rotor	2	5	5	5	0.62	0.62	1.54	1.25
Rectangluar Body	5	5	5	5	0.62	0.72	1.45	1.25

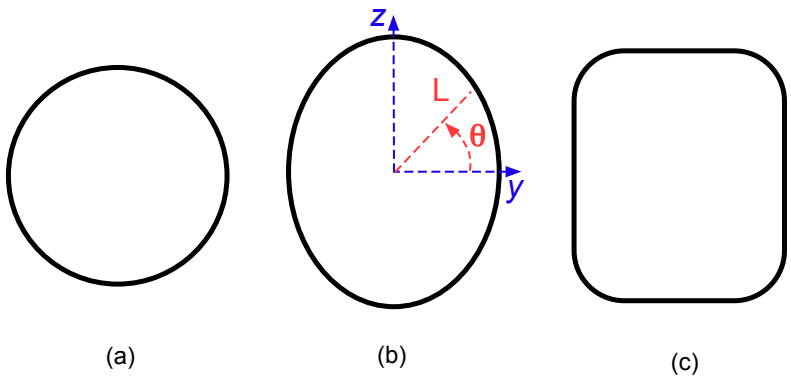

Figure 2.13: Cross-sectional views of the body shapes: (a) circular, (b) elliptical, and (c) rectangular.

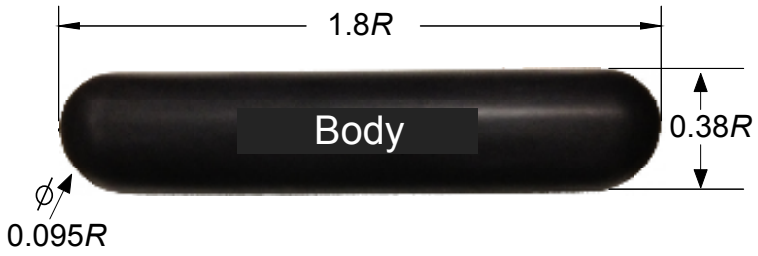

Figure 2.14: Top view of the bodies (same dimensions for all three body shapes).

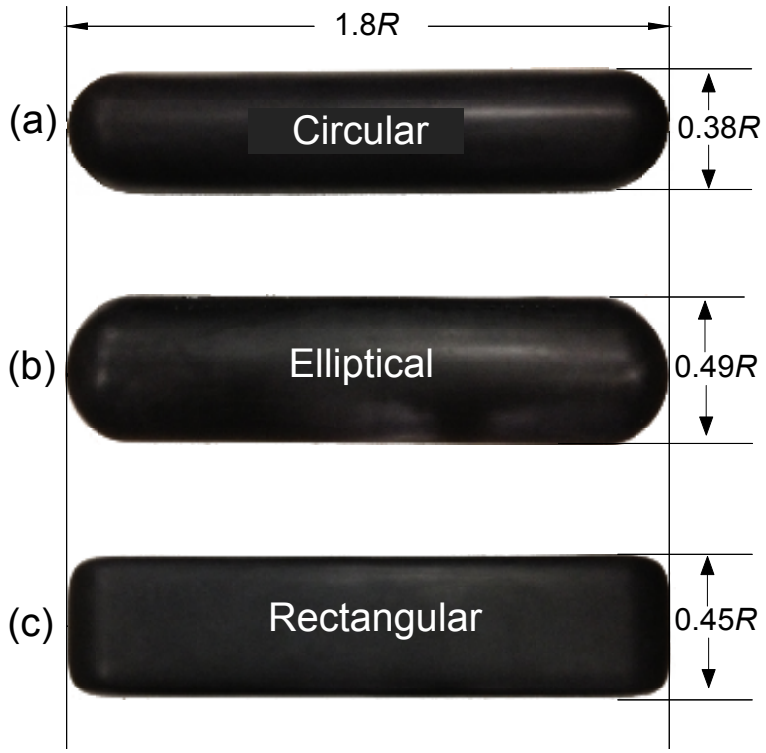

Figure 2.15: Side view of the three bodies used in the present experiments: (a) circular, (b) elliptical, (c) rectangular.

areas were the same, as shown in Fig. 2.14. When viewed from above, the end caps of the bodies were semi-circular revolutions with a radius of $0.095R$. A side view of each body is shown in Fig. 2.15.

The bodies were supported above the ground plane (but below the rotor) by two steel rods that were attached to a stand that was adjustable in height so as to allow different spacings of the bodies relative to the rotor. There was no physical connection between the rotor and the body. Figure 2.16 shows a schematic of the placement and orientation of a body under the rotor.

The experiments with the body shapes were all performed with the two-bladed ro-

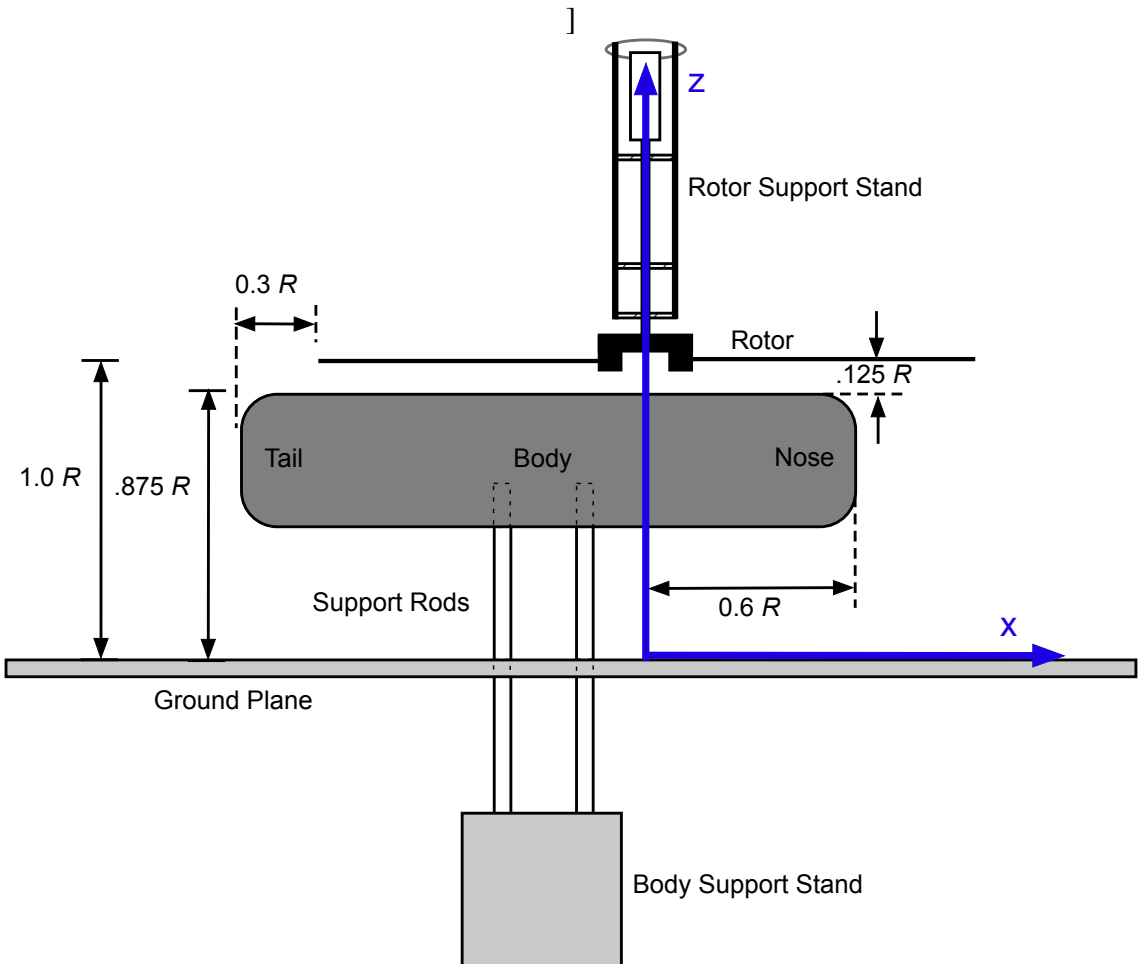

Figure 2.16: Schematic of the rotor/body orientation and support structure.

tor, which was located with its rotor plane at one rotor radius above the ground. In this case, the rotor was operated at a disk loading of 0.049 lbft^{-2} and $C_T/\sigma = 0.133$. Tests were performed in vertical and horizontal ROIs, the test matrix being given in Table 2.3.

2.8 Testing Procedures

For the dual-phase flow experiments, the ground plane was adjusted slightly downward to account for the thickness of the sediment bed (1 cm). To perform flow visualization tests, higher concentrations of seed were introduced into the dust chamber so that the

Table 2.3: Test matrix for the body shape parametric study.

Body Shape	**SP/DP**	**Vertical Measurement Planes**	**Horizontal Measurement Planes**
Isolated Rotor	SP	ROI 1,2,3	$z/R = 0.1$–1.0
Circular Body	SP	ROI 1,2,3	$z/R = 0.1$–1.0
Elliptical Body	SP	ROI 1,2,3	$z/R = 0.1$–1.0
Rectangular Body	SP	ROI 1,2,3	$z/R = 0.1$–1.0
Isolated Rotor	DP	ROI 1,3	$z/R = 0.1$–1.0
Circular Body	DP	ROI 1,3	$z/R = 0.3$
Elliptical Body	DP	ROI 1,3	$z/R = 0.3$
Rectangular Body	DP	ROI 1,3	$z/R = 0.3$

reflections from the seed highlighted the salient features of the rotor wake. For the PIV, a lower concentration of seed particles was more uniformly distributed throughout the dust chamber.

The rotor was then started and was allowed to reach steady-state operation (for approximately 60 rotor revolutions) before data acquisition began. For each test, 1,000 flow realizations were captured at a rate of 750 Hz (i.e., for 90 rotor revolutions or 1.3 seconds). For the dual-phase flow experiments the sediment bed was releveled between each test.

2.9 Particle Image Velocimetry (PIV)

In both the single-phase and dual-phase flow experiments, PIV was used to measure the velocities of the rotor wake. The advantage of PIV is that it is a non-intrusive method (except for seeding) that can make planar flow field measurements, even in areas close to a solid boundary such as the ground plane or a body. The camera trigger was synchronized with the two laser pulses such that the laser pulses straddled the image capture. In the current experiments, a pulse separation time, Δt, of 50 μs was used. This value of Δt was found to give small enough displacements of the seed particles to allow successful PIV cross-correlations while also maintaining large enough displacements to track the movement of the sediment particles when using PTV.

Figure 2.17 shows a schematic of how the PIV software is used to obtain the velocity field measurements from a raw image pair. Each laser pulse illuminated the ROI as the camera captured an image of the seed particle distributions. The first pulse pro-

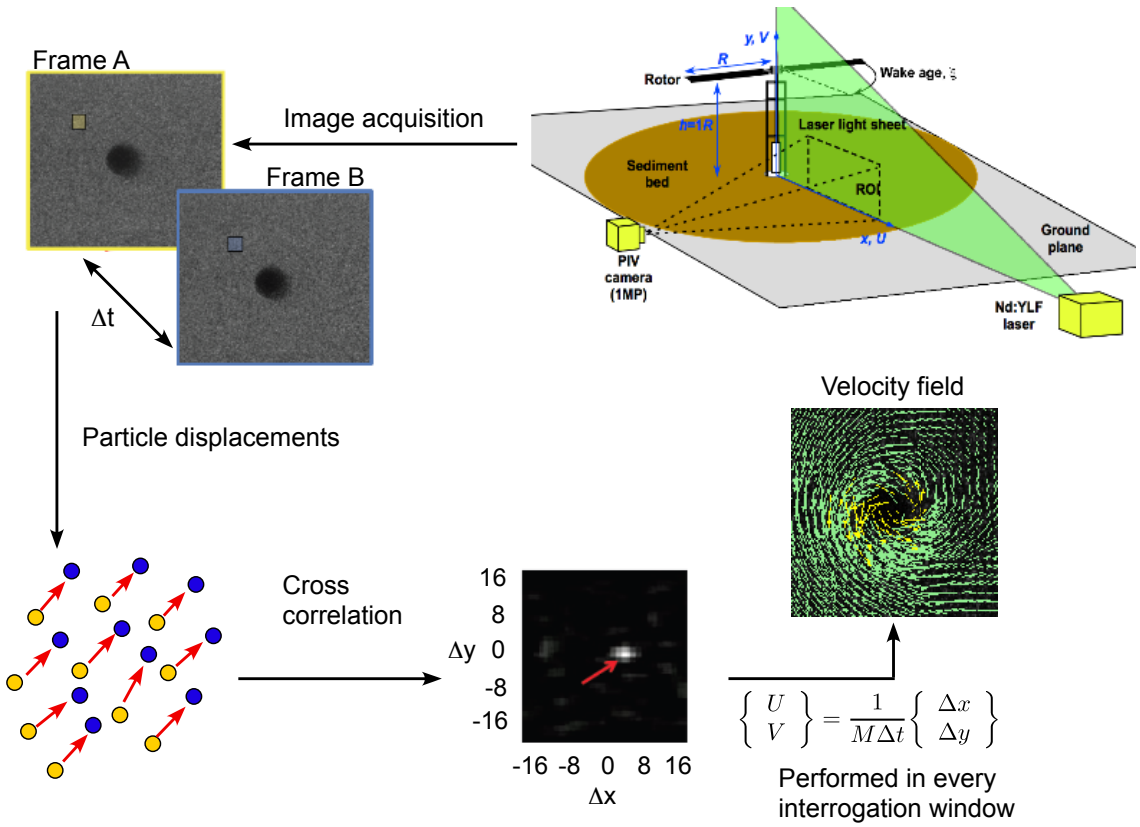

Figure 2.17: Schematic showing the PIV cross-correlation process.

vided frame A and the second pulse provided frame B, with each frame (in this case) being 50 μs apart in time. The software first dissected each frame into a square grid of interrogation windows. These windows were sized such that there were 5–15 seed particles within each window that also moved approximately a quarter of the window length. An inherent assumption in the PIV cross-correlation technique is that the particles within each interrogation window translate linearly, i.e., with negligible curvature or shearing in the flow. With this in mind, the interrogation window size, as well as the value of Δt, were chosen to best resolve the relatively steep velocity gradients induced by the rotor wake.

To determine the flow velocity within each interrogation window, the particle distribution in frame A was compared to the particle distribution for the corresponding in-

terrogation window in frame B. Ideally, the particle distribution in frame B was the same particle distribution in frame A but translated by a quarter of the interrogation window length. The particle distribution between the two frames was computed using a cross-correlation function, Φ_{fg}, given by

$$\Phi_{fg}(m,n) = \sum_{i}\sum_{j} f(i,j) \times g(i+m, j+n)$$

where f and g represent the intensity distributions corresponding to frames A and B respectively, and with m and n corresponding to the pixel displacements in each dimension.

The cross-correlation function took the intensity distribution in each interrogation window in frame B and translated it to each (i,j) coordinate in the corresponding interrogation window in frame A. For each interrogation window, there was one (i,j) coordinate that showed a maximum similarity between the intensity signatures of the two frames.

The displacement of the particles was in units of pixels and so a calibration was required to determine the magnification factor, M, of the camera, which was different for each ROI. This magnification factor was found by placing an object of known length in the imaging region and using it to calibrate the results. The calibration was then used to convert the translation of the particles in each interrogation window from pixels to meters.

The particle velocities for a given interrogation window were then calculated using the translation of the particles and the pulse separation time between the two frames. This process was repeated for all the interrogation windows within each frame to produce a two-dimensional rendering of the velocity field. Depending on the size of the interrogation window, this process can be relatively computationally expensive.

Square interrogation windows were used that started at 32-by-32 pixels and were

subsequently reduced to 16-by-16 pixels. By reducing the window size, the velocity vectors calculated in the larger windows were used as an initial value for the calculation of the velocity vectors in the smaller windows. The ground was artificially masked in the images prior to the velocity calculations to minimize the effect of laser reflections and so to reduce the processing region to decrease computational time.

A signal-to-noise ratio of 2 was implemented in the present work. Any vectors that did not meet the signal-to-noise ratio were iteratively replaced using a non-linear, local median filter on a 3-by-3 grid surrounding the vector in question. The use of a median filter was found to be more robust than other replacement filters (e.g., local and global mean filters). Only a severely contaminated data set would adversley affect a local median filter. The median filter was used to create a probability density function from which the vector in question could be estimated. Details on the replacement algorithm are provided in [76]. Any images with more than 5% interpolated vectors of the total number of vectors was removed from the analysis. Furthermore, PIV images were discarded if the majority of the interpolated vectors were near the ground or within the tip vortices.

2.10 Particle Tracking Velocimetry (PTV)

The dispersed-phase was considerably more dilute than the carrier-phase, and was, therefore, unsuitable for analysis by means of a cross-correlation method such as used in PIV. Instead, each particle in the dispersed-phase was individually identified and tracked between frames A and B; see Fig. 2.18 for a summary of the process. After performing an intensity thresholding technique to determine those pixels in the dispersed-phase (dis-

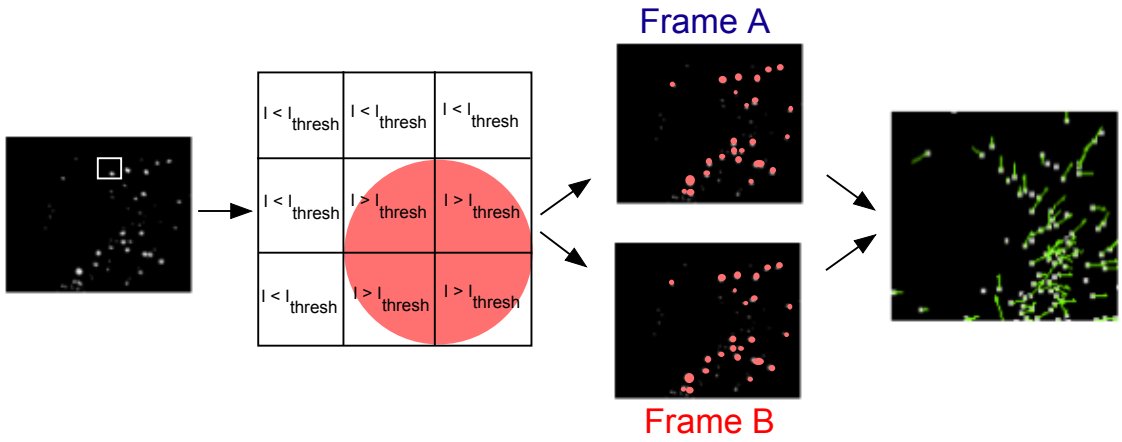

Figure 2.18: Schematic depicting the PTV algorithm used to extract the velocity of the dispersed phase.

cussed next), the resultant image contained mostly sediment particles, as shown in the far left of Fig. 2.18. By examining an example 3-by-3 pixel grid within this image, it can be seen that there were four pixels above the intensity threshold. Each grouping of pixels above the intensity threshold was identified as a distinct sediment particle. For a given particle in frame A, the corresponding location in frame B was scanned to find the same particle.

To determine whether the particle in frame B was the same as the particle in frame A, the following particle characteristics were used: total area, major and minor particle axes, Ferret's diameter, circumference, intensity, background flow deviation, and number of surrounding neighbors. Once the particles were identified, the particle displacements between frames, pulse separation time, and camera magnification factor were used to calculate the velocity of each particle.

2.11 Separation of the Carrier-Phase and Dispersed-Phase

For the dual-phase flow experiments, the carrier-phase was analyzed conventionally using PIV and the dispersed-phase was analyzed using PTV. Phase separation was required before the flow velocities of the carrier-phase and dispersed-phase could be resolved. In the present work, the dispersed-phase particles created more intense reflections than the carrier-phase particles, so an intensity thresholding method could be used.

Figure 2.19 shows a histogram of the typical intensity distribution (labeled as counts) in a dual-phase flow experiment. Notice that there are two peaks in the intensity distribution, one peak below 1,000 counts and the other peak above 4,000 counts. The lower peak corresponds to the intensity signatures of the carrier-phase particles and the higher peak corresponds to the intensity signatures of the dispersed-phase particles. This wide range between the two intensity peaks allowed for the implementation of an intensity thresholding method to separate the two phases of the flow; a schematic of this phase-separation process is shown in Fig. 2.20.

The phase separation was performed by scanning every pixel in the image and assigning pixels under 2,000 counts to be part of the carrier-phase. The upper path of Fig. 2.20 shows the analysis of the carrier-phase flow when using conventional PIV, as previously described. Any pixels in the image that were above the 2,000 count intensity threshold were assigned to be part of the dispersed-phase. The lower path of Fig. 2.20 shows the dispersed-phase analysis as made using the PTV (i.e., the direct tracking of every particle). Finally, the carrier-phase velocity fields and dispersed-phase particle velocities were superimposed to produce the resultant measurements of the dual-phase flow.

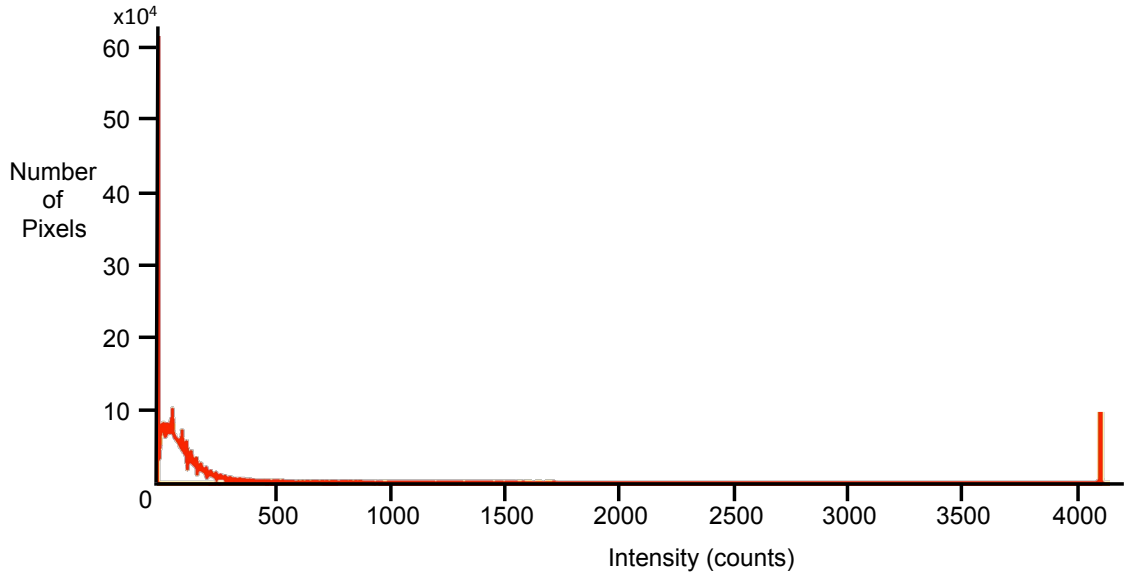

Figure 2.19: Histogram of the typical intensity distribution in a dual-phase flow experiments.

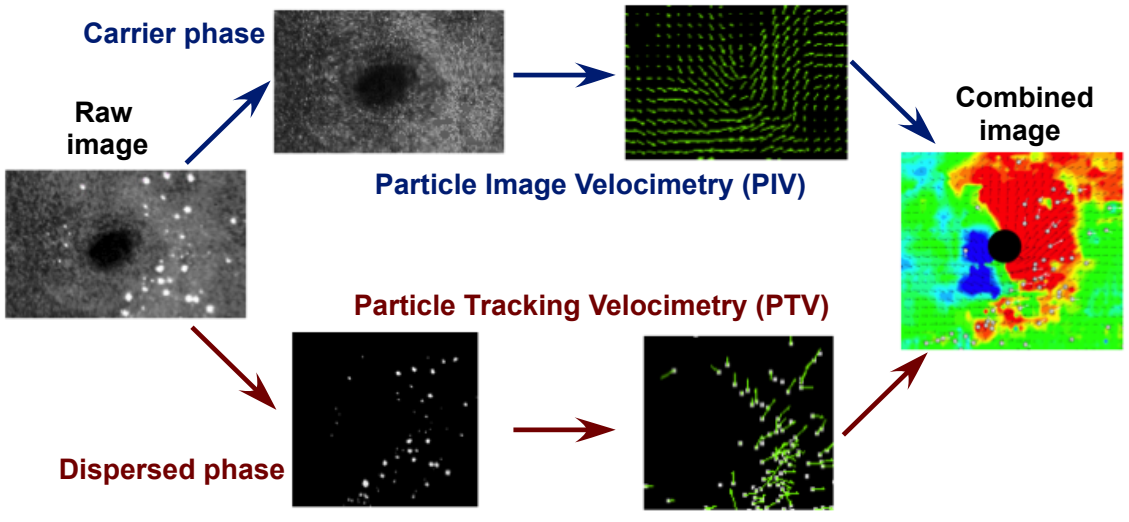

Figure 2.20: Dual-phase image phase separation and processing techniques.

2.12 Technical Challenges

There were a number of technical challenges that were encountered when making the measurements. As such, a goal of the present research was to determine appropriate methods to overcome these challenges, and also to develop better techniques for the future. These challenges can be divided into two categories, namely software and hardware issues, and experimental techniques. The present work has developed various strategies to manage these issues and to advance the state of the art in multi-phase flow measurement techniques.

One challenge was the storage of the large quantities of data that were acquired. For example, each image pair was on the order of 8 MB of data. 1,000 image pairs per test amounted to 8 GB of raw data per test condition. These large data sets posed issues with the speed of data transfer to the computer and with overall data storage. The transfer issue was solved by installing a memory buffer on the camera that was able to store 1,000 contiguous images, which were then transferred to the computer at the end of the experiment. For permanent storage, a double redundant data storage server was used, which was equipped with three 20 TB hard drive units.

The relatively large number of images per test also posed a problem for the PIV processing. The PIV cross-correlation algorithm had to be run 1,000 times per test, which was a very time consuming task. To minimize this processing time, the intensity values from each interrogation window were not directly correlated. Instead, a Fast Fourier Transform (FFT) method was used for each window to create an intensity map, significantly reducing the processing time. For the dual-phase tests, the dispersed-phase had to

be subtracted from the raw image before the PIV cross-correlations could be performed, adding even more processing time.

One of the biggest challenges in the experiments was dealing with laser light reflections, an inevitable outcome of using the laser near any solid objects in the dust chamber. Plexiglass walls were used to minimize such reflections from the dust chamber. However, there were still some internal and surface reflections, causing the presence of weaker secondary light sheets within the chamber. This problem was mitigated by lining the chamber with non-reflective black material, except where the laser light entered the chamber and in the viewing region of the camera.

The laser light also reflected off of surfaces within the chamber, especially the ground plane. Figure 2.21a shows a raw image with reflections off the ground plane. Notice that the reflections have completely obscured the crisp, well defined particles that are required to perform successful PIV cross-correlations near the ground plane. To alleviate these reflections, the laser light sheet was aligned such that the centerline of the sheet was parallel to the ground. However, as shown in Fig. 2.21b, there were still some reflections from the ground plane.

To mitigate such reflections, a post-processing step was implemented in which background subtraction was performed prior to analyzing the image. The subtraction involved finding the minimum intensity of each pixel over all the images in the test run to create a composite minimum intensity image. This minimum intensity image was then subtracted from each raw image. The last step was to implement a processing mask on the image, giving the final image shown in Fig. 2.21c, which can then be used to perform the PIV correlations.

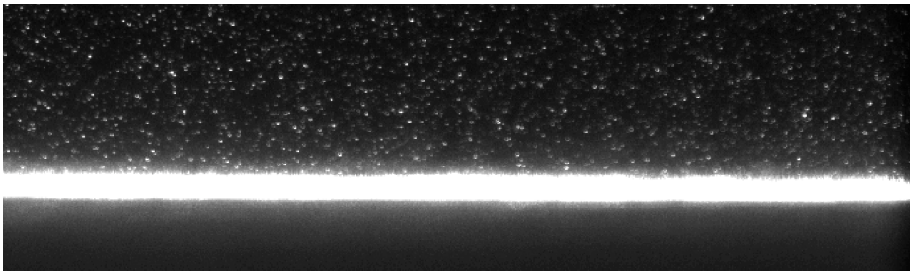

(a) Unaltered raw image

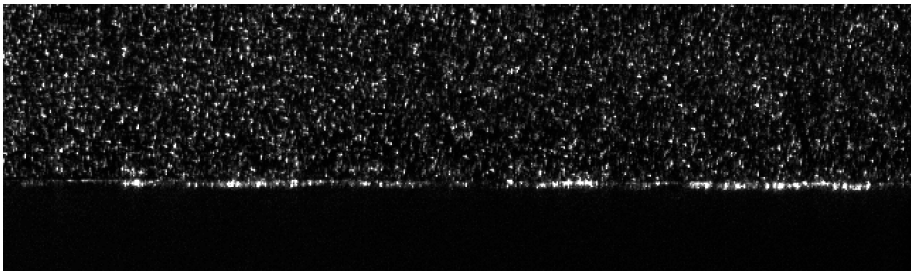

(b) Image taken after judicious laser alignment

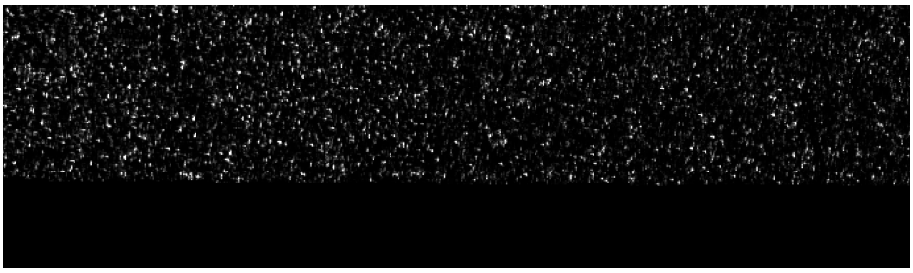

(c) Image after background subtraction and image masking

Figure 2.21: Process used to improve reflections at the ground plane.

Operating the rotor over a surface covered with mobile sediment inevitably caused the bed surface to erode, in particular creating a deflation region where the vortices impinged on the surface. Just downstream of the deflation region, a dune slowly formed as mobilized particles were redeposited on the bed; see Fig. 2.22. Over time, this change in the shape of the sediment bed became larger, reaching a maximum depth of 5% of the rotor radius and so this could begin to alter the near-wall flow. To mitigate any alterations

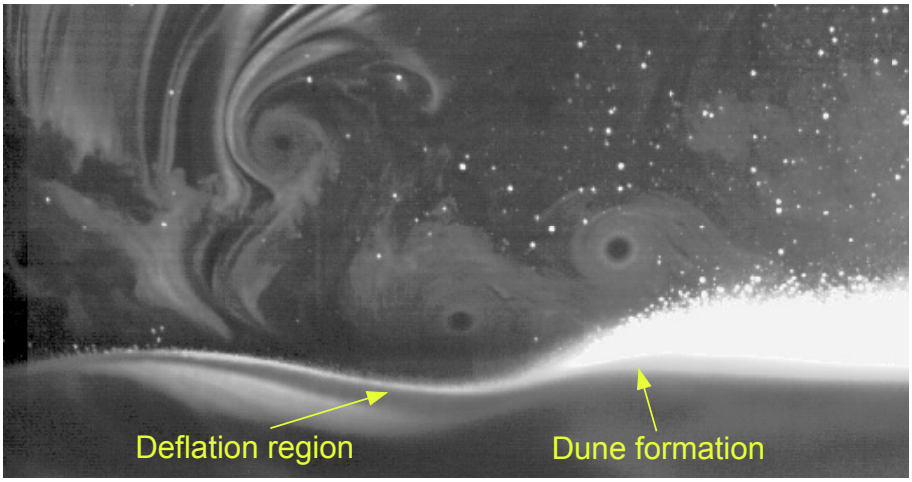

Figure 2.22: FV image showing the deflation and dune regions that can form over extended test times.

to the carrier flow from bed deformations, data acquisition began as soon as the rotor reached its operating frequency.

To quantify the bed erosion over the time-frame of each test, an algorithm was written to identify the surface topology of the bed, an example of this being shown in Fig. 2.23. This algorithm was applied to all 1,000 contiguous flow realizations within a run, and was used to identify the minimum point in the deflation region for all the flow images. As Fig. 2.24 shows, the erosion of the bed within one second (i.e., 1,000 image captures) was less than 0.5% of the rotor radius. Therefore, as long as the data acquisition began as soon as the rotor reached its operating frequency, it could be ensured that there effects of bed erosion on the measurements were negligible.

One challenge associated with performing dual-phase flow experiments was the identification of the individual sediment particles because, in some cases, the rotor uplifted a large quantity of particles; see Fig. 2.25 for an example. The reflections from

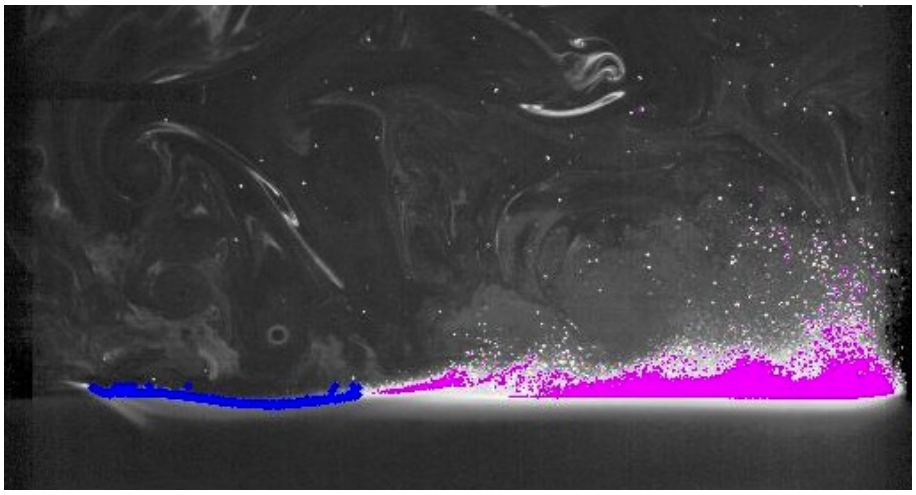

Figure 2.23: Surface delfation region identified by the topology algorithm.

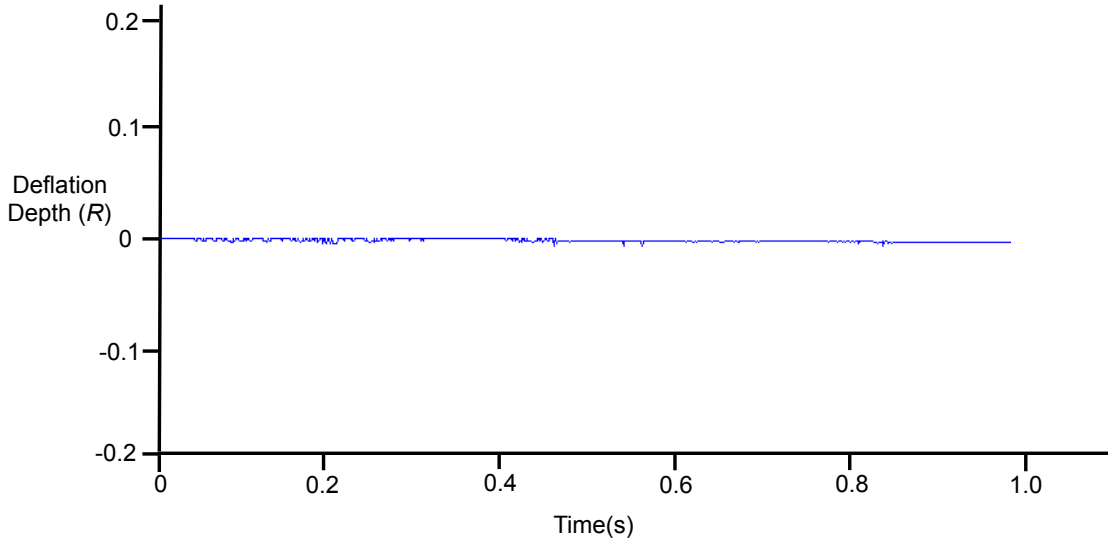

Figure 2.24: Morphology of the deflation region over the course of one complete test (1,000 flow realizations/images).

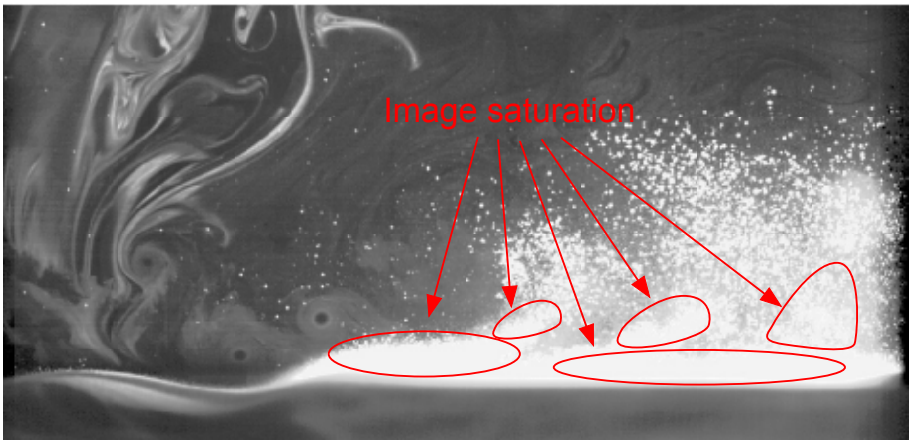

Figure 2.25: Dual-phase image showing the light saturation caused by too many uplifted and suspended sediment particles.

these particles saturated the PIV/PTV images such that individual particles could not be identified. To alleviate this issue, the rotor operating conditions were judiciously adjusted to keep the quantity of uplifted sediment more dilute, i.e., the overall image was not completely saturated by reflections from the particles. Even so, a dense particle layer still formed near the ground in which individual particles were more difficult to identify.

A consequence of the thresholding technique used to separate the dispersed-phase flow from the carrier-phase flow was the presence of "holes" in the resultant carrier-phase image; see Fig. 2.26. If there were too many of these holes in the carrier-phase image then it was not possible to perform successful cross-correlations to obtain good PIV flow vectors. Therefore, a 3-by-3 interpolation grid was used to determine the validity of flow vectors in regions that contained many holes. Furthermore, any regions of the images that were saturated with sediment particles were excluded from the carrier-phase processing and analysis.

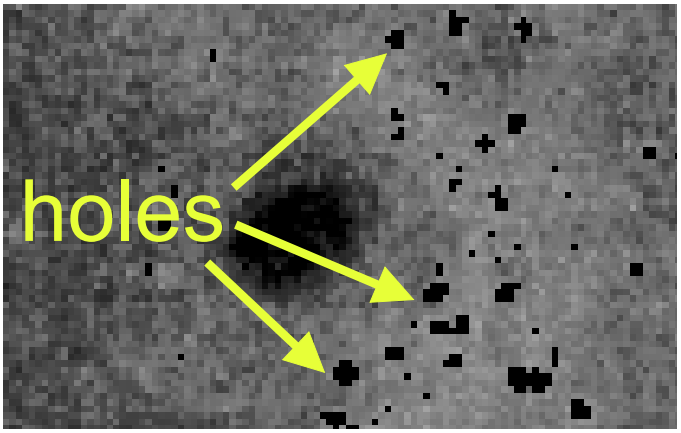

Figure 2.26: Phase separation “holes” in the carrier-phase after thresholding has been performed.

2.13 Uncertainties in the PIV Measurements

Sources of uncertainty in the flow measurements using PIV include tracking errors of the tracer particles, background noise, interrogation window size, pulse separation time, and laser light reflections. Tracer particle errors are a result of the seed particles slipping or not perfectly following the flow. However, in the present work, this latter source of error was very small because the seed particles have been shown to exhibit minimal tracking errors [75].

Background noise and laser light reflections can cause artificial intensities in the raw image that result in inaccurate correlations. To limit this error, a signal-to-noise ratio of 2 was used to assess the validity of each vector; this value of signal to noise ratio is relatively stringent for PIV measurements. Interrogation window size and pulse separation time were chosen such that there is minimal flow curvature or shearing within each window. The interrogation windows were sized to be as small as possible such that they resolved

the velocity gradients in the flow. The smallest window size (16 x 16 pixels) were found to still contain the requisite 5 – 15 seed particles. The pulse separation time was then chosen such that the seed particles displaced approximately a quarter of the interrogation window length. However, in a flow with significant vorticity there is always some deviation of the flow in each interrogation window, so an image deformation approach was implemented to help alleviate this source of error. A conservative assumption for the magnitude of error from these sources is 0.1 pixels, giving a 1.5% error in the resulting flow velocities.

The primary sources of error in the measurements arise from uncertainty in the pixel displacement, pulse separation time, and magnification factor. The error in the pixel displacement was found by processing images with known particle displacements. The error in the pulse separation time was found from the manufacturer of the high-speed, digital synchronizer. The magnification factor was found by placing an object of known length in the imaging region; for the present measurements a scale was used. The points chosen to determine the magnification factor spanned the length of the imaging region and so this error was small.

The uncertainties in the velocity measurements were then quantified using

$$\Delta U = \sqrt{\left(\varepsilon_{\Delta x}\frac{\partial U}{\partial \Delta x}\right)^2 + \left(\varepsilon_{\Delta t}\frac{\partial U}{\partial \Delta t}\right)^2 + \left(\varepsilon_{M}\frac{\partial U}{\partial M}\right)^2}$$

where $\varepsilon_{\Delta x}$, $\varepsilon_{\Delta t}$, and ε_{M} are the errors associated with pixel displacement, pulse separation time, and magnification factor respectively. The combination of all these sources of error resulted in approximately 0.5% error in the pixel displacements and 1% error in the velocity measurements. When combined with the errors from reflections and particle slippage, the total uncertainty of the velocity measurements was 2.5%.

2.14 Uncertainties in the PTV Measurements

There are a number of limitations that hinder the identification of all the imaged particles in PTV. The majority of the unidentified particles arise because the particle do not scatter enough light or is not completely within the laser light. There are also errors in the particle tracking as a result of the parameters used for identification and tracking. In particular, the calculation of the centroid of the particle (X_c, Y_c), which had an error of up to 5 pixels in each dimension. With the centroid defined as $R_c = (X_c, Y_c)$ and the length $|R_c| = X_c + Y_c$, the uncertainty is

$$\Delta|R_c| = \sqrt{\left(\varepsilon_{X_c}\frac{\partial|R_c|}{\partial X_c}\right)^2 + \left(\varepsilon_{Y_c}\frac{\partial|R_c|}{\partial Y_c}\right)^2}$$

where ε_{X_c} and ε_{Y_c} are the uncertainties in X_c and Y_c, respectively. The centroid uncertainty was calculated to be approximately 1.0% of the particle location.

2.15 Summary

The present chapter has described the experiments there were performed in the present work. A detailed description of the test cell (dust chamber), rotor system, ground plane, seed particles, sediment particles, body shapes, and PIV system has been given. The basis of the measurement techniques, namely PIV and PTV, were explained. Single-phase flow and dual-phase flow measurements were made to examine the effects of the rotor groundwash, tip vortices, tip vortex impingement rate, and body shapes to examine their effect on the development of the rotor wake and the rotor-induced dust fields. For the dual-phase experiments, a phase separation technique was implemented to differ-

entiate between the carrier-phase and the dispersed-phase. PIV cross-correlations were used to analyze the carrier-phase while PTV was used to analyze the dispersed-phase. The technical issues in this process have been described, along with the methods used to overcome these issues.

Chapter 3

Results and Discussion

This chapter describes the results obtained from the single-phase and dual-phase flow experiments that were performed on the rotor when it was hovering over the ground plane, and also when it was operating over the plane when covered with a sediment bed of mobile particles. The experiments were conducted by using a time-resolved PIV and PTV system, which simultaneously measured the temporal evolution of the rotor wake as well as the instantaneous particle motions. Measurements were performed using both one-bladed and two-bladed rotors.

The present work has contributed a fundamental understanding of the detailed fluid dynamics of rotor wake developments near the ground, and also the interdependent mechanisms that are involved in rotor-induced particle motion, i.e., toward a better understanding the problem of rotorcraft brownout. The results discussed in this chapter are divided primarily into three parts. The first part shows results that describe the basic physics of rotor-induced particle motion. The rotor wake was initially examined in a single-phase flow environment to better quantify the fluid dynamic behavior of the rotor wake as it evolved near the ground plane. Results are then presented for the rotor hovering over the same plane but covered with a mobile sediment bed, which was used to examine the physics of particle mobilization and transport by the rotor wake, as well as the overall development of the particle field around the rotor. Results documenting the

three-dimensional evolution of the rotor wake near the ground are presented, along with a detailed study of the three-dimensionality of the resulting particle field.

The second part of this chapter describes the results from a study performed with both the one-bladed and two-bladed rotors that specifically addresses the effects that disk loading (DL), blade loading coefficient (C_T/σ), and wake shedding frequency (Ω_s, as defined by Milluzzo and Leishman [27]) had on the processes of particle mobilization and transport. Particular emphasis was placed on understanding how the different fluid dynamic structures induced by the rotor near the ground influence the mobilization and uplift of particles and the development of the overall particle field near the rotor. The resulting dual-phase flows produced by each of the two rotors were compared in terms of the quantity and concentration of particles, as well as the spatial and temporal distribution of the uplifted particles.

The third part if this chapter discusses the effects that an airframe or body shape had on the development of the rotor wake, and also on the corresponding particle mobilization and transport of particles. This latter study was performed by using three different body shapes that were placed, in turn, between the rotor and the ground plane. The dual-phase flow measurements that were taken in both vertical and horizontal ROIs are discussed. These results provided a better understanding of how the rotor wake was distorted by the presence of a body and how this distortion affected the particle field.

3.1 Fluid Dynamics of Rotor Wakes and Particle Fields

There is a need to understand the basic physics of particle mobilization and entrainment produced by a rotor wake. While some studies have examined the sediment mobilization and transport mechanisms below a rotor, there are still many aspects of the resultant particle field that remain to be understood. The foregoing discussion has explained why, in general, the particle fields induced by rotor flows are likely to be highly three-dimensional, with distinct local uplift events and intermittent characteristics. However, the reasons for this three-dimensionality and the differences in the local uplift events has never been properly quantified, which was one goal of the present research.

3.1.1 Single-Phase Flow Results

A prerequisite toward understanding the rotor-induced particle field was to first characterize the single-phase flow environment, i.e., the carrier-phase of the flow produced by the rotor. To this end, FV and PIV experiments were performed on an isolated, two-bladed rotor that was hovering with its rotor plane one rotor radius above the ground plane. The rotor pitch was set such that the rotor produced a disk loading, DL, of 2.35 Nm^{-2}, a blade loading coefficient, C_T/σ, of 0.133, an estimated tip vortex strength, Γ_v, of 0.15 (using Eq. 2.2), and a corresponding non-dimensional tip vortex strength, $\widehat{\Gamma_v}$, of 0.266. In the present work, this rotor configuration and operating condition are referred to as the "baseline" case.

3.1.1.1 Rotor Wake Development

Figure 3.1 shows a schematic for a case when the rotor is operating far away from the ground (also see Fig. 1.7 in Chapter 1). The rotor performs work on the air to increase its momentum and so produce the thrust required. A jump in pressure across the rotor disk causes the air to accelerate through the rotor, resulting in a slipstream velocity or downwash flow below the rotor. Initially the rotor wake contracts, but at further downstream distances the wake begins to expand as turbulent diffusion and the dissipation of energy progressively reduces the flow velocities in the wake.

Each blade of the rotor continuously trails a helicoidal tip vortex filament and an associated vortex sheet into the downstream wake. The schematic of a two-dimensional vertical plane of the flow shown in Fig. 3.1 identifies the cross-sections of these vortex filaments and wake sheets. The wake sheet is created by the merging of the upper and lower boundary layers on the blade [77–79], which leaves small-scale vorticity and turbulence in the flow. The tip vortices roll up along the side edge of the blade tip, and then convect axially downward along the wake boundary. Of particular interest when the rotor is operating away from the ground is that these tip vortices begin to diffuse their initially concentrated vorticity after only 2–3 rotor revolutions; see Fig 3.1.

The schematic in Fig. 3.2 shows that the structure of the rotor wake is significantly altered when the rotor is hovering near the ground (i.e., in so called IGE operation). The rotor wake initially contracts, as it does in hover, but then rapidly expands radially outward as it approaches the surface of the ground plane. The wake then continues to develop, but now it is confined to a region near the ground and is convected outward away

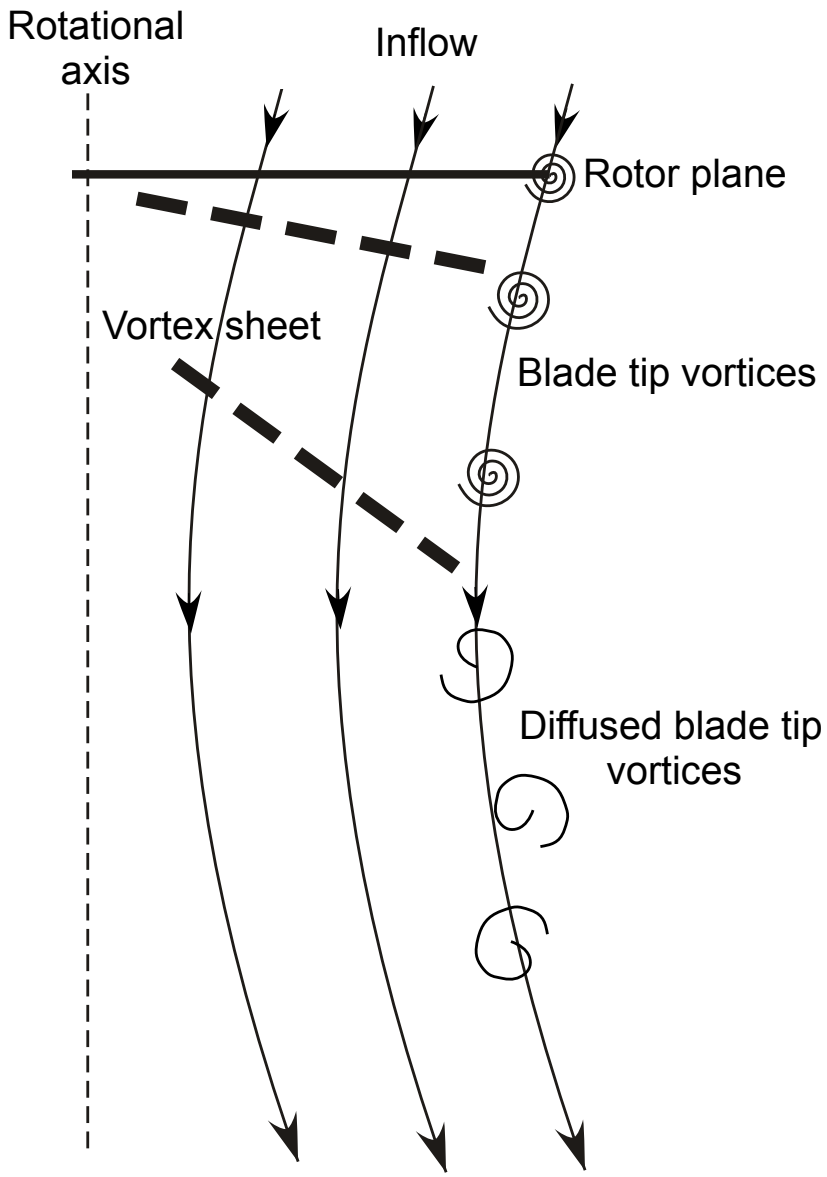

Figure 3.1: Schematic of the flow for the rotor operating OGE at $z/R = \infty$. $\psi_b = 0^\circ$.

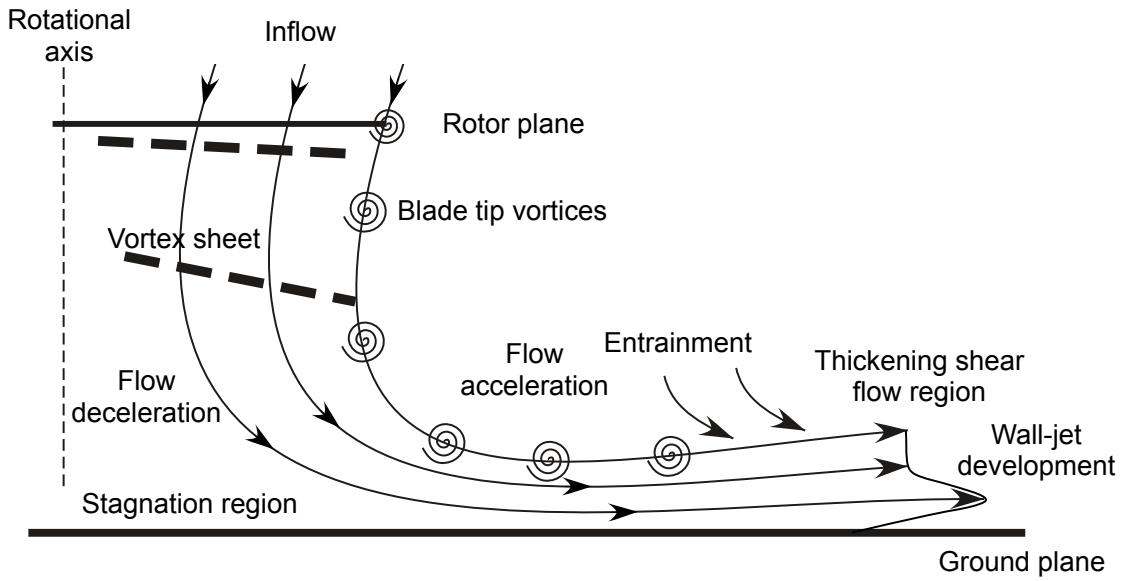

Figure 3.2: Schematic of the flow for a rotor operating IGE at $z/R = 1.0$ above a ground plane. $\psi_b = 0^\circ$.

from the rotor and more parallel to the surface. In this case, the vortical structures in the rotor wake persist to much older wake ages (up to 5–6 rotor revolutions) than when the rotor is operating further away from the ground, which is primarily because of vortex stretching [17].

Flow visualization (FV) experiments were undertaken in the present research to investigate the structure and time-history of the flow produced by the rotor operating near the ground. The FV was performed by judiciously introducing the smoke seed particles directly above the rotor disk, causing the particles to be entrained into the rotor wake. The concentrated vortical flows within the wake (such as the tip vortices) were easily identified in the FV as almost circular regions of concentrated seed particles with a darker region in their very centers. These darker regions had a more dilute distribution of seed because of the centrifugal and Coriolis forces acting on the particles as they spin within

the vortices. It is important to note that the relative size and shape of these darker regions do not directly imply the strength, core size, or swirl velocity of the vortices because the distribution of seed in the FV was non-uniform and also differed between successive images.

Figure 3.3 shows a sequence of FV images for the two-bladed isolated rotor when it was hovering over the ground; each image is separated in time by 90° of blade rotation. The FV shows that the wake initially contracted as the flow was accelerated through the rotor and then rapidly expanded radially outward as is it approached the ground. The vortex filaments that convected along the ground plane were continuously trailed into the wake from the rotor blades. Previous studies have shown that the tip vortex cores were initially mostly laminar [80–83]. The FV in Fig. 3.3 shows that the vortices convected along the slipstream boundary of the rotor wake, with the slipstream boundary effectively being a shear layer that separated the higher velocities within the wake from the relatively quiescent flow outside. Closer to the ground, the vortices were then observed to interact with the flow there, creating secondary vortical flows near the wall (discussed later in more detail). Further downstream, the vortices were seen to, at times, interact with each other by either pairing and/or merging together, a process that is qualitatively shown in Fig. 3.3e. The downstream wake consisted of the vortical remnants of the originally discrete vortices that had either diffused or had radially redistributed their vorticity because of vortex pairing and/or merging.

The FV also clearly showed the vortical wake sheet that was trailed from each blade. These wake sheets are comprised of small, counterrotating vortex pairs, sometimes known as Taylor-Görtler vortices [77–79]. Notice that in the contiguous sequence of flow

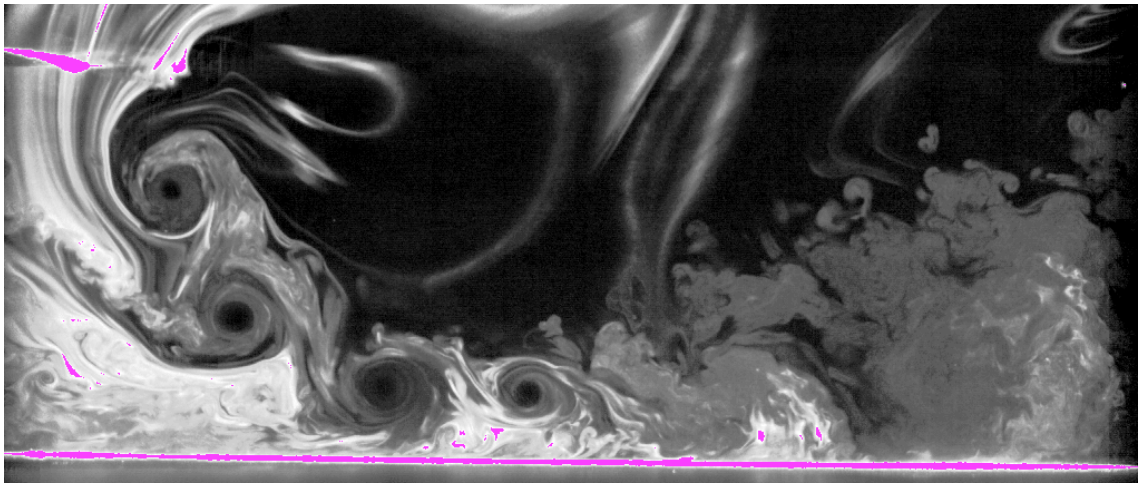

(a) ψ_b =30°

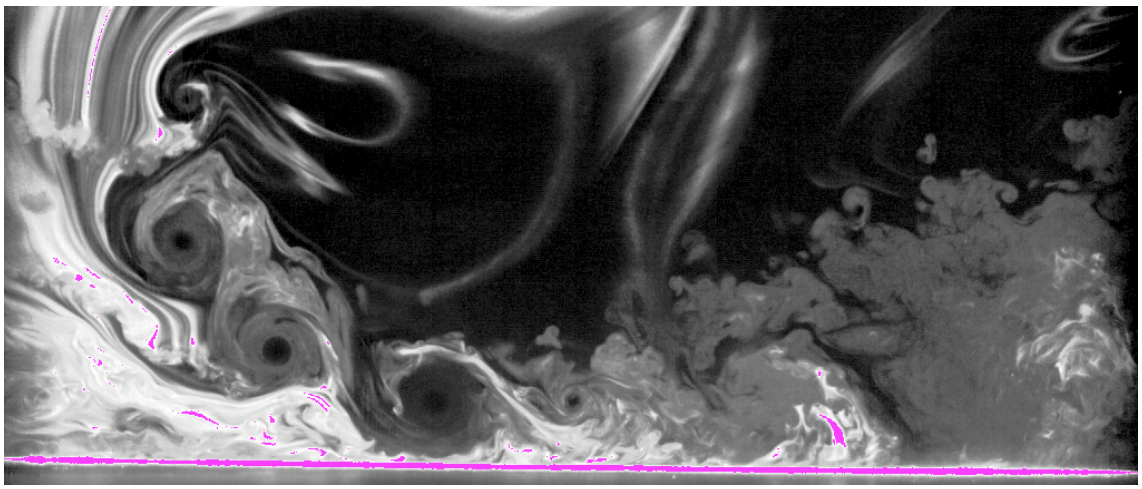

(b) ψ_b =120°

Figure 3.3: Sequence of flow visualization images for the two-bladed rotor in ROI 1.

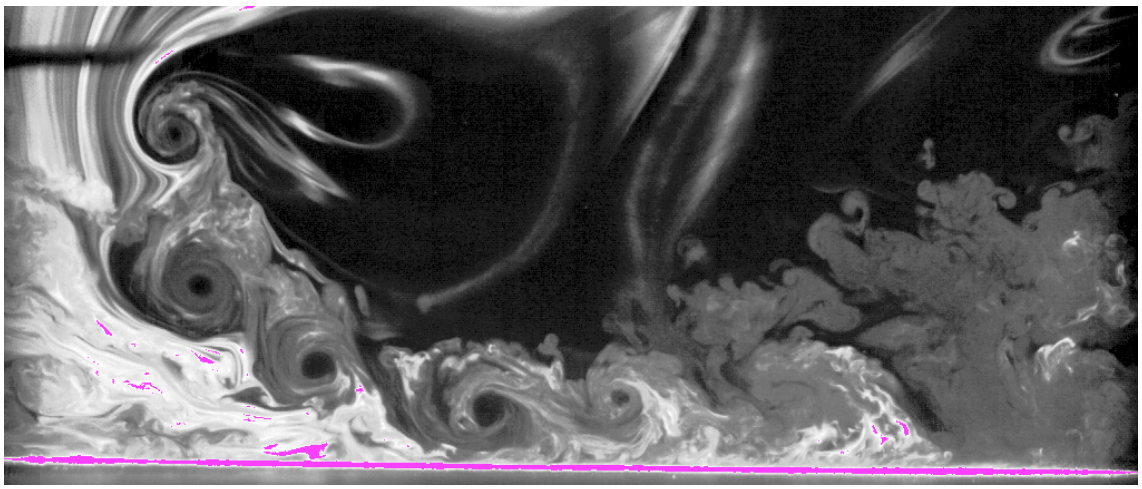

(c) ψ_b =210°

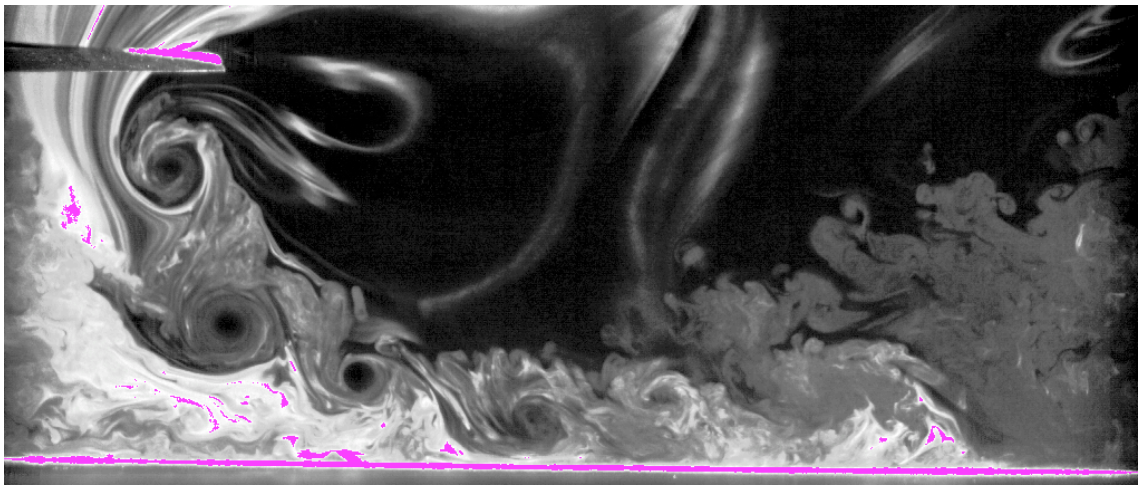

(d) ψ_b =300°

Figure 3.3: (Cont'd) Sequence of flow visualization images for the two-bladed rotor in ROI 1.

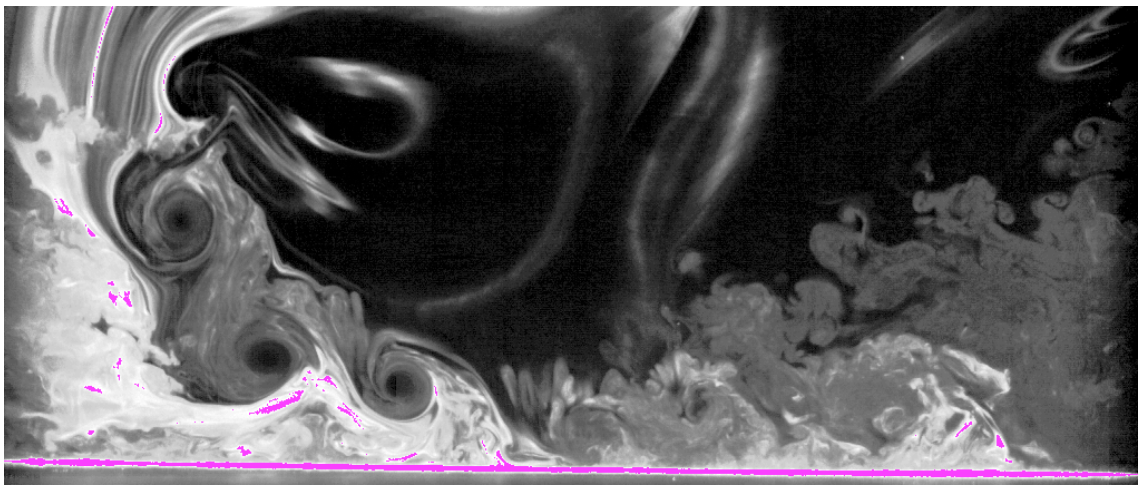

(e) ψ_b =30°

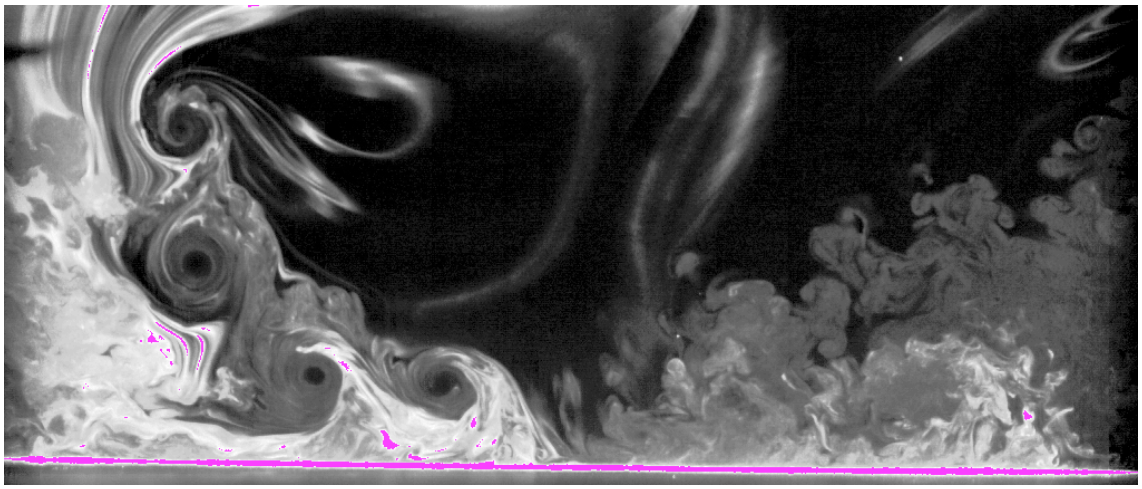

(f) ψ_b =120°

Figure 3.3: (Concluded) Sequence of flow visualization images for the two-bladed rotor in ROI 1.

realizations in Fig. 3.3, the wake sheet had convected non-uniformly downward below the rotor, with the outer portion of the sheet being convected relatively faster than the tip vortex to which it was originally attached. By approximately one rotor revolution, the vortex sheet had overtaken the original tip vortex to which it was attached and had proceeded to interact with the tip vortex formed by the previous blade [52]. Ultimately, the wake sheet convected within the rotor wake to the ground, where it proceeded to convect along the ground within the developing groundwash flow, also introducing vorticity and turbulence into this radially expanding flow.

The FV provided a good qualitative understanding of the rotor flow field and exposed the basic fluid dynamic structures that were present in the rotor wake and also near the ground. However, to better understand the development of these structures and the interaction between them, it was necessary to perform quantitative measurements that characterized, in detail, the evolution of the flow.

To examine the overall wake structure, the PIV measurements taken in ROI 1 (the larger viewing region) were first ensemble time-averaged. In the present work, 1,000 contiguous flow measurement realizations (80 rotor revolutions) were used to produce the time-averaged velocity field; see Appendix B for the details of this time-averaging procedure. While time-averaging the measurements ameliorated the transient flow structures in the rotor wake (i.e., the tip vortices and wake sheets), it provided good insight into the development of the rotor-induced flow as it interacted with the ground. Figure 3.4 shows the time-averaged results in ROI 1 as contours of total velocity, which in ROI 1 is defined as $V_{xz} = \sqrt{u^2 + w^2}$, where u and w are the velocities in the x and z directions, respectively; only every third measured flow vector is shown here for clarity.

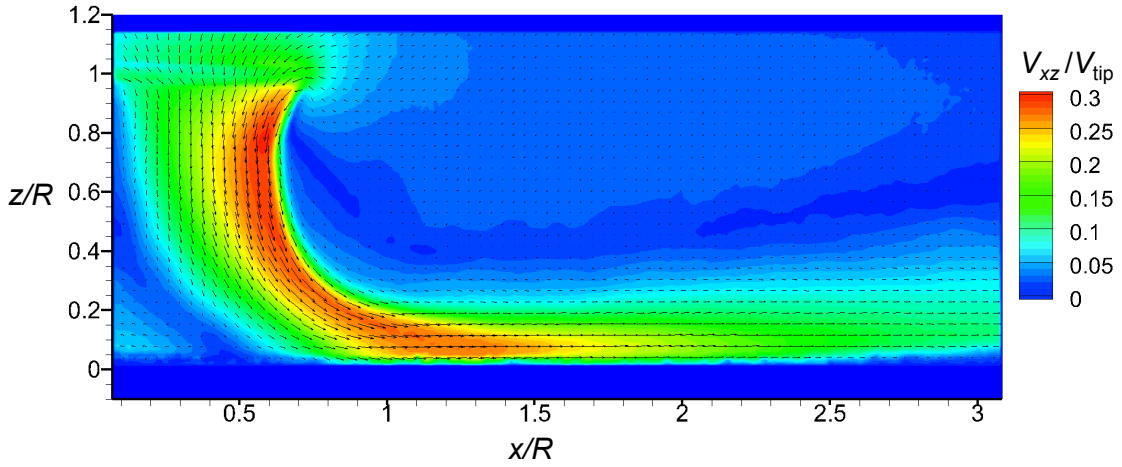

Figure 3.4: Time-averaged single-phase flow measurements as contours of total velocity in ROI 1.

The slipstream boundary between the rotor wake and the quiescent flow can be identified by the steep velocity gradient distinguishing the rotor flow from the relatively still air outside of the wake boundary, which is marked in Fig. 3.4. At the rotor plane, the flow was seen to enter the rotor disk and quickly accelerate to a higher velocity. The flow below the outboard portions of the blade (i.e., closer to the tip) had higher velocity magnitudes than the flow velocities further inboard (i.e., closer to the root), implying that there was a non-uniform loading and inflow distribution across the blade; this non-uniform inflow distribution is expected for an untwisted blade with rectangular planform. Furthermore, this inflow along the blade span explains the non-uniform convection of the wake sheet observed in the FV, with the outboard portion of the wake sheet experiencing the higher downwash velocities.

Figure 3.5 shows the direction of the flow velocities in terms of the horizontal and vertical components of velocity, u and w, respectively. Figure 3.5a shows that above

$z/R = 0.2$ the flow was primarily a downwash, i.e., it was convecting towards the ground. Figure 3.5b shows that below $z/R = 0.2$, the flow had begun to turn and convect horizontally along the ground, with the velocity vectors being mostly parallel to the wall by a downstream distance of $x/R = 1.5$. Further examination of the results in Fig. 3.5b shows that there was a stagnation point below the rotor at a location of $x/R = 0.45$. To the right of this point the flow was a wall-jet type of flow that was developing radially outward. To the left of $x/R = 0.45$, the flow direction was more towards the rotor shaft axis and displayed evidence of recirculation directly below the rotor.

While an examination of the time-averaged flow provided valuable information on the general structure of the rotor wake near the ground, time-resolved measurements were needed to reveal the transient and more intermittent developments of the rotor-induced flow. Figure 3.6 shows a sequence of instantaneous flow realizations as background contours of total velocity. In Fig. 3.6 the signature of the vortices can be identified as circular regions in red (i.e., relatively high velocity). The results show that as the vortex filaments convected toward the ground, they created local regions of increased outward velocities and also produced a highly unsteady flow environment near the ground. Ultimately, the vortices either diffused or paired and merged together, a process alluded to earlier and one that is also discussed in more detail in Section 3.1.1.3.

Figure 3.7 shows a representative instantaneous flow realization in ROI 1, now as background contours of w and u velocity. Examining the results showing the vertical component of velocity (Fig. 3.7a), a vortex location can be identified as a red/blue pair, with blue being a downwash region and red being an upwash. As the vortices aged and convected closer the ground, they created local regions of downwash and upwash near

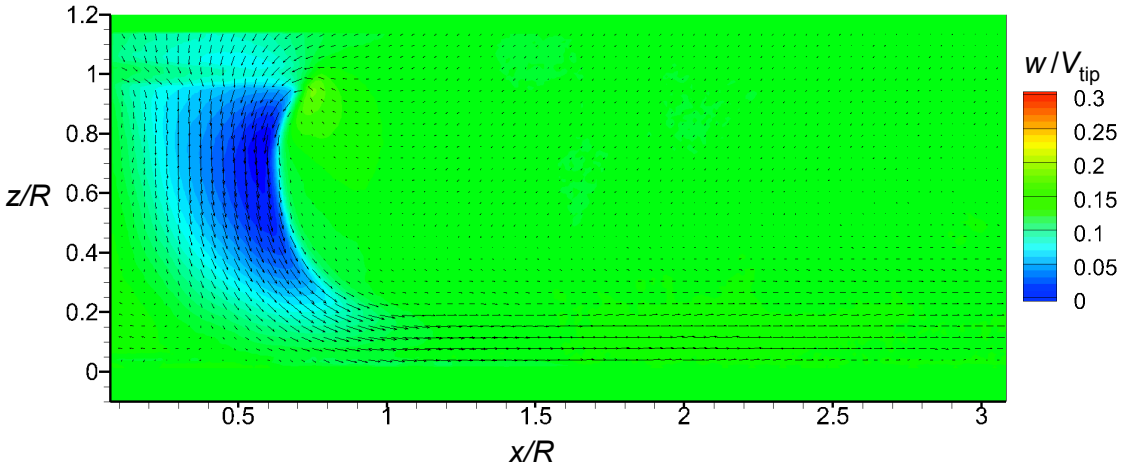

(a) *w* component of velocity

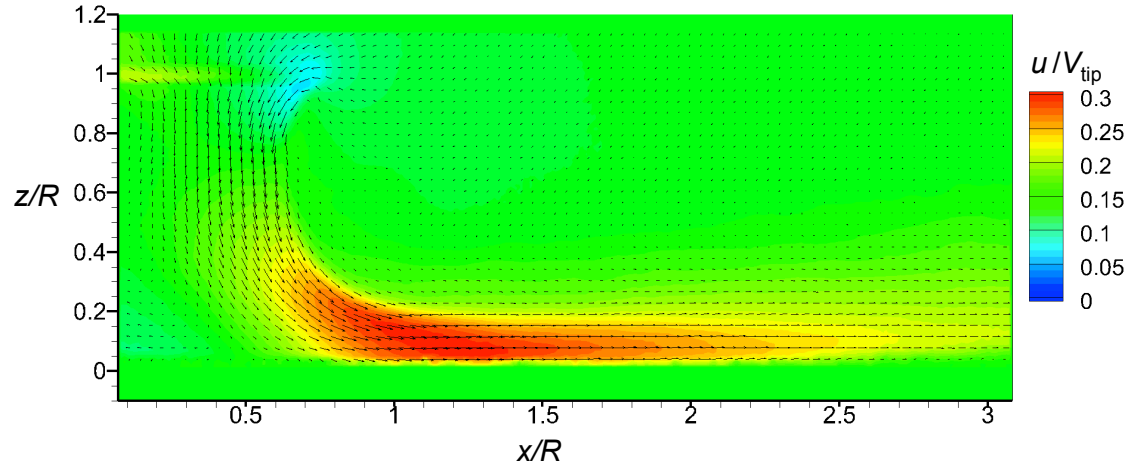

(b) *u* component of velocity

Figure 3.5: Time-averaged single-phase PIV measurements showing the different components of velocity, *w* and *u*.

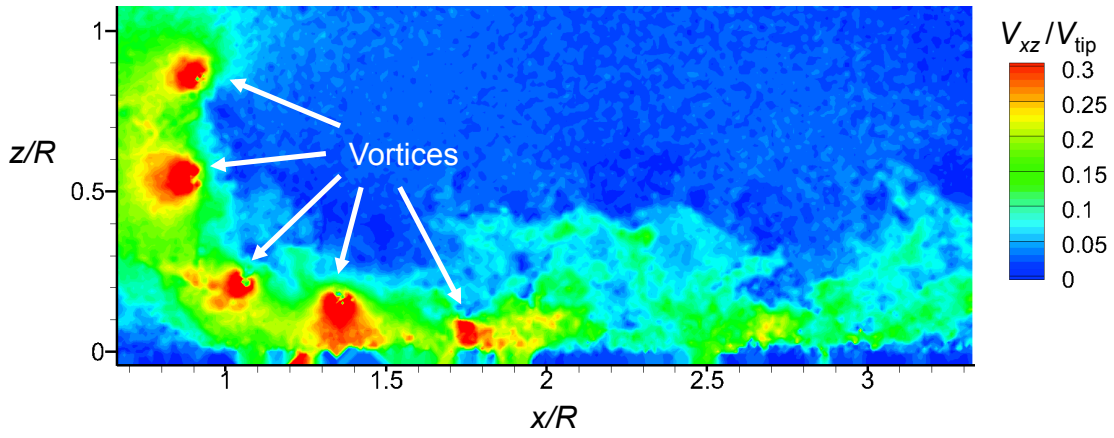

Figure 3.6: Instantaneous single-phase flow measurements as contours of total velocity in ROI 1.

the ground. When adjacent turns of the vortex filaments interacted with each other, these upwash and downwash regions were combined, creating a larger, and more turbulent region of the flow that now contained the circulation of both original vortices (again, the more detailed aspects of this process is discussed later). The significance of these stronger upwash regions near the ground is that they will affect the uplift of sediment particles [7].

Results for the *u* component of velocity are shown in Fig. 3.7b, where a red/blue pair again indicates the signature of a vortex. In this case, red contours denote outward flow velocities (away from the rotor) while blue contours denote inward flow velocities. The vortices were, again, seen to create local regions of higher velocities near the ground. Of particular interest is the counterclockwise rotation of the vortices was observed to combine with the near-wall flow velocities and create local regions of relatively higher flow velocities along the ground. These regions of higher velocity also caused steeper velocity gradients near the wall, which can also be expected to affect the mobilization of sediment particles (discussed later in Section 3.1.1.3).

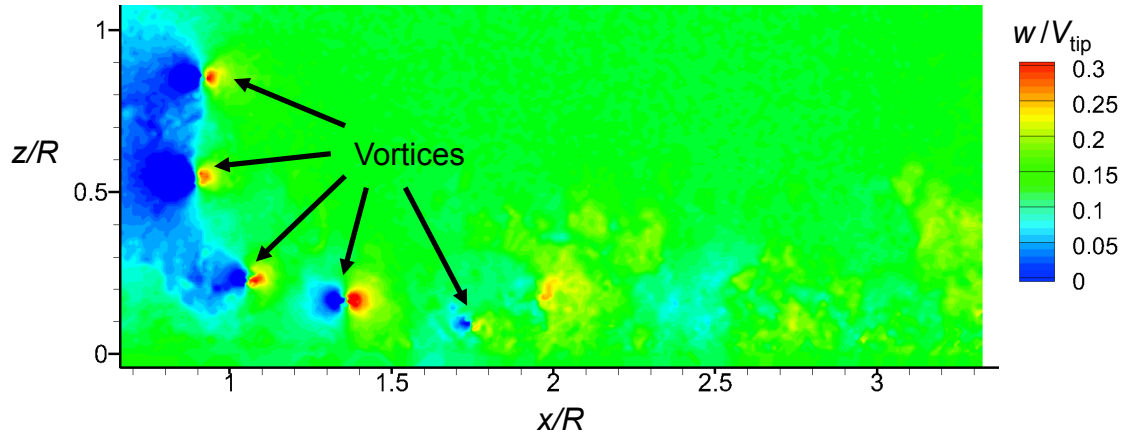

(a) *w* component of velocity

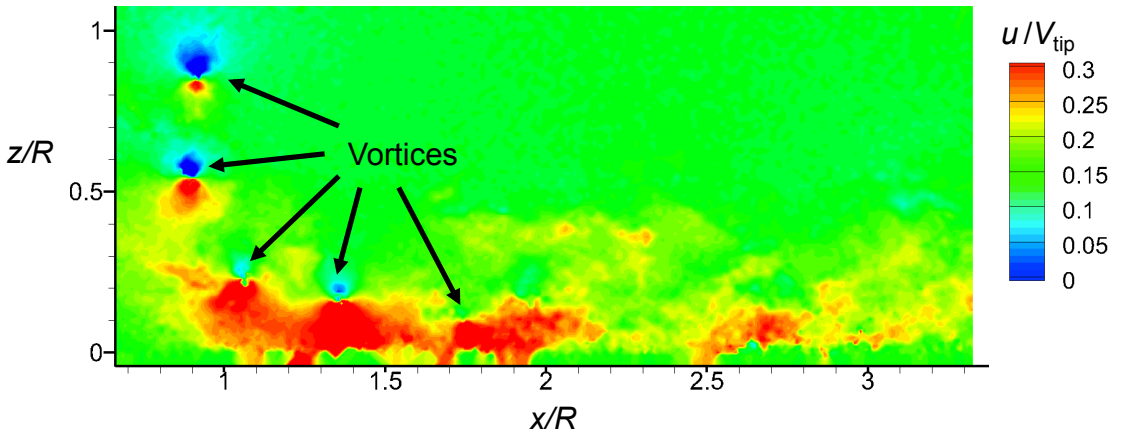

(b) *u* component of velocity

Figure 3.7: Instantaneous single-phase PIV measurements showing the different components of velocity, *w* and *u*.

3.1.1.2 Behavior of the Tip Vortices and Wake Sheet

The FV and instantaneous PIV results have shown that the rotor wake contained a number relevant of vortical flows, namely the tip vortices and wake sheets. Therefore, it was important to understand the initial development of these vortices, as well as why they persistented in the rotor wake when the rotor was in ground effect operation.

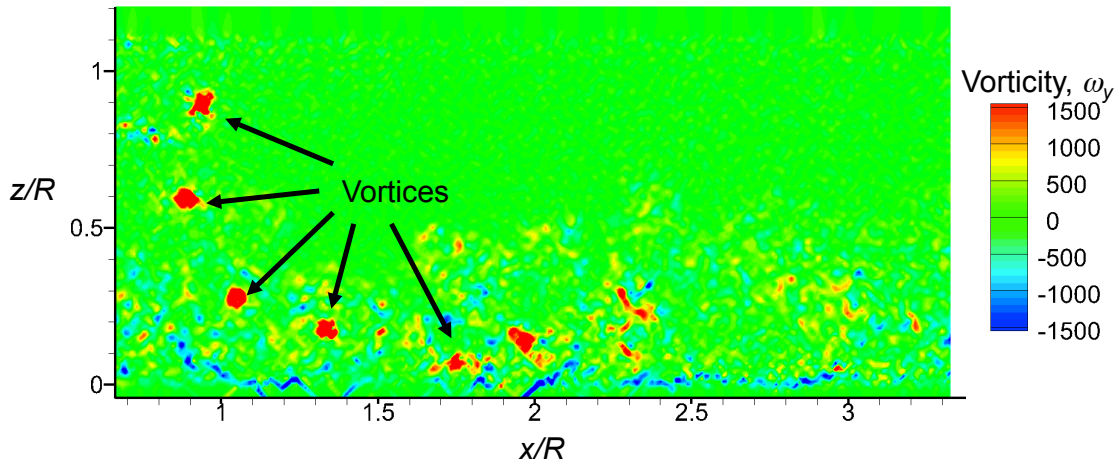

Figure 3.8: Instantaneous single-phase flow measurements as contours of vorticity, ω_{xz}, in ROI 1.

Figure 3.8 shows a representative instantaneous flow realization in ROI 1 of the two-bladed rotor hovering over the ground as background contours of vorticity, which served to highlight the vortical elements in the flow. In this case, the vorticity, ω_y, was perpendicular to the x-z plane and defined as

$$\omega_y = \frac{\partial w}{\partial x} - \frac{\partial u}{\partial z}$$

where the velocity gradients were calculated from the measured data by using a spatial five point central differencing scheme. The color of the vorticity map in Fig. 3.8 is determined by the direction of the sign of the vorticity, with red being a counterclockwise (positive) motion and blue being a clockwise (negative) motion.

The tip vortices can be identified as distinct red regions of concentrated vorticity in the image shown in Fig. 3.8. The vortex closest to the rotor plane was the youngest part of the trailed vortex in this flow realization ($\zeta \approx 40°$). Attached to this vortex was a wake sheet, which as previously mentioned is comprised of smaller scale and relatively weaker

vorticity. As the wake sheet aged in the flow, it was observed to interact with the older tip vortices.

To further investigate this interaction, a more detailed region with a higher measurement resolution (600 vectors/radius) near the blade tip was studied at a higher frame rate of 5,000 images-per-second, equivalent to approximately 4.3° of blade rotation between flow realizations, which allowed for the examination of the tip vortex and wake sheet formation and development.

Figure 3.9 shows a contiguous sequence of flow realizations in this detailed region as background contours of vorticity. This sequence shows the early development of both the tip vortex and the wake sheet. The first realization in the sequence, Fig. 3.9a, shows the tip vortex at $\zeta = 12.9°$ and the outboard portion of the wake sheet, which can be seen to be comprised of counterrotating vortical pairs (i.e., red/blue pairs of vorticity). By $\zeta = 17.2°$ (Fig. 3.9b), the wake sheet had begun to develop into smaller and less coherent vortical flows. At $\zeta = 21.5°$ (Fig. 3.9c), the vortical flows within the outboard part of the wake sheet were observed to merge with the tip vortex until the tip vortex was a combination of its original vorticity and the vorticity contained in the outboard part of the wake sheet.

Another phenomenon that was observed in this detailed region of the flow was the relaminarization of turbulent eddies near the core of the tip vortex. Figure 3.10 shows a sequence of contiguous flow images as contours of vorticity in which the tip vortex entrained and relaminarized the surrounding turbulence. Relaminarization of turbulence by a tip vortex has been observed before [52, 79], but these are the first time-resolved measurements of the phenomenon. In Fig. 3.10a, the tip vortex can be seen to be sur-

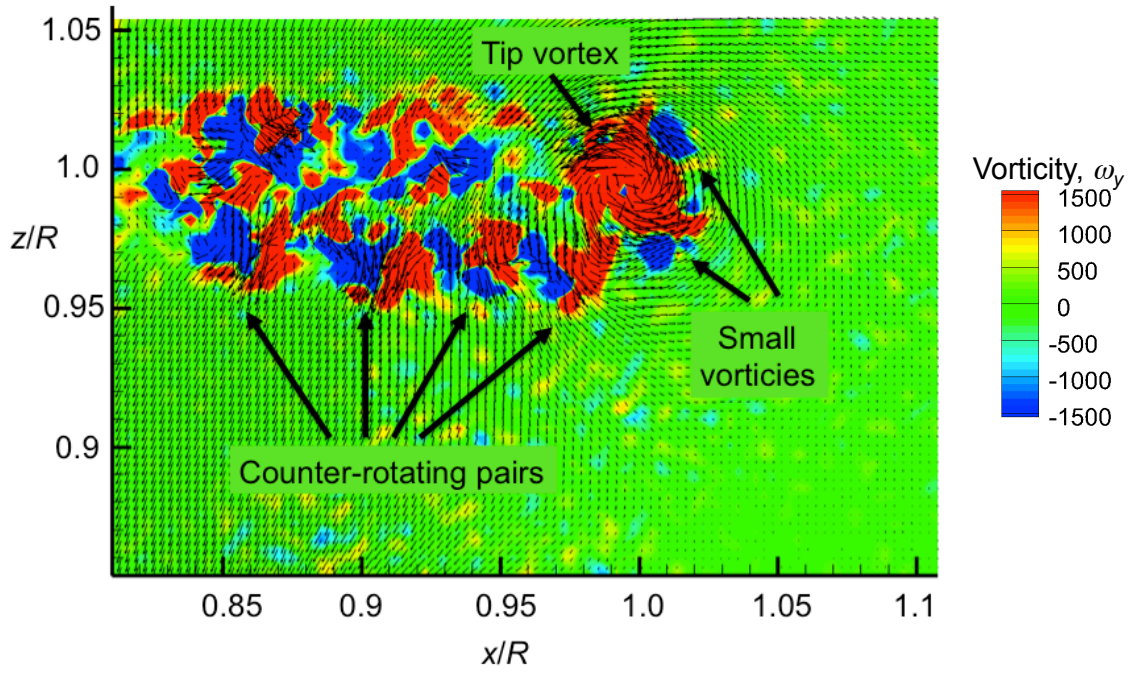

(a) $\zeta = 12.9°$

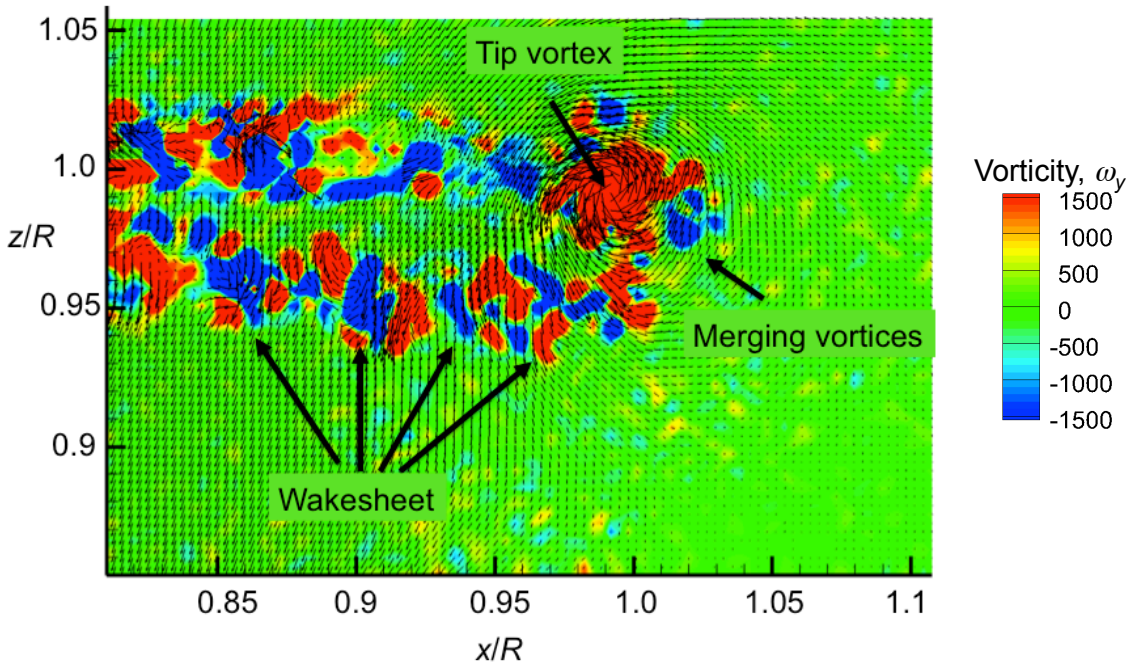

(b) $\zeta = 17.2°$

Figure 3.9: Instantaneous sequence of vorticity showing the roll-up of the tip vortex.

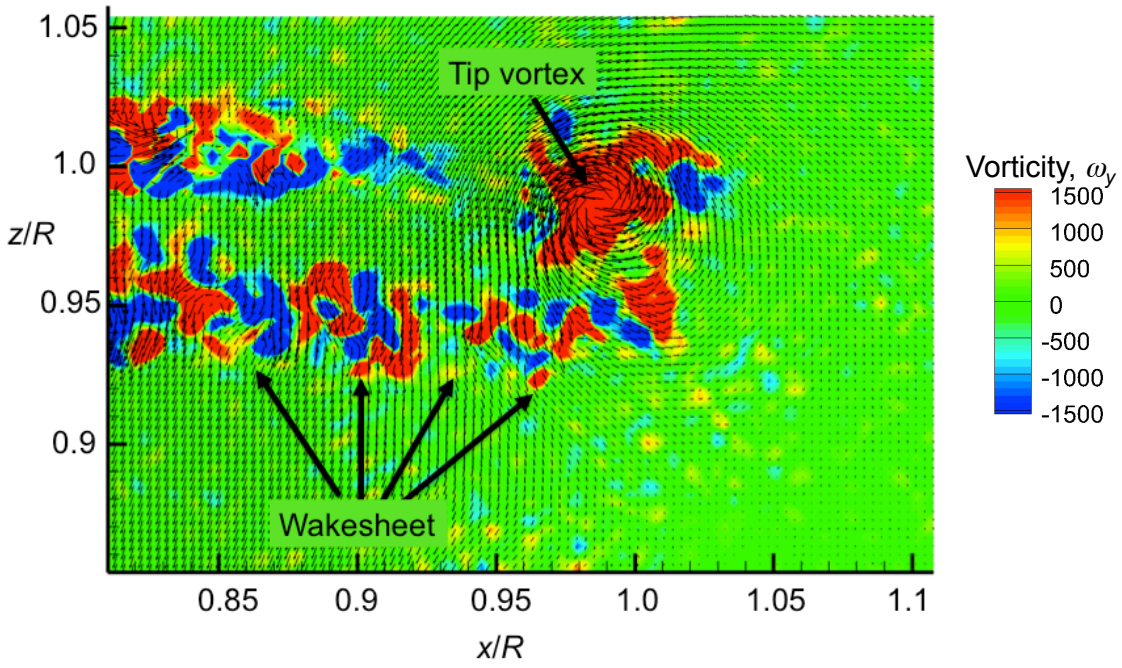

(c) $\zeta = 21.5°$

Figure 3.9: (Concluded) Instantaneous sequence of vorticity showing the roll-up of the tip vortex.

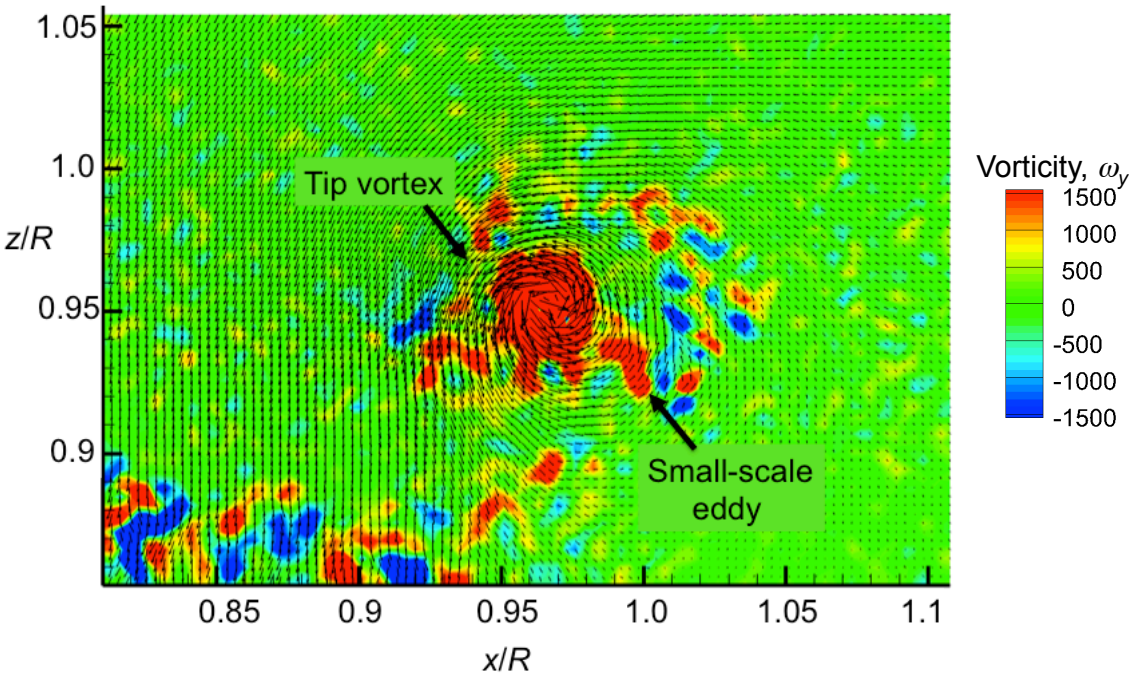

(a) $\zeta = 34.4°$

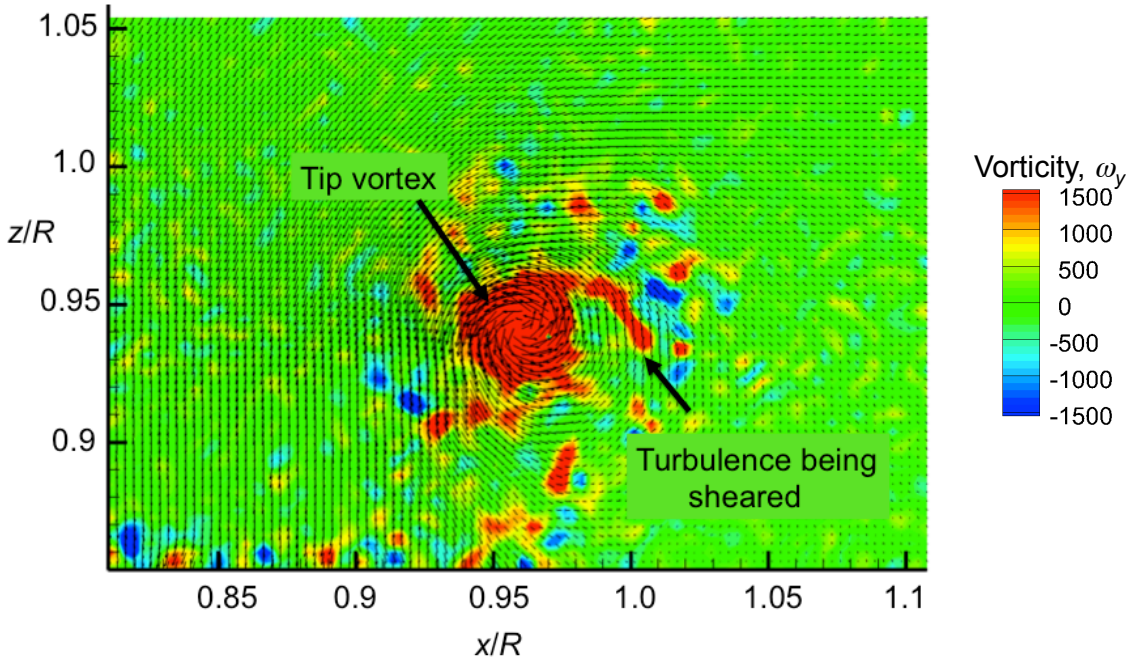

(b) $\zeta = 38.7°$

Figure 3.10: Instantaneous sequence of vorticity showing the relaminarization of turbulence by the tip vortex.

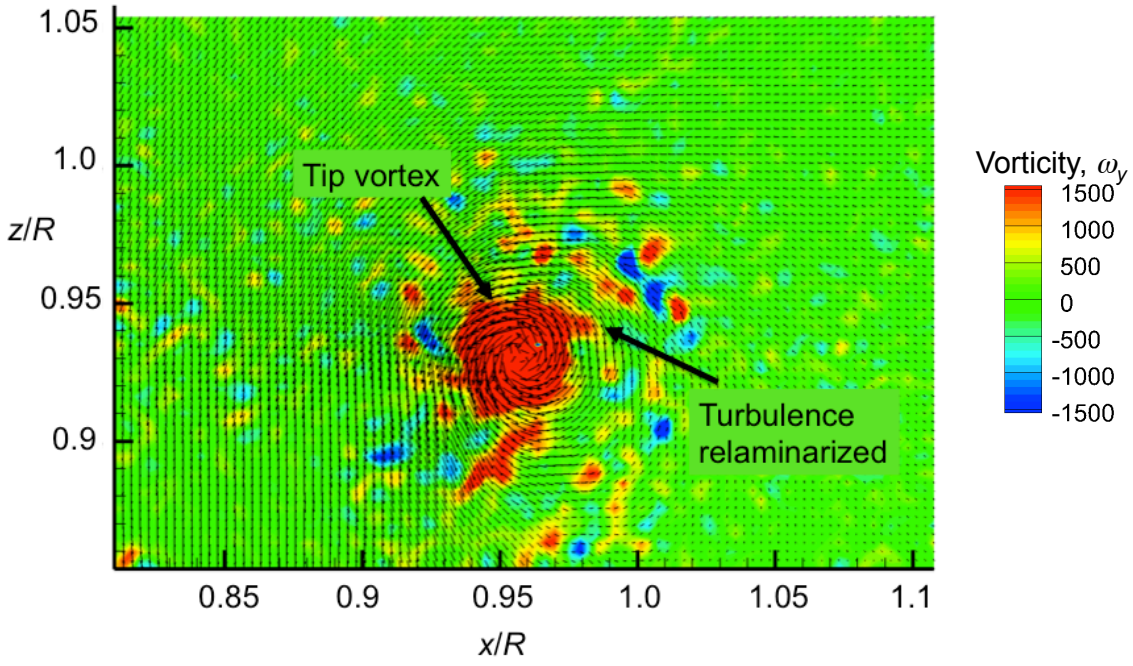

(c) ζ =43.0°

Figure 3.10: (Concluded) Instantaneous sequence of vorticity showing the relaminarization of turbulence by the tip vortex.

rounded by turbulent eddies, some of which have originated in the wake sheet. In this flow realization, one vortical eddy at the periphery of the tip vortex has been identified. In the subsequent flow realization (Fig. 3.10b) this eddy was sheared and elongated by the tip vortex. Ultimately, the eddy was squeezed to a point where it was ingested by the vortex core and "relaminarized." This outcome shows why, in general, rotor tip vortices tend to persist in the flow, i.e., they have laminar cores that diffuse mainly by the action of viscosity, which is a relatively slow process.

With the initial development of the tip vortices and wake sheet being better quantified, it was important to further investigate the persistence of the tip vortices in the wake. To do this, the locations of the tip vortex filaments were tracked from their initial formation at the blades to the point where they diffused their vorticity. It was necessary to use a parameter that could accurately determine the center of the vortex, and previous work [84] has shown that the Q-criterion (which is based on velocity gradients) was found to best locate the vortex center. The value of Q is given by

$$Q = \frac{1}{4}\left(\frac{\partial u}{\partial x} + \frac{\partial w}{\partial z}\right)^2 + \frac{\partial u}{\partial x}\frac{\partial w}{\partial z} - \frac{\partial u}{\partial z}\frac{\partial w}{\partial x}$$

which comes from [84]. A spatial five point central differencing scheme was used to calculate the gradients from the PIV data.

An example contour map of the Q-criterion for an instantaneous flow realization is shown in Fig. 3.11. This result shows that the Q-criterion identified the stronger vortical elements in the flow, with the tip vortices being clearly discriminated from the surrounding flow. A white circle has been placed where the vortex tracking algorithm has identified a vortex location that had aged to $\zeta = 30^\circ$. This part of the vortex filament was further

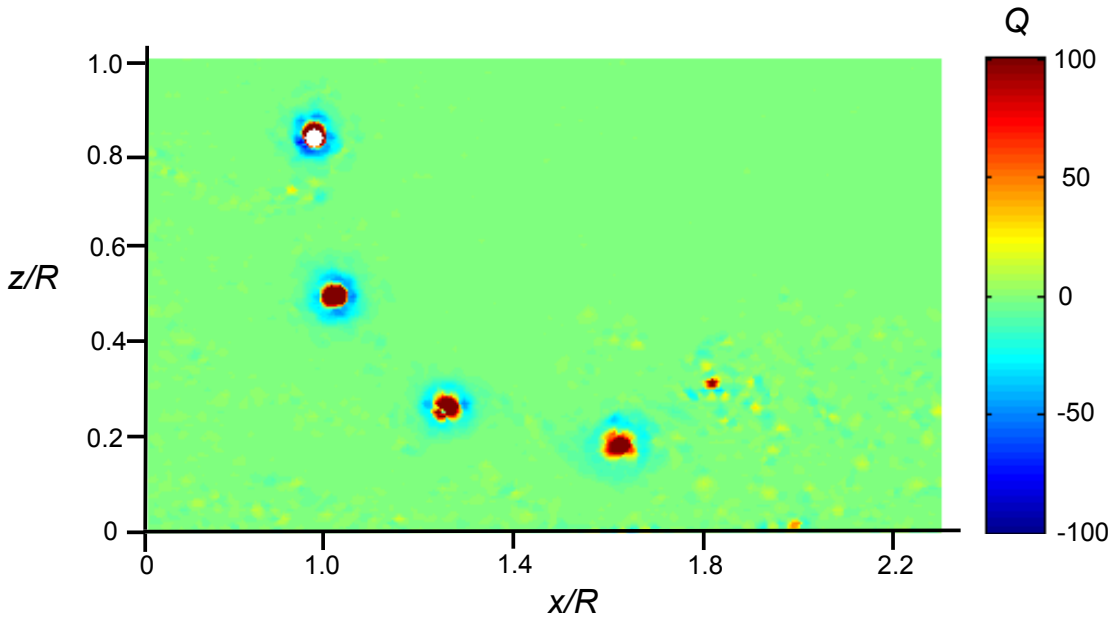

Figure 3.11: Instantaneous single-phase flow contours of Q-criterion showing an identified vortex.

tracked in increments to $\zeta = 720^{\circ}$, the results being shown in Fig. 3.12.

To better quantify the persistence of the vortices in the flow, the swirl velocity profile was extracted from the PIV measurements at each of the locations identified in Fig. 3.12. This velocity profiles was extracted by taking a vertical cut through the center of the vortex flow and plotting the variation in the u (wall-parallel) component of velocity. An example of such a swirl velocity profile is shown in Fig. 3.13; this swirl profile is shown in the reference frame of the vortex.

The profile was transformed to the vortex reference frame by taking the convection rate of the center of the vortex and subtracting it from the entire profile. The velocity profile, V_{θ}, in Fig. 3.13 is plotted as non-dimensional horizontal velocity (i.e., $V_{\theta} \equiv u/V_{\text{tip}}$) as a function of non-dimensional height off the ground, z/R. The profile showed that the

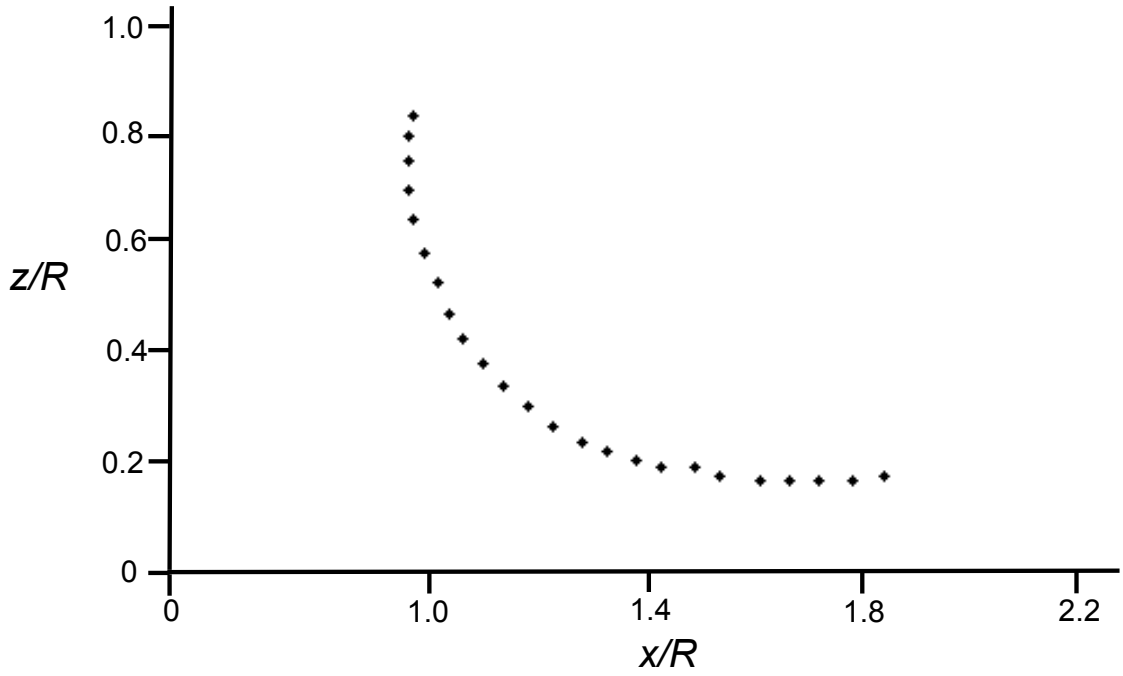

Figure 3.12: Tracked vortex location from $\psi = 30^\circ$ to $\psi = 720^\circ$.

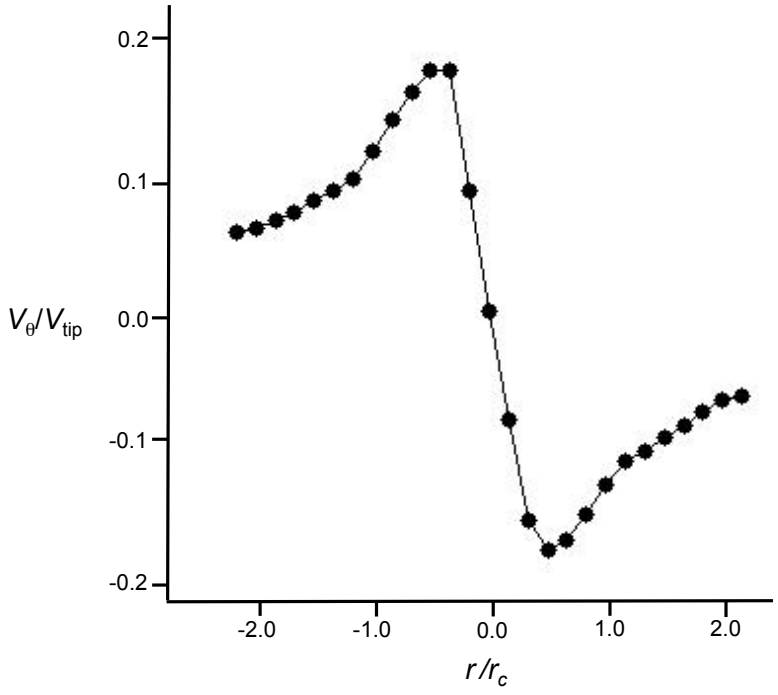

Figure 3.13: Representative swirl velocity profile of a vortex.

maximum and minimum peak velocities were observed on either side of the vortex core. The core radius, r_c, of the vortex was defined as the distance between these maximum and minimum peak velocities. Another important vortex characteristic was the maximum swirl velocity, $V_{\theta_{max}}$. For the example shown in Fig. 3.13, the non-dimensional core radius, r_c/R, was 0.05 and the non-dimensional maximum swirl velocity, $V_{\theta_{max}}/V_{tip}$, was 0.35.

These vortex characteristics were determined for all the wake ages, ζ, over which the measurements could be obtained. This procedure was then repeated for all 1,000 flow realizations. The core radius and maximum swirl velocity were ensemble-averaged, with the results being shown in Figs. 3.14 and 3.15, respectively. The core growth showed the expected trend for a rotor operating in-ground-effect, i.e., as the vortex aged in the flow, the core size initially grew. The rate of growth of the core then slowed before continuing to grow at a higher rate at older wake ages. The core size could only be determined to $\zeta = 570^\circ$ because after this age the core had grown to a point where it was much more diffused.

The variation of the maximum swirl velocity, $V_{\theta_{max}}$, shown in Fig. 3.15 provided some insight into the persistence of the tip vortices. Initially, at $\zeta = 30^\circ$, the vortex had a relatively high maximum swirl velocity, though the swirl velocity rapidly decreased as the vortex further aged. However, from $\zeta = 150^\circ$ to $\zeta = 420^\circ$ the maximum swirl velocity began to increase, i.e., the vortices persisted in the flow instead of diffusing. After $\zeta = 420^\circ$, there was a steep decline in the maximum swirl velocity until $\zeta = 720^\circ$.

Previous studies [17, 18, 85] have shown that the reason for the persistence of the vortices is the stretching of the vortices as they convect along the ground. Because the tip vortices were actually part of a longer, continuous vortex filament, the expansion of

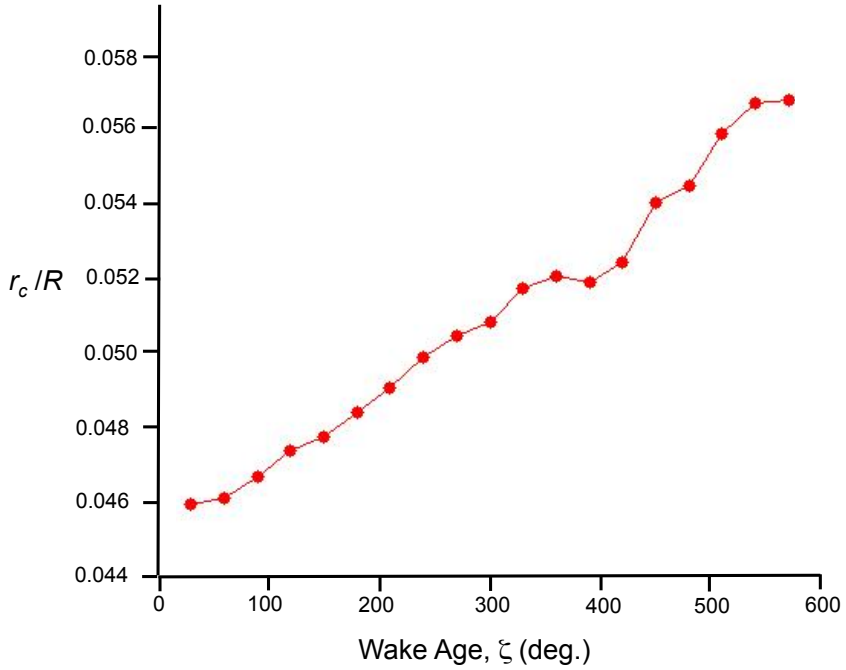

Figure 3.14: Average core growth for 180 tracked vortices.

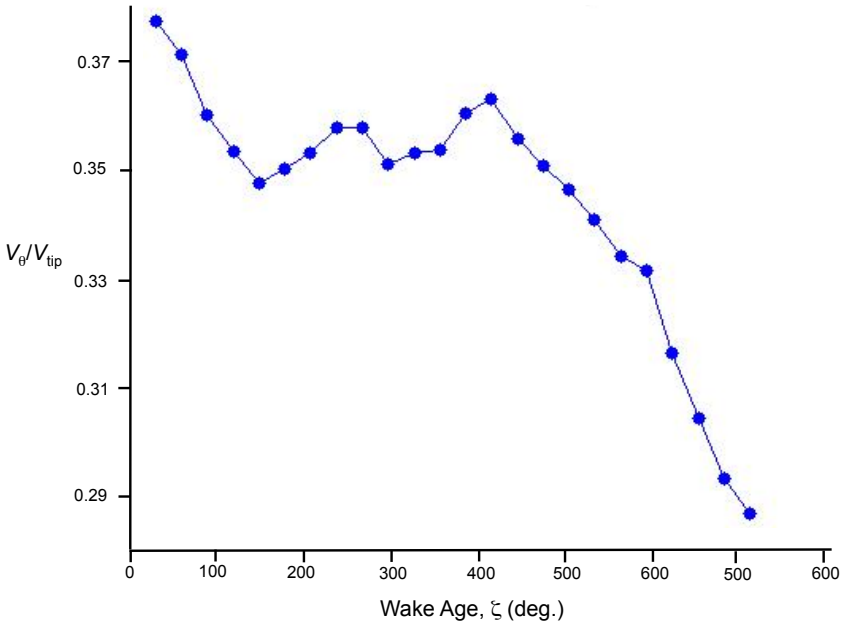

Figure 3.15: Average peak-to-peak velocity profile for 180 tracked vortices as a function of wake age.

the rotor wake boundaries caused the vortices to stretch along their lengths, significantly increasing their vorticity, a schematic of this stretching process being shown in Fig. 3.16. This process is accompanied with a corresponding increase in the maximum swirl velocity of the vortices. When the rotor is operating far away from the ground, the vortices do not expand radially outward and so they do not stretch much along their lengths. Therefore, the vortices undergo diffusion and spin down at relatively young wake ages. However, in the presence of the ground, the stretching of the vortices balances or counteracts the process of turbulent diffusion, causing the vortices to persist in the flow to much older wake ages [17, 85]. The results in the present work show the time-history of the peak swirl velocity and the growth of the vortex core, which are both clearly affected by the stretching of the vortices.

Another phenomenon that was observed in the present work was the aperiodicity in the vortex trajectories. Figure 3.17 shows the vortex locations that were identified over 1,000 flow realizations. Above the plane at z/R =0.7, the locations were seen to be more periodic, i.e., the locations did not change much at a given wake age. However, as the wake began to expand the vortex locations became increasingly aperiodic. Near the ground there, was a large region of possible vortex locations for a given wake age, which had a significant effect on particle mobilization and transport (discussed later).

3.1.1.3 Near-Wall Flow Analysis

Obviously, the flow environment near the ground is of critical importance to the problem of rotor-induced particle motion. The FV and PIV experiments made in ROI 1

(a) Filament "spins-down" by viscous diffusion

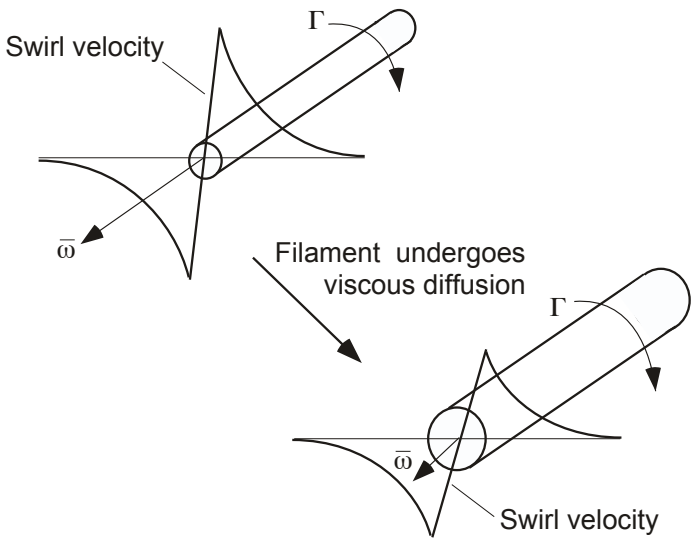

(b) Filament is "stretched" by the action of velocity gradients

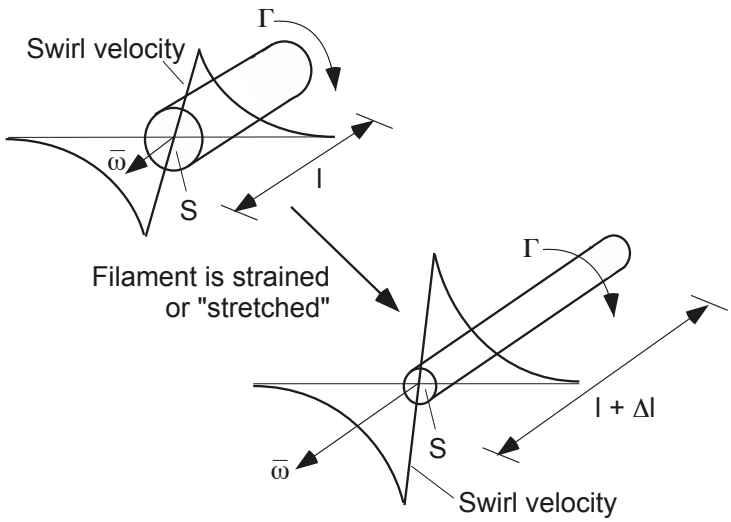

Figure 3.16: Schematic showing the reintensification or diffusion of vortex swirl velocity from stretching and straining.

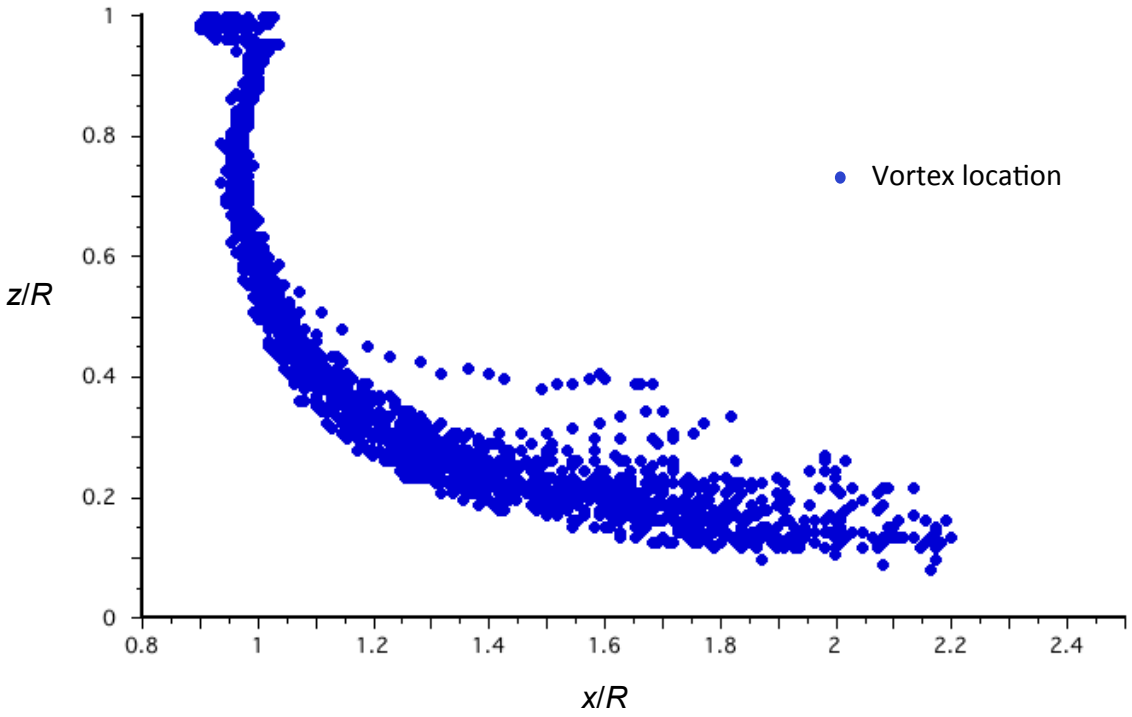

Figure 3.17: All 180 tracked vortex trajectories super imposed.

showed that there were two dominant features of the flow, the wall-jet type of flow (similar to that found in boundary layer problems), and also the presence of concentrated vorticity. The larger measurement region in ROI 1 did not allow for a detailed analysis of the flow near the ground. However, an analysis of the flow field was also performed in ROI 3, which had a higher measurement resolution (300 flow vectors/R) and which allowed for the detailed examination of the development of the wall-jet like flow and the action of the near-wall concentrated vorticity.

Time-averaged results of total velocity in ROI 3 are shown in Fig. 3.18. Notice that the velocity vectors are colored by the total velocity, and only every 15th measured vector is shown in the wall-parallel direction to better show the velocity profiles. The results show that from $x/R = 0.95$ to $x/R = 1.0$, the downwash of the rotor was still

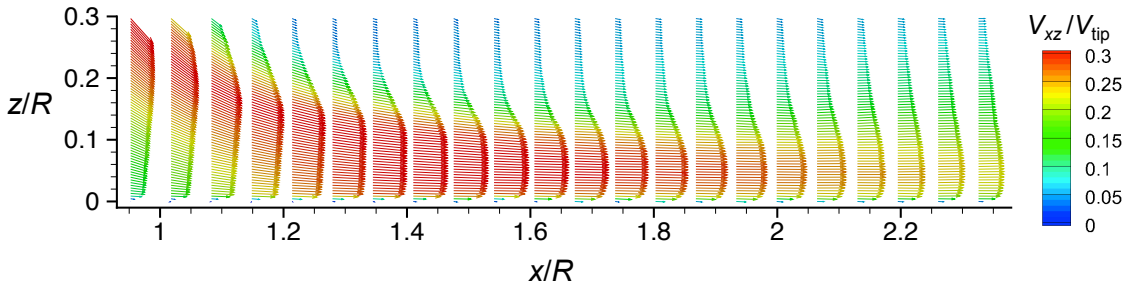

Figure 3.18: Time-averaged total velocity profiles near the ground for the isolated rotor.

turning radially outward to form the wall-jet. As the wall-jet developed outward along the ground, it thinned and the wall-jet velocities increased. Further downstream at $x/R \approx 1.6$, the wall-jet began to thicken and the wall-parallel velocities decreased in magnitude.

To better quantify the flow at the ground, velocity profiles (i.e., vertical "cuts") were taken at five different downstream locations, $x/R = 1.0$, 1.3, 1.6, 1.9. and 2.2; see Fig. 3.19. At $x/R = 1.0$, the wake was still turning radially outward and the peak wall-jet velocity was at a height of $z/R = 0.25$, i.e., the peak was relatively far above the ground plane. By $x/R = 1.3$, the downwash from the rotor had almost fully turned to flow parallel to the wall, and had begun to better resemble a classical wall-jet flow. At $x/R = 1.6$, the wall-jet had fully developed and reached a maximum peak velocity of $u/V_{\text{tip}} = 0.19$. Notice that the relatively steep velocity gradient found between the ground and the peak velocity implied that a boundary layer had formed there. Beyond $x/R = 1.6$, the wall-jet had began to thicken and the peak wall-jet velocity had began to decrease.

Understanding the boundary layer characteristics (such as the gradient of the flow velocity at the ground) is important for the problem of rotor-induced particle motion. The boundary layer forms as a consequence of a no-slip condition at the surface. The gradient of the flow at the ground is of particular importance because the steeper velocity gradients

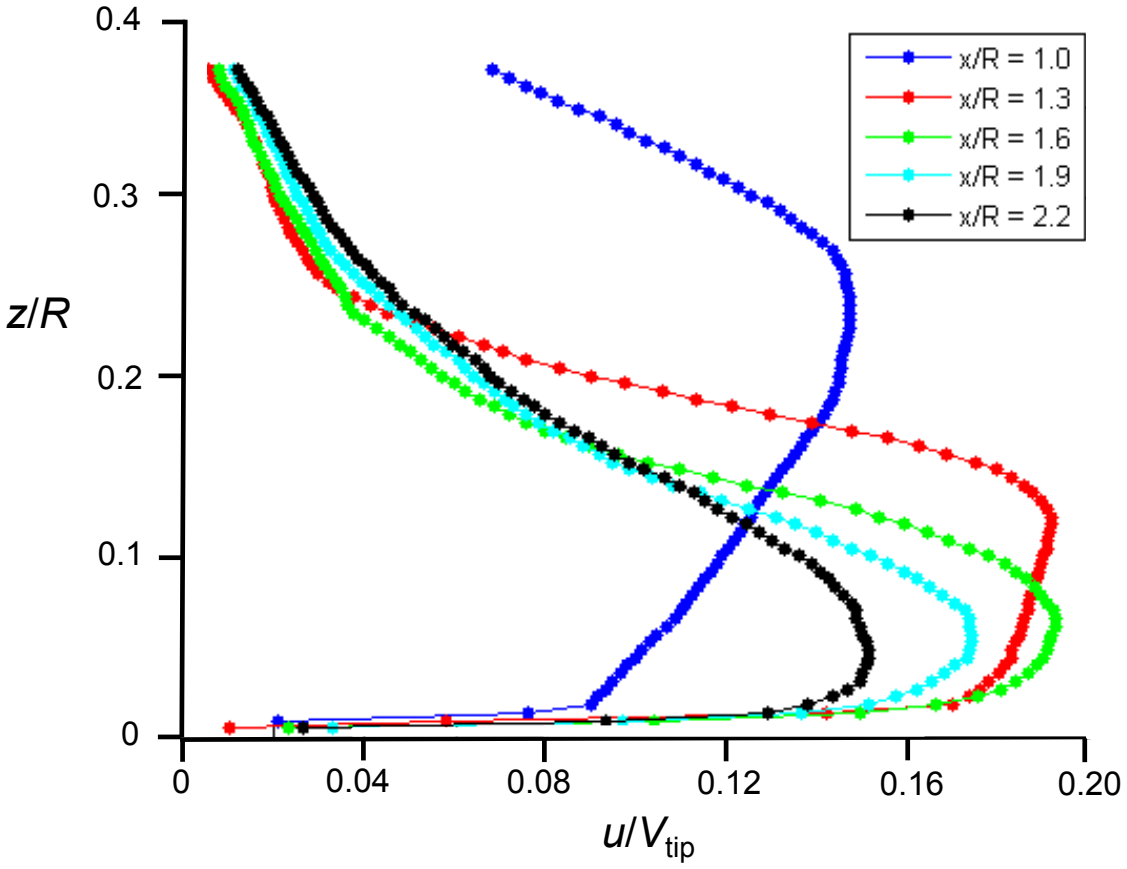

Figure 3.19: Time-averaged total velocity profiles taken at different downstream distances.

will cause a higher shear stress at the wall (and particle bed). Previous studies [21, 23–25, 72] have shown that if the wall shear becomes high enough, then sediment particles will be mobilized. The equation for wall shear stress, τ_w, is

$$\tau_w = \mu \frac{\partial u}{\partial z}\bigg|_{z=0}$$

where $\partial u/\partial z$ is the gradient of the u component of velocity in the z direction and μ is the coefficient of dynamic viscosity. the above equation was used to calculate the wall shear stress, the results being shown in Fig. 3.20. As the wake began to turn radially outward, that is between $x/R = 1.0$ and $x/R = 1.2$, the wall shear stress increased. The shear peaked

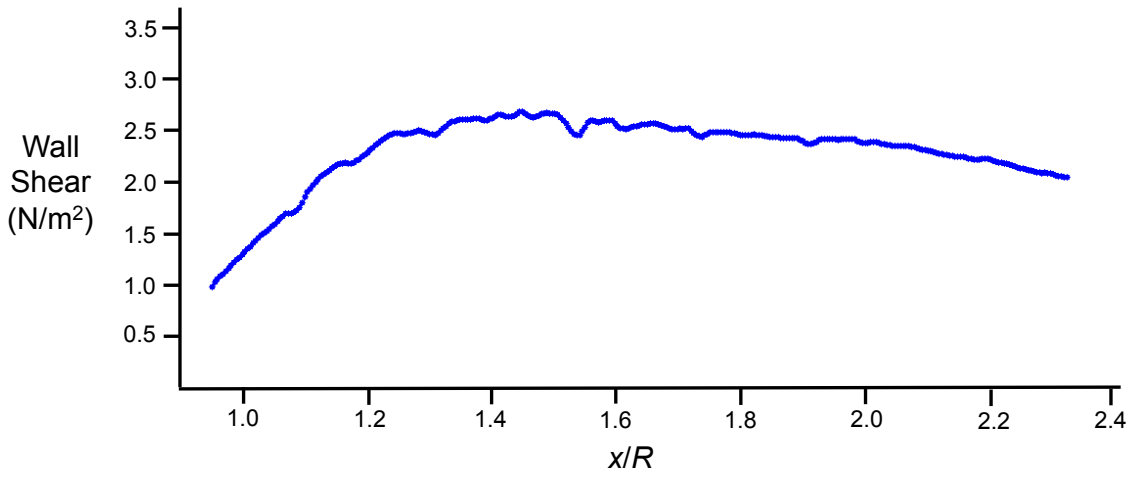

Figure 3.20: Time-averaged shear stress variation along the ground.

between $x/R = 1.4$ and $x/R = 1.6$, which is known as the "impingement region" because it was also where the vortices began to closely interact with the ground plane (Fig. 3.6). The importance of this impingement region is that the wall shear stress may be above the threshold required to mobilize particles from the sediment bed. Beyond $x/R = 1.6$, the wall-jet began to decelerate and the values of the wall shear stress decreased.

While the time-averaged flow results provided valuable insight into the developments of the rotor wake at the ground, the problem of rotor-induced particle mobilization is more of a transient and unsteady one, and so examining the instantaneous values of near-wall flow velocities was also important. One consequence of time-averaging the flow measurements is that they ameliorated the signatures of the tip vortices, however, the vortices clearly affect the transient mobilization and transport of sediment particles.

To examine the transient nature of the rotor wake, an instantaneous flow realization is shown in Fig. 3.21 as contours of total velocity, u, and w. The total velocities shown in Fig. 3.21a indicate that the vortices affected relatively large regions of the velocity field

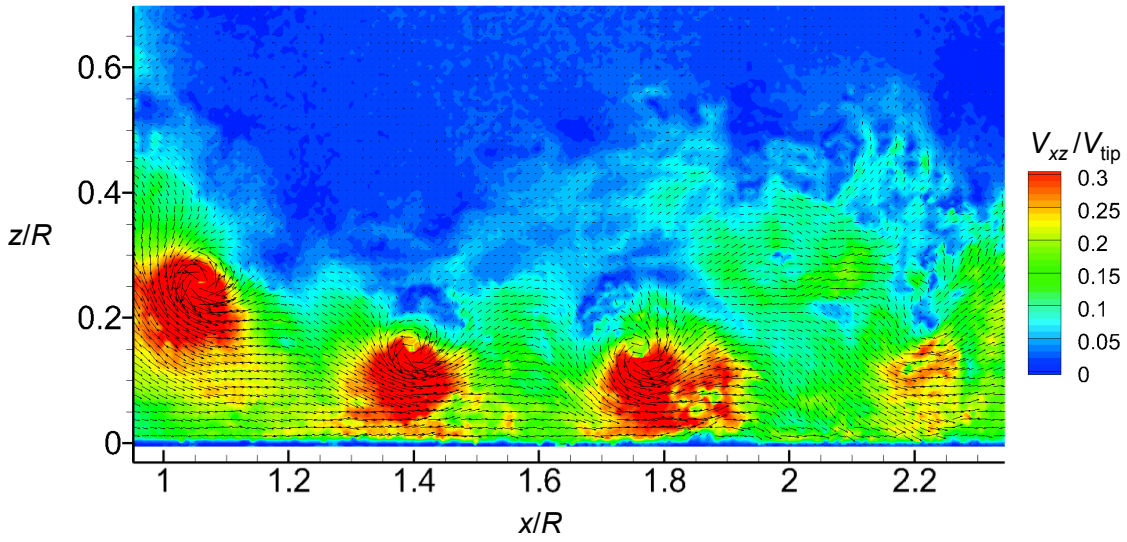

(a) V_{xy}

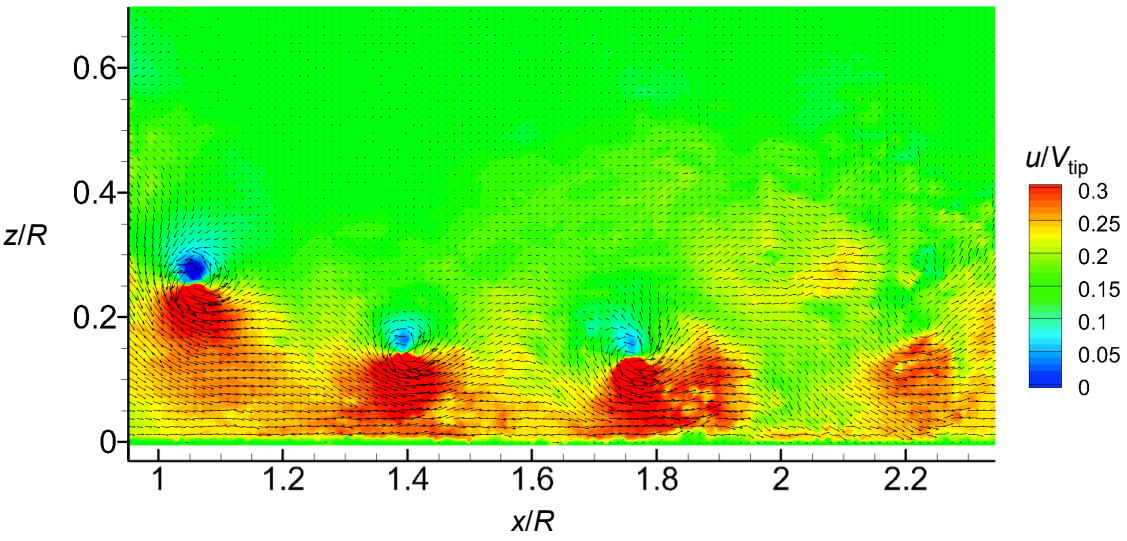

(b) u

Figure 3.21: Instantaneous contours of V_{xz}, u, and w velocity in a near-wall region.

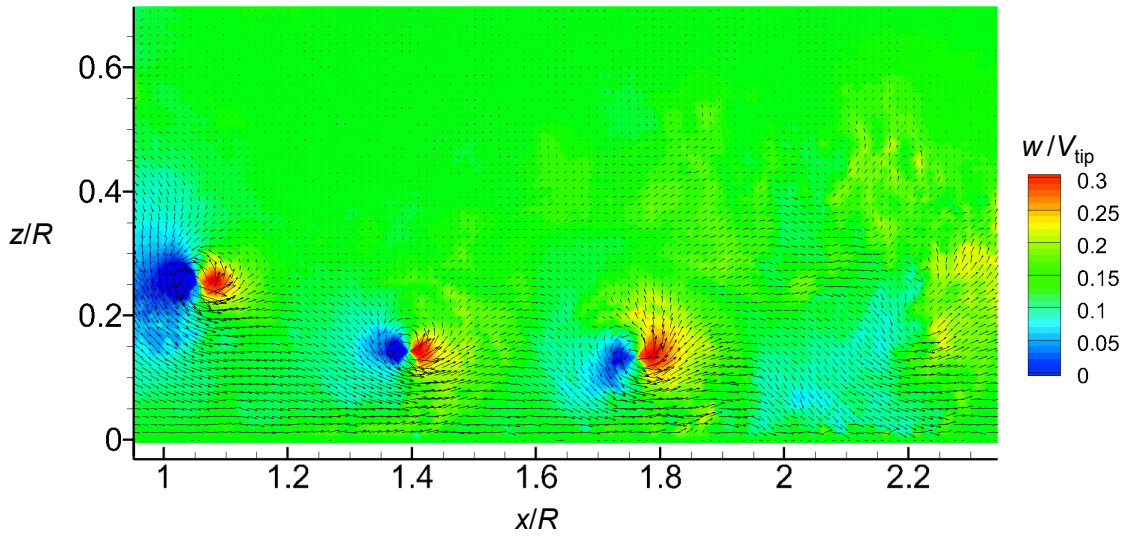

(c) v

Figure 3.21: (Concluded) Instantaneous contours of V_{xz}, u, and w velocity in a near-wall region.

near the ground. Examining the contour of u (wall-parallel) velocity in Fig. 3.21b, it can be seen that the vortices induced flow velocities of relatively high magnitude directly above the surface, locally affecting the boundary layer and wall-jet characteristics (discussed in detail next). Another important consequence of the near-wall vorticity was the presence of both an upwash and downwash region, as shown for example in Fig. 3.21c, where a red/blue pair indicates the signature of a vortex flow.

The magnitude of wall shear was found to be dependent on the local height of the vortex core above the ground, which varied, in part, because of the aperiodic nature of the flow. For example, Fig. 3.22a and 3.22b each show an instantaneous flow realization in ROI 3 as contours of total velocity for a blade azimuthal position of $\psi_b = 90°$; every third measured flow vector is shown here fo clarity. These two particular flow realizations

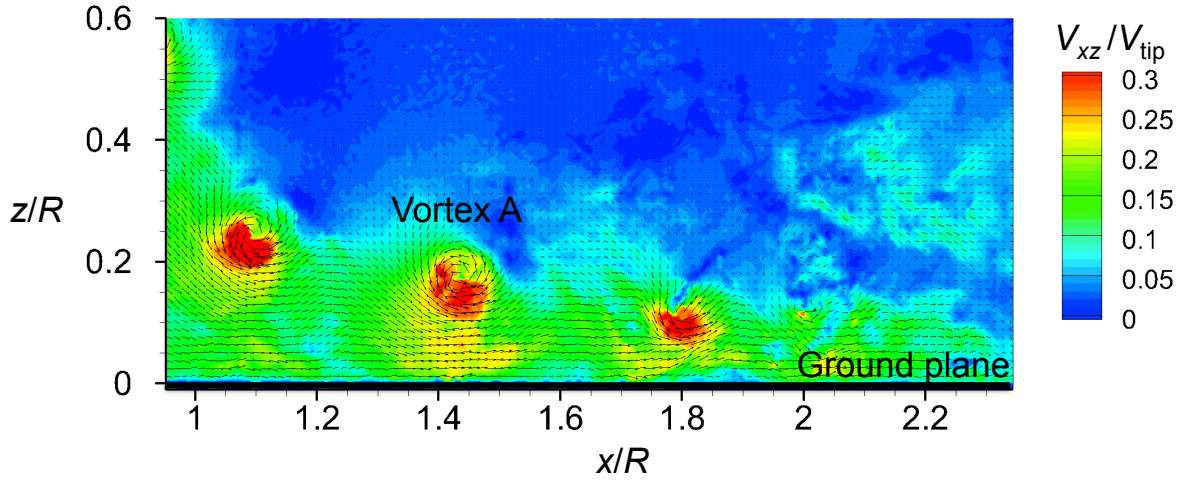

(a) Flow realization 1

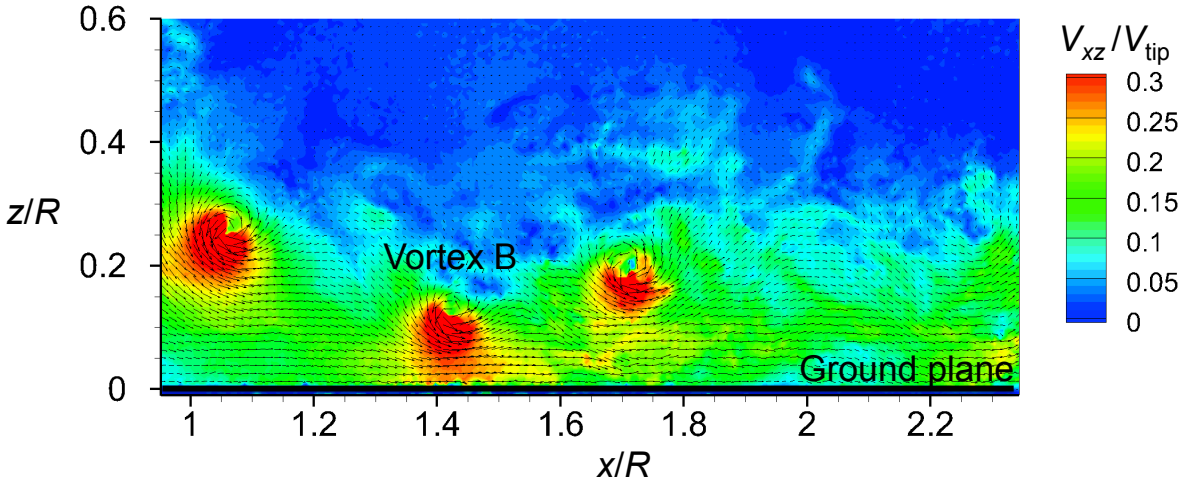

(b) Flow realization 2

Figure 3.22: Two representative instantaneous PIV flow realizations showing the effects of aperiodicity on the near-wall flow as contours of total velocity ($\psi_b = 90°$), (a) Flow realization 1, (b) Flow realization 2.

were chosen because they illustrate the generally aperiodic nature of the flow near the ground. In both flow realizations, a vortex was convecting directly over the downstream position at $x/R = 1.4$ (labeled in Fig. 3.22a and Fig. 3.22b as Vortex A and Vortex B, respectively). Notice that Vortex A and Vortex B were at the same wake age of $\zeta = 540^\circ$. However, Vortex B had convected closer to the ground and so the near-wall velocities below this vortex were relatively higher than those shown in Fig. 3.22a.

Figure 3.23 shows the velocity profiles for a vertical cut taken through both Vortex A and Vortex B. Notice that the proximity of the vortex significantly changed the boundary layer profile along the ground. However, the relatively higher velocities induced by Vortex B caused a steeper velocity gradient in the near-wall flow, which will result in a higher shear stress at the wall (and particle bed).

The effects the vortices had on the transient wall shear over a larger region near the ground is shown in Fig. 3.24, which gives the instantaneous variation in the wall shear along the ground as well as the corresponding contours of u velocity for an instantaneous flow realization at $\psi_b = 90^\circ$. Notice that the wall shear had a number of transient excursions from the corresponding time-averaged values; see Fig. 3.20, with each excursion occurring below a tip vortex.

Another phenomenon that was observed in the near-wall region was the pairing and merging of adjacent vortex filaments. While this behavior has been observed before [7, 16, 26], the present measurements have given new insight into the merging process and the resulting three-dimensionality of the flow.

Figure 3.25 shows the merging of two near-wall tip vortices (marked Vortex 1 and Vortex 2) as a sequence of contiguous flow realizations separated in time by 60° of blade

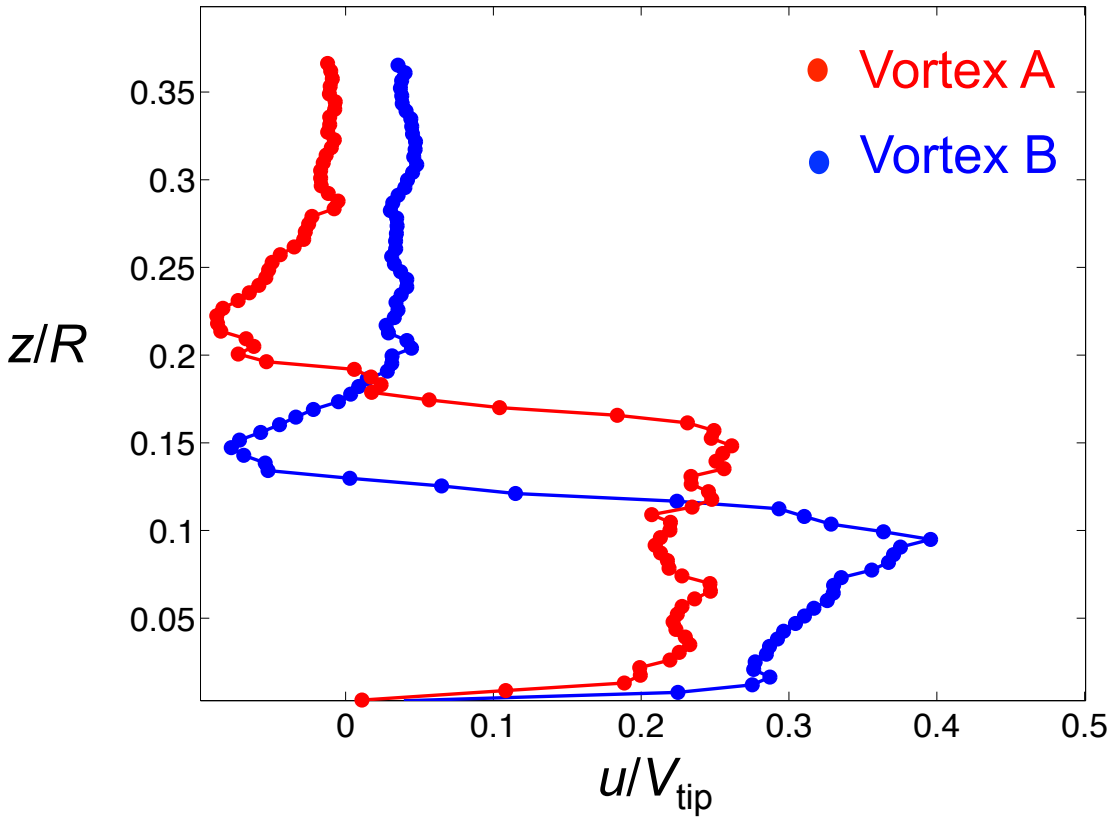

Figure 3.23: Velocity profiles taken at $x/R = 1.4$ for the two instantaneous flow realizations shown in Fig. 3.22.

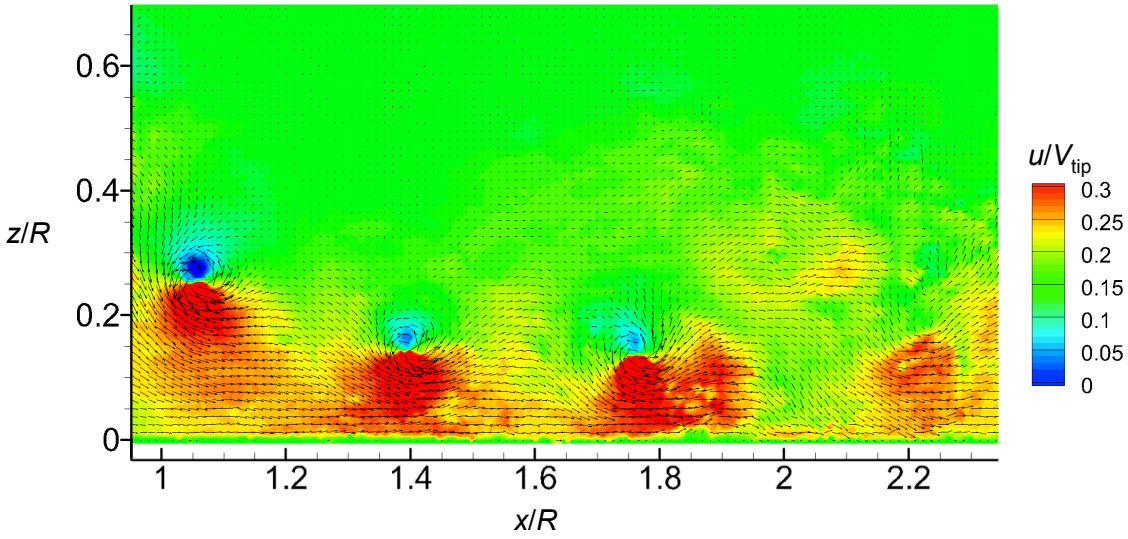

(a) Instantaneous u velocity contours

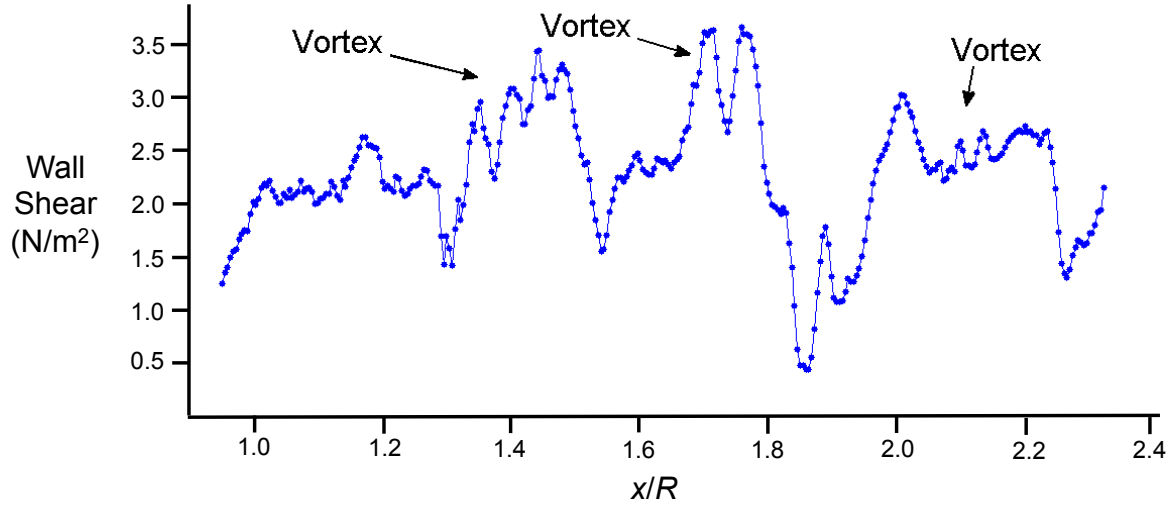

(b) Instantaneous shear stress

Figure 3.24: Instantaneous u velocity contours with the corresponding shear stress variation along the ground.

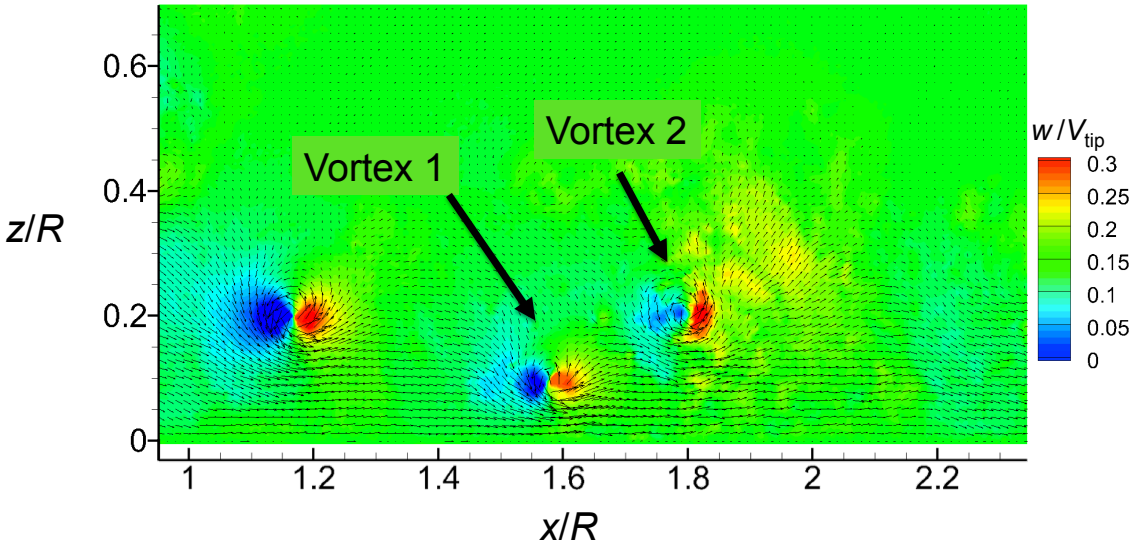

(a) ψ_b =150°

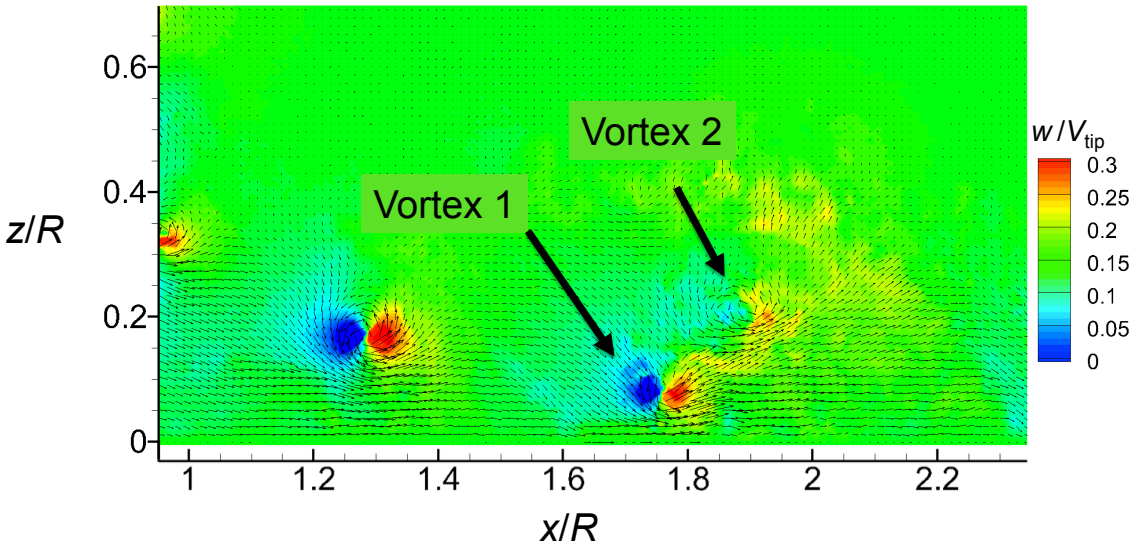

(b) ψ_b =210°

Figure 3.25: Contiguous flow realizations of v velocity contours showing the merging of adjacent vortices.

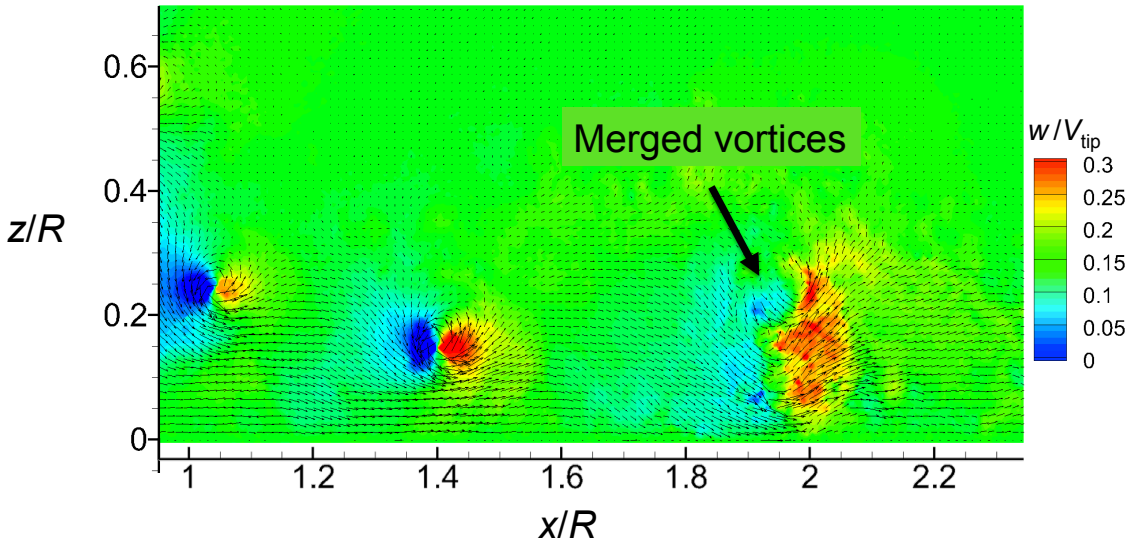

(c) ψ_b =270°

Figure 3.25: (Concluded) Contiguous flow realizations of v velocity contours showing the merging of adjacent vortices.

rotation as background contours of the w component of velocity. Because these results are for the 2-bladed rotor, these vortices are actually cross-sections of two interdigitated helicoidal vortex filaments. In Fig. 3.25a, Vortex 2 (the older vortex) had begun to roll over Vortex 1, a process otherwise known as pairing. The pairing process caused the younger vortex, Vortex 1, to convect closer to the ground, resulting in a transient increase in the flow velocities just above the surface. In Fig. 3.25b, the vortices had begun to merge together, with the upwash region of each vortex reinforcing the other. The merging process created a vortical flow with the combined circulation of both original vortices, resulting in a larger upwash/downwash region near the ground, as marked in Fig. 3.25c.

While the merging of the two vortices created a relatively coherent upwash/downwash region, the resultant vorticity field was more complex, as shown in Fig. 3.26, which gives

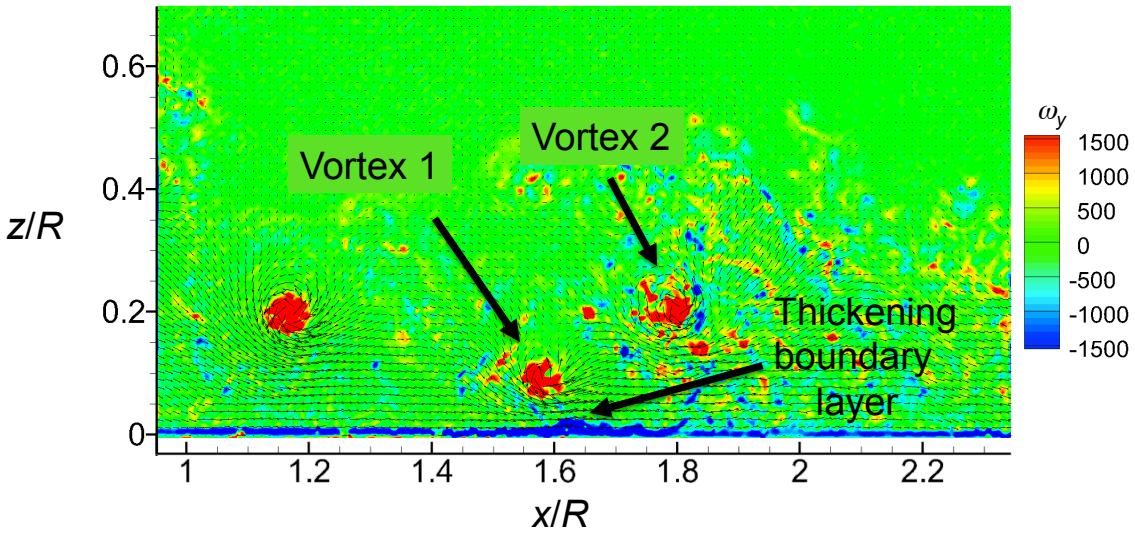

(a) $\psi_b = 120^\circ$

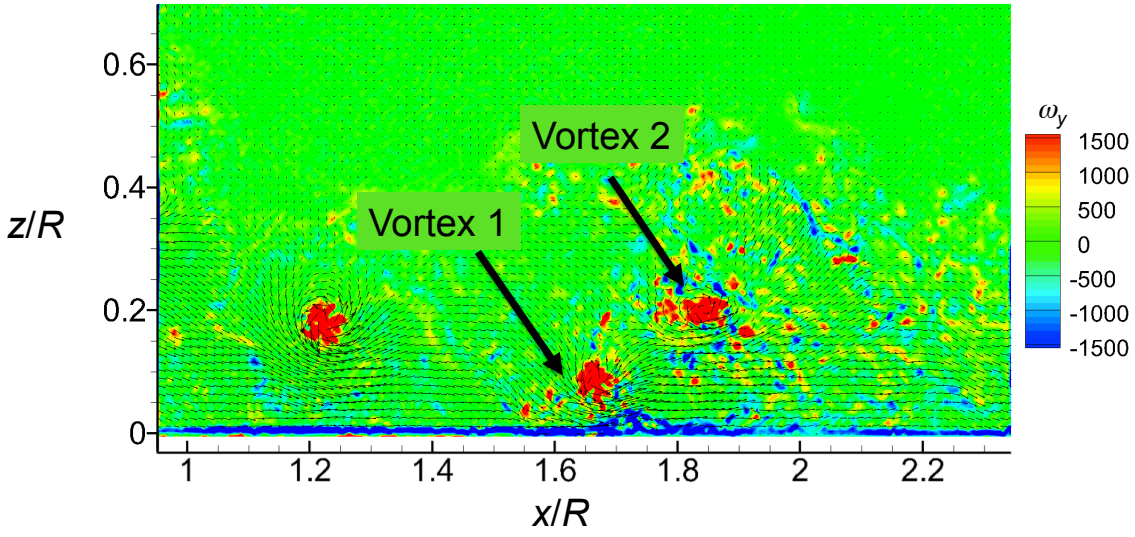

(b) $\psi_b = 150^\circ$

Figure 3.26: Contiguous flow realizations with contours of vorticity showing the merging of adjacent vortices.

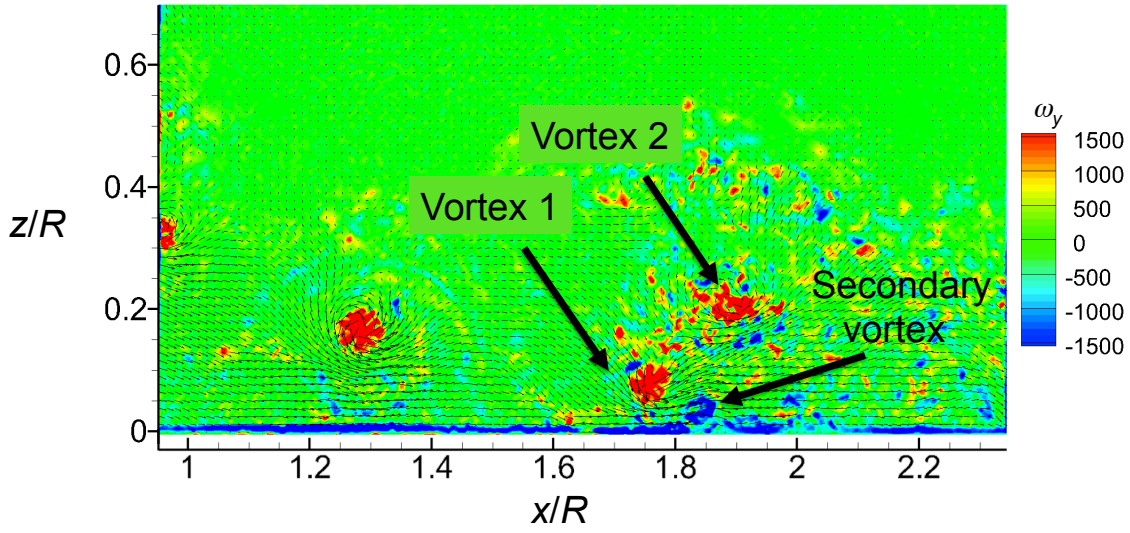

(c) ψ_b =180°

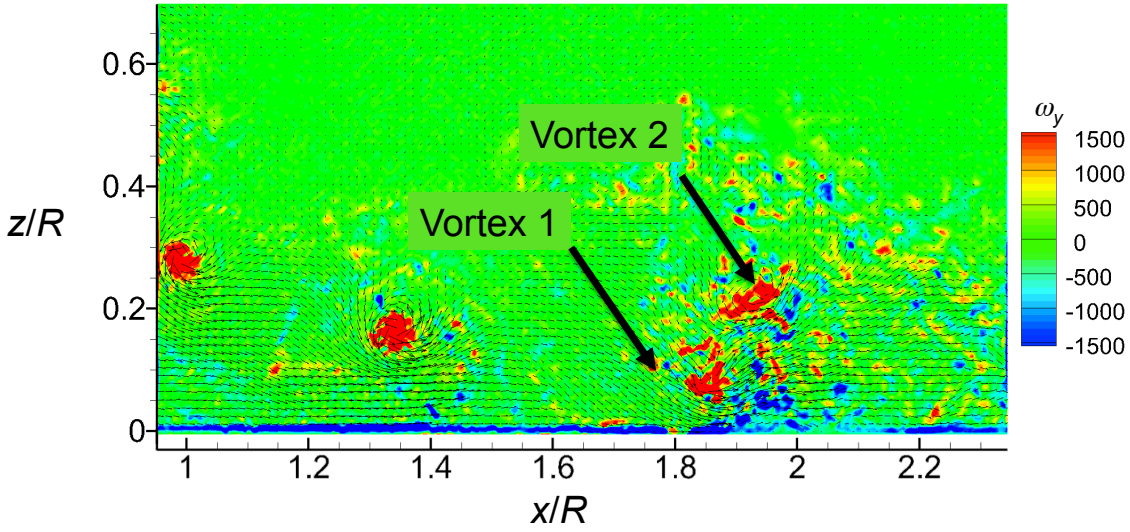

(d) ψ_b =210°

Figure 3.26: (Cont'd) Contiguous flow realizations with contours of vorticity showing the merging of adjacent vortices.

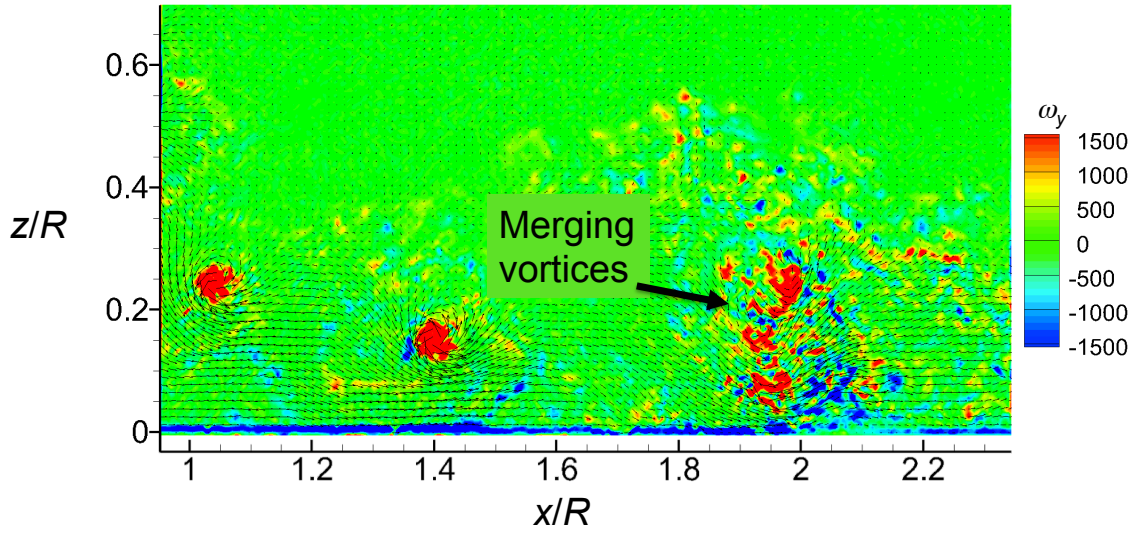

(e) ψ_b =240°

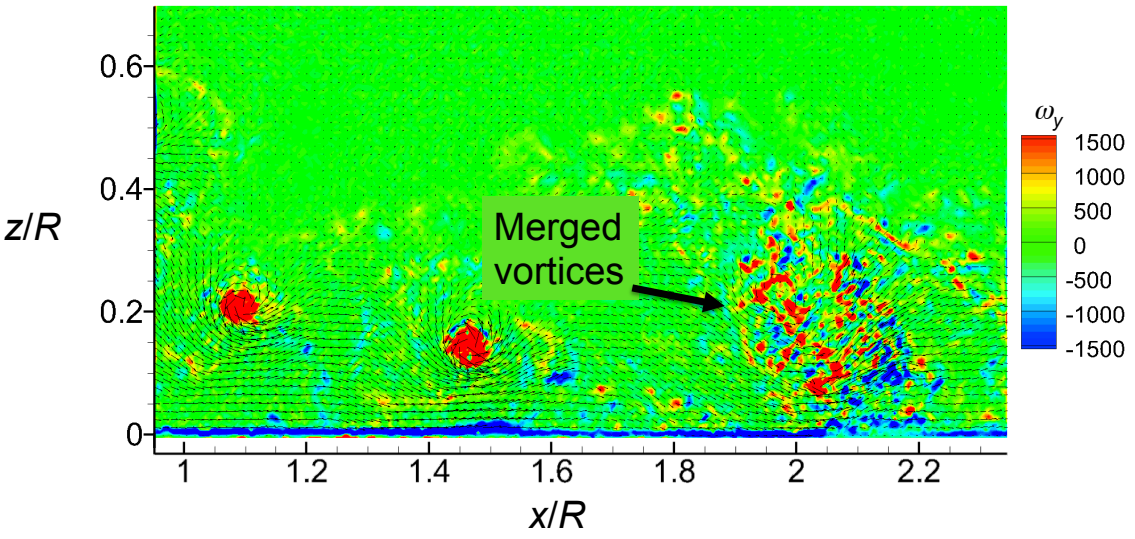

(f) ψ_b =270°

Figure 3.26: (Concluded) Contiguous flow realizations with contours of vorticity showing the merging of adjacent vortices.

the same temporal sequence of flow realizations as in Fig. 3.25 but with the background being contours of vorticity. It can be seen that there was a region of counter vorticity (indicated by blue contour coloring) produced near the ground, which is the signature of the boundary layer that had formed there. The vortices were observed to interact with the boundary layer region, usually causing it to thicken and sometimes momentarily separate from the wall, which introduced secondary vorticity into the surrounding flow, as identified in Fig. 3.26c.

Figure 3.27 shows this secondary vorticity in more detail as contours of vorticity and w velocity. Of particular interest is that the secondary vorticity was of opposite sign to the tip vortices. This secondary vorticity produced small upwash and downwash regions that can clearly be seen in Fig. 3.27b. Because the secondary vorticity had the opposite sign to the tip vortices, there was a local increase in flow velocities between the tip vortex and the secondary vorticity (marked in Fig. 3.27). This increase in the local flow velocities has also been observed for vortex rings impinging on a ground plane [64].

Continuing through the flow realizations in Fig. 3.26, increased flow separation and secondary vorticity creation were observed below the two vortices as they began to merge; see Fig. 3.26d. Ultimately, the cores themselves became turbulent and, as shown in Fig. 3.26e, the vortices then quickly diffused and redistributed their vorticity radially outward. Consequently, the merging process also entrained the secondary vorticity that was produced at the ground. Previous studies [7, 26] have shown that the merging of vortices can be responsible for increased quantities of sediment uplift. Therefore, the merging of adjacent vortices in the rotor wake is likely to be a mechanism that is at least partly responsible for localized particle uplift events, which is discussed later.

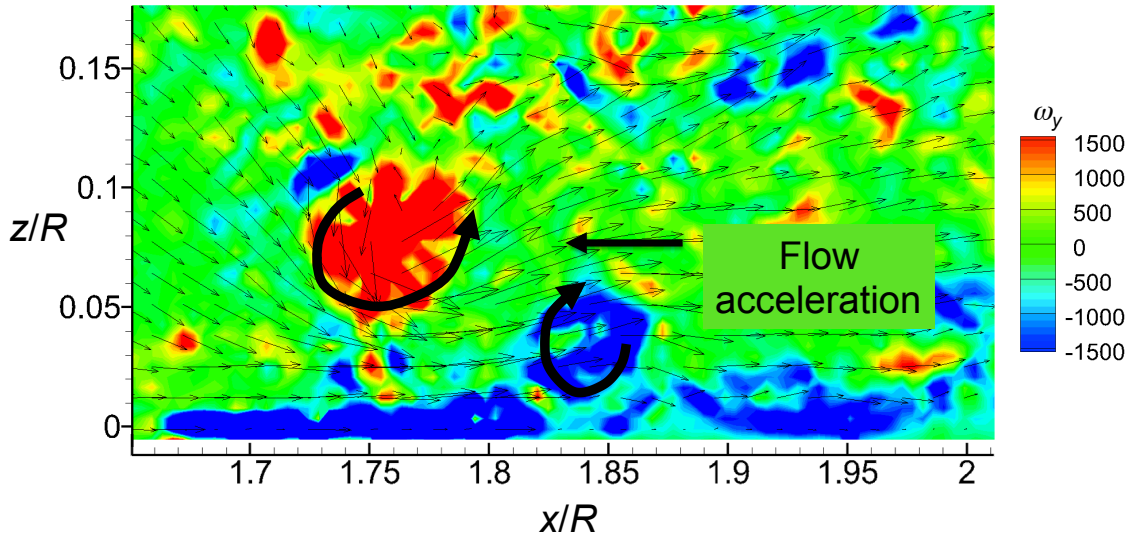

(a) vorticity

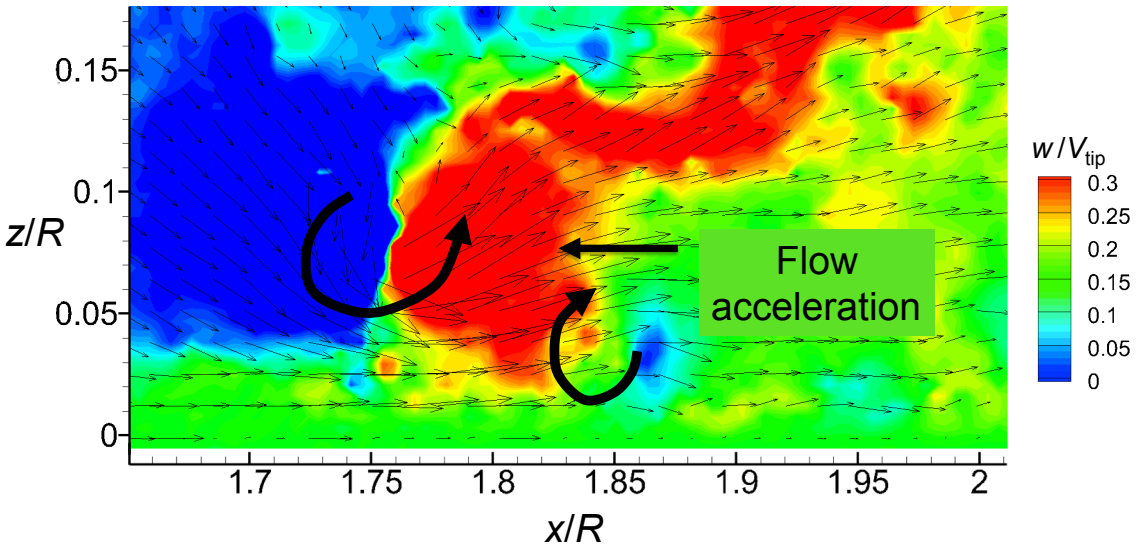

(b) v velocity

Figure 3.27: Detailed view of the secondary vortex produced by boundary layer separation as contours of vorticity and w velocity.

3.1.1.4 Three-Dimensional Rotor Wake Development

The measurements made in the vertical (x-z) plane provided much insight into the interactions of the rotor wake with the ground. However, to quantify the three-dimensionality of the wake, measurements were made in horizontal (x-y) planes, and in this case at ten different heights above the ground plane, as shown previously in Fig. 2.11. These horizontal ROIs were imaged by placing the camera on a support above the ground plane and by viewing downward onto a horizontally aligned laser sheet; a schematic of the viewing region is shown in Fig. 3.28.

Figure 3.29 shows a sequence of contiguous instantaneous flow realizations in a horizontal imaging plane at z/R =1.0 (i.e., coincident with the rotor tip-path-plane) as contours of total velocity. In the x-y imaging planes, the total velocity is defined as $V_{xy} = \sqrt{u^2+v^2}$, where u and v are the velocities in the x and y directions, respectively. In this imaging region, the tip vortices manifested as localized regions of increased velocity at the edge of the rotor wake.

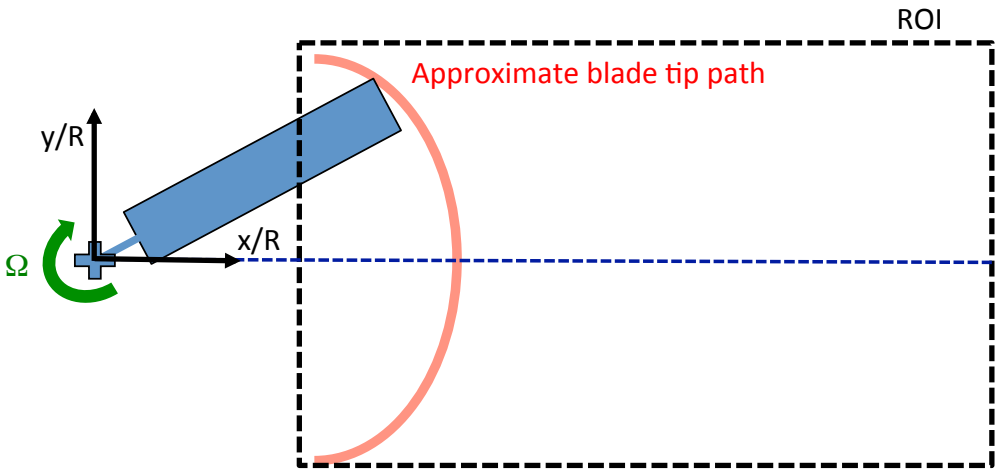

Figure 3.28: Schematic of the horizontal plane viewing region.

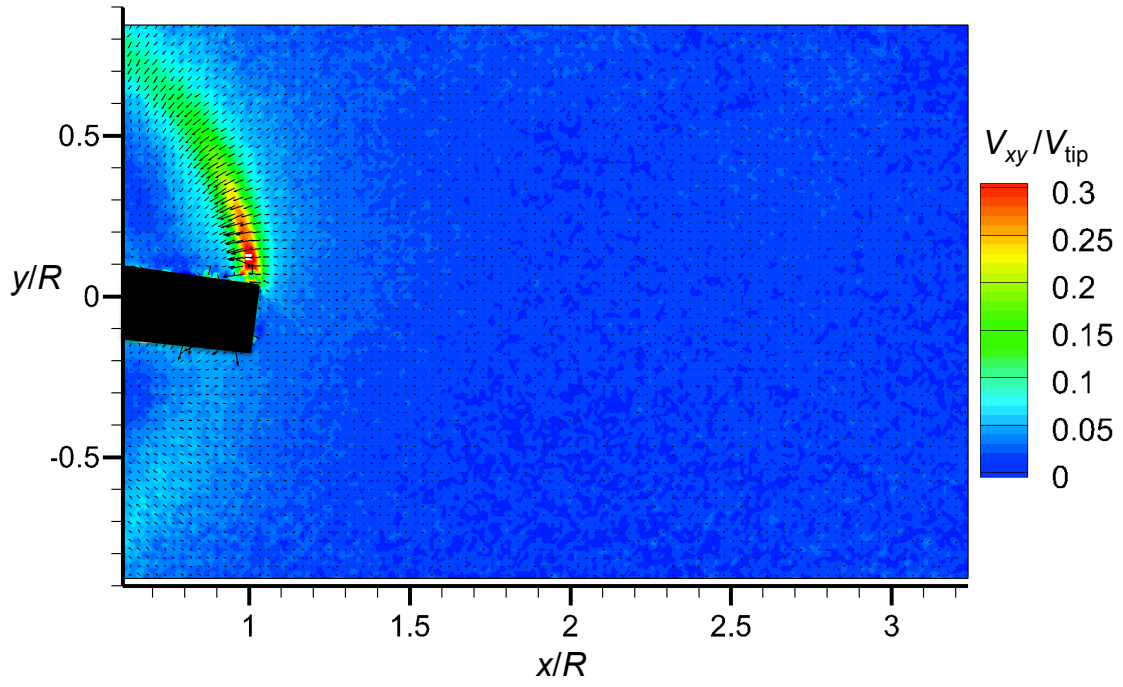

(a) $\psi_b = 10°$

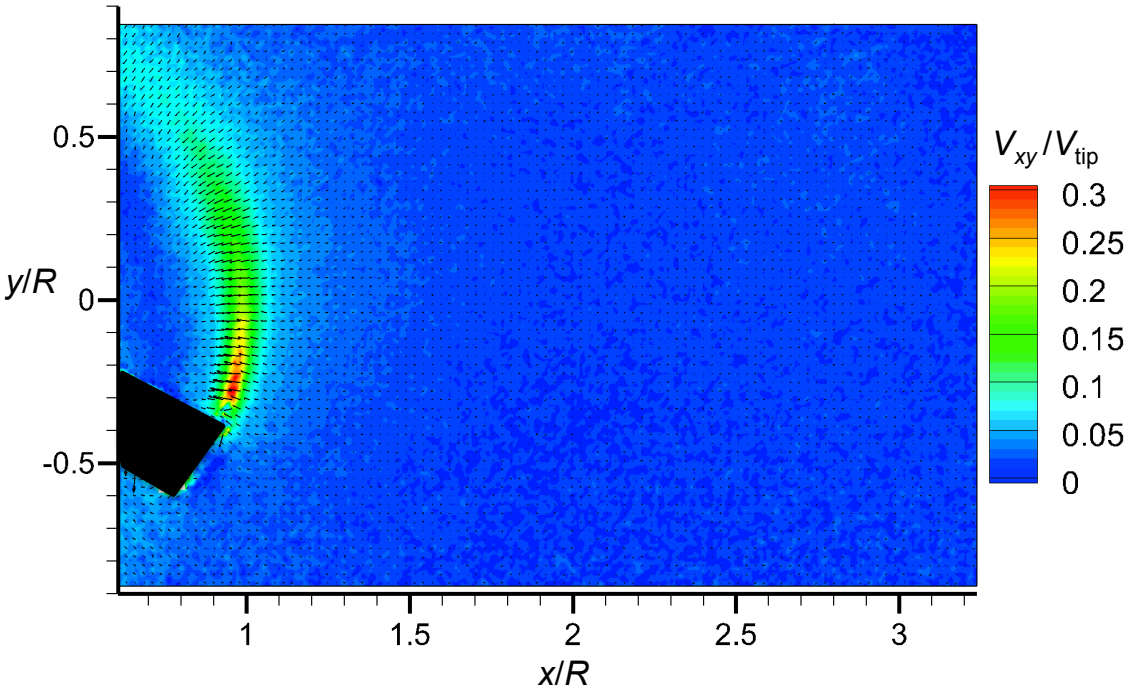

(b) $\psi_b = 40°$

Figure 3.29: Two contiguous flow realizations showing the out of plane convection of the tip vortex filament in a plane at $z/R = 1.0$ as contours of total velocity, (a) $\psi_b = 10°$, (b) $\psi_b = 40°$.

Notice that in the first flow realization (Fig. 3.29a) the tip vortex appeared as a continuous filament. The highest velocities in the filament were observed to form directly behind the blade where the tip vortex had first rolled-up. The results in the vertical plane (see previously in Fig. 3.5a) showed that the wake velocities at $z/R = 1.0$ were primarily directed toward the ground. Therefore, as shown in Fig. 3.29 (a horizontal plane at $z/R = 1.0$), as the filament had aged and convected toward the ground plane, it moved out of the imaging plane. The flow realization in Fig. 3.29b shows that as the blade rotated, only the part of the filament immediately near the blade remained in the measurement plane.

To better understand the overall three-dimensional development of the rotor wake, the flow measurements in each of the horizontal planes were ensemble time-averaged. Figure 3.30 shows contours of time-averaged total velocity in the horizontal plane at $z/R = 1.0$. These time-averaged results showed that there was a region of higher flow velocities all around the edge of the rotor wake, which is the signature of the tip vortices.

Figure 3.31 shows a detailed view of the velocity vectors within the wake boundary at $z/R = 0.8$, with the background contours being of total velocity, V_{xy}. The results show that a significant component of the velocity within the rotor wake followed the direction of blade rotation, i.e., the rotor induced a swirl velocity into the rotor wake. For the present operating conditions, the peak swirl velocity was found to be approximately 7% of the blade tip speed and was directed in the same direction as the rotor rotation.

The contraction of the wake can also be seen in the time-averaged flow measurements in the planes at $z/R = 0.9$, 0.8, and 0.7, as shown in Fig. 3.32. Comparing the results at $z/R = 0.7$ (Fig. 3.32c) to the results at $z/R = 0.9$ (Fig. 3.32c), the velocities at the edge of the rotor wake were decreased, indicating that the in-plane velocities in the

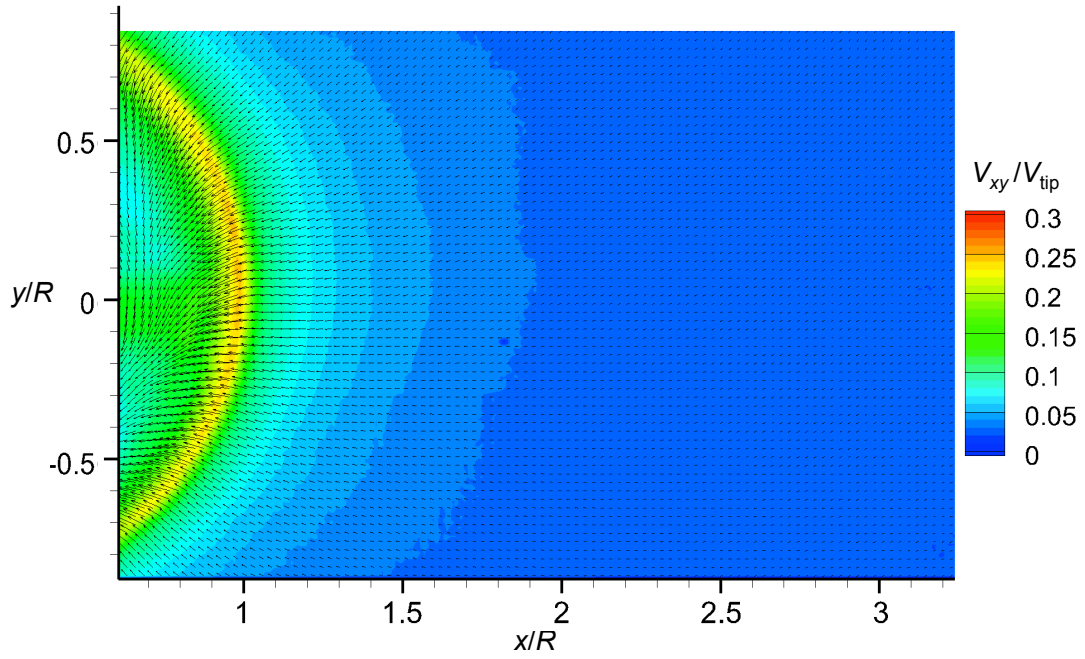

Figure 3.30: Time-averaged total velocity in a horizontal plane at z/R=1.0.

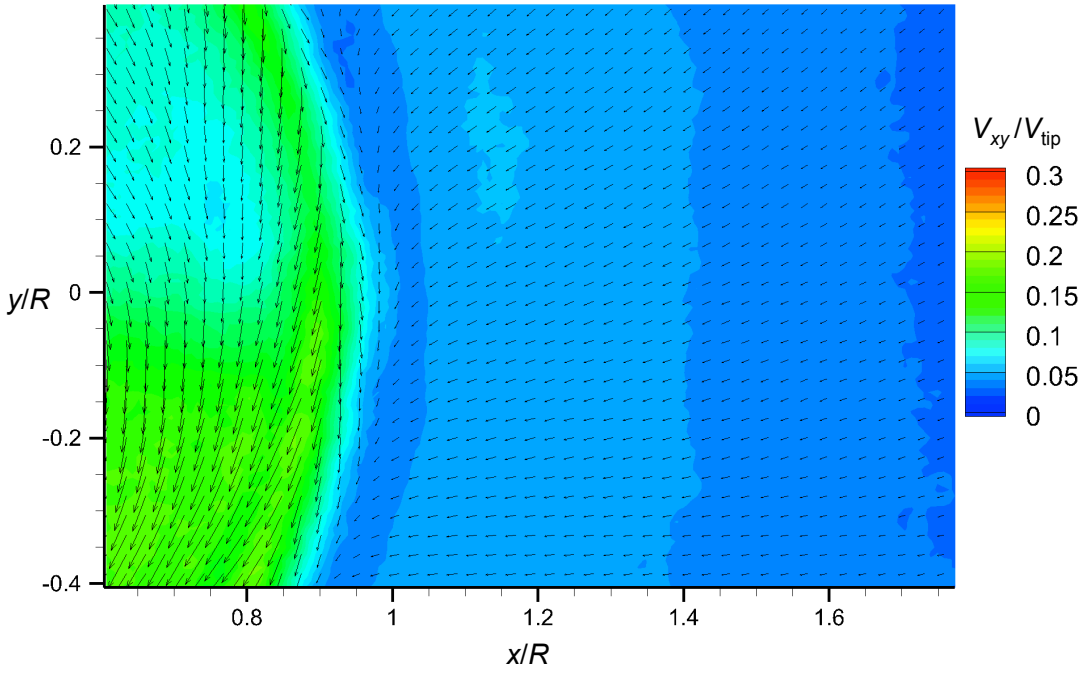

Figure 3.31: Time-averaged total velocity in a horizontal plane at $z/R = 0.8$ showing the swirling flow within the rotor wake.

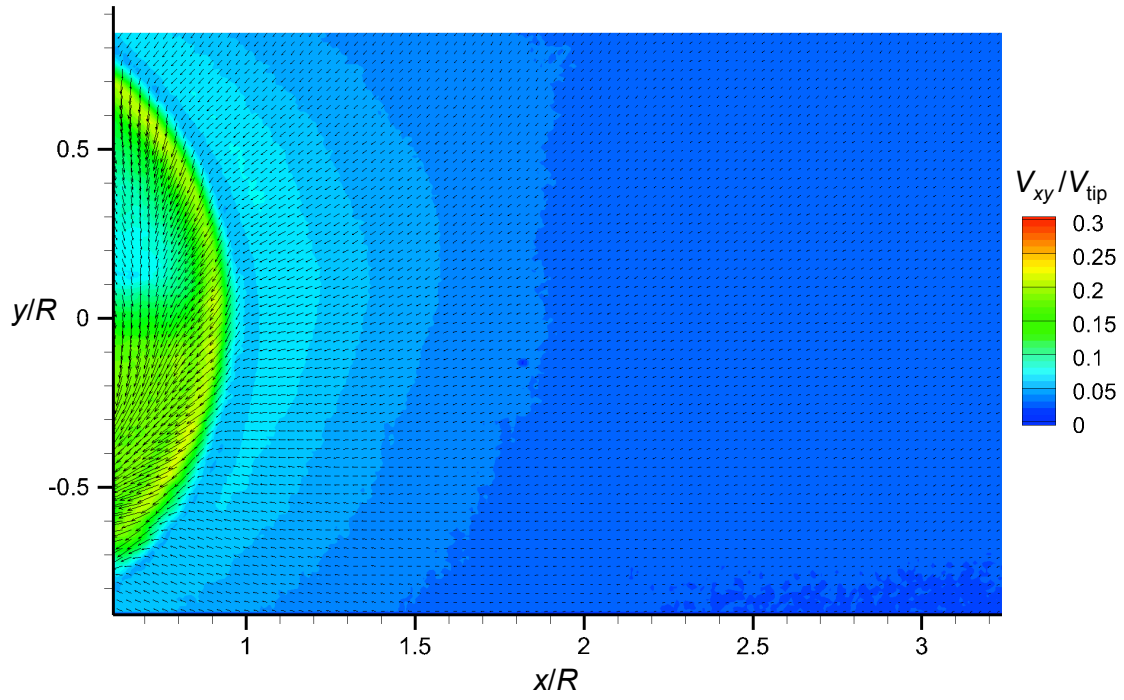

(a) $z/R = 0.9$

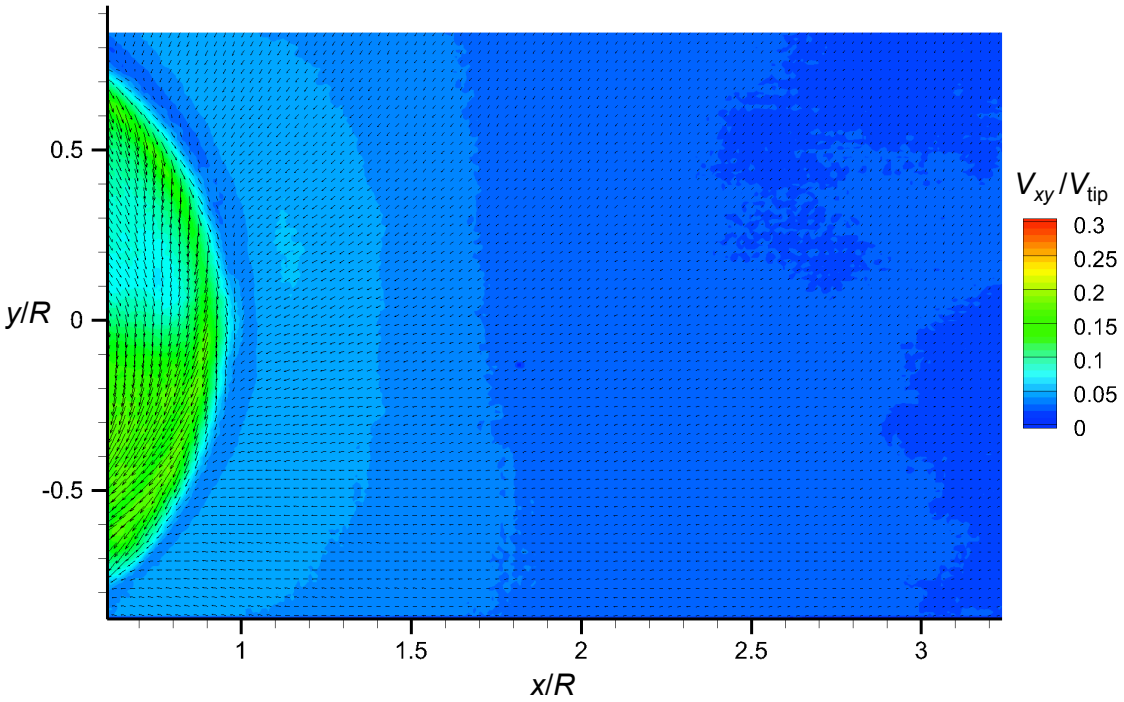

(b) $z/R = 0.8$

Figure 3.32: Contours of time-averaged total velocity in horizontal planes showing the contraction of the rotor wake.

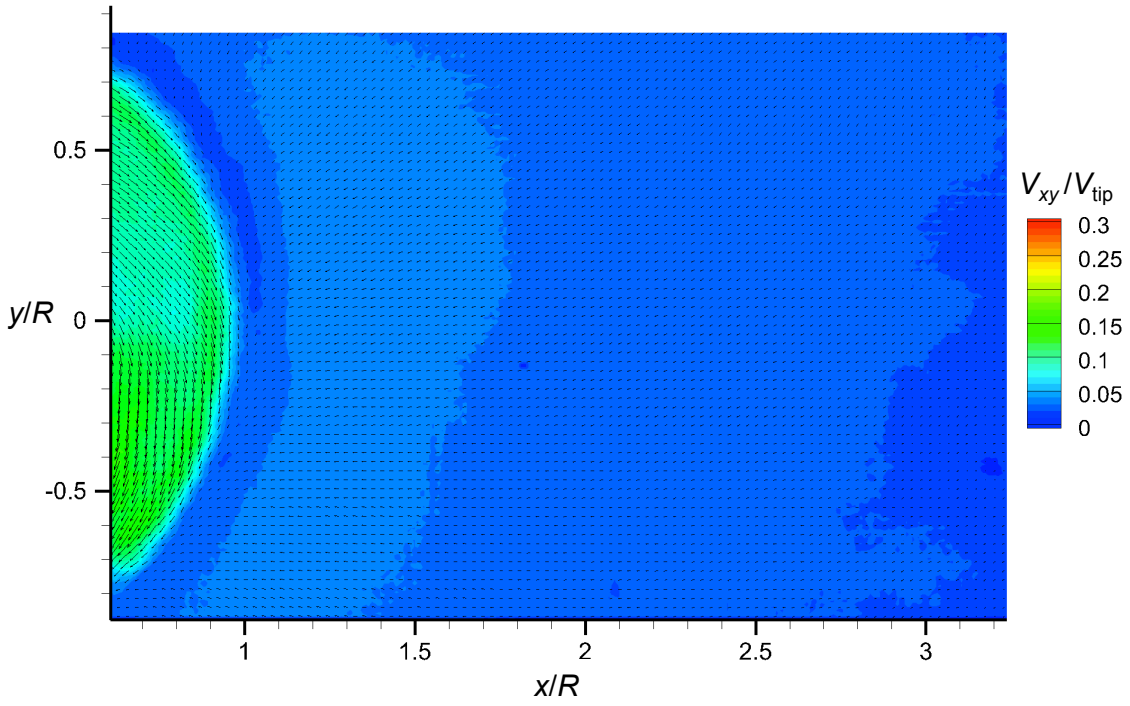

(c) $z/R = 0.7$

Figure 3.32: (Concluded) Contours of time-averaged total velocity in horizontal planes showing the contraction of the rotor wake.

tip vortices have decreased as the wake contracted. However, the results in Fig. 3.33 at $z/R = 0.6$, 0.5, and 0.4 showed that the flow velocities at the edge of the wake had began to increase again as the wake expanded, which is because of vorticity reintensification effects, as discussed previously and also documented [17, 54].

The time-averaged flows at $z/R = 0.4$ (Fig. 3.33c) indicated that there was also an increase in the flow velocities further downstream and away from the rotor wake, as shown by the light blue regions on the right-side of the image. These higher velocity regions suggest that some flow interactions occurred closer to the ground, which caused an increase in flow velocity in this otherwise fairly quiescent flow region.

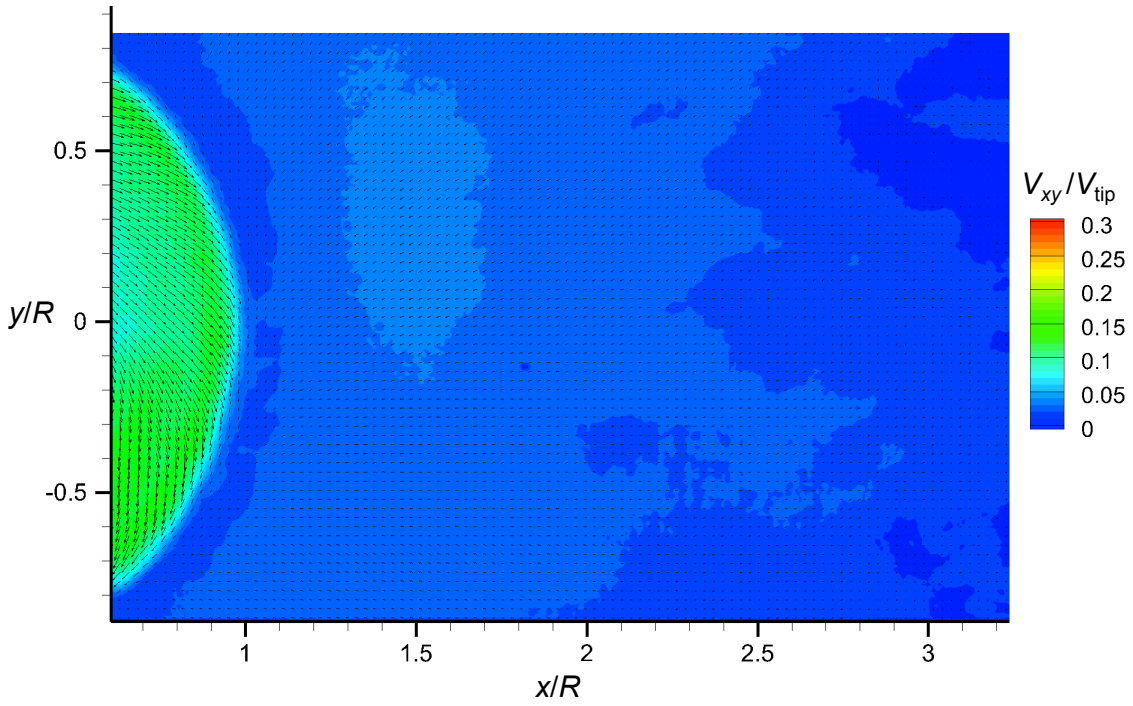

(a) $z/R = 0.6$

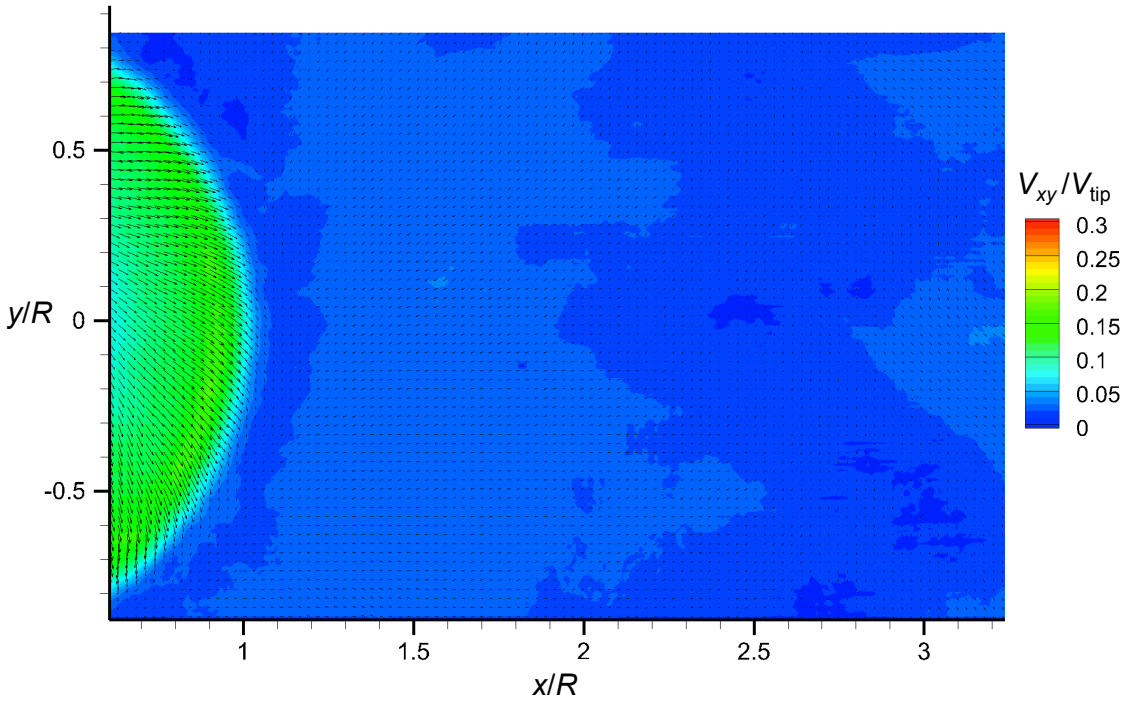

(b) $z/R = 0.5$

Figure 3.33: Contours of time-averaged total velocity in horizontal planes showing the transition from contraction to expansion of the rotor wake.

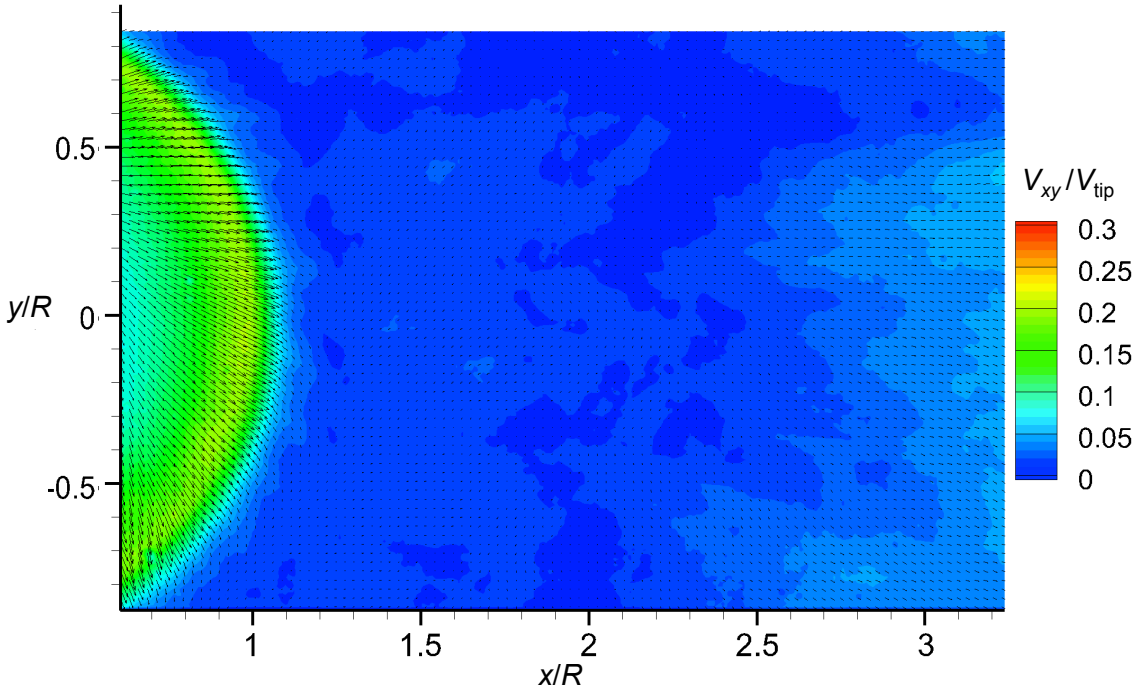

(c) $z/R = 0.4$

Figure 3.33: (Concluded) Contours of time-averaged total velocity in horizontal planes showing the transition from contraction to expansion of the rotor wake.

To investigate the origin of these higher velocities, two instantaneous flow realizations as contours of total velocity in the plane at $z/R = 0.4$ are shown in Fig. 3.34, these flow realizations being part of a contiguous time-history of measurements. A local region of higher flow velocities has been marked in the center of the image in Fig. 3.34a (ψ_b =240°). In the following flow realization, shown in Fig. 3.34b, the flow velocities in this region can be seen to have increased. Recall from the results shown in the vertical plane (Fig. 3.25) that the merging of adjacent turns of the vortices caused an increase in the flow velocities above the slipstream boundary of the rotor wake. In the horizontal plane at $z/R = 0.4$, the merging of the adjacent vortices manifested as regions of increased velocities further downstream in the flow away from the rotor.

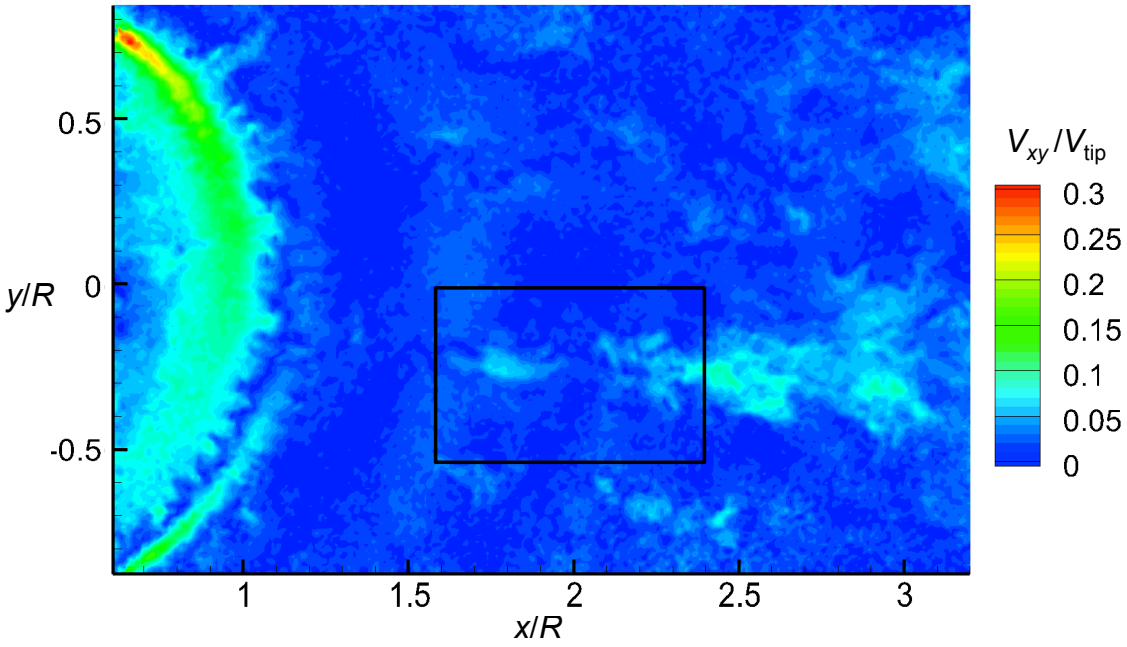

(a) $\psi_b = 150°$

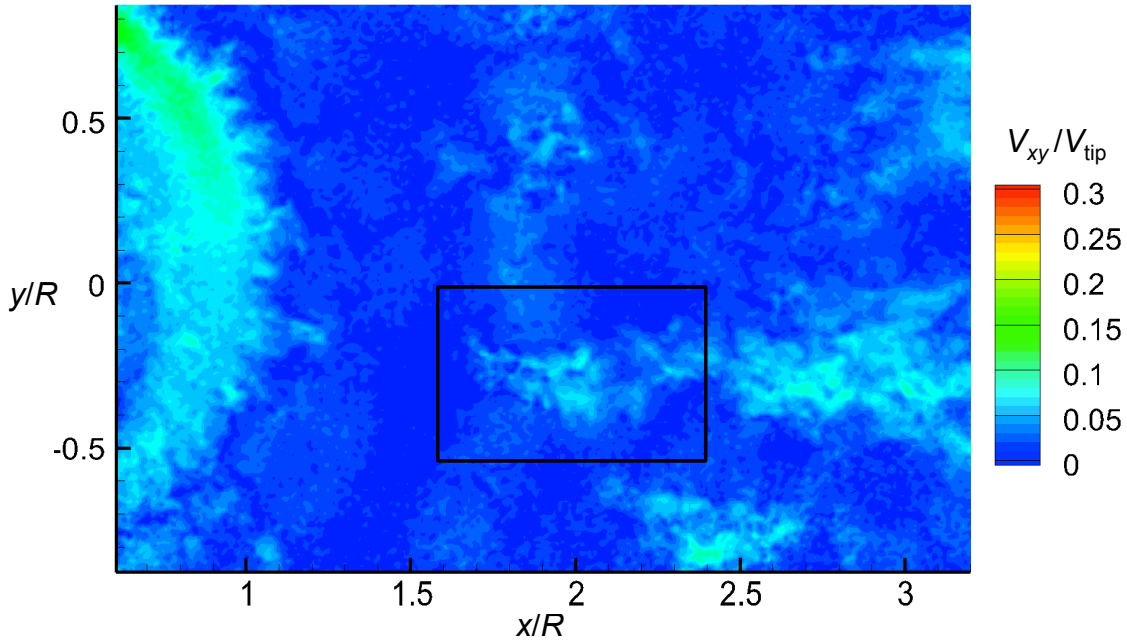

(b) $\psi_b = 240°$

Figure 3.34: Two contiguous flow realizations in a plane at at $z/R = 0.4$ as contours of total velocity showing the convection of the tip vortex filament out of the imaging plane with the box marking a local region of higher velocity, (a) $\psi_b = 150°$, (b) $\psi_b = 240°$.

Figure 3.35 shows a detailed view of one of these transient excursions in the flow velocities as contours of total velocity (Fig. 3.35a) and vorticity (Fig. 3.35b), these measurements being for the plane at $z/R = 0.4$. The results indicate that the merging of the two filaments from below this measurement plane resulted in the creation of small, but significant swirling flow velocities in the horizontal planes, i.e., they were perpendicular to the centerline of the vortex filaments. This latter flow can be better seen in the vorticity plot shown in Fig. 3.35b; the red region of vorticity shows that while this region of vorticity is weaker than the tip vortices, it may possibly cause small regions of swirling particle motion in the dual-phase flow environment.

Of particular interest to the problem of rotor-induced particle motion was the three-dimensional evolution of the rotor wake as it interacted with the ground plane. To this end, Fig. 3.36 shows the time-averaged total velocity of the wake in measurement planes at $z/R = 0.3$, 0.2, and 0.1. The time-averaged results at $z/R = 0.3$ and $z/R = 0.2$ (Fig 3.36a and Fig. 3.36b) show a further increase in the downstream flow velocities. In these lower measurement planes, these regions of increased flow velocities extend radially outward, as marked in Fig 3.36b.

To further investigate the evolution of the rotor wake behavior near the ground, a time-history of instantaneous measurements taken in a plane at $z/R = 0.1$ are shown in Fig. 3.37, with the measurements being shown as contours of total velocity. The tip vortices manifested as localized regions of increased velocities, indicated by the red regions marked as Filament 1 and Filament 2 in Fig. 3.37. On examination of the first flow realization in the sequence (Fig. 3.37a), a significant three-dimensionality of the flow was clearly evident. From $x/R = 0.6$–0.8, a lower flow velocity (stagnation) region under

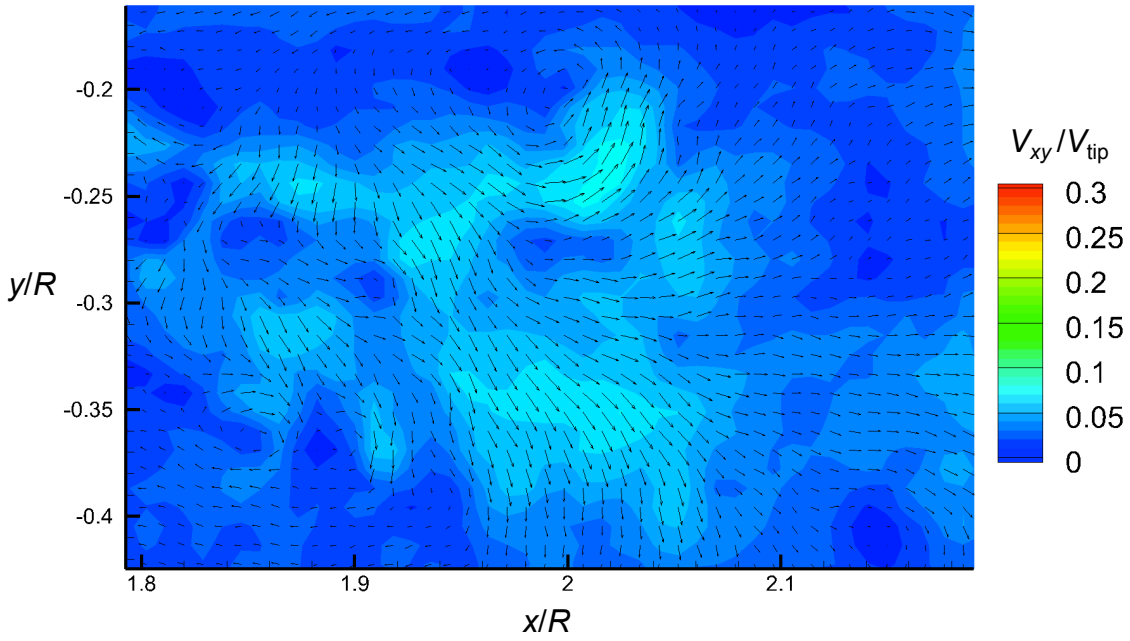

(a) Total Velocity

(b) Total Velocity

Figure 3.35: Detailed view of the swirling flow at z/R =0.4 as contours of a.) total velocity and b.) vorticity.

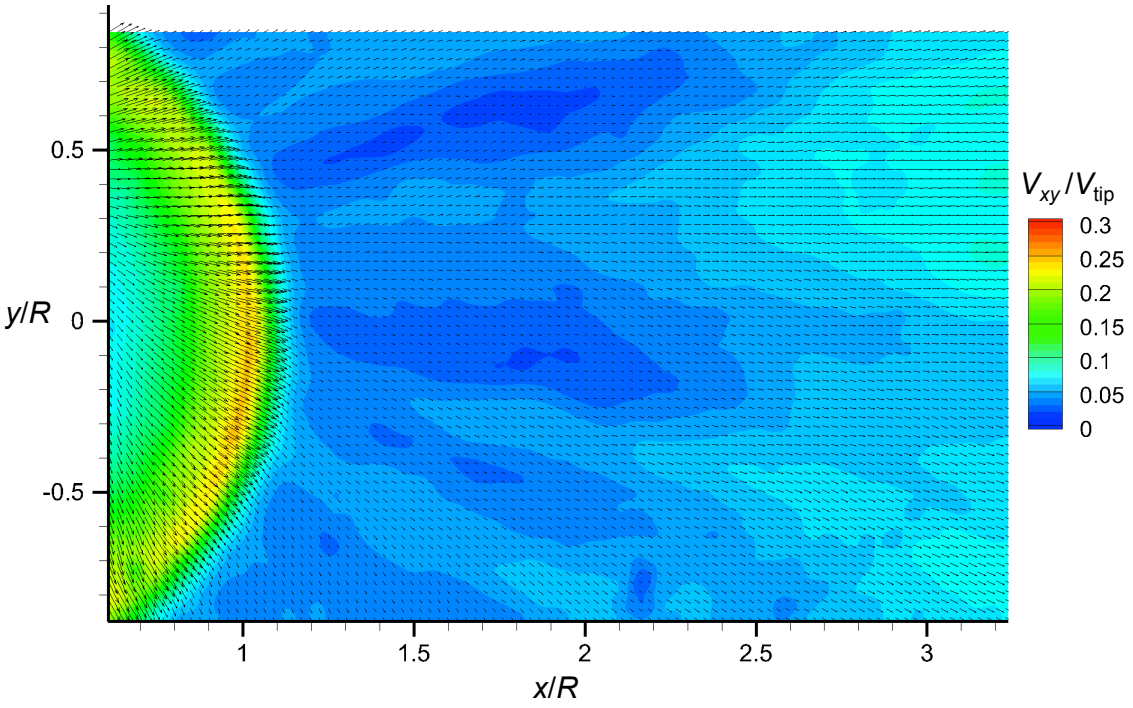

(a) z/R =030

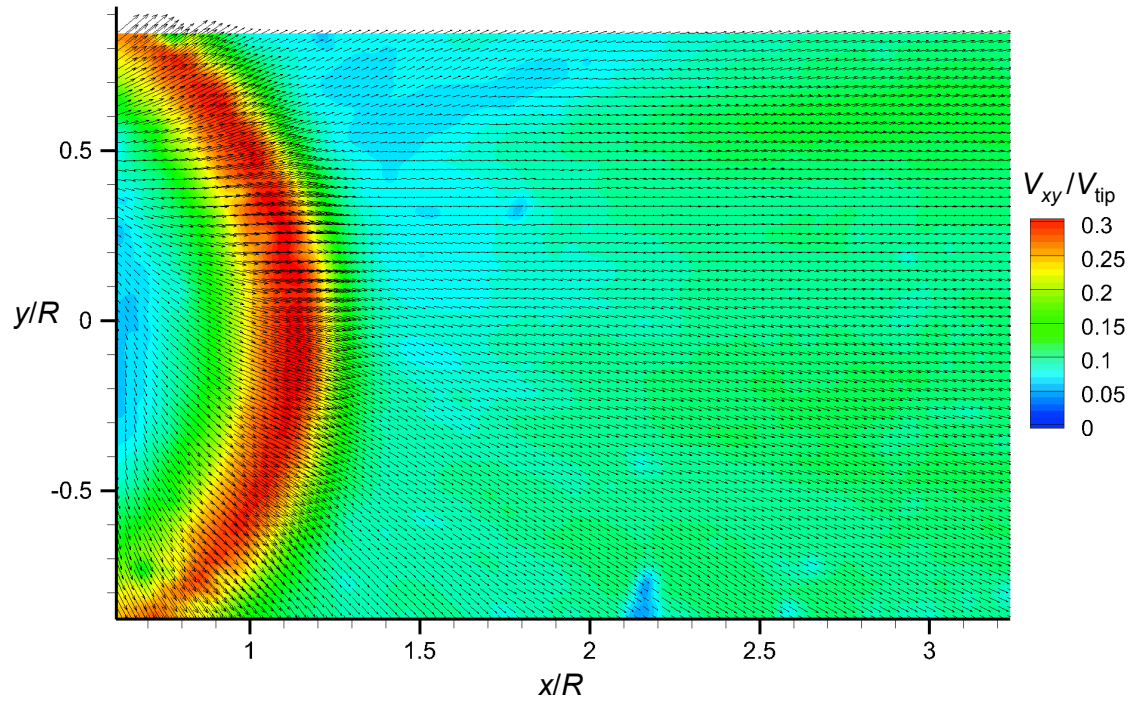

(b) z/R =020

Figure 3.36: Contours of time-averaged total velocity in horizontal planes showing the expansion of the rotor wake along the ground.

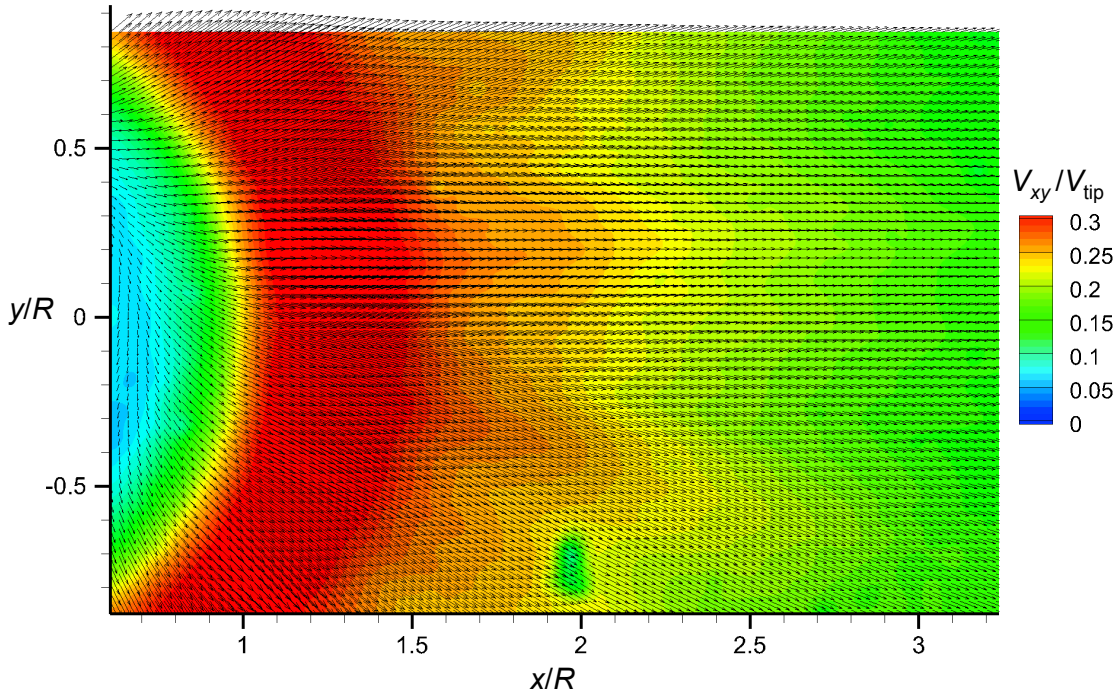

(c) z/R =010

Figure 3.36: (Concluded) Contours of time-averaged total velocity in horizontal planes showing the expansion of the rotor wake along the ground.

the rotor was observed. By $x/R = 0.9$, however, the rotor wake had turned from being convected mostly downward to being mostly radially outward, a result also seen in the vertical plane (Fig. 3.4). Beyond $x/R = 1.5$ the flow was clearly radially non-uniform as it developed further downstream.

Also of interest in the formation of the three-dimensionality of the flow near the ground, was the impingement process of the tip vortices on the ground plane. Because of the helicoidal shape of the vortices, only a part of Filament 1 had entered the measurement plane in Fig. 3.37a ($\psi_b = 300°$). In the subsequent flow realization, Fig. 3.37b ($\psi_b = 330°$), a larger part of Filament 1 had impinged on the ground and the filament had begun

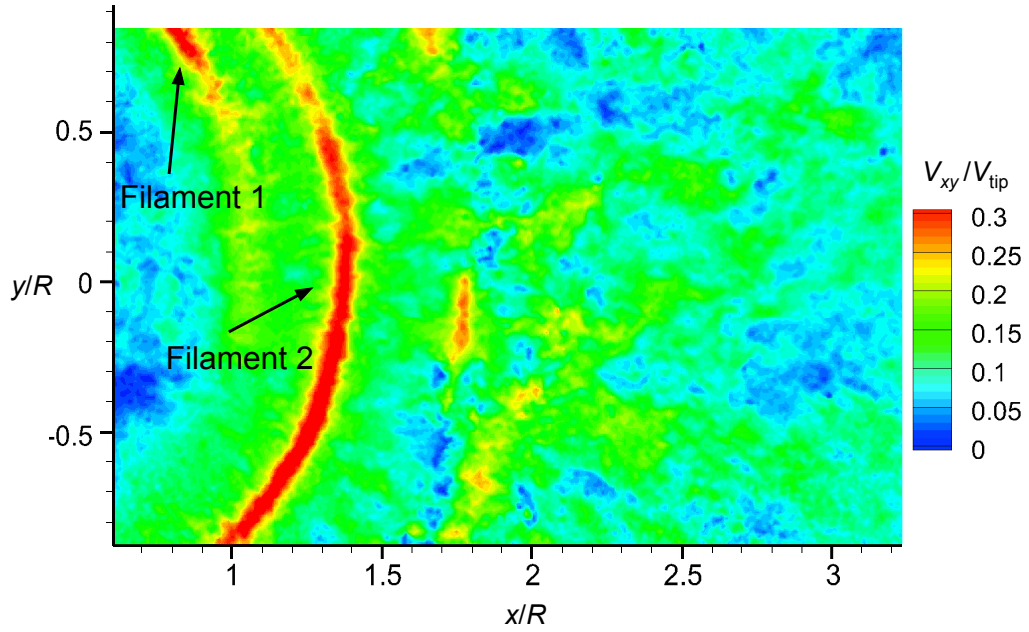

(a) PIV time step 1, $\psi_b \approx 270°$

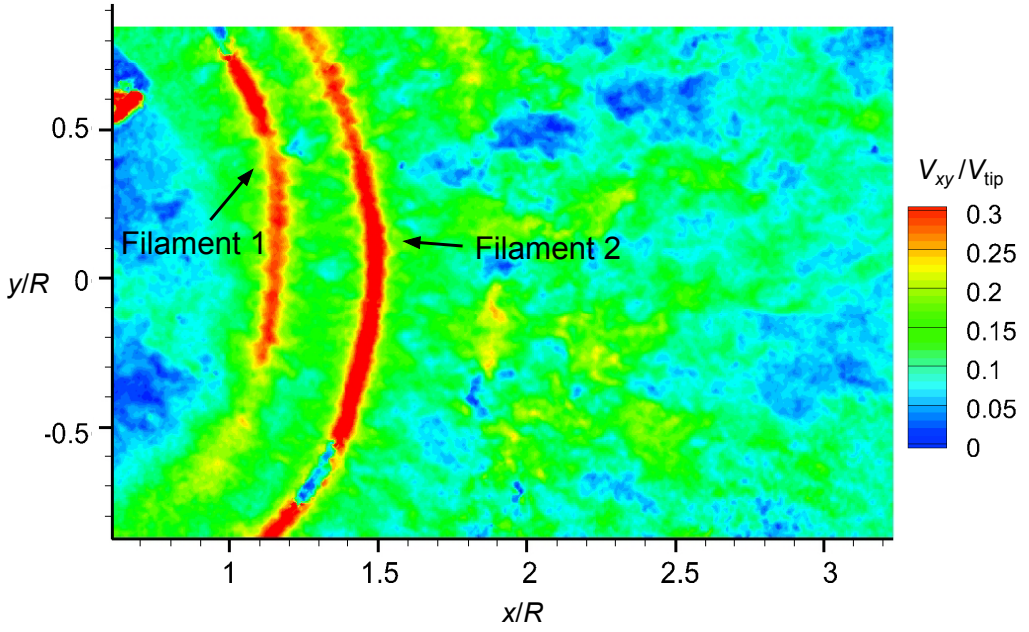

(b) PIV time step 2, $\psi_b \approx 330°$

Figure 3.37: Sequence of instantaneous total velocity field contours for the isolated rotor in a plane at $z/R = 0.1$ showing the impingement and subsequent merging of adjacent turns of the tip vortices near the ground, (a) $\psi_b \approx 270°$, (b) $\psi_b \approx 330°$

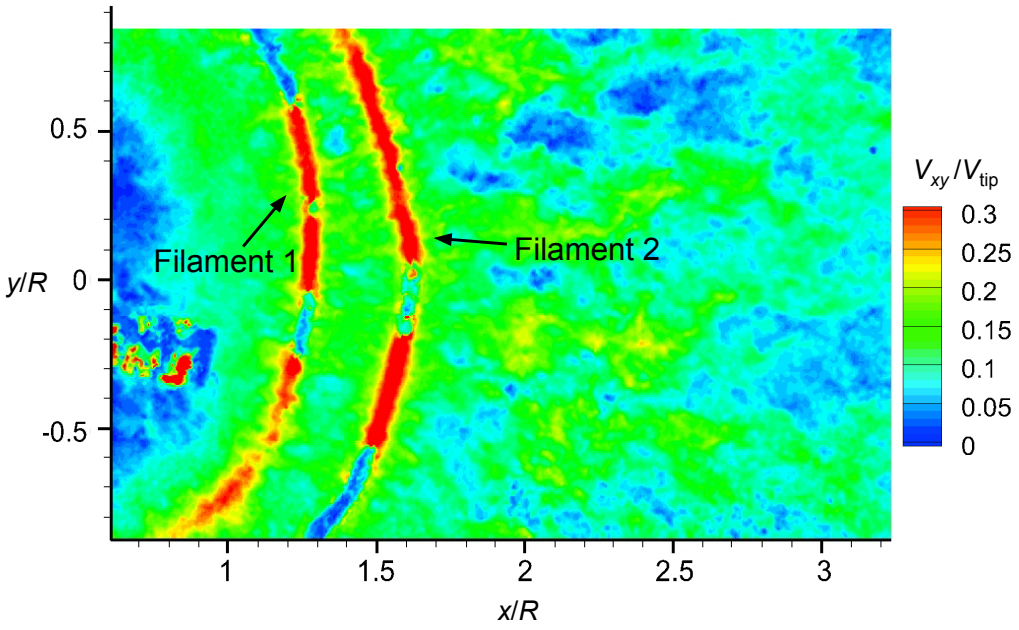

(c) PIV time step 3, $\psi_b \approx 30°$

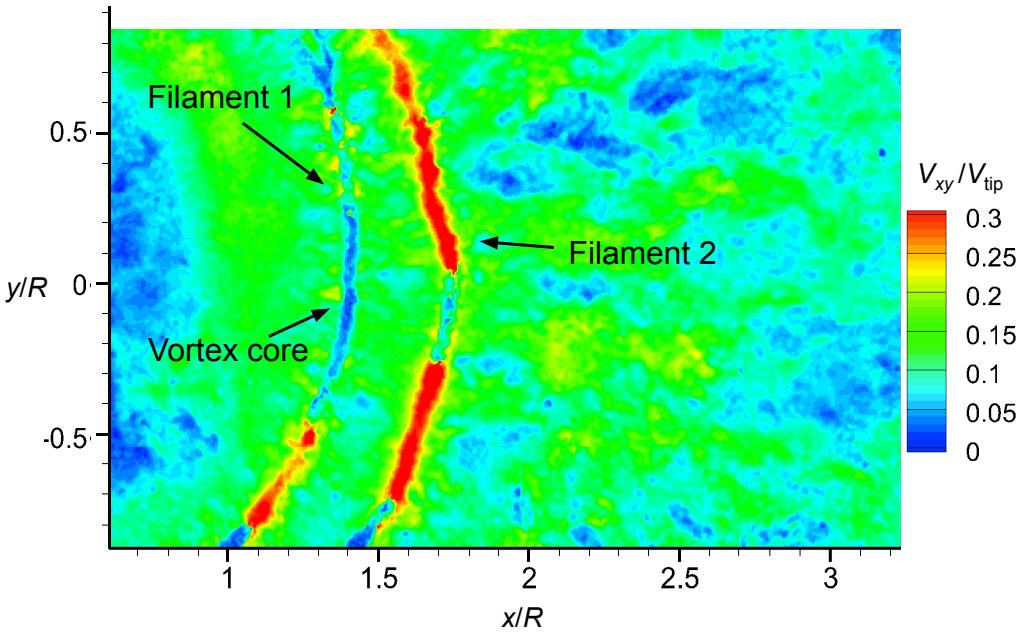

(d) PIV time step 4, $\psi_b \approx 90°$

Figure 3.37: (Cont'd) Sequence of instantaneous total velocity field contours for the isolated rotor in a plane at $z/R = 0.1$ showing the impingement and subsequent merging of adjacent turns of the tip vortices near the ground, (c)$\psi_b \approx 30°$, (d)$\psi_b \approx 900°$.

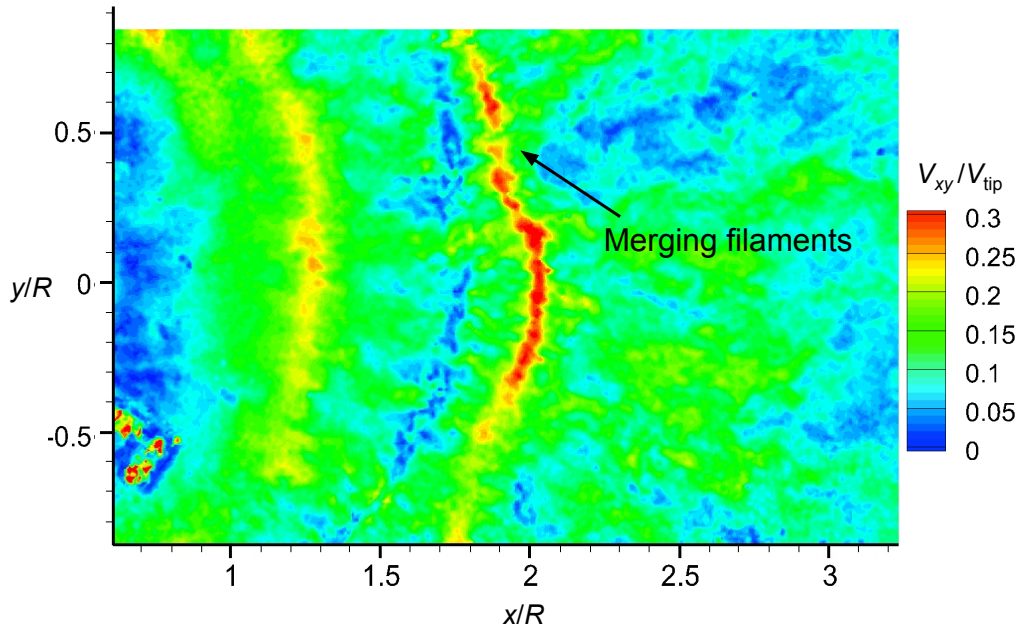

(e) PIV time step 5, $\psi_b \approx 120°$

Figure 3.37: (Concluded) Sequence of instantaneous total velocity field contours for the isolated rotor in a plane at $z/R = 0.1$ showing the impingement and subsequent merging of adjacent turns of the tip vortices near the ground, (e)$\psi_b \approx 120°$.

to convect radially outward. By $\psi_b = 30°$ (Fig. 3.37c) the entire length of Filament 1 had impinged on the ground and was convecting radially outward. Therefore, it is apparent that the filaments convected outward at different rates, as shown by the non-uniform spacing along the lengths of both Filaments 1 and 2. Figure 3.37c shows that there was a closer spacing between the vortex filaments at the top of the image when compared to their spacing at the bottom. These differences in filament spacing are one reason why local parts of each filament paired and/or merged with each other, as can be seen in the subsequent flow realizations in Fig. 3.37d ($\psi_b = 60°$) and Fig. 3.37e ($\psi_b = 240°$).

Another interesting phenomenon that was observed in the present experiments was

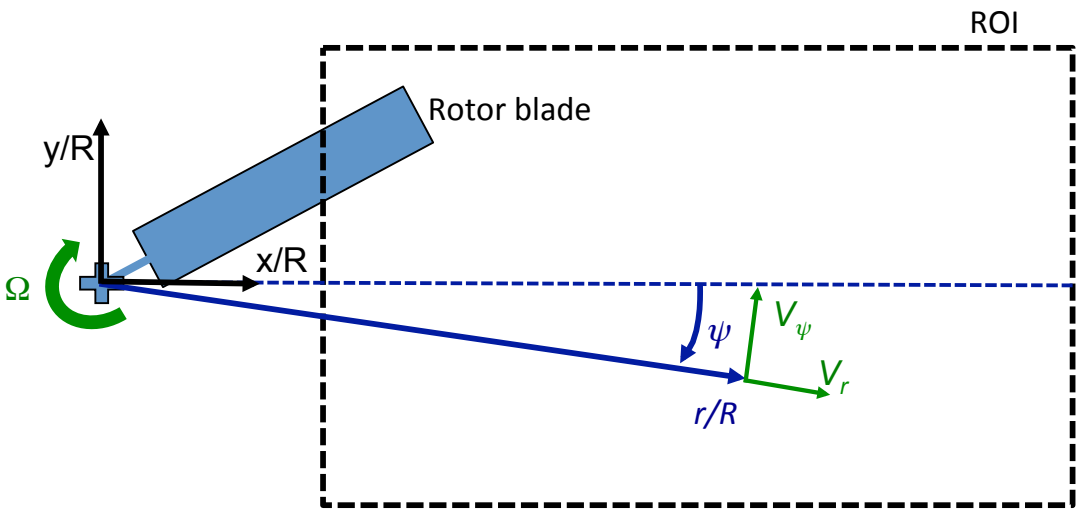

Figure 3.38: Schematic showing the Cartesian and polar coordinate systems used.

the tendency for the tip vortices in the rotor wake to develop wave-like displacements along their lengths. To examine this behavior in more detail, the measurements were transformed from a Cartesian reference frame (x,y,z) into a polar (or cylindrical) reference frame (r,θ,z), with the origin being located at the rotor shaft axis; see Fig. 3.38. In this case, θ was defined as the angle from the horizontal centerline of the ROI and positive in the clockwise direction. The non-dimensional radial distance, r/R, was defined as the non-dimensional distance from the rotor shaft axis. Using this reference frame, velocity profiles could be identified at a constant radial location, i.e., for a "circular" cut.

An example of the wave-like displacements observed on the vortices is shown in Fig. 3.39a, with the corresponding velocity profiles in Fig. 3.39b, as taken at radially downstream locations of r/R = 1.6, 1.8, 2.0, and 2.2. Notice that parts of Filament 2 were convected closer to the ground plane than other parts of the vortex such that the core region periodically intersected the imaging plane; this observation suggests that the cen-

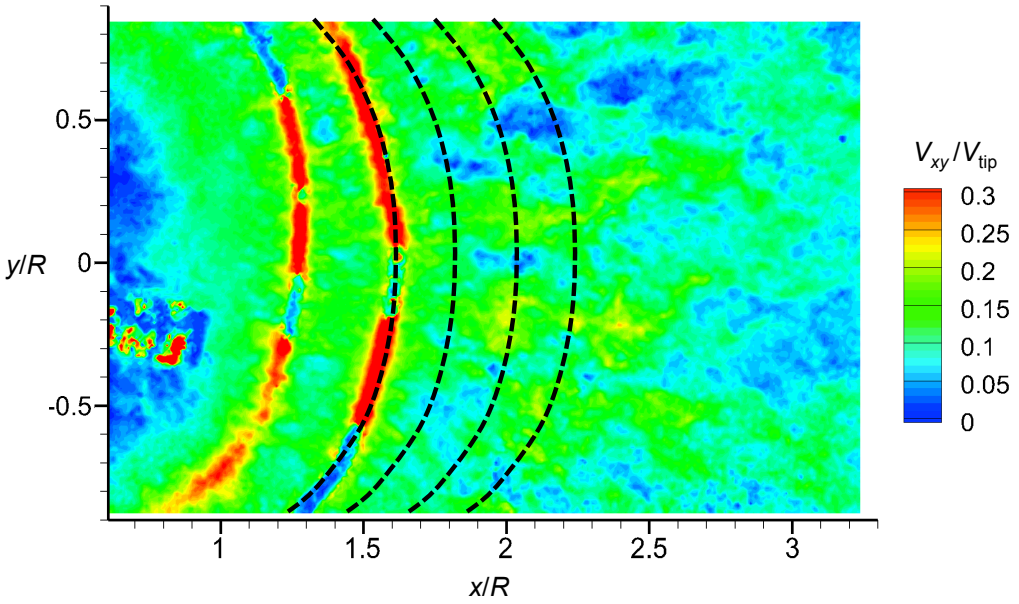

(a) Total velocity contours

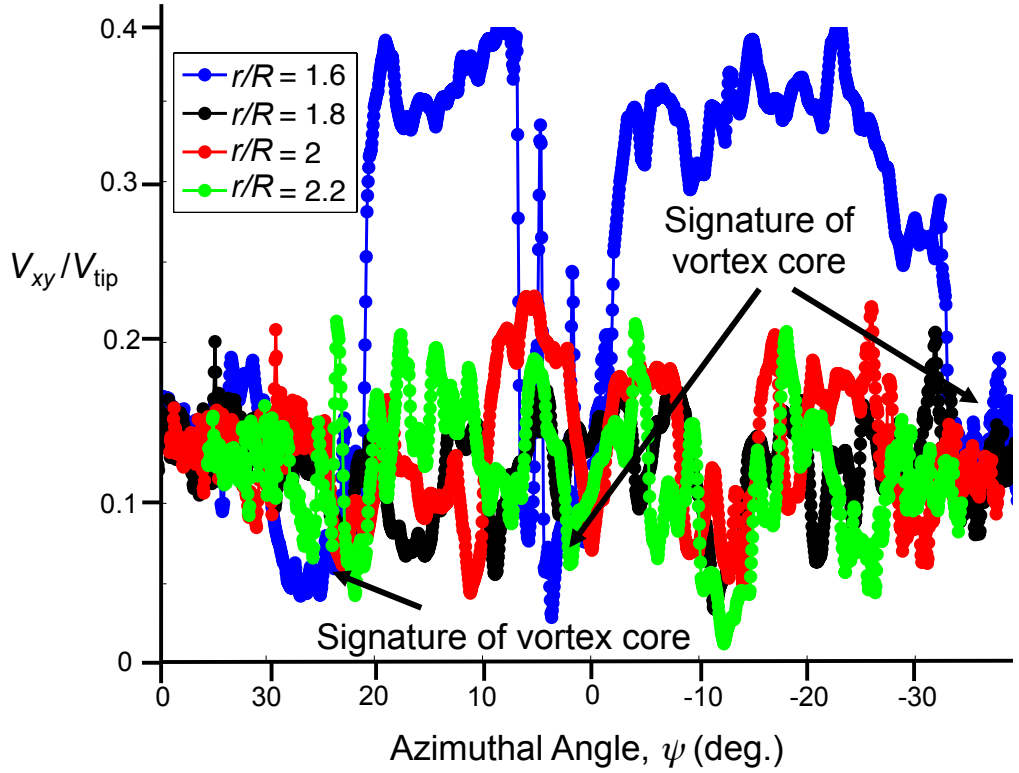

(b) Radial velocity profiles

Figure 3.39: Instantaneous flow velocities showing the wave-like displacements of the vortex filaments in a plane at $z/R = 0.1$ as (a) contours of total velocity, (b) radial velocity profiles.

terline of the vortex filament along its length was not at the same height above the ground. The velocity profile taken at $r/R = 1.6$ was through the entire length of Filament 2 and clearly shows the signature of the vortex core, as marked in Fig. 3.39b. In fact, the wave-like displacements were large enough such that their signatures were also observed in the time-averaged flow results in the plane at $z/R = 0.1$, as shown in the contours of total velocity in Fig. 3.40a.

Time-averaged velocity profiles were also obtained at radial locations of r/R = 1.6, 1.8, 2.0, and 2.2; see Fig. 3.40b. The velocity profiles showed that while the flow was relatively more uniform when compared to the instantaneous flow measurements, the in-plane velocity field still formed a distinct wave-like pattern. This observation shows that wherever the centerlines of the filaments were closer to the ground, locally higher induced flow velocities were produced.

3.1.1.5 Summary of Single-Phase Flow Results

The single-phase flow measurements have shown the the wake produced by a hovering rotor near the ground is complex, containing regions of discrete vorticity and non-uniform velocities near the ground. The results have shown that the tip vortices interact with each other and also with the boundary layer near the ground, causing transient regions of high wall shear that will likely mobilize particles. These results have also provided insight into the three-dimensionality of the flow and can be used to better understand the dual-phase flow environment (discussed next).

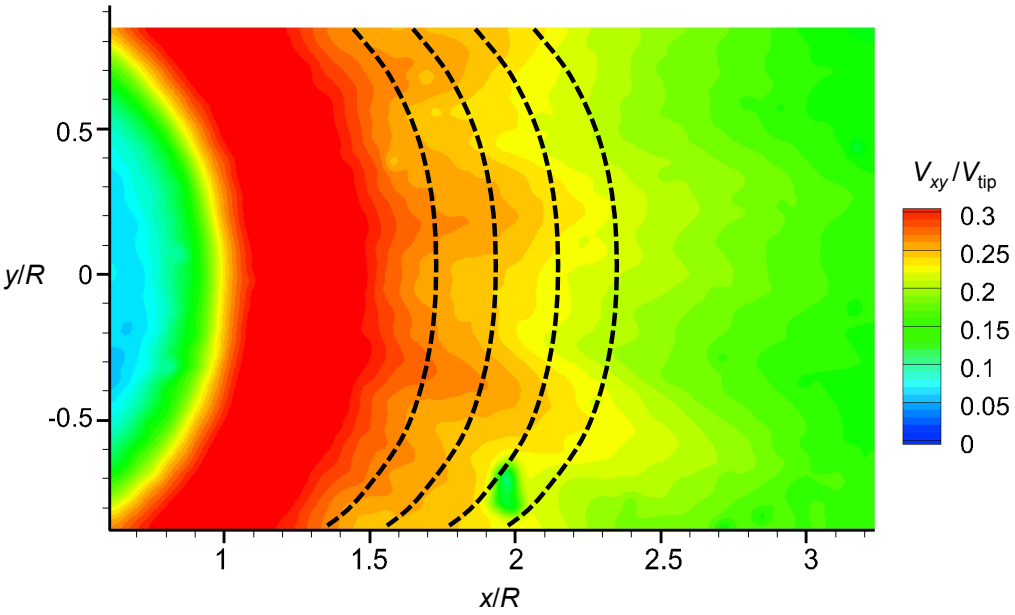

(a) Total velocity contours

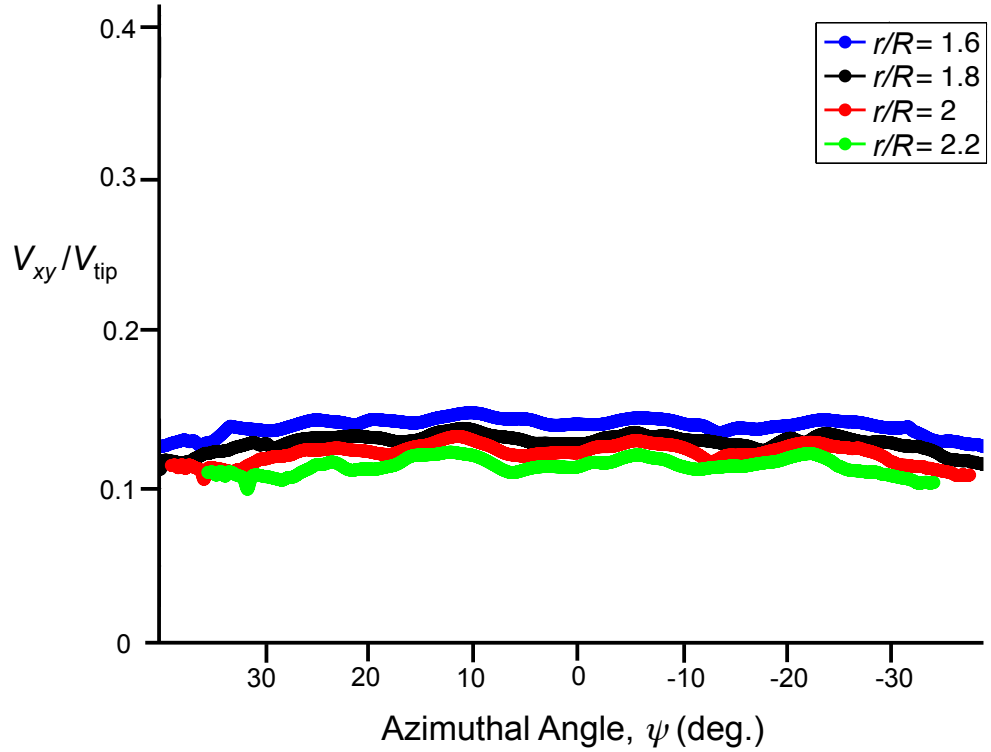

(b) Radial velocity profiles

Figure 3.40: Time-averaged flow velocities showing the wave-like displacements of the vortex filaments in a plane at $z/R = 0.1$ as (a) contours of total velocity, (b) radial velocity profiles.

3.1.2 Dual-Phase Flow Results

Figure 3.41 shows representative dual-phase PIV/PTV measurements taken in ROI 1 (see previously in Fig. 2.10). The background contours are of the total velocity in the *x*-*z* plane, V_{xz}, of the carrier-phase as measured in the dual-phase flow evironment, and the circular markers represent the locations of the sediment particles. For clarity, these markers are shown here to be bigger relative to the actual size of the sediment particles. The results show that, as expected, there is a complex flow environment produced near the sediment bed, and in general the particle paths do not exactly follow the directions of the flow.

The results in Fig. 3.41 show that each vortex uplifted a wave of sediment that was convected radially outward over the bed. The measurements have suggested that these waves are similar to the vertical cross-sections of the columnar plumes of sediment that are often observed in rotor-induced brownout clouds, as shown previously in Fig. 1.1. Marked in Fig. 3.41 are discrete uplift events that caused the particles on the bed to form these plumes. Notice that each event uplifted a different quantity of sediment and also to varying heights off the bed. One goal of the present work was to investigate what causes the differences in these local uplift events and how these events affect the overall three-dimensional distribution of particles that are in suspension around the rotor.

3.1.2.1 Mobilization and Entrainment

To understand the overall formation of the particle field around the rotor, it was important to first investigate the initial mobilization and entrainment of particles. The

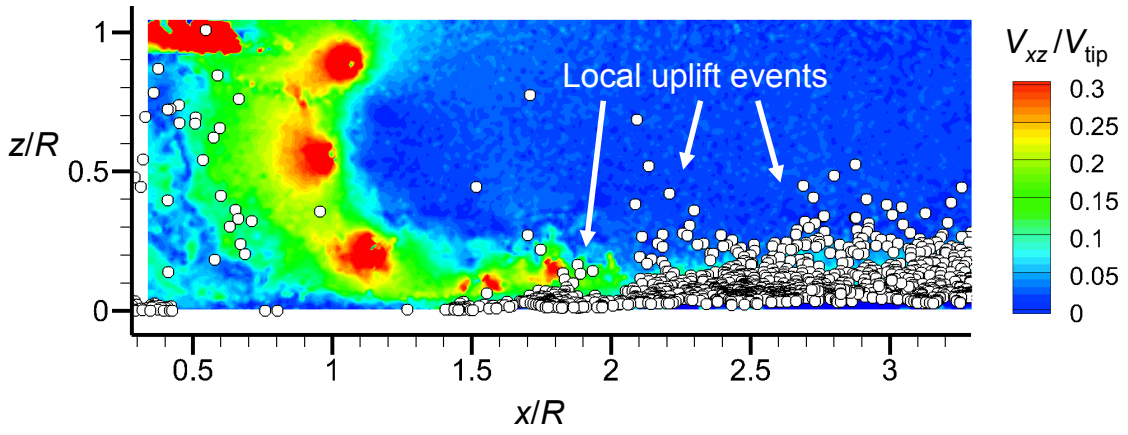

Figure 3.41: Instantaneous dual-phase flow measurement as a background contour of total velocity with white circles for particle location (particle size exaggerated for clarity).

single-phase results in the vertical plane showed that, on average, the maximum shear stress along the ground was observed at a distance of $x/R \approx 1.4$ (see Fig. 3.20). The instantaneous flow realization shown in Fig. 3.41 suggests that this location is approximately where the particles first began to be mobilized, i.e., the location of incipient motion.

Previous studies have characterized the fluid dynamic mechanisms responsible for the mobilization of sediment below a hovering rotor [7, 26, 38]. Once the shear stress at the wall becomes sufficiently high, the stationary particles lying on the surface can become mobilized. Initially, the heavier particles just roll along the bed, a mechanism known as creep. However, if the particles encounter an upward flow velocity such as induced by a turbulent eddy, they can be entrained briefly into the flow but then follow ballistic-like trajectories back to the bed under the action of gravity. These particles then bombard the bed and eject more particles into the near-wall flow. This continuous process of particle ejections creates a saltation layer in which the contained particles can be much more readily uplifted by any passing vortical flows [7].

To further investigate the formation of the saltation layer, a detailed instantaneous flow realization (close the ground) is shown in Fig. 3.42. The carrier-phase of the dual-phase flow is shown as background contours of u and w velocity. In both figures, the sediment particles are represented by white circles, with red vectors showing the corresponding particle velocities. Notice that in this flow realization, there were no vortices above the part of the sediment bed that can be seen in Fig. 3.42. Figure 3.42 also shows that the carrier-phase velocity was primarily radially outward, i.e., there was relatively little flow in the wall-normal direction. Therefore, the particles that were within the saltation layer were convected primarily radially outward.

The near-wall flow and wall-jet induced on the ground as produced by the rotor wake was clearly of sufficient magnitude to create a relatively thick saltation layer just above the sediment bed. As shown in Fig. 3.42, this near-wall region had a relatively high concentration of sediment particles, which was observed to affect the development of the rotor wake near the ground. For example, Fig. 3.43 shows the time-averaged flow velocities induced near the ground for both the single-phase flow (without the sediment) and the carrier-phase of the dual-phase flow (with the sediment). The vectors are, in each case, colored by total velocity. Notice that in the single-phase flow, the wall-jet developed on the surface of the ground plane. However, for the dual-phase flow, the developing wall-jet was deflected above the saltation layer, in this case starting at $x/R \approx 1.2$. This observation suggests a rather obvious and strong form of two-way coupling between the carrier-phase and the dispersed-phase of the dual-phase flow.

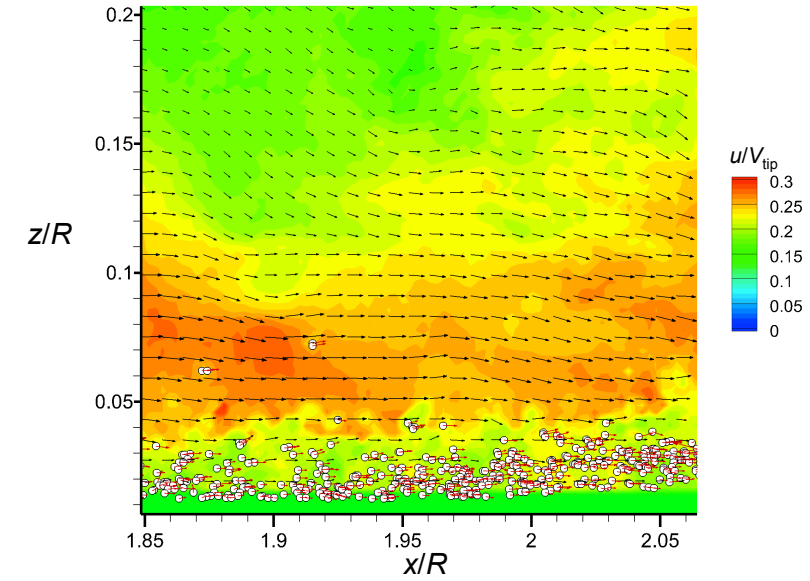

(a) u velocity

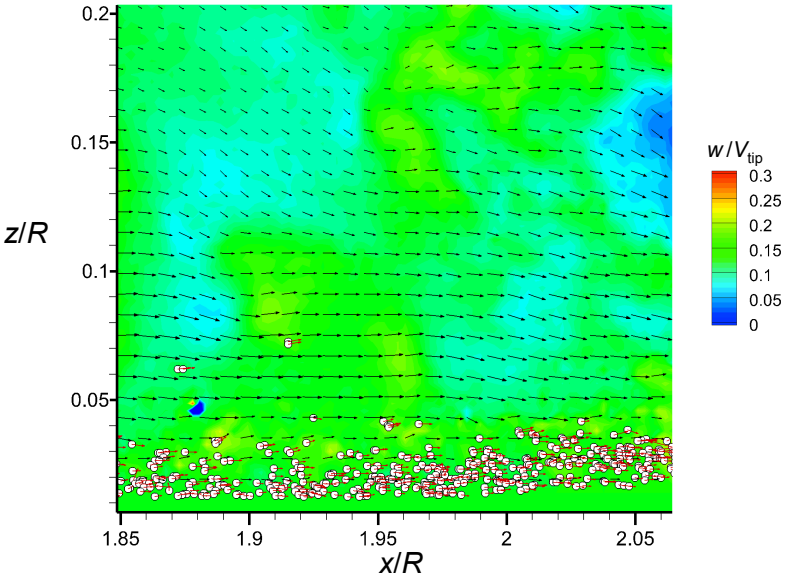

(b) w velocity

Figure 3.42: Instantaneous dual-phase PIV/PTV results showing the saltation layer with carrier-phase contours of u and w velocity.

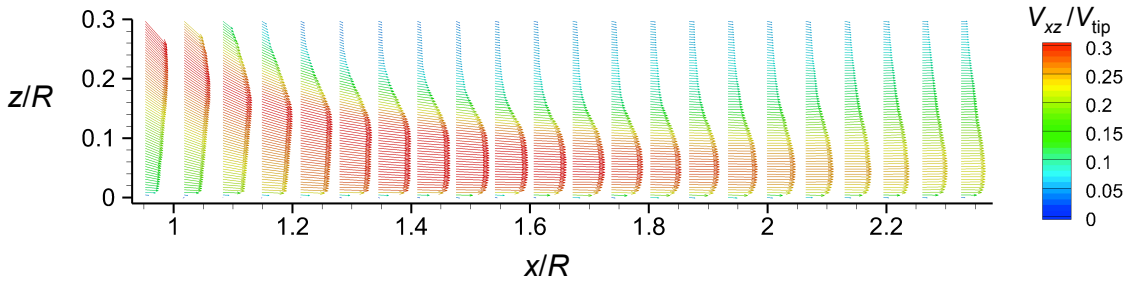

(a) Single-phase

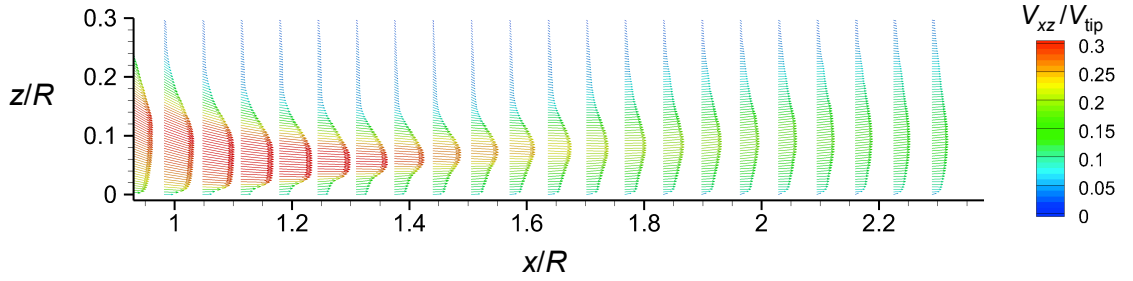

(b) Dual-phase

Figure 3.43: Time-averaged single-phase and carrier-phase wall-jet velocity shown with contours of total velocity.

3.1.2.2 Uplift and Suspension

An important mechanism associated with the uplift and suspension of sediment particles was vortex-induced particle trapping. As a vortex passed in proximity to the bed, particles within the saltation layer were entrained in the upwash region of the vortex and uplifted into the main flow, this process being shown in Fig. 3.44. The sediment particles are represented by white circles and the carrier-phase flow velocities are shown as background contours of total velocity in the vertical plane, V_{xz}.

In Fig. 3.44a, there were no vortices present in the ROI and, therefore, the particles on the bed formed a mobile saltation layer with velocities that were directed primarily radially outward. After 60° of blade rotation (Fig. 3.44b), a vortex had entered the ROI and

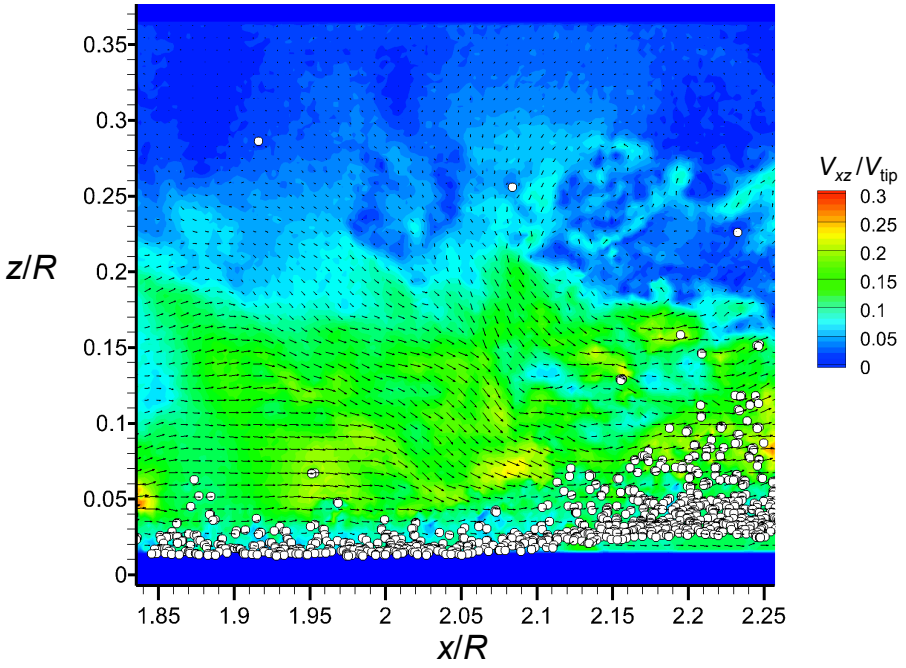

(a) ψ_b =360°

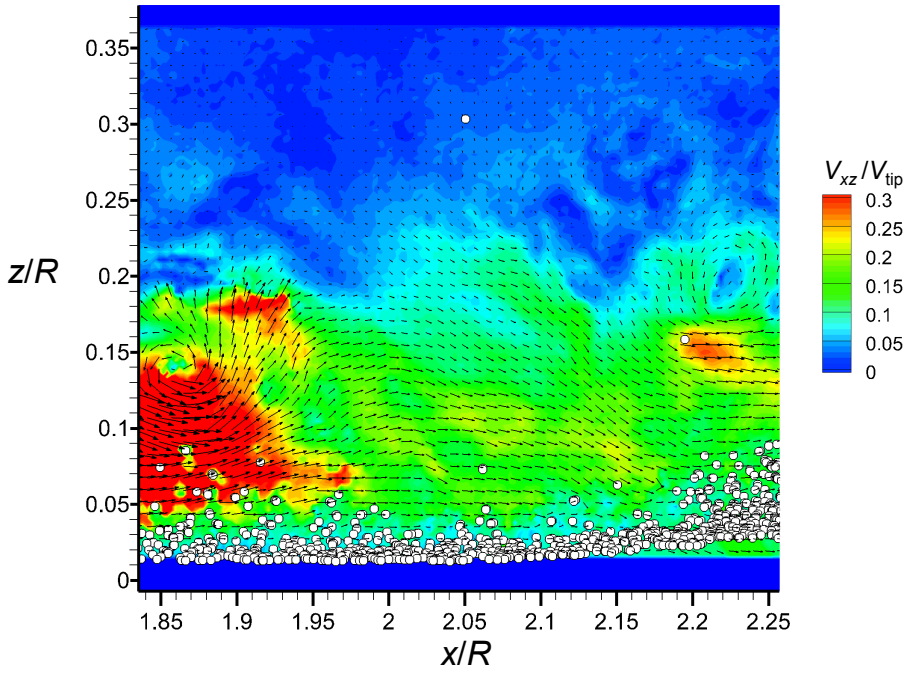

(b) ψ_b =30°

Figure 3.44: Contiguous sequence of PIV/PTV flow realizations showing the process of vortex-induced particle trapping.

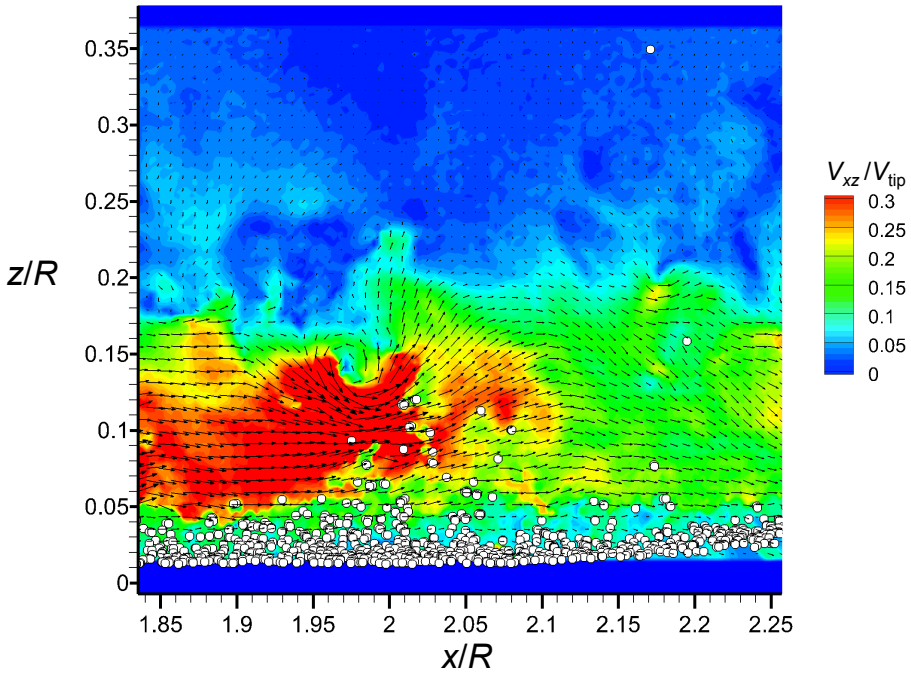

(c) ψ_b =60°

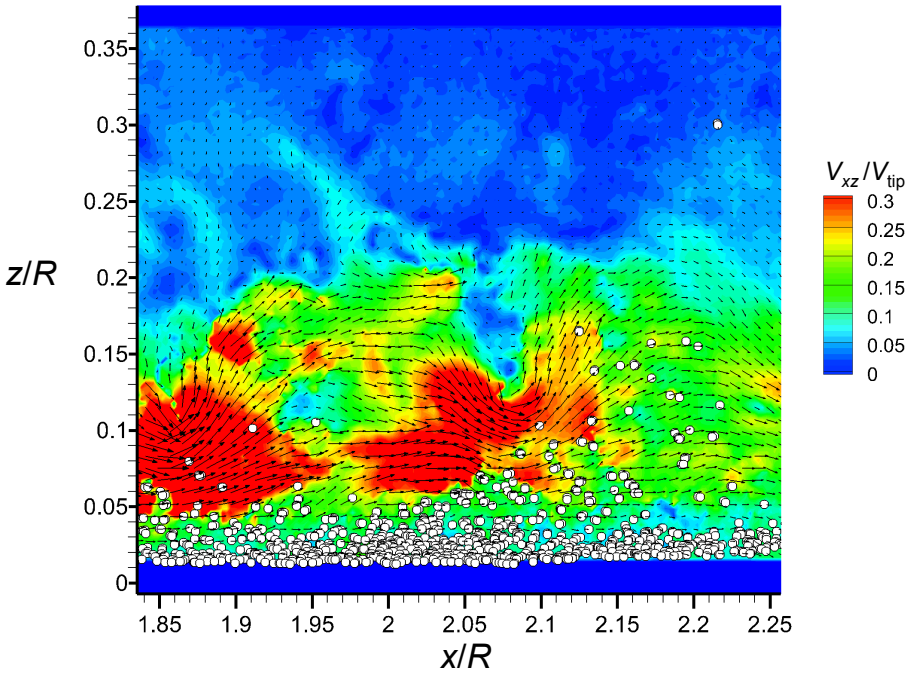

(d) ψ_b =90°

Figure 3.44: (Concluded) Contiguous sequence of PIV/PTV flow realizations showing the process of vortex-induced particle trapping.

was observed to interact with the particles in the saltation layer as well as with the particles on the bed. Recall that the single-phase results (Fig. 3.24b) showed that the near-wall presence of a vortex caused a local increase in the velocity gradients and shear stress on the ground. The following realization (Fig. 3.44c) shows that the vortex-induced velocity caused a thickening of the saltation layer directly below the vortex and the entrainment of further particles into the flow. The particles within the saltation layer were observed to be easily caught in the vortex upwash and uplifted out of the saltation layer, as shown in Fig. 3.44d. These are the basic steps of the vortex-induced particle trapping process.

Particle trapping significantly altered the trajectories and velocities of the uplifted particles. Figure 3.45 shows an instantaneous PIV/PTV flow realization of a vortex interacting with the saltation layer as well as the sediment bed. The particles are shown as white circles and the carrier-phase is shown as background contours of u and w velocity in Fig. 3.45a and Fig. 3.45b, respectively. Figure 3.45a shows that particles were mobilized under the action of the impinging vortex.

Figure 3.45b clearly shows that the particles in the saltation layer were trapped by the upwash region of the passing vortex. However, the uplifted particles did not exactly follow the direction of the surrounding flow velocities. For example, the corresponding u and w components of the particle velocities are shown in Fig. 3.46a and Fig. 3.46b, respectively. These velocity contours were created by overlaying a uniform grid on the PTV results and interpolating the velocity at the grid nodes by using the velocity values of the closest neighboring particles.

In Fig. 3.46b (w-component of velocity), red indicated particles moving upward away from the bed and blue indicated particles moving downward toward the bed. Notice

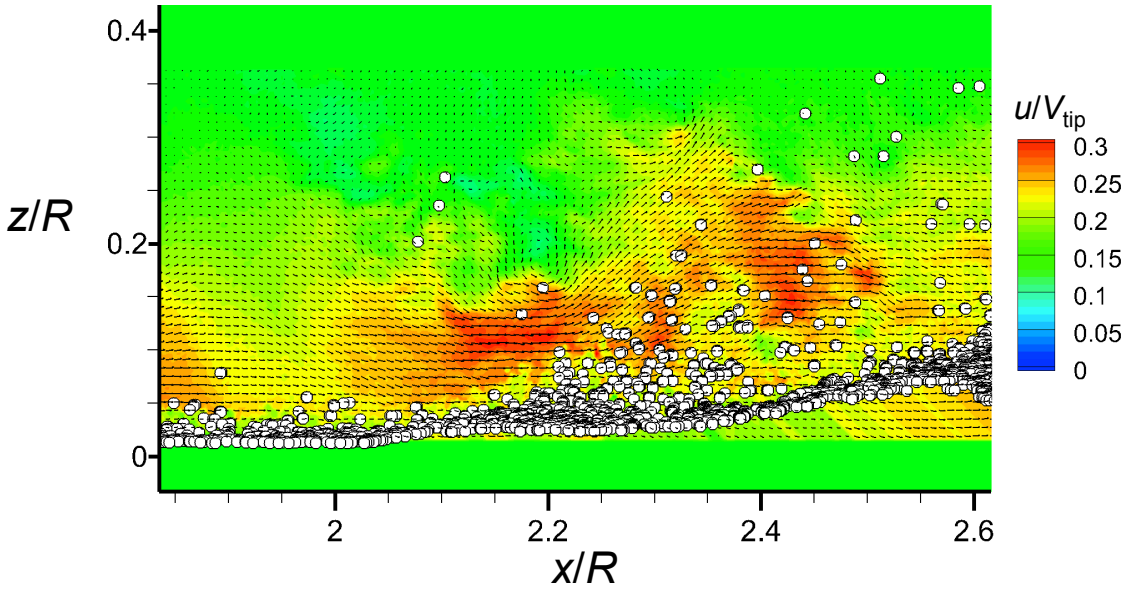

(a) *u* velocity

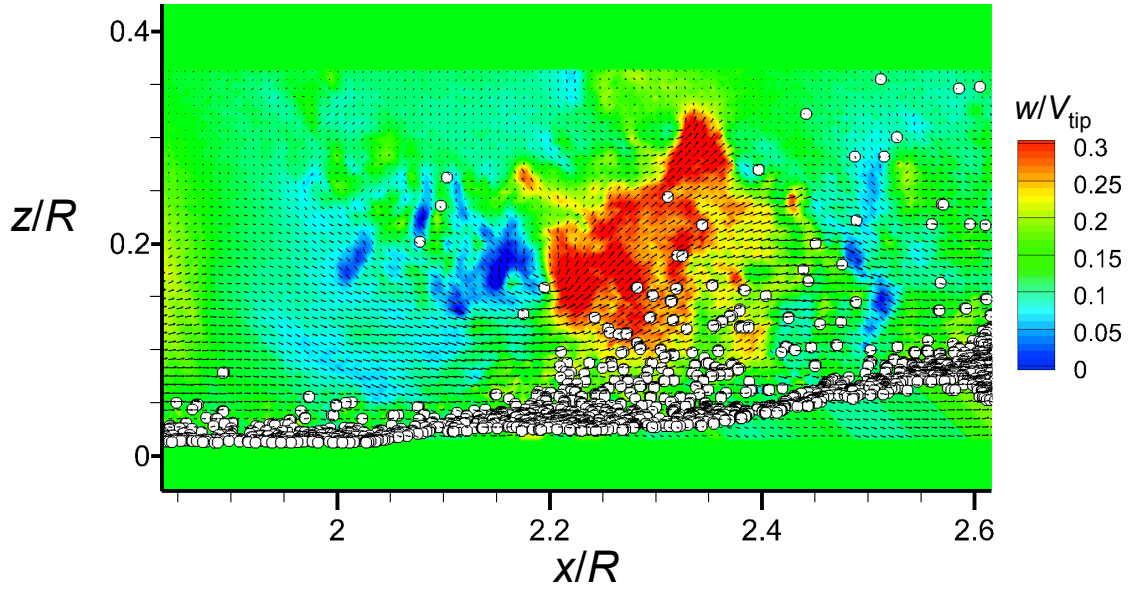

(b) *w* velocity

Figure 3.45: Instantaneous dual-phase PIV/PTV results showing vortex-induced particle trapping with carrier-phase contours of *u* and *w* velocity.

in Fig. 3.46b that there were a number of distinct regions within the flow. The particles trapped in the upwash were quickly transported upward, with a relatively high w-component of velocity. However, some of the larger particles that were entrained by the vortex flow were "spun-out" by centrifugal forces and convected back toward the bed. Other particles closely followed the vortex flow and were caught in the downwash region of the vortex where they were convected down to bombard the bed. The bombardment of particles onto the bed by the vortices served to rapidly concentrate the saltation layer and so increase the number of uplift-eligible particles.

Recall from Fig. 3.41 that the quantity of particles and height to which they were uplifted significantly varied between uplift events. One potential explanation for the differences observed in the uplift events was noted previously in the single-phase flow results, where the trajectories of the blade tip vortices significantly altered the near-wall flow velocities; see previously in Fig. 3.22. Figure 3.47 shows two instantaneous, dual-phase flow measurements taken at the same blade azimuthal position, in this case for $\psi_b = 120^\circ$. Notice that the vortex in Fig. 3.47a (labeled Vortex A) was closer to the bed than the vortex in Fig. 3.47b (labeled Vortex B); the results showed that Vortex A had mobilized and uplifted more particles. While both of these vortices created local particle uplift events (or particle bursts), the quantity of particles and their corresponding velocities varied rather significantly based on the local height of the vortex off the bed.

Another phenomenon that was observed to cause local particle uplift events was the pairing and merging of adjacent vortices. Figure 3.48 shows two adjacent turns of the tip vortices that were in the processing of merging together. In this case, the background contour is of the vertical component of flow velocity. The larger upwash region created by

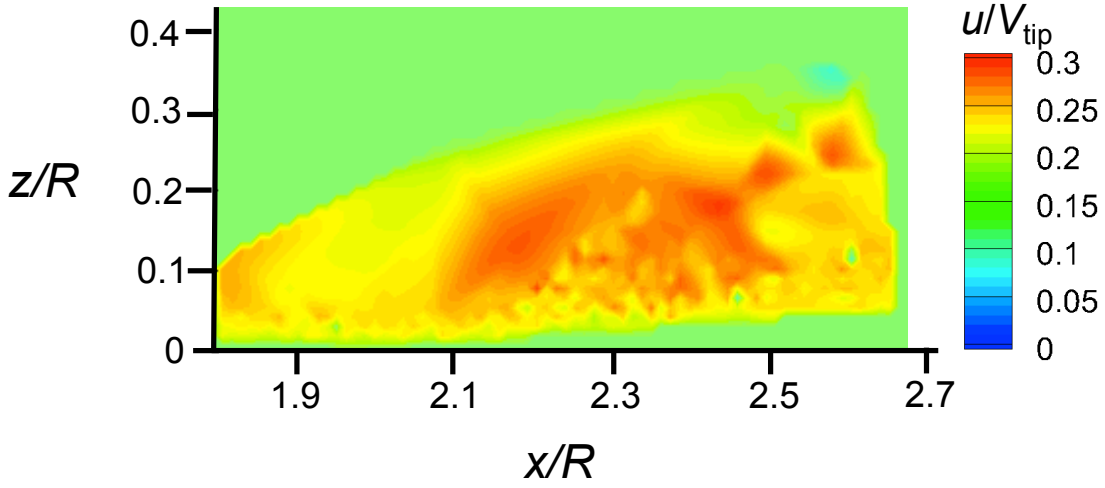

(a) *u* velocity

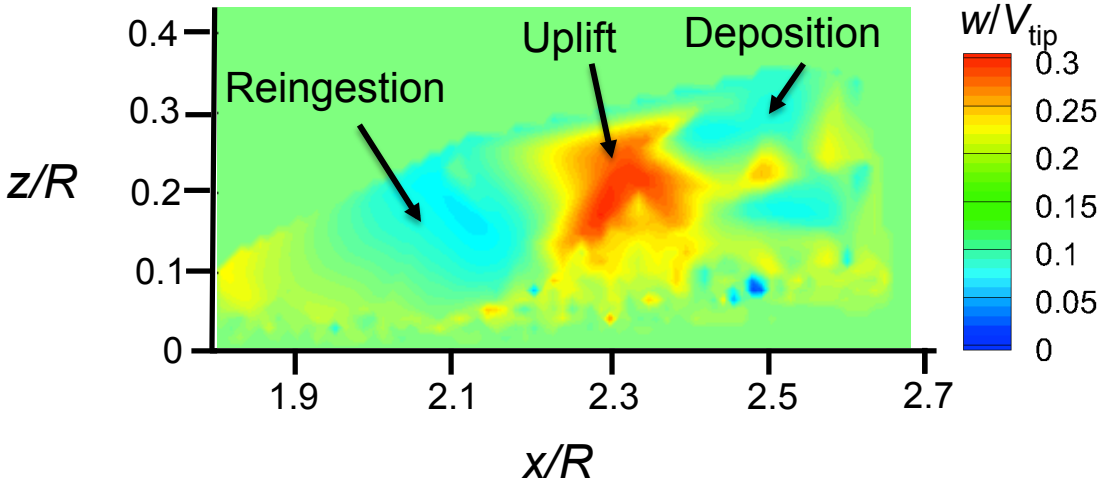

(b) *w* velocity

Figure 3.46: Instantaneous dispersed-phase contours of *u* and *w* velocity.

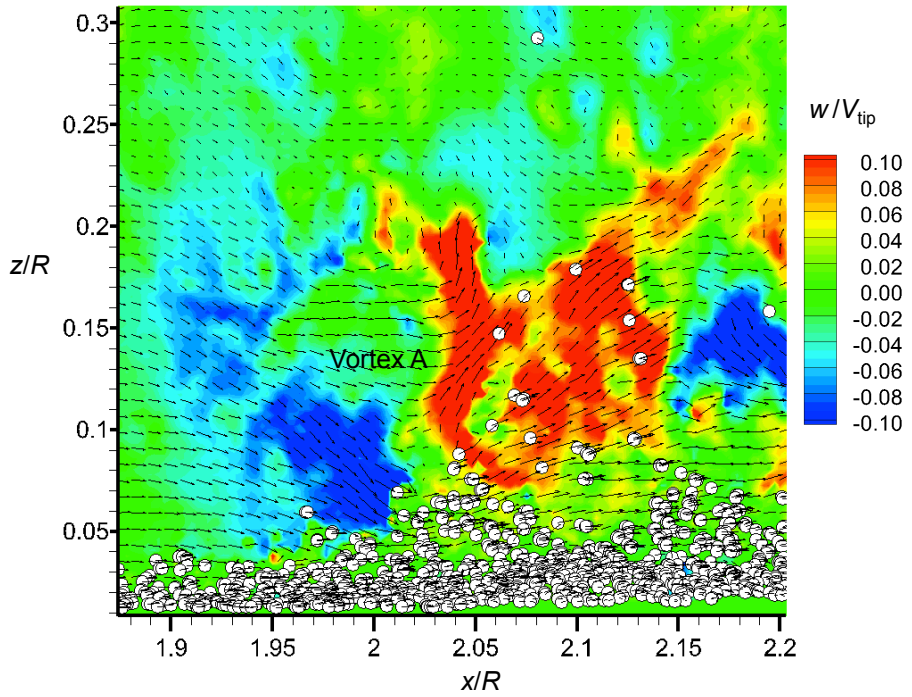

(a) Flow realization 1

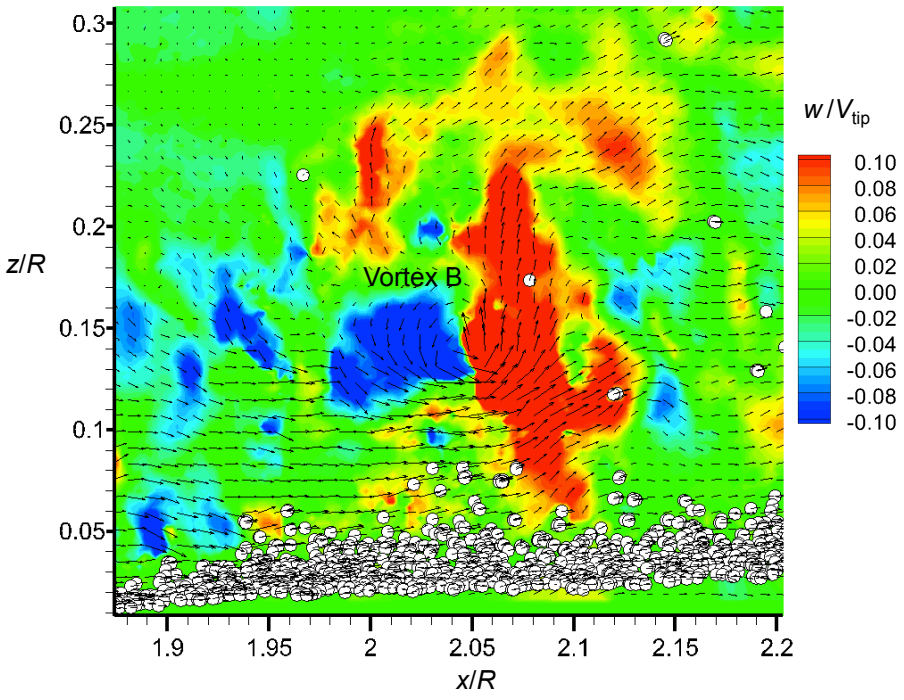

(b) Flow realization 2

Figure 3.47: Two dual-phase instantaneous flow realizations showing the differences in local uplift events caused by vortex proximity to the ground.

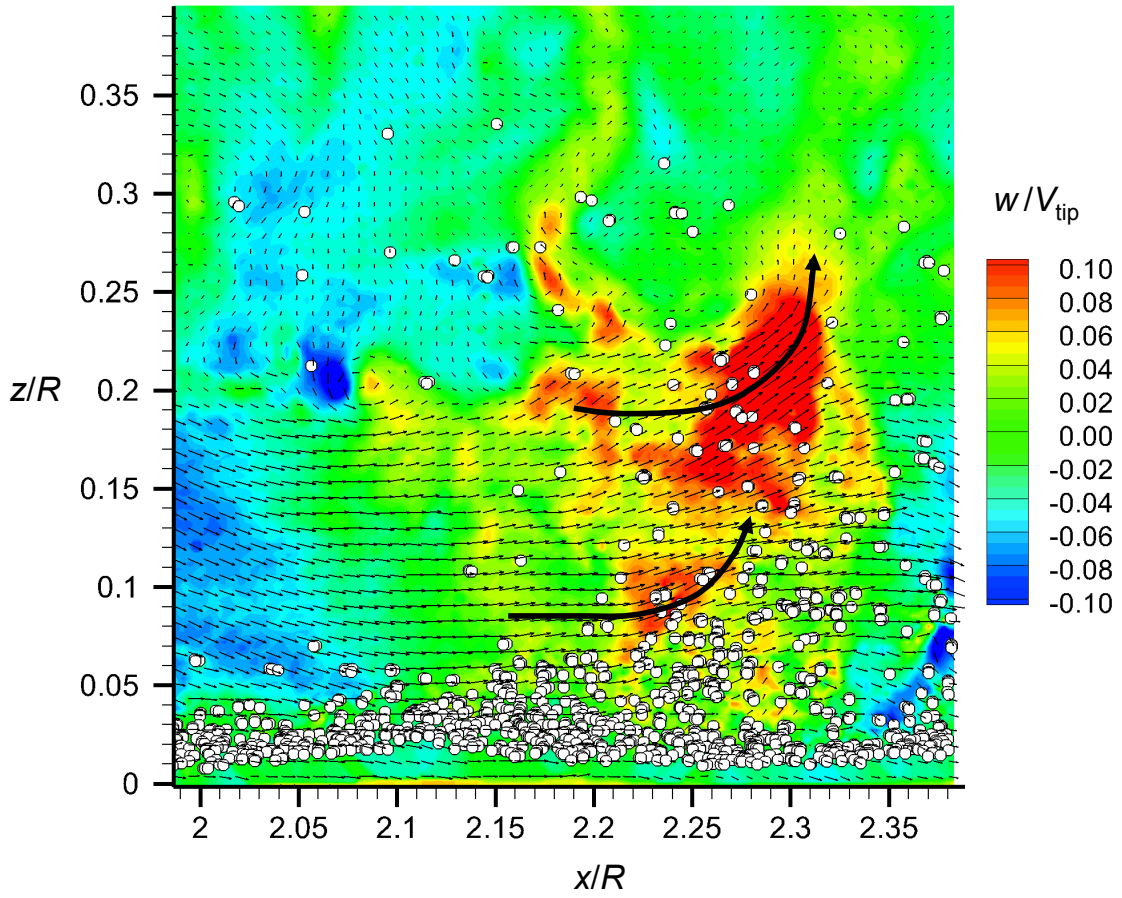

Figure 3.48: Instantaneous dual-phase flow measurements of two adjacent vortices merging together.

the merging of the vortices elevated a larger quantity of sediment to much higher above the bed than was produced by the upwash field induced by a single vortex. This observation suggests that the local merging of adjacent vortices will likely cause local uplift events that manifest as more significant plumes within the rotor-induced particle field.

3.1.2.3 Three-Dimensional Particle Field

Images of brownout clouds generated by landing helicopters show that these rotor-induced particle fields have a significant three-dimensional, time-varying structure. To

investigate the three-dimensionality of the rotor-induced particle field, Fig. 3.49 shows a sequence of dispersed-phase images that were taken in a horizontal plane at $z/R = 0.2$. These images were obtained by subtracting the carrier-phase flow from the dispersed-phase, producing a resultant image that contained only the sediment particles (colored black in this case for clarity). Figure 3.49a shows that there was clearly a highly non-uniform (i.e., three-dimensional) distribution of particles throughout the imaging region. The larger dark region located at the upper right corner of the image was the horizontal cross-section of the saltation layer as it develops over the bed. The measurements made in this plane showed that the saltation layer comprised an accumulating concentration of sediment that was convected radially outward away from the rotor.

The measurements made in the vertical plane (see previously in Fig. 3.41) have shown that the rotor-induced dust fields developed into a saltation layer at the ground. Figure 3.49 shows the three-dimensional formation of this saltation layer in the horizontal planes in the near-wall region (at $z/R = 0.2$). The first particle realization (Fig. 3.49a) showed a radial streak of entrained sediment, which is marked as an initial event. The particles here were noted to originate from below the imaging plane, i.e., from the sediment bed. The subsequent particle realization (Fig. 3.49b) shows that the process of creep and saltation caused the particle concentrations in this region to increase rapidly. However, the particles did not develop along one radial path in the flow but also azimuthally. In Fig. 3.49c and Fig. 3.49d, it can be seen that the region of entrained particles quickly expanded and significantly increased in concentration, forming a non-uniform saltation layer over much of the sediment bed.

In Figs. 3.47 and 3.48, the results showed that in the vertical plane the mobile

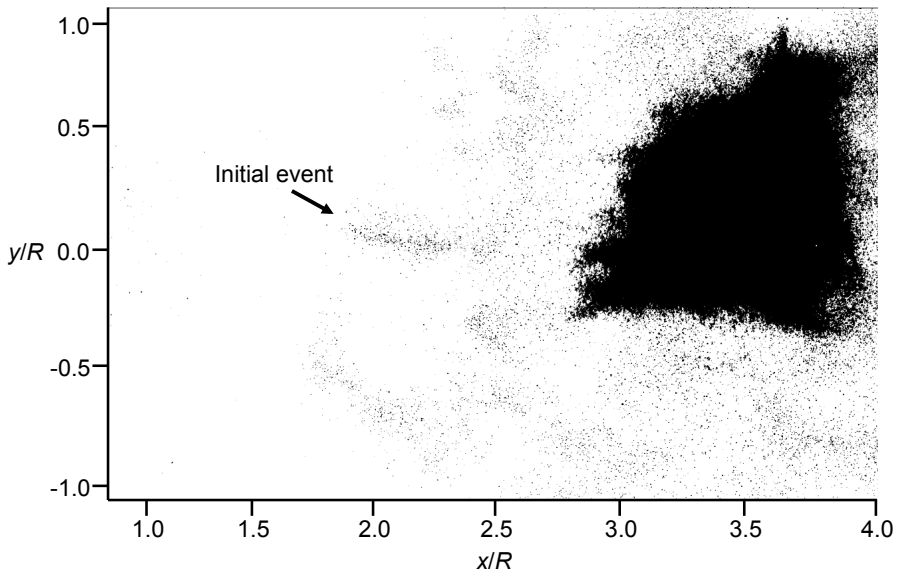

(a) Particle realization 1

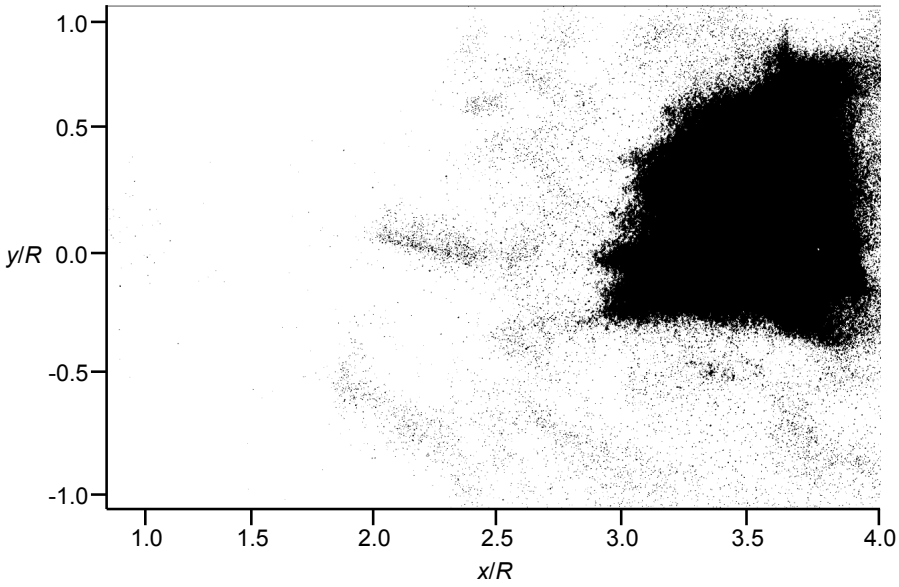

(b) Particle realization 2

Figure 3.49: Dispersed phase images in a plane at $z/R = 0.2$ showing the entrainment of sediment, (a) Particle realization 1, (b) Particle realization 2

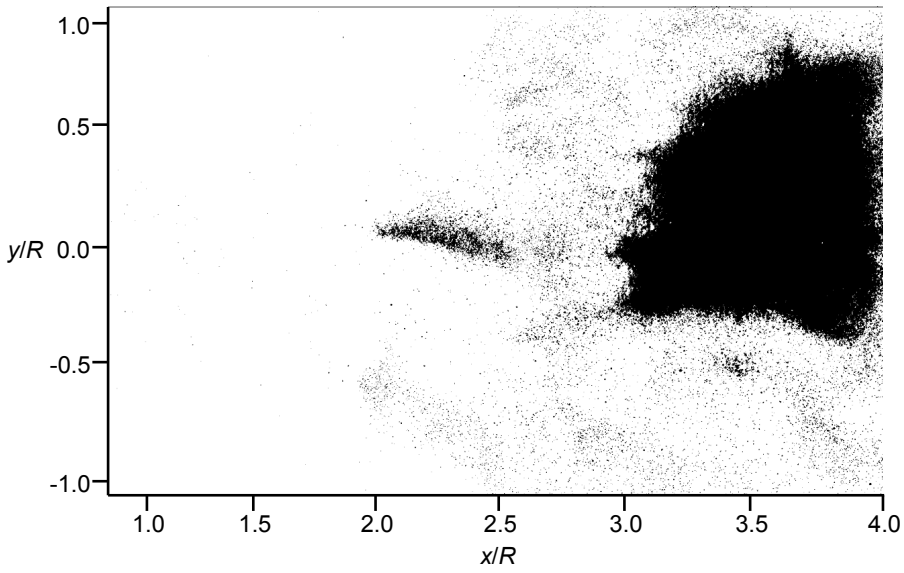

(c) Particle realization 3

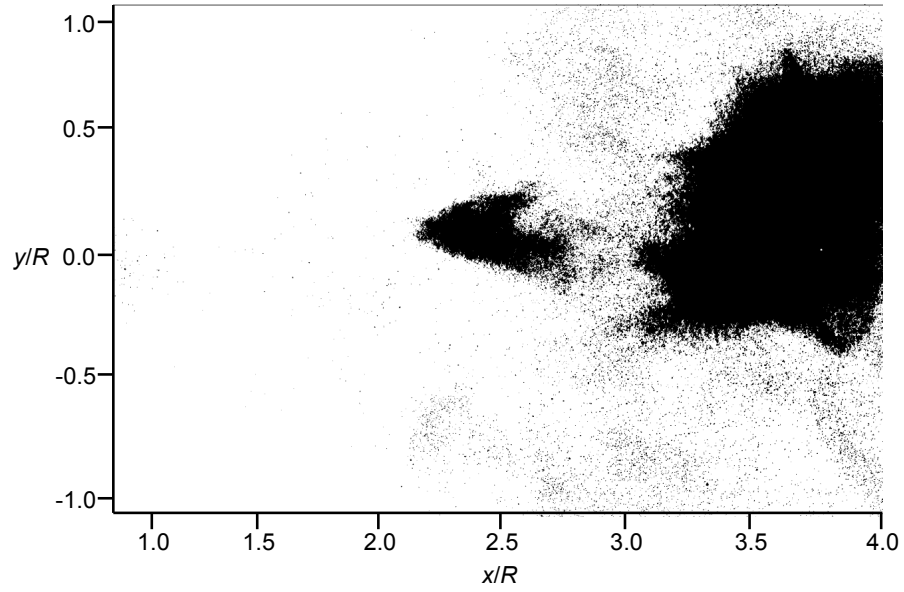

(d) Particle realization 4

Figure 3.49: (Concluded) Dispersed phase images in a plane at $z/R = 0.2$ showing the entrainment of sediment, (c) Particle realization 3, (d) Particle realization 4.

particles in the saltation layer were easily uplifted by the upwash field produced by a vortex. Because the vortices are actually continuous filaments, a relatively long length of the filament will interact with the saltation layer and so create a more complex and more three-dimensional dust cloud. Therefore, to better examine the three-dimensionality of the particle field, the dual-phase flow results in the horizontal planes were stacked together so as to create a pseudo three-dimensional measurement volume; a schematic of how these results are presented is shown in Fig. 3.50. Notice that while the planes are at $z/R = 0.1$–0.8 , the vertical space between the planes has been increased in Fig. 3.50 to better show the results. The results are presented as total velocity, radial velocity, and azimuthal velocity (i.e., V_{xy}, V_r, V_θ). The polar coordinate system is shown in Fig. 3.38, with the equations to transform from Cartesian to polar velocity components being $V_r = u\cos\theta + v\sin\theta$ and $V_\theta = -u\sin\theta + v\cos\theta$.

One of the factors that influences landing in brownout conditions is the pilot's perceived relative velocity of the dust cloud, which may cause the pilot to experience vection illusions. Figure 3.51 shows the time-averaged total, radial, and azimuthal component of the particle field velocities. The total velocity field in Fig. 3.51a showed that the highest particle velocities were observed to be in the plane closest to the bed ($z/R = 0.1$), i.e., mostly within the saltation layer. In the planes further from the ground, the particle velocities decreased, however, discrete patterns appeared in the clouds. For example, at $z/R = 0.3$, there were regions of higher particle velocities that extended radially outward; the higher velocity regions had also moved further outboard. Of particular interest was that in higher planes ($z/R = 0.5$–0.8), there were noticeable particle velocities that were produced further inboard, albeit of lower magnitude.

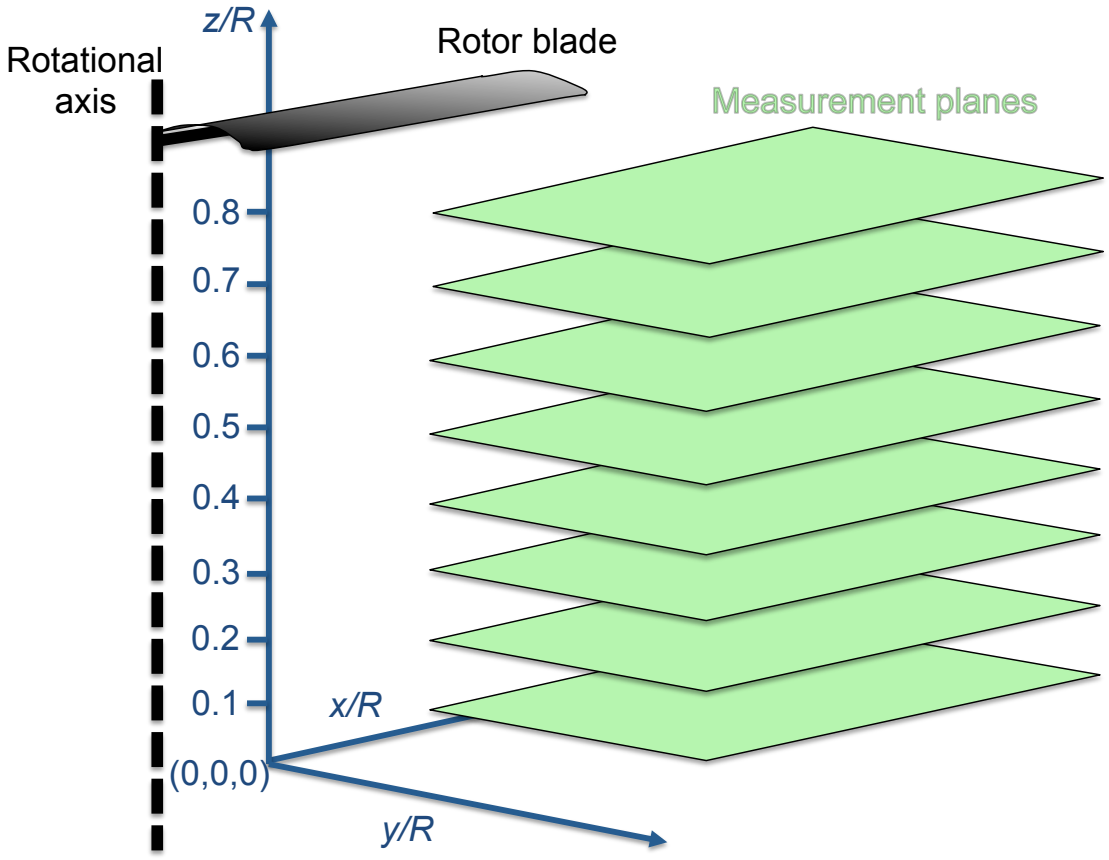

Figure 3.50: Schematic of the horizontal planes shown in the following figures.

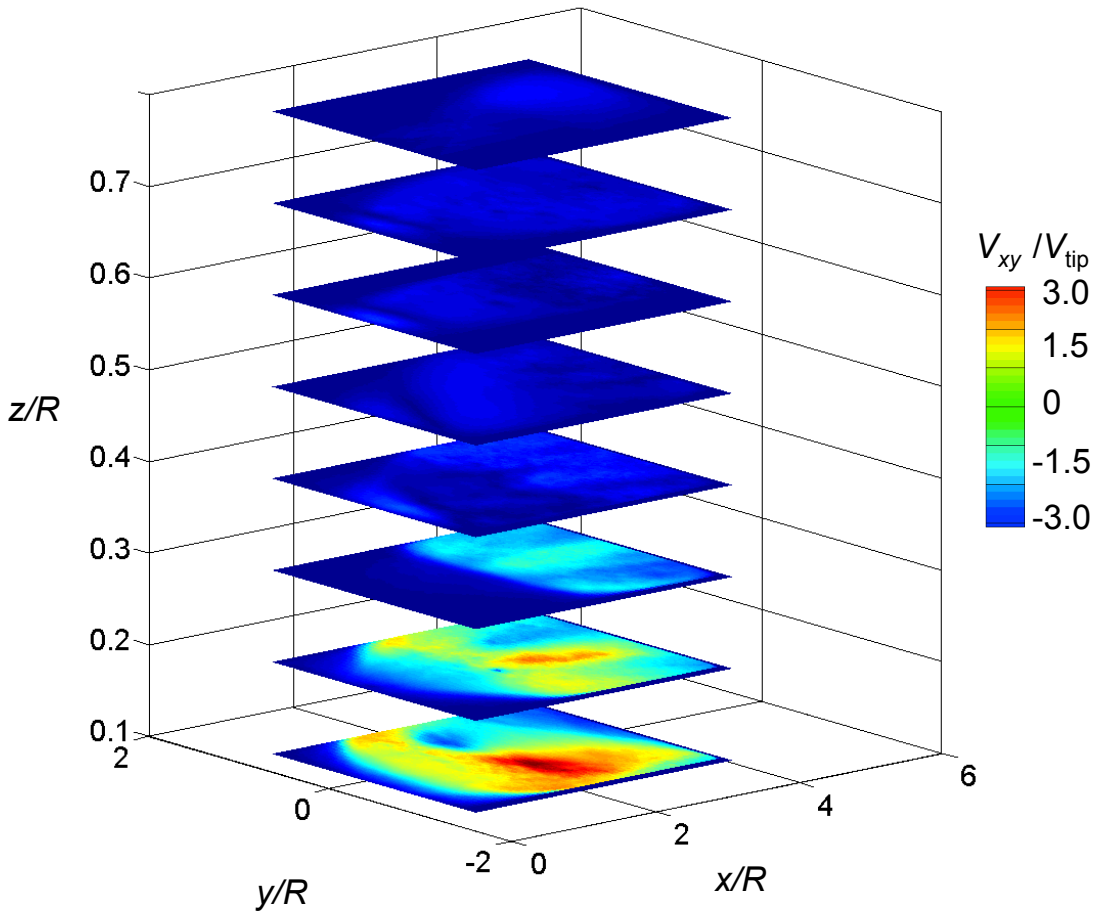

(a) Total velocity

Figure 3.51: Three-dimensional time-averaged particle velocities, (a) Total velocity

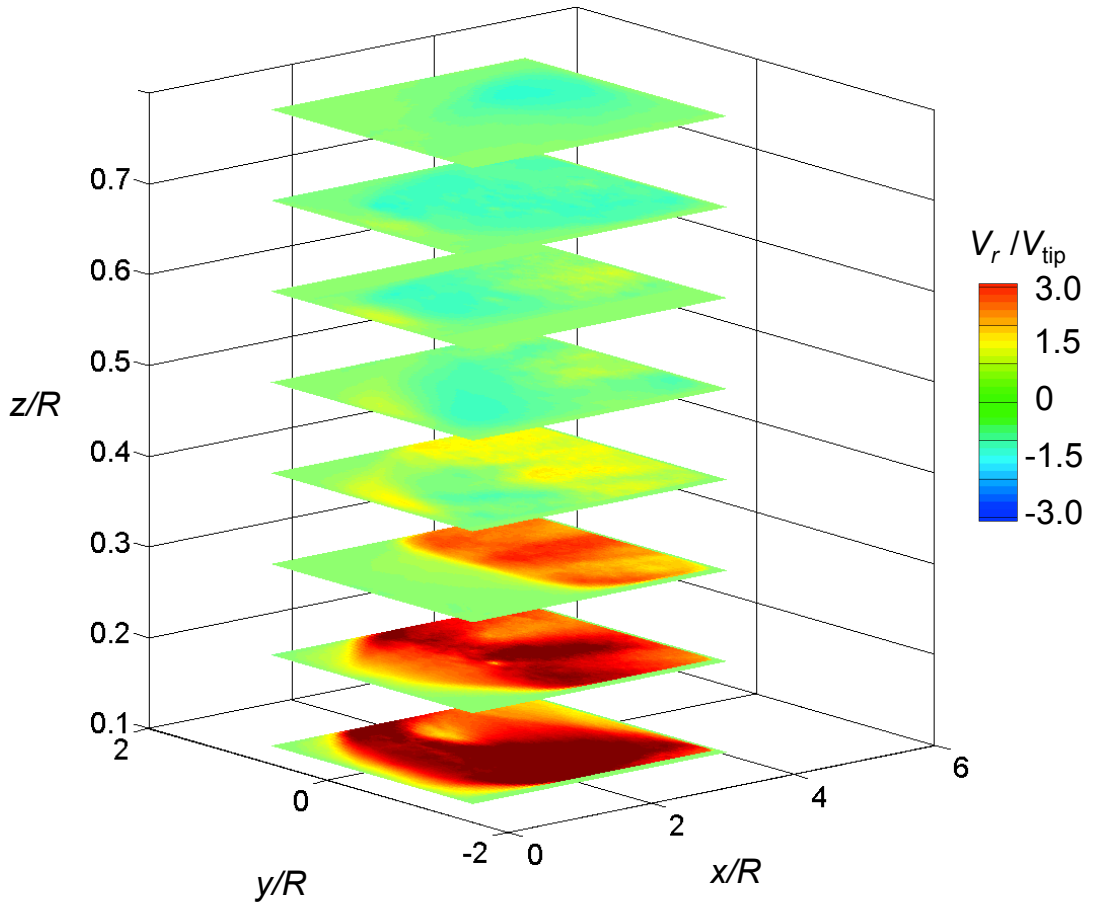

(b) Radial velocity

Figure 3.51: (Cont'd) Three-dimensional time-averaged particle velocities, (b) Radial velocity

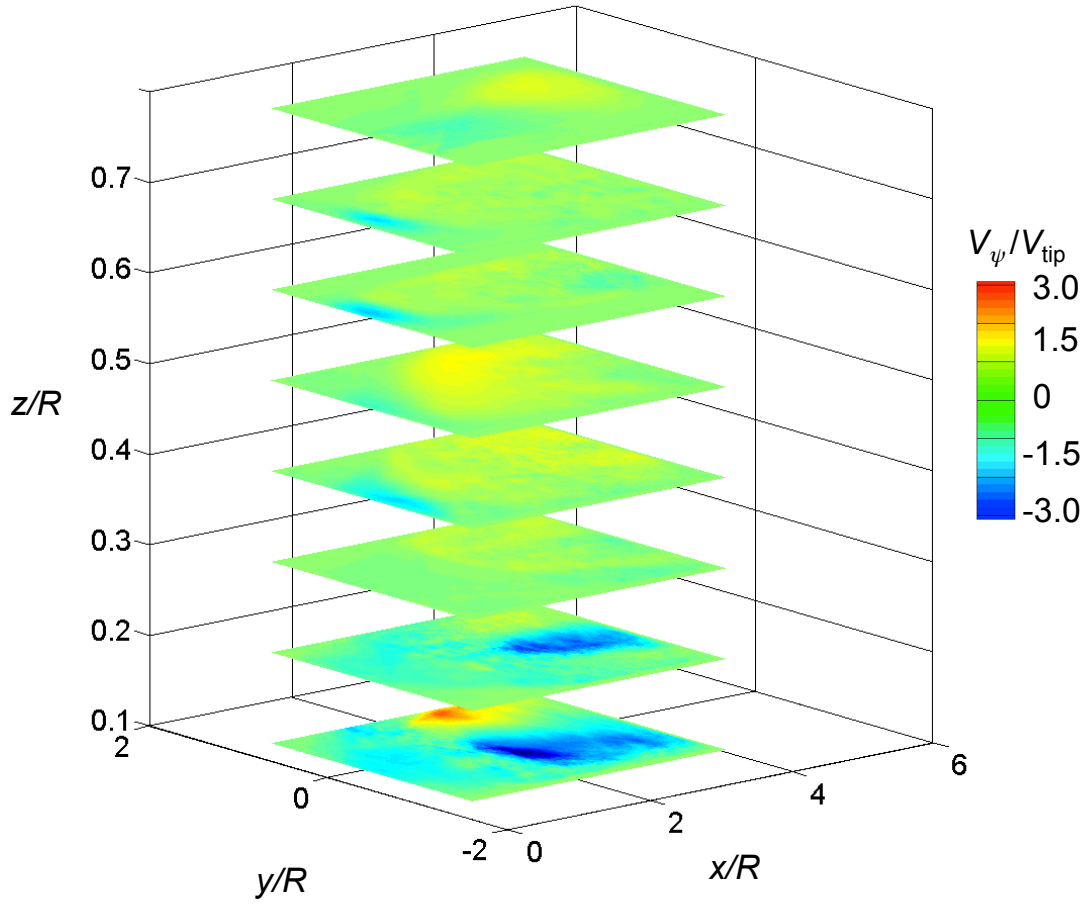

(c) Azimuthal velocity

Figure 3.51: (Concluded) Three-dimensional time-averaged particle velocities, (c) Azimuthal velocity.

The radial component of the particle velocities is shown in Fig. 3.51b. In this figure, red denotes an outward velocity (away from the rotor) while blue denotes an inward velocity. The results showed that the particle velocity field near the bed ($z/R = 0.1$–0.3) was dominated by the radial component of velocity, with the particles moving primarily outward. Recall from the single-phase flow results (Fig. 3.40), that the time-averaged velocities in the horizontal planes showed wave-like patterns in the carrier phase flow. These waves caused parts of the dust cloud to convect faster radially outward such that a discrete pattern was formed in the overall dust field.

At the higher planes ($z/R = 0.5$–0.8), the radial components of particle velocity shows that the inboard particles near the rotor were being reingested through the rotor disk, i.e., that the particles were being entrained in the downwash field produced by the rotor. These results confirm observations from previous studies [7, 26] that have shown that a rotor can reingest previously suspended sediment particles; reingestion occurs when particles are entrained in either the local downwash of a vortex flow or in the global downwash of the rotor. The consequence of this reingestion is that the particles bombard the bed with higher velocities and, as a consequence, will eject many more particles into the flow.

Figure 3.51c shows the azimuthal component of velocity, with blue being in the direction of blade rotation and red/yellow being opposite to the direction of rotation. Notice that near the bed ($z/R = 0.1$–0.2) the particles were convected in the direction of blade rotation. However, further from the bed the particle velocities were seen to be in the opposite direction. The significance of this observation is that the dust cloud was not simply a uniform field of particles that were moving up and toward the rotor but it was

comprised of more discrete and regular patterns, with the particles being uplifted and also swirling around the rotor. These results suggest that the three-dimensional velocities of the particles contained in dust clouds may create some sense of relative motion from the pilot's perspective, i.e., an illusion of aircraft motion where indeed there is none.

The time-averaged particle concentrations of the three-dimensional dust cloud are shown in Fig. 3.52. The particle concentrations were calculated by binning the particle locations over a two-dimensional grid. The number of particles in each bin were divided by the area of each bin to produce an effective particle concentration for each bin. It is important to note that the particle concentrations are being shown as area concentrations (i.e., particles/cm^2). It is important to note that while the particle concentrations are being shown as planar area concentrations (i.e., particles/cm^2), the light sheets had a finite thickness ($\approx$3 mm). Notice that the two lowest planes in Fig. 3.52 ($z/R = 0.1$ and 0.2) showed that, as expected, the highest concentration of particles were within the saltation layer along the bed. In the planes at $z/R = 0.3$–0.6, there were regular patterns observed in the cloud, as seen by the regions of relatively higher particle concentrations, although these concentrations were lower in magnitude than found near the bed. At $z/R = 0.7$ and 0.8, the particle concentrations were noted to increase further inboard because the particles were being reingested by the rotor.

In the vertical plane, waves of sediment were observed to form just upstream of the passing vortices (Fig. 3.41). These waves, however, are the vertical cross-sections of the three-dimensional particle plumes. The horizontal cross-sections of these plumes were also observed in the measurements. Figure 3.53 shows a sequence of images that indicate the formation and evolution of a dust plume in a horizontal plane at $z/R = 0.3$. As shown

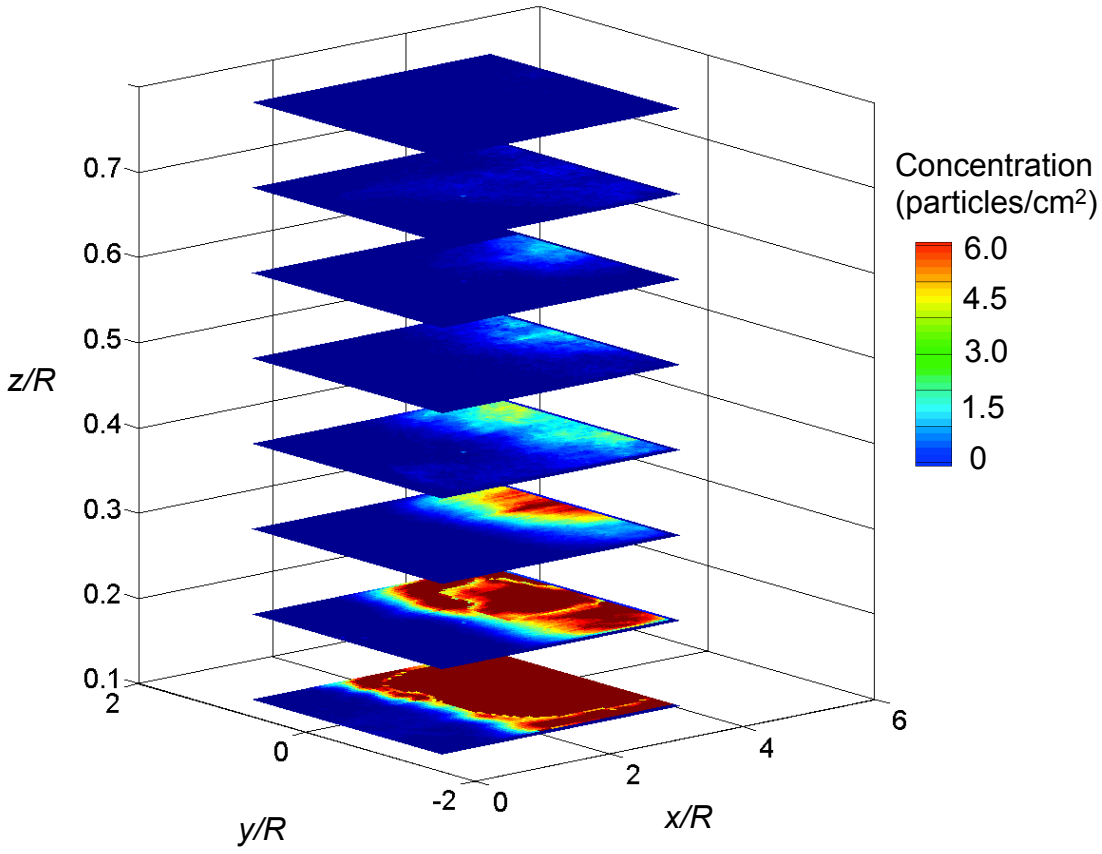

Figure 3.52: Three-dimensional time-averaged cloud particle concentration.

in Fig. 3.53a, a region is marked where there were relatively low particle concentrations. In the subsequent particle realization (Fig. 3.53b), the concentration of particles in the marked region increased rapidly because particles had entered the imaging region from below, which is likely because of adjacent vortices merging near the bed or because a part of a single vortex filament had convected closer to the bed. In the final particle realization (Fig. 3.53c), the particle concentration had rapidly increased in the marked region. In fact, local areas with relatively high particle concentration (i.e., plumes) were observed throughout the imaging plane.

Figure 3.54 shows a three-dimensional rendering of the instantaneous particle concentrations in horizontal planes ranging from $z/R = 0.2$–0.6. In each plane, the regions of relatively high particle concentration are marked. While the measurements in each plane were not simultaneously acquired, these planes are representative of the results obtained and show how the higher particle concentrations in each region are likely to form columnar, plume-like structures. The results suggest that these three-dimensional plumes are a fairly intermittent type of phenomenon that can occur anywhere throughout the flow.

The dual-phase results in the vertical plane showed that the height of the vortices off the bed significantly affected the concentration of uplifted sediment particles, and also the height to which they were uplifted. Furthermore, the merging of vortices was observed to uplift large quantities of particles. The single-phase results in the horizontal plane showed that each continuous vortex filament formed wave-like displacements as it convected along the bed, i.e., parts of the filament were closer to the bed than others. Furthermore, the non-uniform convection of the vortex filaments caused local parts of the filament to merge together. The local merging along with the wave-like disturbances in

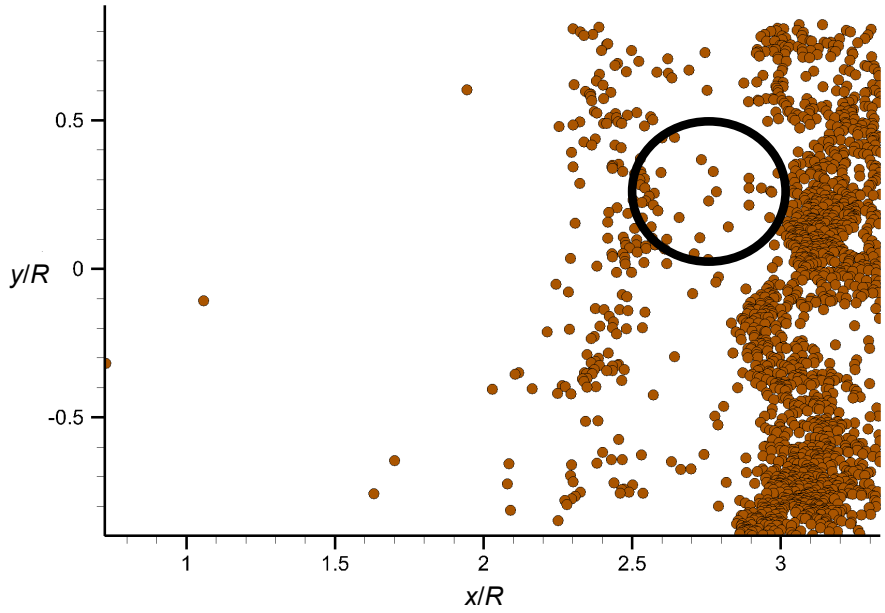

(a) Particle realization 1

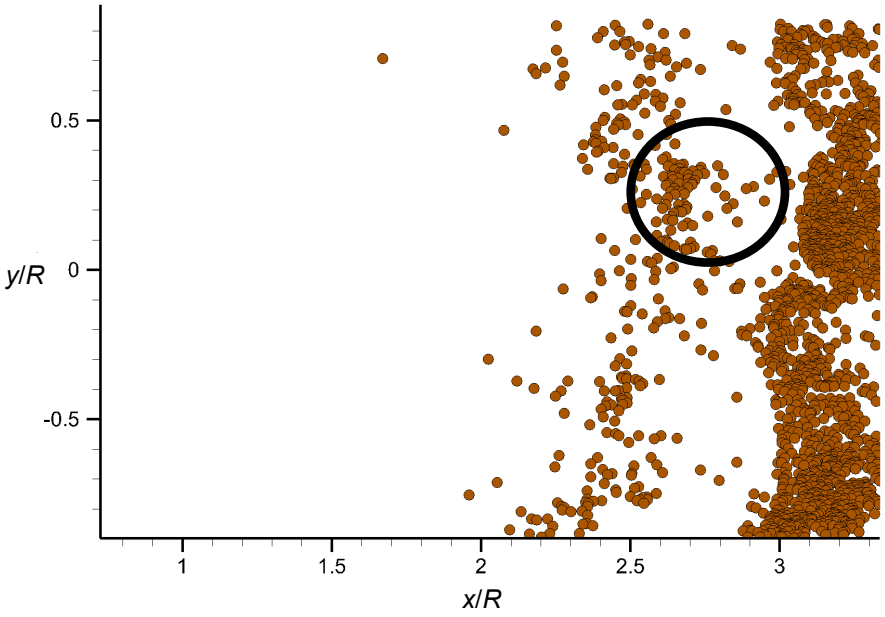

(b) Particle realization 2

Figure 3.53: Sequence of PTV realizations showing the formation of a particle plume as a horizontal cross-section at $z/R = 0.3$, (a) Particle realization 1, (b) Particle realization 2.

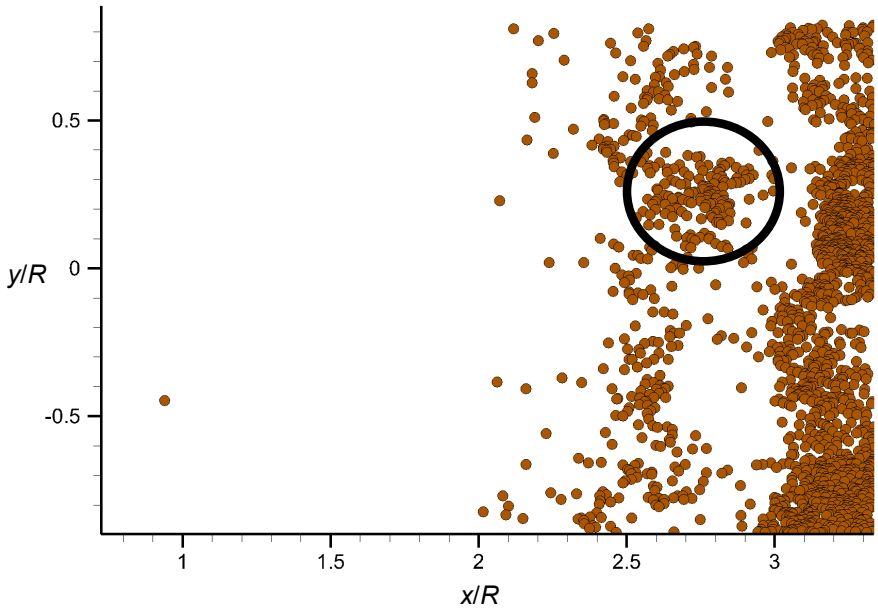

(c) Particle realization 3

Figure 3.53: PTV realizations showing the formation of a particle plume as a horizontal cross-section at $z/R = 0.3$, (c) Particle realization 3.

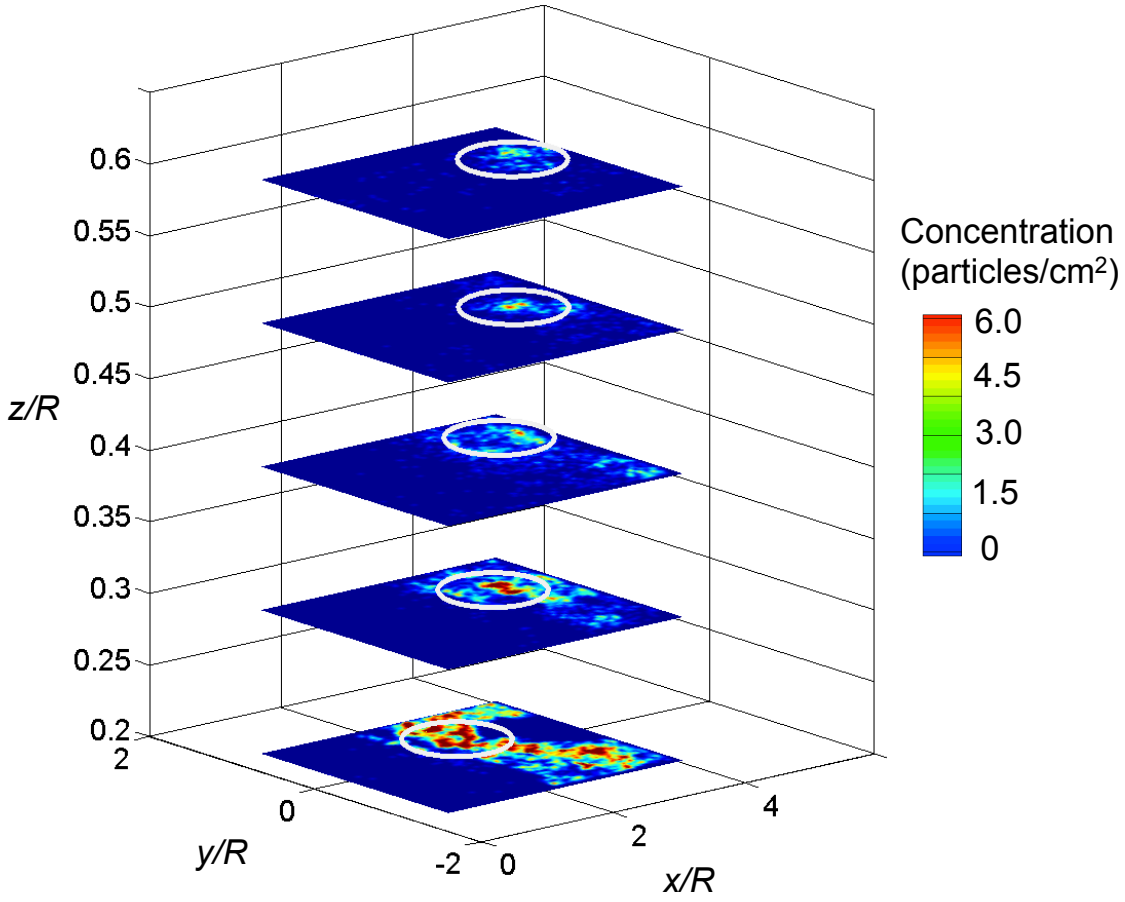

Figure 3.54: Three-dimensional instantaneous particle concentration showing a plume.

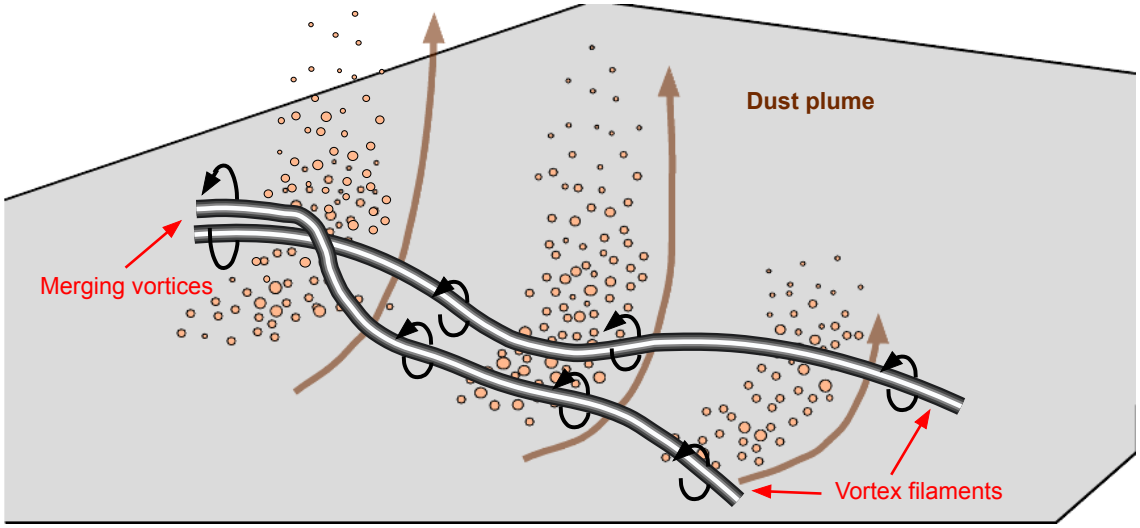

Figure 3.55: Schematic of plumes caused by waves in vortex filament.

the filaments were responsible for the local uplift events that created the vertical plumes in the dust cloud.

In summary, Fig. 3.55 shows a schematic interpretation of the wave-like formation and merging of vortices in the dual-phase flow environment. Without the waves in the filament and the merging of vortices, it is likely that the rotor-induced particle field would be more uniform in concentration and probably more axisymmetric in shape around the rotor. However, the local displacements of the vortex filaments and the aperiodic merging of vortices occur in space and time as the rotor wake develops, and so the resultant dust cloud is actually highly three-dimensional with discrete plume-like features. Clearly, for simulations to better capture the details observed in brownout clouds, it will be important to model the three-dimensional wave-like displacements of the vortex filaments and also the interactions between adjacent vortex filaments.

3.2 One-Bladed and Two-Bladed Rotors

This section describes the results from a study that compared the flows produced by the one-bladed and two-bladed rotors. Specifically, flow measurements were conducted to examine the effects that disk loading (DL), blade loading coefficient (C_T/σ), and wake shedding frequency (Ω_s) on the rotor wake developments and resultant dust particle field produced by each rotor. Experiments were first performed with both rotors operating at matching disk loadings, and then further experiments were performed with the rotors at matching blade loading coefficients. In all the cases, the rotors were operated at the same rotational frequency.

For the single-phase flow experiments, the work focused on understanding the structure and development of the tip vortices and the wall-jet that developed over the ground plane. For the dual-phase flow results, the quantity, concentration, and distribution of the uplifted particles produced by the rotor at different operating conditions were examined to assess the distribution and concentrations of particles that were uplifted and suspended near the rotor.

3.2.1 Single-Phase Flow Results

Understanding the interdependent effects of the rotor operating conditions on the flow features within the rotor wake was a prerequisite to understanding the corresponding dual-phase flow environment. The results shown in this section specifically address the wall-jet flow produced over the ground plane, the tip vortex structures and strengths produced by each of the rotors, and the overall structure of the rotor wakes.

3.2.1.1 Matched Disk Loading

Experiments were first conducted by matching the disk loading of the two rotors. Recall from Section 2.7.1 that the disk loading can be related to the average downwash of the rotor, w, by using outcomes from the simple momentum theory, i.e., $w = 2v_i = 2\sqrt{DL/2\rho}$. Therefore, matching the disk loadings for the one-bladed and two-bladed rotors should result in nominally the same distribution of flow velocities near the ground and probably also very similar velocity profiles.

In this set of experiments, the disk loading was matched by adjusting the pitch of the one-bladed rotor to produce the same thrust as the two-bladed rotor. The rotor thrust was measured using a balance. Because the one-bladed rotor had to produce the same thrust as the two-bladed rotor, each blade of the two-bladed rotor will carry half the thrust of the single blade used in the one-bladed rotor. As such, the one-bladed rotor will produce a vortex filament that is stronger (because of a higher value of C_T/σ) than the vortices produced by the two-bladed rotor. A more thorough discussion of the interdependent relationship between the disk loading and C_T/σ has been given previously in Section 2.7.1.

In this set of experiments, the DL was 0.039 lbft^{-2}, C_T/σ for the one-bladed rotor was 0.21, C_T/σ for the two-bladed rotor was 0.105, Ω_s for the one-bladed rotor was 377 rads^{-1}, and Ω_s for the two-bladed rotor was 745 rads^{-1}. These parameters are also given in Table 3.1.

Figure 3.56 shows the time-averaged velocity profiles that were produced at the ground plane by the one-bladed and two-bladed rotors, respectively. The blue vectors are the velocities for the one-bladed rotor and the red vectors are the velocities for the

Table 3.1: Operating parameters for one- and two-bladed rotor experiments at the same disk loading.

Number of Blades	**Disk Loading** (lbft^{-2})	C_T/σ	Ω_S (rads^{-1})
1	0.039	0.21	377
2	0 .039	0.105	745

two-bladed rotor. The results show that the velocity profiles produced by both rotors are very similar in shape and magnitude, perhaps an expected result when matching the rotor disk loadings. There were, however, some minor differences in the time-averaged flows in the near-wall region. For example, further inboard toward the rotor, the one-bladed rotor produced a slightly thicker wall-jet, with the thickness in this case being defined as the distance from the ground to the height of maximum velocity in the profile for any given downstream location. As the flow developed along the wall, the velocities began to decrease (i.e., conservation of mass in a radially expanding flow) and the downstream velocity profiles more closely matched each other.

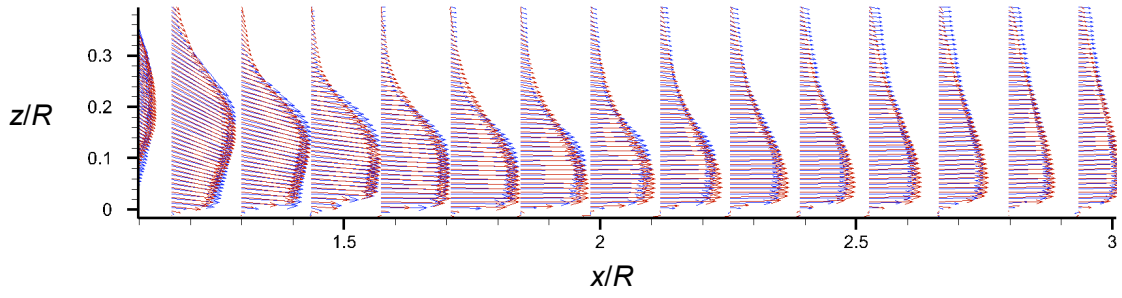

Figure 3.56: Time-averaged velocities near the ground for the one-bladed rotor (blue vectors) and two-bladed rotor (red vectors) operating at the same disk loading.

Keeping the disk loading constant, however, caused the vortex strengths of the one-bladed and two-bladed rotors to be different. To better highlight the vortical features in the flow, Fig. 3.57 shows a representative flow realization for each rotor at a blade azimuthal position of $\psi_b = 60^\circ$ with the background contours being of vorticity. The two-bladed rotor produces two trailed interdigitated vortices (Fig. 3.57a) while the one-bladed rotor produces just one trailed vortex (Fig. 3.57b). For both flow realizations, the circulation of the tip vortices, Γ_v, was calculated for the part of the vortex filament that had aged to $\zeta = 60^\circ$, this part of the vortex being marked in Fig. 3.57. The circulation was calculated using

$$\Gamma = \iint_A \omega_y \, dA$$

where A is the area of the vortex and ω_y is the vorticity contained within the vortex. A trapezoidal integration scheme was used to numerically calculate the integral from the discrete PIV measurements.

The circulation for the vortex in the two-bladed flow realization was found to be $\Gamma_{v2} = 0.103$ and the circulation for the vortex in the one-bladed flow realization was $\Gamma_{v1} = 0.201$. Therefore, the one-bladed rotor produces a vortex that is approximately twice as strong as the vortices produced by the two-bladed rotor, which also confirms what would be expected based on elementary theory.

To further investigate the differences in the flows produced by the one-bladed and two-bladed rotors, Fig. 3.58 shows the same flow realizations with background contours of velocity magnitude. Notice that the stronger one-bladed vortex showed larger regions of higher velocities, while the two-bladed rotor generated vortices that had lower ve-

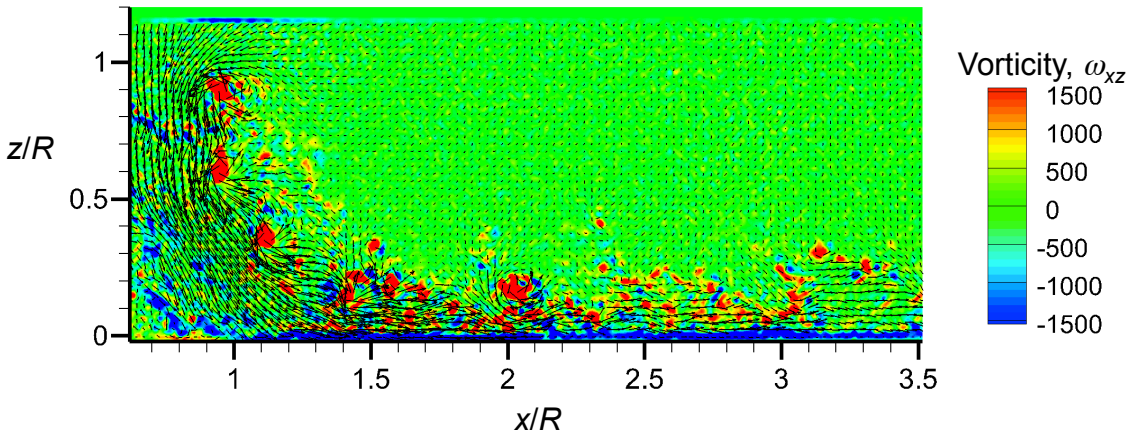

(a) Two-bladed rotor

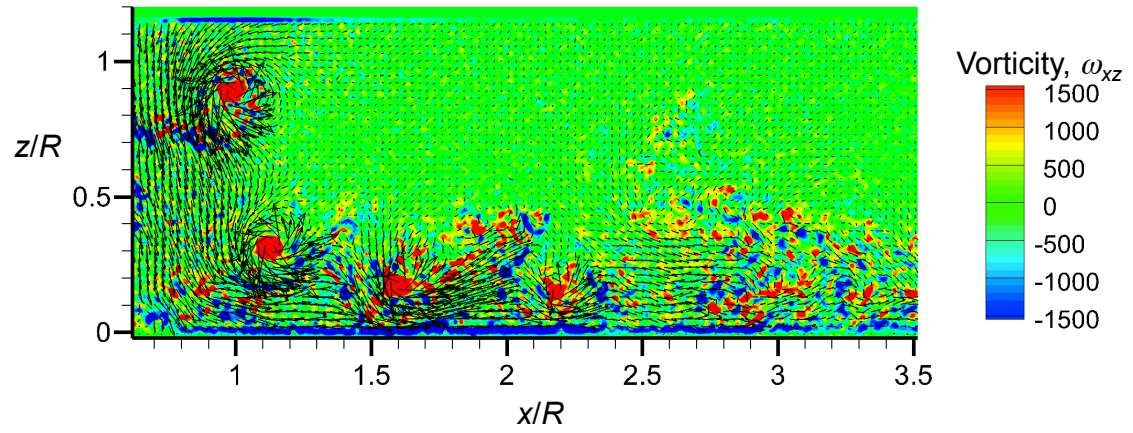

(b) One-bladed rotor

Figure 3.57: Instantaneous flow realizations shown as contours of vorticity comparing a.) two-bladed rotor, and b.) one-bladed rotor at a matched disk loading.

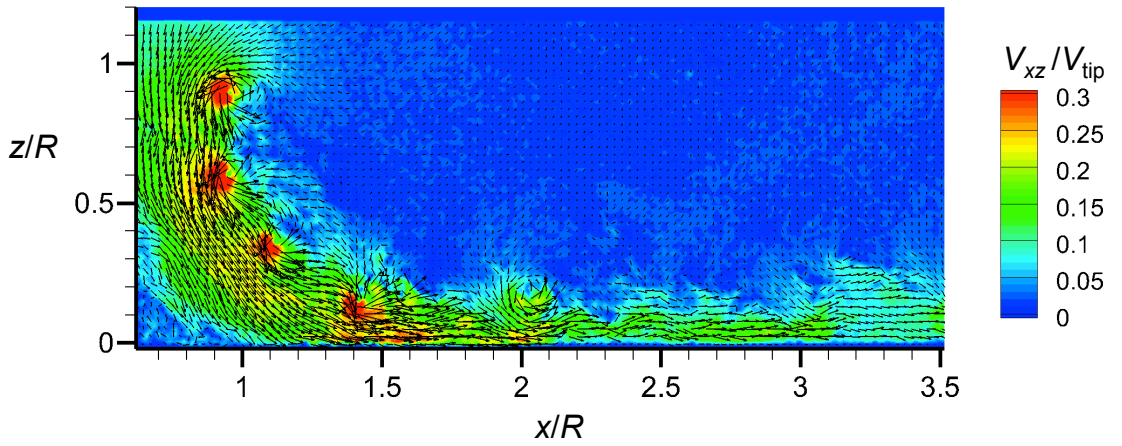

(a) Two-bladed rotor

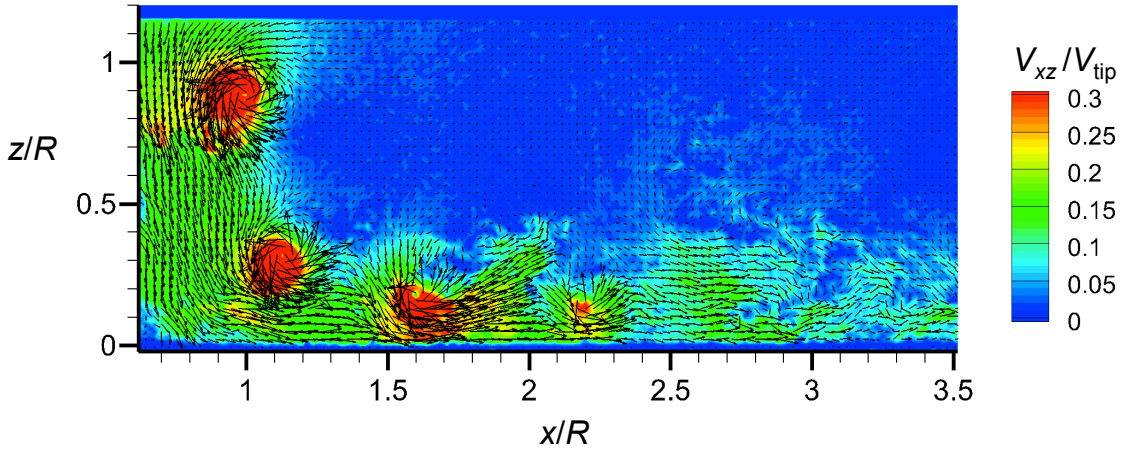

(b) One-bladed rotor

Figure 3.58: Instantaneous flow realizations shown as contours of total velocity comparing a.) two-bladed rotor, and b.) one-bladed rotor at a matched disk loading.

locities, although there were twice as many vortices present as for the one-bladed rotor. Therefore, it can be expected that each turn of the vortex produced by the one-bladed rotor will uplift more sediment locally, but the two-bladed rotor will cause more uplift events along the ground, but with each event uplifting fewer particles. The actual dual-phase flow environment produced by the rotors at these operating conditions will be discussed in detail later in Section 3.2.2.

It was also useful to examine any differences in the overall structure of the wake produced by the two rotor systems. Figure 3.59 shows the spatial location of each turn of the vortex filaments in ROI 1 over 90 rotor revolutions, these results providing a good representation of the wake boundary produced by each rotor. Notice that near the rotor plane, the wake for the two-bladed rotor contracted more than that of the one-bladed rotor. However, as the vortices convected towards the ground, the wake boundaries became more similar to each another.

3.2.1.2 Matched Blade Loading Coefficient

Experiments were also performed for matched blade loading coefficient between the two rotors. The blade loading coefficient can be related to the strength of the vortices by using Eq. 2.2 where the ideal value for k is 2 and in practice k is slightly greater than 2 [66]. In the present experiments, Ω, R, and c were held constant for both rotors. Therefore, matching the values of C_T/σ effectively matched the tip vortex strength produced by the one-bladed and two-bladed rotors. However, because the blade loading coefficient and the disk loading are interdependent parameters, matching C_T/σ gives different disk

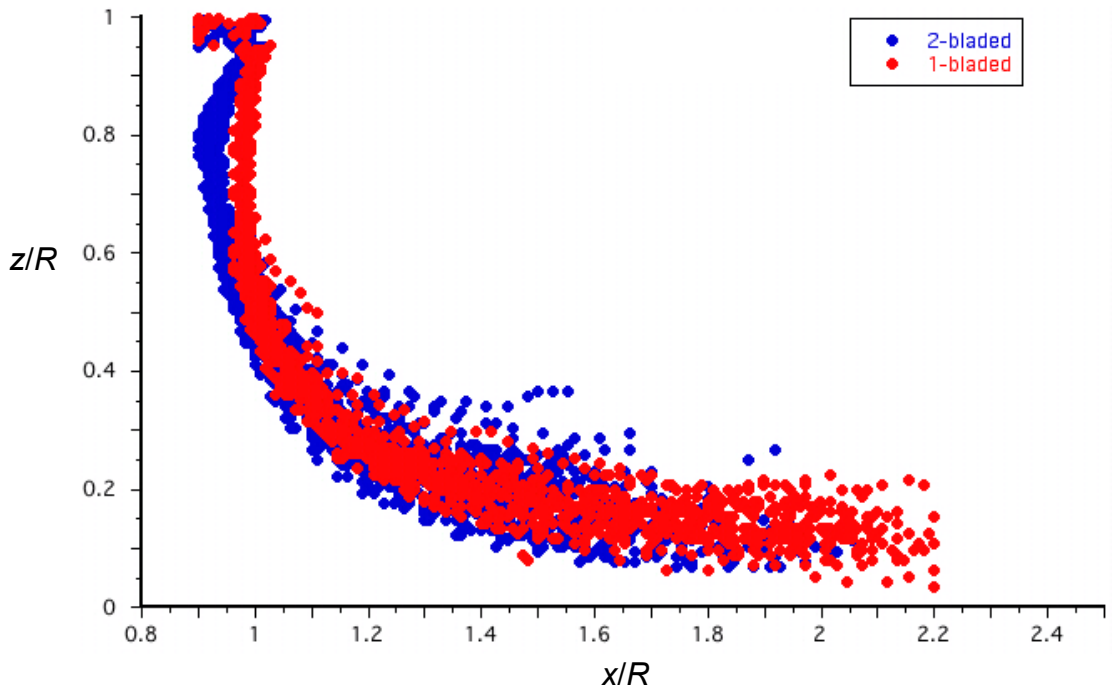

Figure 3.59: Wake boundaries at a matched disk loading shown as the locations of each turn of the vortex filaments over 90 rotor revolutions.

loadings for the two rotors, i.e., $DL_1 = (1/2)DL_2$. The simple momentum theory suggests that different disk loadings will result in different downwash (and groundwash) velocities between the one-bladed and two-bladed rotors (i.e., $w = 2\sqrt{DL/2\rho}$).

To match C_T/σ, the one-bladed rotor was operated at half the thrust of the two-bladed rotor, which was achieved by resetting the blade pitch. In this set of experiments, C_T/σ was 0.133, the DL for the one-bladed rotor was 0.24 lbft^{-2}, the DL for the two-bladed rotor was 0.49 lbft^{-2}, Ω_s for the one-bladed rotor was 377 rads^{-1}, and Ω_s for the two-bladed rotor was 745 rads^{-1}. These parameters are also given in Table 3.2.

Figure 3.60 shows the time-averaged velocity profiles produced over the ground plane by the one-bladed and two-bladed rotors, respectively. Because the downwash for

Table 3.2: Operating parameters for one- and two-bladed rotor experiments at the same blade loading coefficient.

Number of Blades	**Disk Loading** (lbft^{-2})	C_T/σ	Ω_S (rads^{-1})
1	0 .024	0.133	377
2	0 .049	0.133	745

each rotor was different, the averaged velocity profiles showed significant differences between the two rotors. On one had, the one-bladed rotor produced a downwash with lower velocities, which caused the wall-jet to have lower peak velocities at all downstream locations. On the other hand, the two-bladed rotor produced much higher velocities near the ground and also showed a thicker wall-jet.

The upshot of this observed behavior is that the two-bladed rotor produced steeper velocity gradients near the ground and so will likely reach the threshold wall shear required to mobilize particles closer to the rotor axis (i.e. further upstream than for the one-bladed rotor). Upon entrainment, however, the particles mobilized by the two-bladed

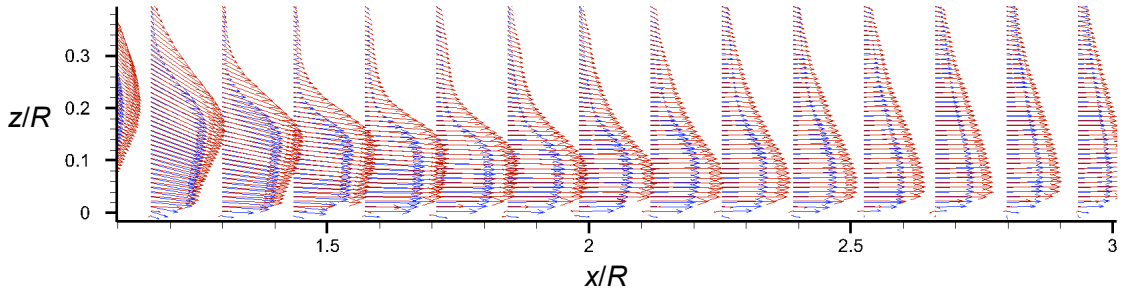

Figure 3.60: Time-averaged velocities near the ground for the one-bladed rotor (blue vectors) and two-bladed rotor (red vectors) operating at the same C_T/σ.

rotor will be susceptible to the relatively higher convection velocities from the surrounding flow. Further downstream, the results show that as the wall-jets produced by each rotor developed along the ground, their velocities were reduced as the flow expanded radially, and eventually any differences in the velocity profiles began to decrease. Again, the actual dual-phase flow environment produced under these conditions will be discussed in detail in Section 3.2.2.

To examine the differences in the vortical features within the rotor wake, the flow realizations from the two rotors are also shown as contours of vorticity in Fig. 3.61. Again, the two-bladed rotor produced twice the number of vortices as the one-bladed rotor, but in this case the tip vortices were nominally the same strength, these strengths being calculated using the PIV measurements. The circulation in the vortices for the two-bladed rotor case was $\Gamma_{v2} = 0.1799$ and the circulation for the vortex in the one-bladed flow realization was $\Gamma_{v1} = 0.1803$, i.e., very close to the same value and again confirming the validity of the basic theoretical relationship given in Eq. 2.2.

The consequence of having the same vortex strengths was that both rotors produced similar velocities wherever the imaging plane intersected the vortex filaments. This outcome is clearly seen in Fig. 3.62, which shows representative instantaneous flow realizations produced by the two rotors with background contours in this case being of total velocity. Notice, however, that the vortices produced by the two-bladed rotor appeared to persist to older wake ages, as is indicated by the relatively higher velocity regions further downstream. This outcome will have a significant effect on the uplift of sediment particles because particles can potentially be uplifted over a longer distances over the ground, potentially resulting in higher overall concentrations of particles in the dust cloud. Again,

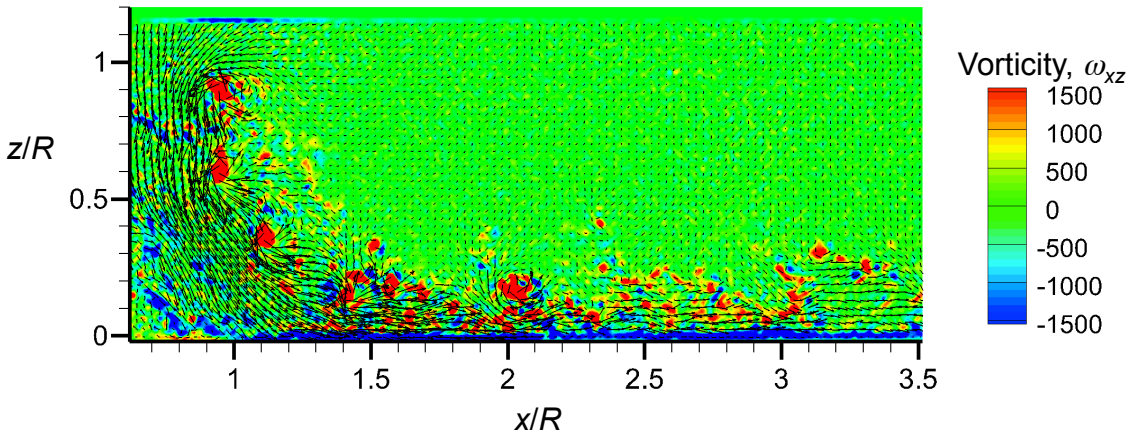

(a) Two-bladed rotor

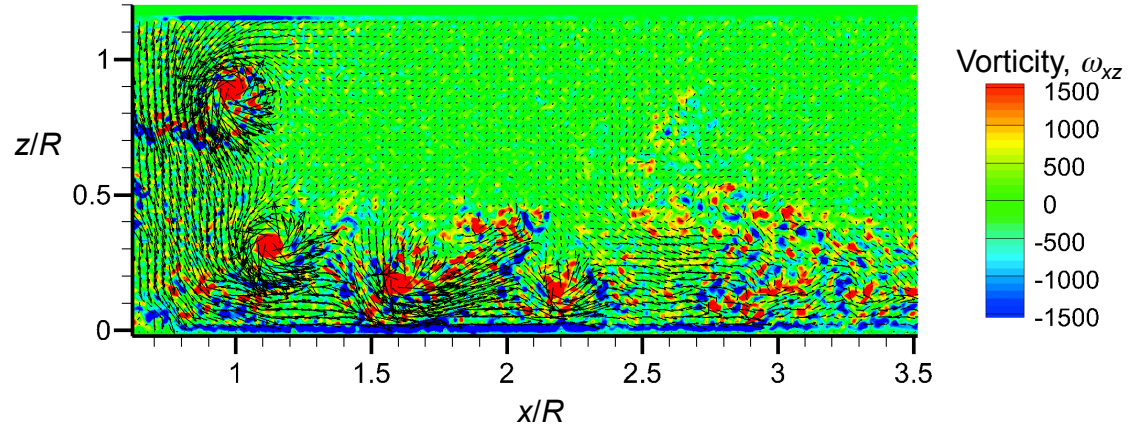

(b) One-bladed rotor

Figure 3.61: Instantaneous flow realizations shown as contours of vorticity comparing a.) two-bladed rotor, and b.) one-bladed rotor at a matched C_T/σ.

the actual dual-phase flow environment will be discussed in detail later in Section 3.2.2.

Matching the values of C_T/σ caused significant differences in the wake structures between the one-bladed and two-bladed rotors. Figure 3.63 shows instantaneous locations of each turn of the vortex filaments over 90 rotor revolutions for both rotors. The one-bladed rotor wake clearly contracted more than the two-bladed rotor wake. Furthermore, the vortices for the one-bladed rotor also convected closer to the ground and were observed to be more periodic than the vortices produced by the two-bladed rotor. Results shown previously (Fig. 3.46) showed that if a vortex convected closer to the ground it had the tendency to uplift more sediment particles. Furthermore, a higher wake frequency (i.e., more of the vortices reaching the ground per unit time) will increase the likelihood of particles within the saltation layer near the ground encountering an upwash region. Therefore, the combination of the different wake shedding frequencies and the different proximities of the vortices to the ground plane will likely cause unique particle fields for both the one-bladed and two-bladed rotors, a behavior that is discussed further in Section 3.2.2.

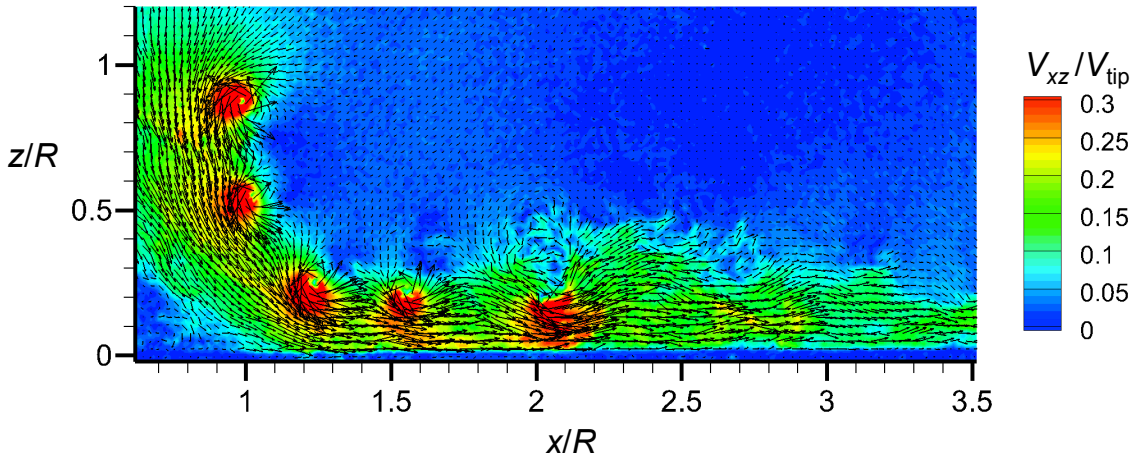

(a) Two-bladed rotor

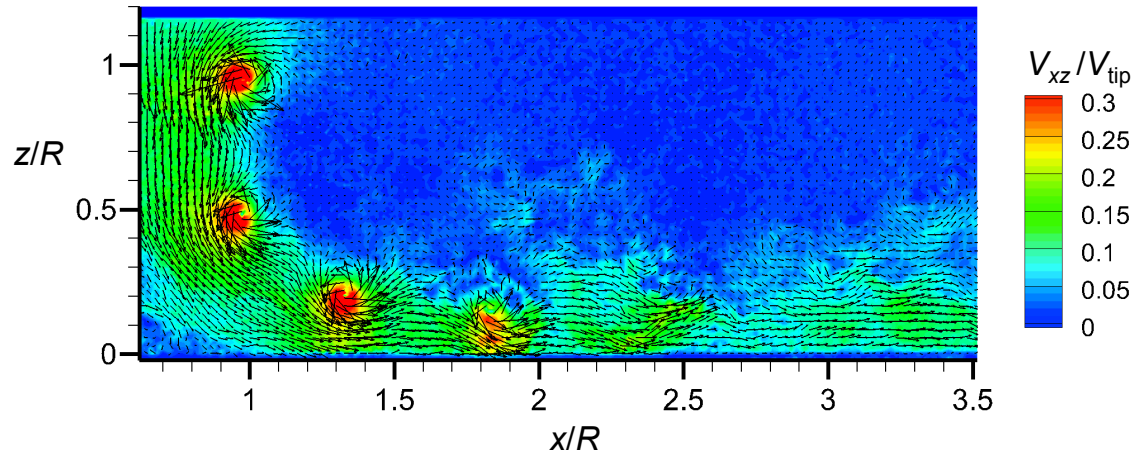

(b) One-bladed rotor

Figure 3.62: Instantaneous flow realizations shown as contours of total velocity comparing a.) two-bladed rotor, and b.) one-bladed rotor at a matched C_T/σ.

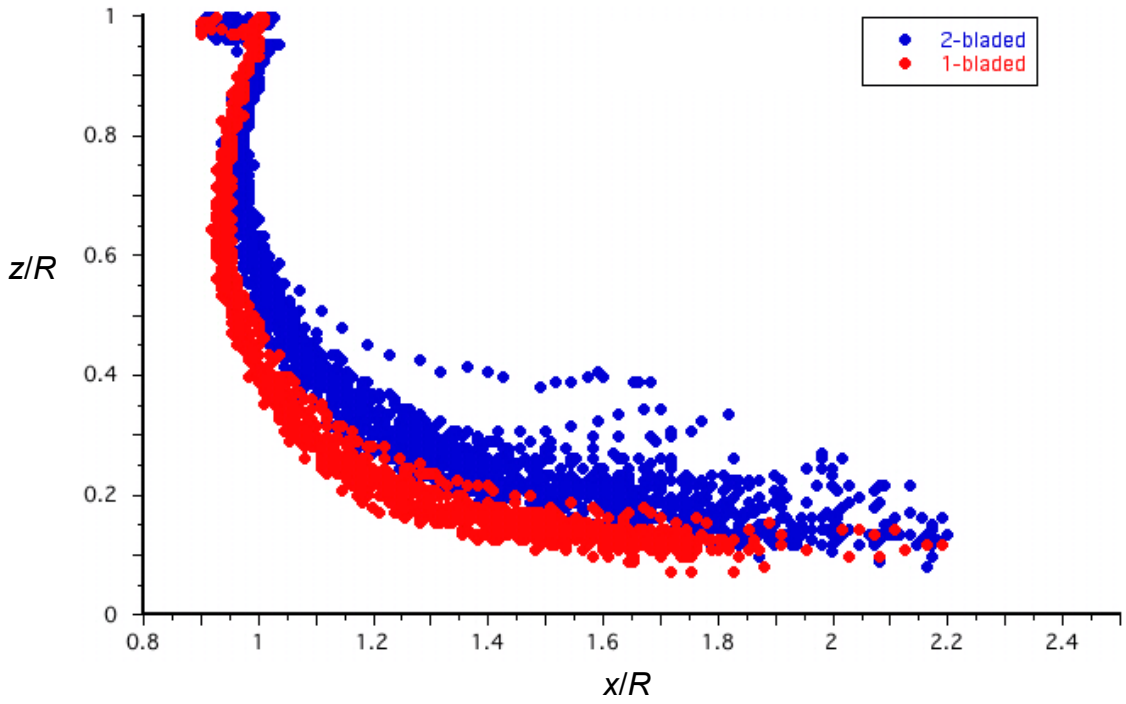

Figure 3.63: Wake boundaries at a matched C_T/σ shown as the locations of each turn of the vortex filaments over 90 rotor revolutions.

3.2.2 Dual-Phase Flow Results

The single-phase flow results discussed in Section 3.2.1 showed that the one-bladed and two-bladed rotors affected differently the near-wall flow environment, which is expected to also cause differences in the rotor wake-induced particle field. To characterize the effects of disk loading, blade loading coefficient, and wake shedding frequency (i.e., the frequency of the vortices passing over a given point on the ground) on the mobilization, entrainment, and transport of particles, dual-phase flow measurements using PIV and PTV were made with the one-bladed and two-bladed rotors operating over the mobile sediment bed. These results were then post-processed to examine the distribution of sediment particles relative to the ground and to the rotor, as well as the velocities of the airborne particles. The dual-phase measurements were also used to develop a set of metrics that could be used categorize the relative severity of the rotor-induced particle fields.

The severity of rotor-induced particle fields can be separated into four categories, namely 1. *Location of particles*: The size and overall geometry of the particle cloud, which dictates the overall distribution of particles around the rotor, and is useful in practice because it can be used as one measure of brownout severity. 2. *Particle velocities*: The movement of the particles, which explains exactly where the particles are moving to under the influence of the rotor wake, and is significant in practice because it can create relative motion effects or vection illusions for a pilot in brownout conditions. 3. *Particle concentration*: The concentration of particles around the rotor, which is important in practice because it can be related to the amount of light the dust cloud obscures in the

pilot's line of sight. 4. *Rate of development*: The rate at which particles are uplifted and suspended, which affects the time span over which the suspended particles accumulate around the rotor, and is important because in practice it can be a measure of how quickly brownout conditions will develop.

Therefore, to quantify the differences in the relatively severity of the particle fields produced by the rotors, this section discusses the results for the time-averaged particle velocity fields, the distribution of particles in the form of time-averaged particle field concentrations, and also gives a measure of the potential for optical obscuration caused by the particle field based on the concentration of particles in an assumed line of sight.

3.2.2.1 Matched Rotor Disk Loadings

Figure 3.64 shows time-averaged contours of the wall-parallel (u) component of particle velocities that are induced by the one-bladed and two-bladed rotors, respectively, when they are operating at the same value of disk loading. Recall from Section 3.2.1.1 that at this operating condition, the rotors produce nominally the same downwash velocities and the same near-wall flow velocities; see previously in Fig. 3.56. However, the results showed that the wall-parallel particle velocities induced by the two-bladed rotor were significantly higher when compared to those of the one-bladed rotor. While this result may seem counterintuitive, an explanation comes from the fact that the two-bladed rotor trails vortices toward the ground at twice the frequency of the one-bladed rotor (i.e., the two-bladed rotor has a higher wake shedding frequency). Because the mobilized particles are strongly influenced by the transient velocity field induced by the tip vortices as they

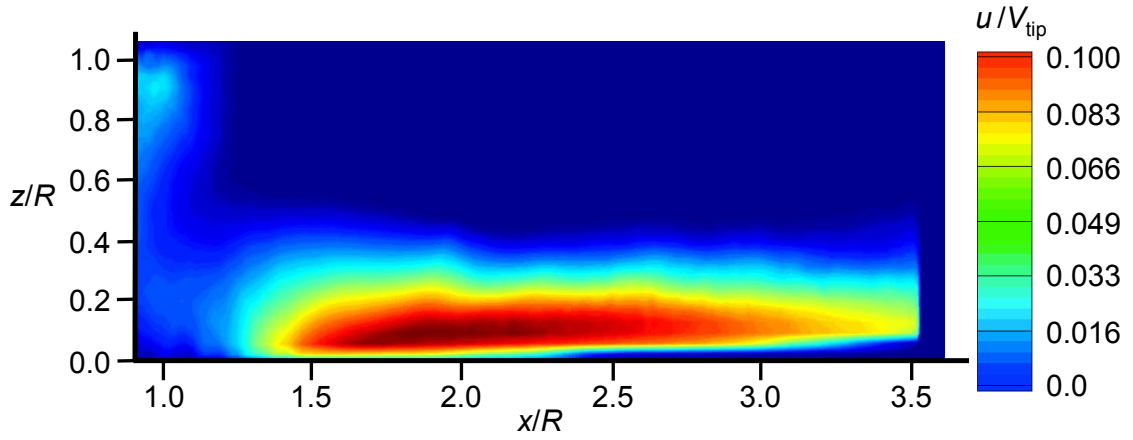

(a) Two-bladed rotor

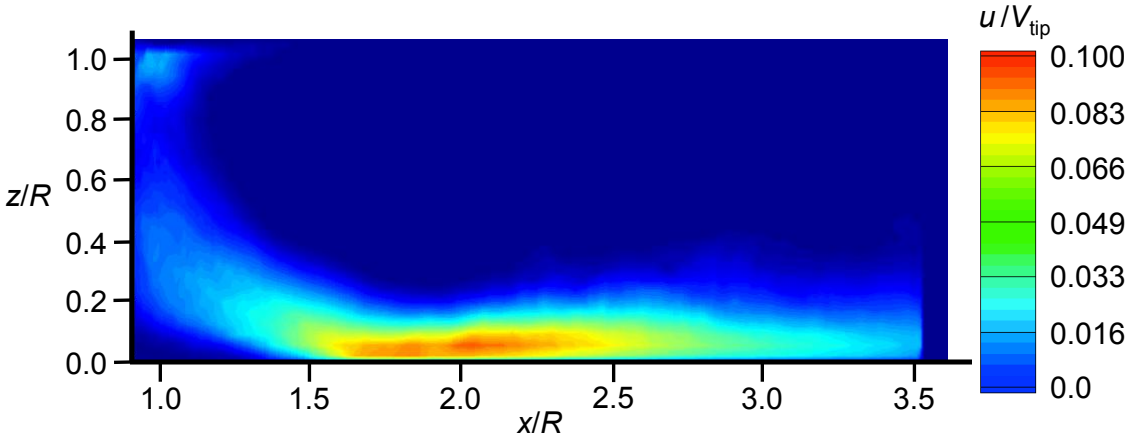

(b) One-bladed rotor

Figure 3.64: Time-averaged PTV measurements showing contours of wall-parallel (u) velocity for the a.) two-bladed rotor and b.) one-bladed rotor operating at the same disk loading.

approach the ground, the more frequent encounters with the tip vortices generated by the two-bladed rotor caused the particles to achieve relatively higher convection velocities than those that were mobilized by the one-bladed rotor.

Effects of the wake shedding frequency were also observed in the wall-normal (w) component of particle velocities, as shown in Fig. 3.65, where it can be seen that the vertical velocities induced by the two-bladed rotor are higher. This outcome is, again, because the particles mobilized by the two-bladed rotor more frequently encounter the vortex-induced velocity fields. The time-averaged particle velocity fields in both the wall-normal and wall-parallel directions clearly indicated that the wake shedding frequency had significantly affected the particle velocities near the ground.

The time-averaged particle concentrations produced by the one-bladed and two-bladed rotors is shown in Fig. 3.66. Of particular interest, is that even though the particle velocities induced by the two-bladed rotor were higher, the one-bladed rotor uplifted particles closer to the rotor, as indicated by the higher particle concentrations that were observed further upstream, i.e., compare Fig. 3.66a to Fig. 3.66b. There are two likely reasons for this latter outcome. The first is that the higher wall-parallel particle velocities induced by the two-bladed rotor caused particles to be convected further downstream before they could be uplifted into suspension. The second is that the one-bladed rotor produced stronger vortices with higher swirl velocities that uplifted greater quantities of particles in each uplift event. Therefore, the combined effect of the lower wall-parallel velocities and stronger vortex-induced upwash velocities from the one-bladed rotor caused particles to be uplifted closer to the rotor.

The combined effects of the particle concentration and the geometric shape of the

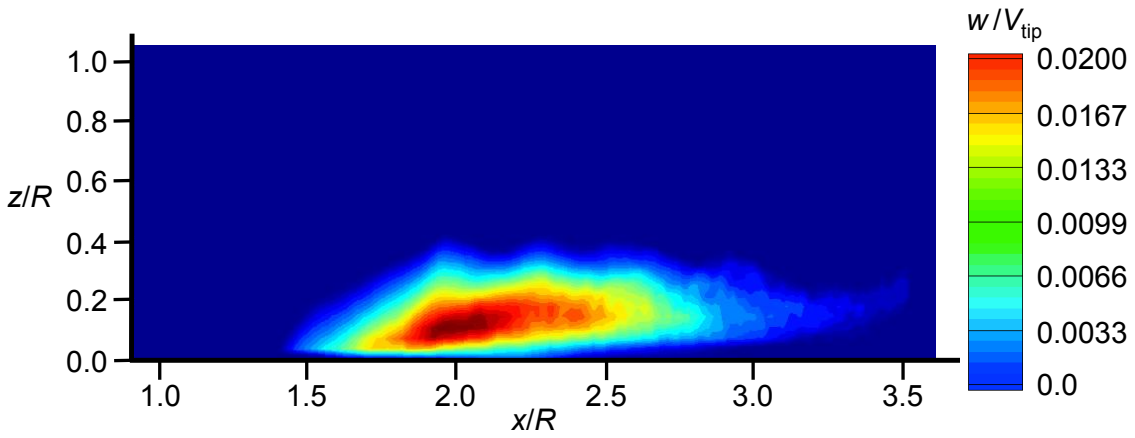

(a) Two-bladed rotor

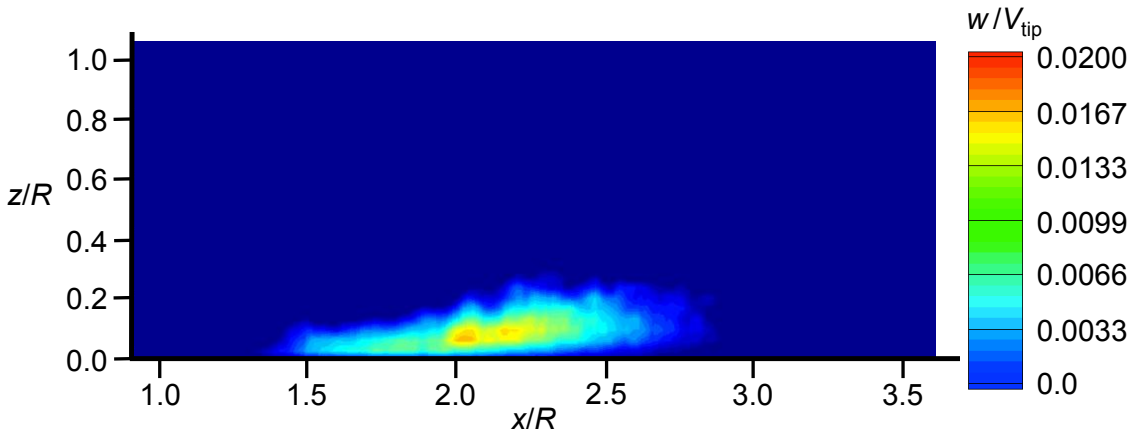

(b) One-bladed rotor

Figure 3.65: Time-averaged PTV measurements showing contours of wall-normal (w) velocity for the a.) two-bladed rotor and b.) one-bladed rotor operating at the same disk loading.

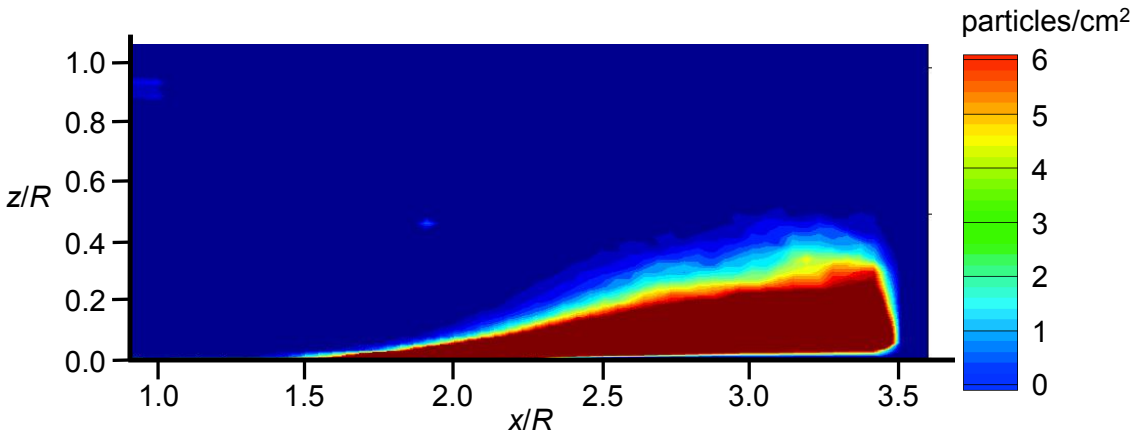

(a) Two-bladed rotor

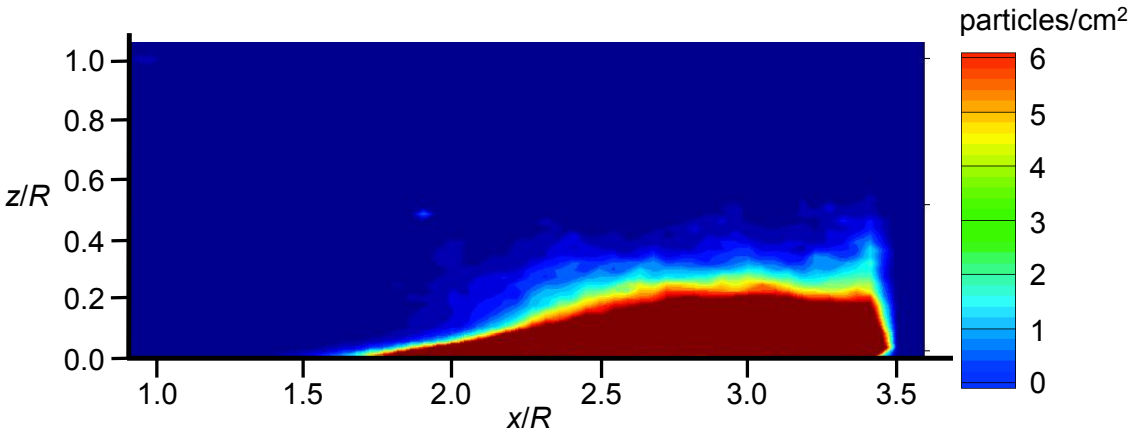

(b) One-bladed rotor

Figure 3.66: Time-averaged PTV measurements showing contours of particle concentration for the a.) two-bladed rotor and b.) one-bladed rotor operating at the same disk loading.

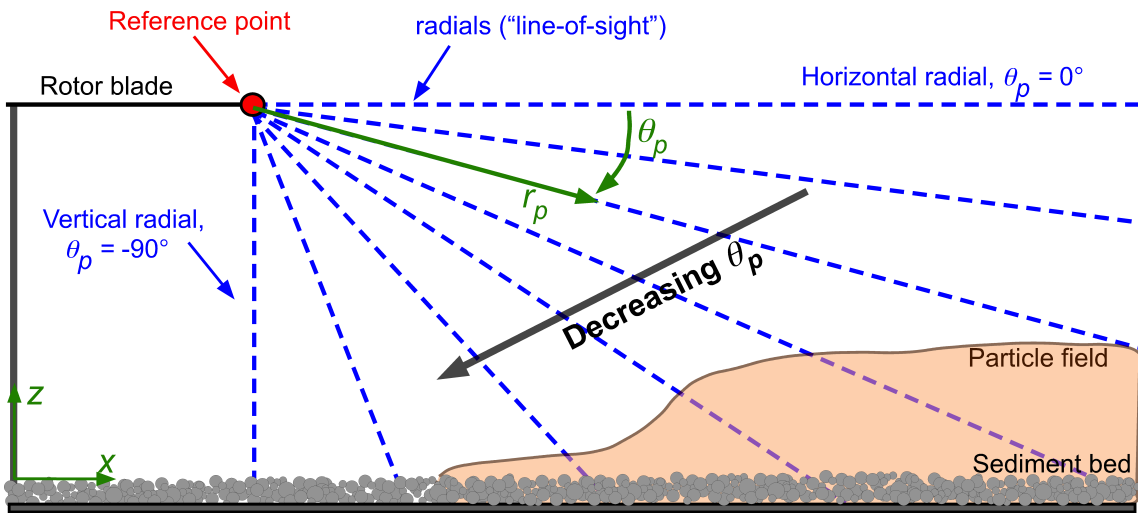

Figure 3.67: Schematic showing the polar coordinate system centered at the reference point at the rotor tip.

cloud will result in a unique obscuration along a given line of sight. In the present work, a method was developed to estimate the optical obscuration produced by each particle field based on the particle concentration within a certain field of view. For the time-averaged particle concentration maps developed for the one-bladed and two-bladed rotors, a single point was chosen as a point of reference. The Cartesian coordinate system (x,z) used for the measurements was then transformed to a polar coordinate system (r_p, θ_p) centered at the reference point; Fig. 3.67 shows a schematic of the coordinate systems and an explanation of the methodology used. In this case, r_p extends radially outward from the reference point and the "viewing" angle, θ_p, is the angle measured from a horizontal line passing through the reference point; θ_p is defined as positive in the counter-clockwise direction.

A measure of the "obscuration," O, of the particle field, was calculated by integrating the particle concentration along a radial (or line-of-sight) that passed through the

reference point, which provided a value at each angle; see Fig. 3.67. This calculation was performed by using

$$O = \int_{r_p} P(r_p, \theta_p)\, dr_p$$

where $P(r_p, \theta_p)$ is the particle count or concentration as a function of radial distance and viewing angle from the reference point. A trapezoidal integration scheme was used to calculate the integral from the concentration maps developed for each rotor. In practice, a reference point would normally be chosen as the location of the pilot's eyes because line-of-sight is most important from the pilot's point of view. However, because the present work is a more fundamental study of the flow physics involved in rotor-induced particle motion (i.e., without any pilot-induced effects), the reference point was chosen as the point where the blade tip passed through the imaging plane.

A comparison of the effective obscuration induced by the one-bladed and two-bladed rotors when operating at a matched disk loading is shown in Fig. 3.68; the vertical axis shows the obscuration level and the horizontal axis shows the angle from the horizontal, with $\theta_p = 0^\circ$ being the angle along the horizontal radial going through the reference point and θ_p =-90° being the angle along the radial going vertically through the reference point; see Fig. 3.67. Notice that the one-bladed rotor produced slightly higher levels of obscuration, but more importantly the higher obscurations were closer to the reference point. This outcome further supports that the relatively lower particle velocities induced by the one-bladed rotor, in combination with the stronger tip vortices, produced a particle field that would optically obscure regions of the ground that are closer to the rotor.

Examining the results in Fig. 3.68 in more detail show that for the two-bladed rotor

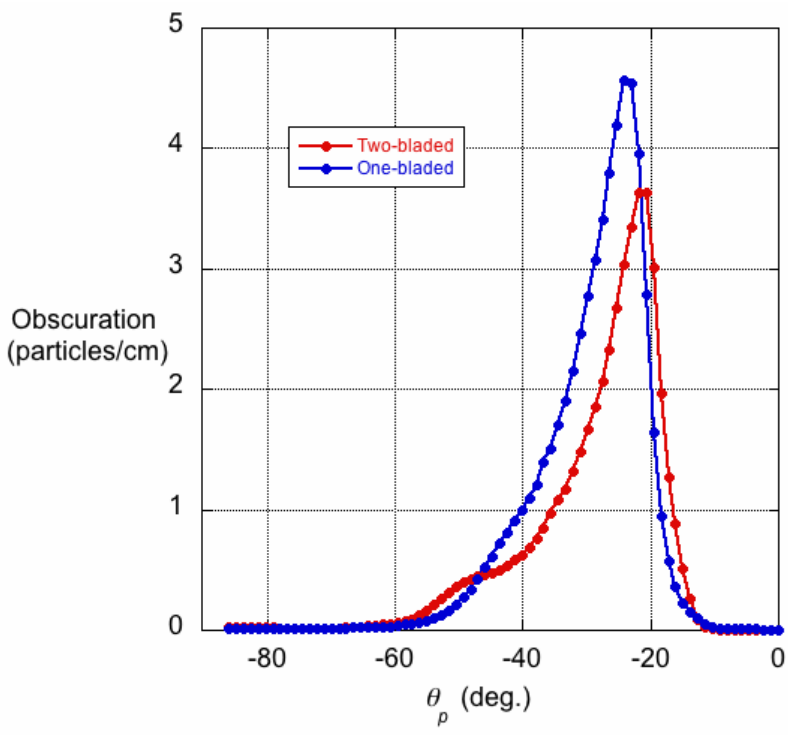

Figure 3.68: Plot showing the particle field obscuration as a function of line-of-sight angle, θ_p, for the one- and two-bladed rotors operating at the same disk loading.

there is a slight inflection point at approximately $\theta_p = 50°$, where the obscuration was slightly higher. This higher concentration of particles can be attributed to the higher wake shedding frequency of the two-bladed rotor. Because the two-bladed rotor caused vortices to impinge on the sediment bed at a twice the frequency of the one-bladed rotor, the particles under the two-bladed rotor were more likely to encounter a near-wall upwash flow causing an increase in particle concentrations in the zone where the vortices impinged on the ground.

3.2.2.2 Matched Blade Loading Coefficients

Figure 3.69 shows the time-averaged contours of the wall-parallel particle velocities that were induced by the one-bladed and two-bladed rotors when they were operating at the same blade loading coefficient. Recall that this operating condition caused both rotors to produce tip vortices of nominally the same strength; see Section 3.2.1.2 . The rotor-induced particle velocities are clearly very different, with the two-bladed rotor convecting particles radially outward significantly faster compared to the particles mobilized by the one-bladed rotor. This is an expected outcome based on the single-phase flow measurements (see Fig. 3.60), which showed that the two-bladed rotor produced much higher wall-parallel flow velocities.

The time-averaged wall-normal particle velocities induced by the one-bladed and two-bladed rotors operating at the same value of C_T/σ are shown in Fig. 3.70, with the two-bladed rotor, again, showing higher velocities. This outcome is because the two-bladed rotor produced twice as many vortices that convected past a point per unit time, even though both rotors produced vortices of nominally the same strength, and so the particles in the saltation layer were more likely to encounter an upwash region. Therefore, the time-averaged wall-normal particle velocities induced by the two-bladed rotor were significantly higher.

The time-averaged particle concentrations revealed further differences between the particle fields induced by the one-bladed and two-bladed rotors; see Fig. 3.71. The two-bladed rotor clearly uplifted more sediment particles to greater heights and also showed higher concentrations of particles throughout the near-wall region. This outcome is some-

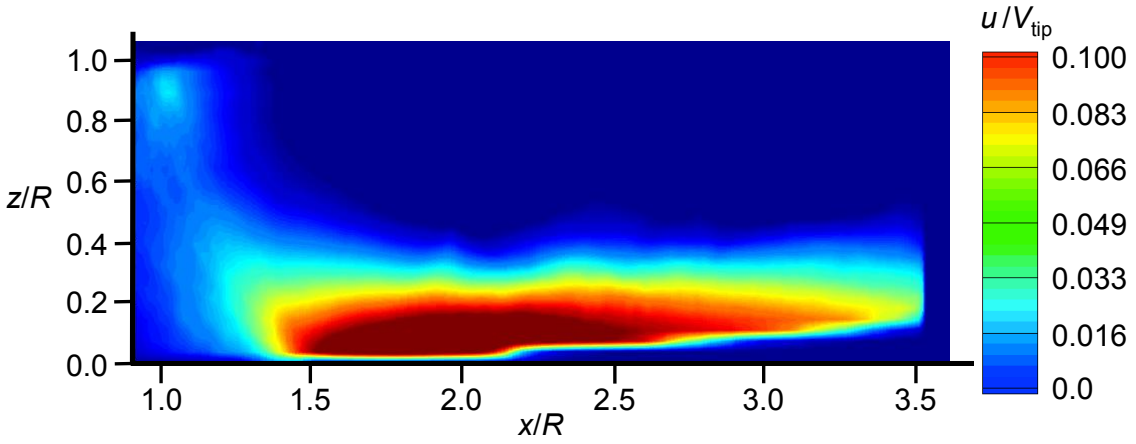

(a) Two-bladed rotor

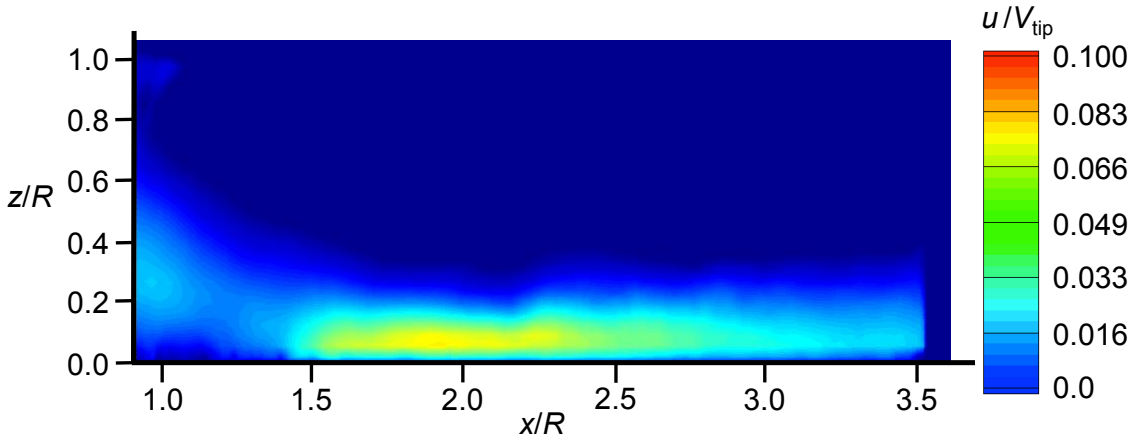

(b) One-bladed rotor

Figure 3.69: Time-averaged PTV measurements showing contours of wall-parallel (u) velocity for the a.) two-bladed rotor and b.) one-bladed rotor operating at the same value of C_T/σ.

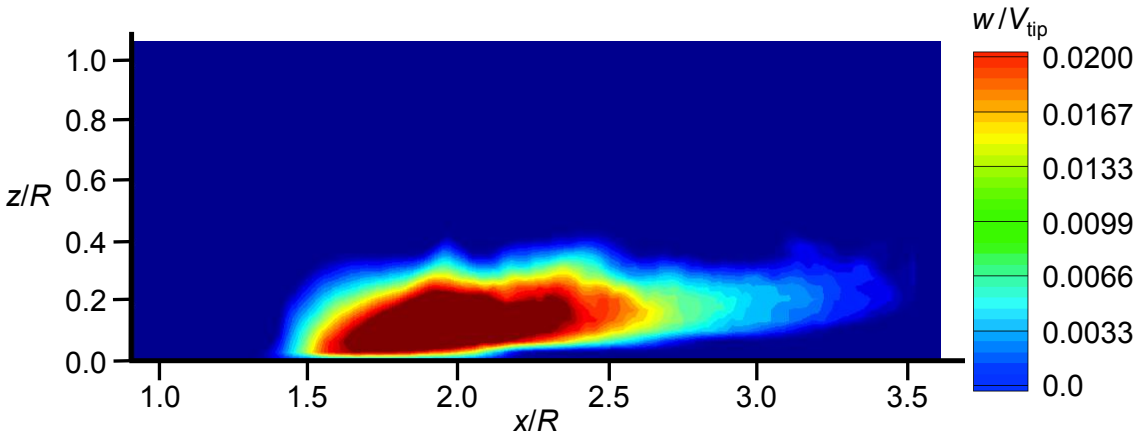

(a) Two-bladed rotor

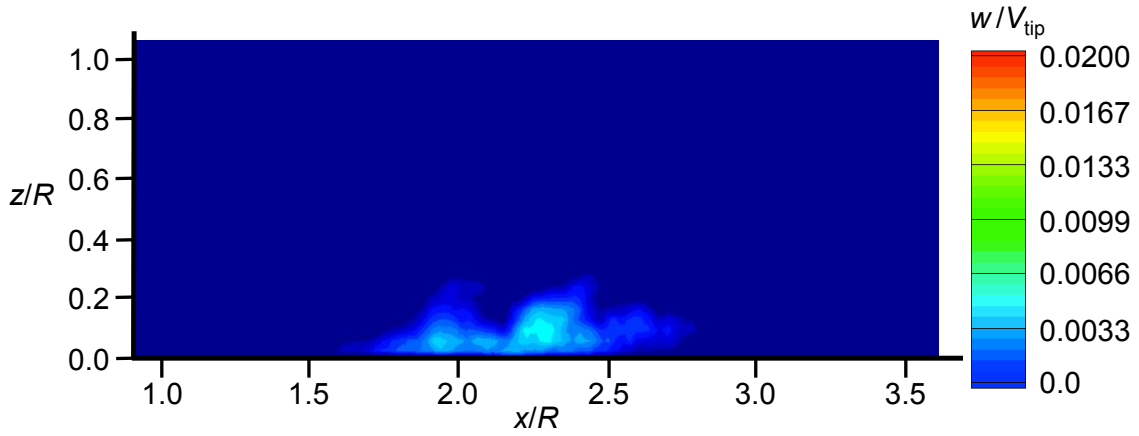

(b) One-bladed rotor

Figure 3.70: Time-averaged PTV measurements showing contours of wall-normal (w) velocity for the a.) two-bladed rotor and b.) one-bladed rotor operating at the same value of C_T/σ.

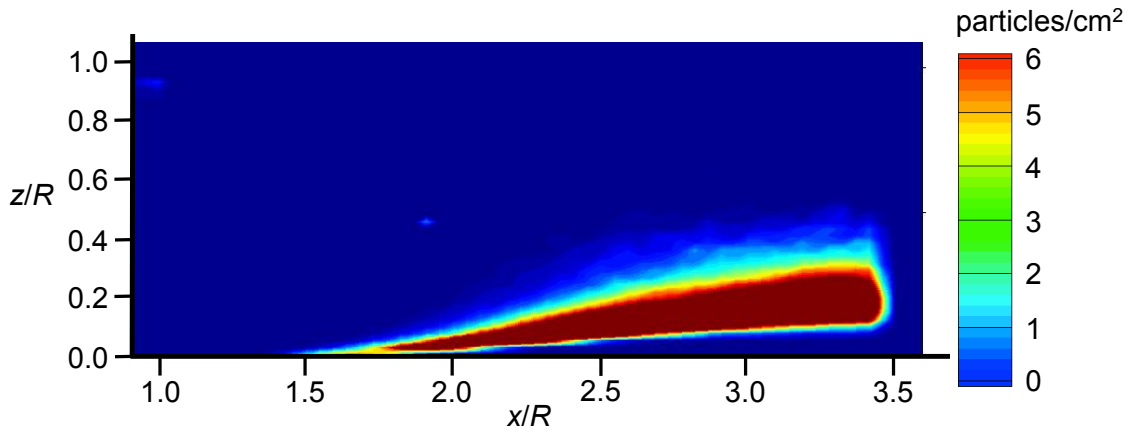

(a) Two-bladed rotor

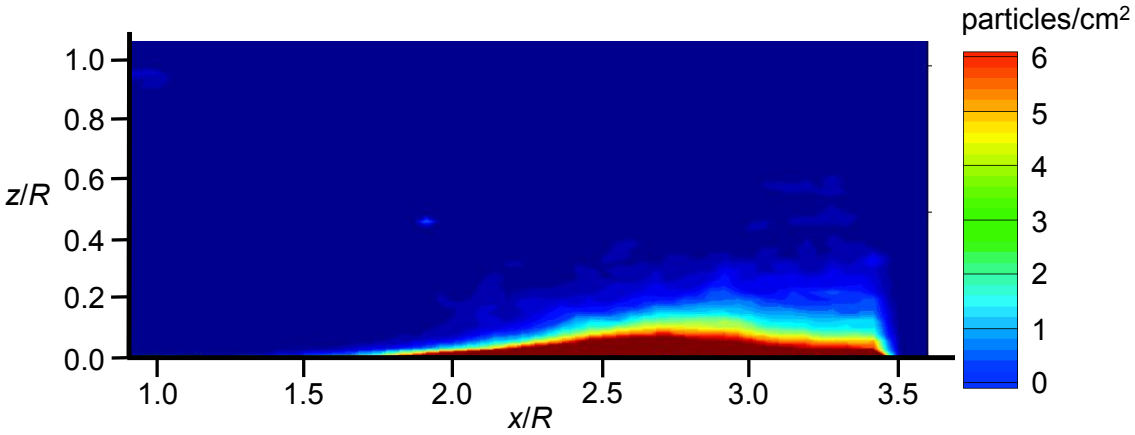

(b) One-bladed rotor

Figure 3.71: Time-averaged PTV measurements showing contours of particle concentration for the a.) two-bladed rotor and b.) one-bladed rotor operating at the same value of C_T/σ.

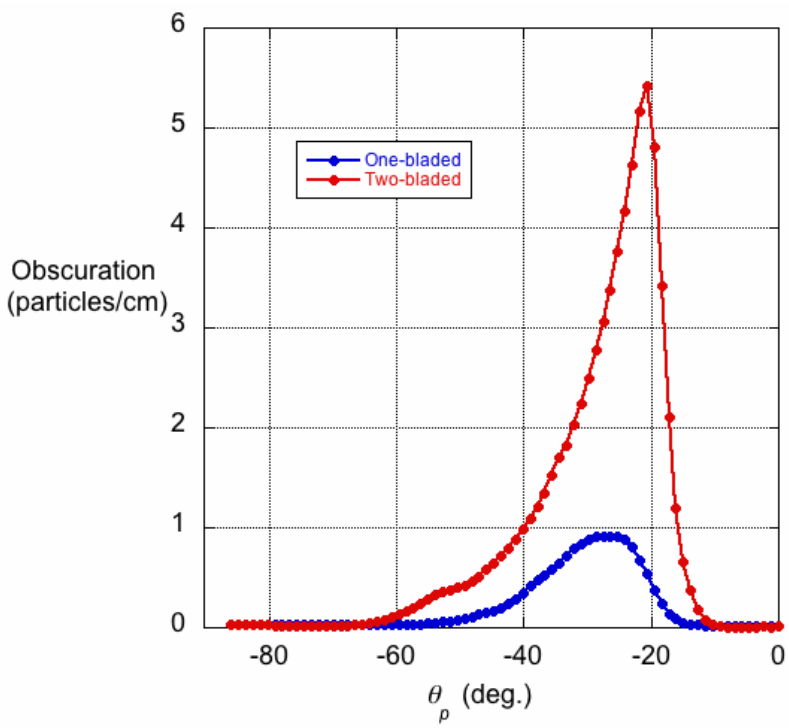

Figure 3.72: Plot showing the particle field obscuration as a function of line-of-sight angle, θ_p, for the one- and two-bladed rotors operating at the same value of C_T/σ.

what counterintuitive when compared to the matched disk loading results (Fig. 3.66), which showed that the higher radial velocities produced by the two-bladed rotor caused the particles to be convected further downstream before being uplifted.

Further detail is revealed by comparing the effective obscuration induced by the one-bladed and two-bladed rotors operating at the same value of C_T/σ; see Fig. 3.72. The two-bladed rotor clearly uplifted more particles and obscured the near-wall region more than the one-bladed rotor. However, the peak obscuration produced by the one-bladed rotor was located further inboard, as indicated by the maximum value of obscuration occurring at a steeper angle of $\theta_p = 28^\circ$. The peak obscuration produced by the two-bladed rotor occurred at $\theta_p = 21^\circ$ (i.e., a shallower viewing angle). This outcomes

shows that while the two-bladed rotor uplifted more particles and potentially would cause higher levels of obscuration, the particles were convected further downstream than the particles mobilized by the one-bladed rotor. This behavior suggests that for the same vortex strength, the number of vortices, and also the magnitude of velocities in the near-wall flow, play an important role in the mobilization of particles and their subsequent transport.

3.2.3 Summary

The results in this section have shown that the near-wall flow velocities, the strength of the rotor blade tip vortices, and the rate at which tip vortices impinged on the ground all (and interdependently) affected the evolution of the rotor wake and the resultant particle field. A higher value of rotor disk loading produces higher downwash velocities and higher near-wall flow velocities, which tends to intitially mobilize particles closer to the rotor while also convecting the particles further radially outward. The strength of the vortices as well as the wake shedding frequency both affected the radial and vertical transport of the particles. The results show that the combination of lower wall-jet velocities with higher vortex strengths will most likely result in particles being suspended closer to the rotor.

3.3 Body Shapes

The present work has examined a number of the phenomena that can affect the development of the rotor wake and resulting dust cloud produced by an isolated rotor operating near the ground. However, in practice, rotorcraft also have a fuselage that can potentially affect the development of the rotor wake close to the rotor as well as near the ground. This section describes the alterations to the structure of the rotor wake and the flow conditions at the ground that were caused by the introduction of a body into the rotor wake flow. The results for the three different body shapes (circular, elliptical, and rectangular cross-sections) were then compared to those produced by the isolated rotor. For these experiments, the rotor was operated in its 2-bladed configuration with the rotor thrust set with the bodies present in the flow. The rotor had a rotational frequency, Ω, of 60 Hz and was set to a disk loading of 0.049 lbft^{-2} with a corresponding C_T of .02 and C_T/σ of 0.133.

3.3.1 Single-Phase Results

Results are first presented for the isolated rotor and for the three different body shapes in a single-phase flow environment. In this way, the effects of the bodies on the development of the rotor wake could be isolated from the effects caused by any uplifted sediment particles. The FV results are presented first, followed by the PIV results.

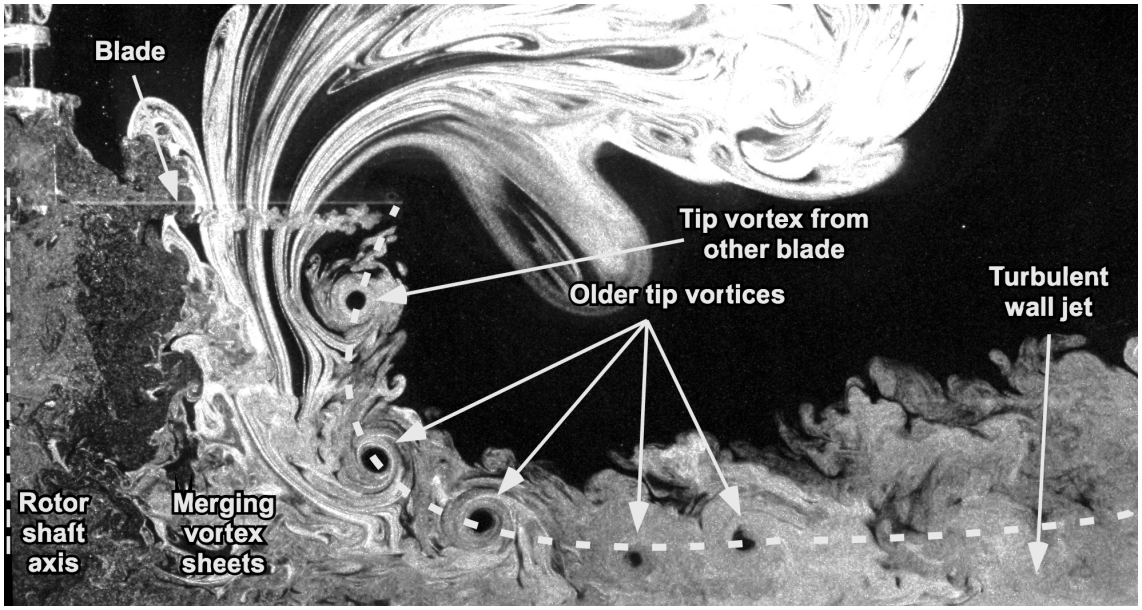

Figure 3.73: Flow visualization of a hovering rotor operating IGE at $z/R = 1.0$ above a ground plane.

3.3.1.1 Flow Visualization (FV)

FV experiments were conducted on the isolated rotor when it was operating over the ground plane, and also with the rotor operating above each body shape in turn. For the isolated rotor, the FV showed the presence of concentrated vorticity and turbulent eddies in the rotor wake; see Fig. 3.73. Each blade trailed a coherent tip vortex and wake sheet as it passed through the imaging plane, which were then convected toward the ground.

Figure 3.74 shows examples of the FV images with the circular, elliptical, and rectangular cross-sectional bodies in the flow below the rotor. The ROI encompassed the entire flow field such that the rotor, the nose and tail of the body, and the ground plane could all be observed together. The tip vortices were seen to convect by the nose of each body and were relatively unimpeded until they reached the ground, where they interacted

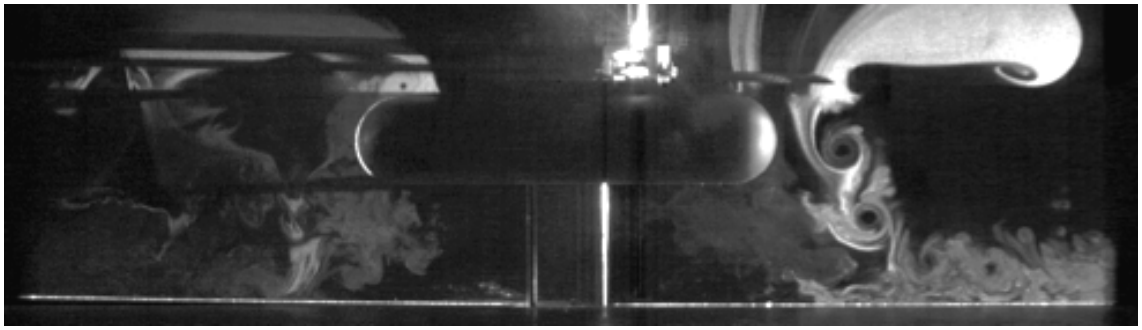

(a) Circular body

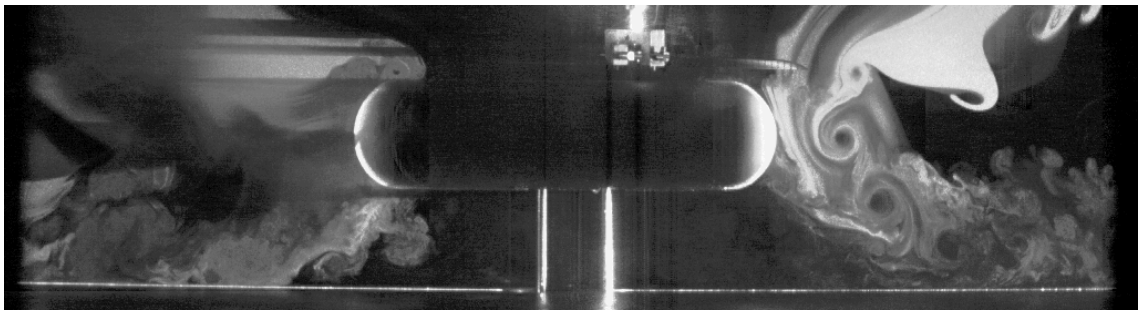

(b) Elliptical body

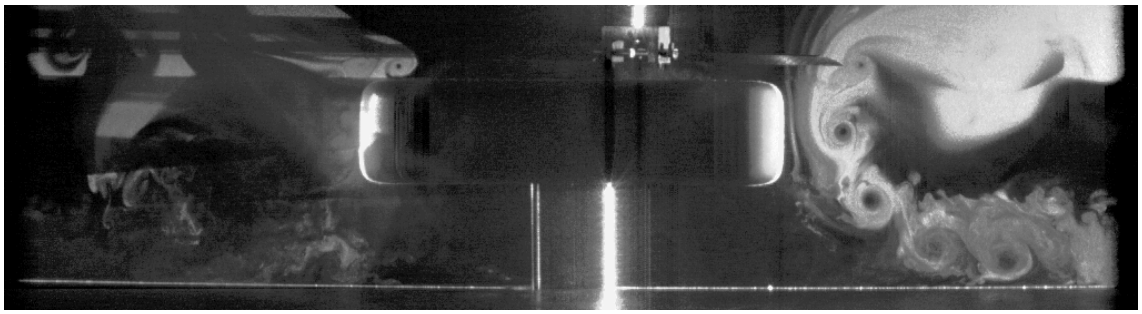

(c) Rectangular body

Figure 3.74: Flow visualization of the rotor wake developments with the bodies below the rotor.

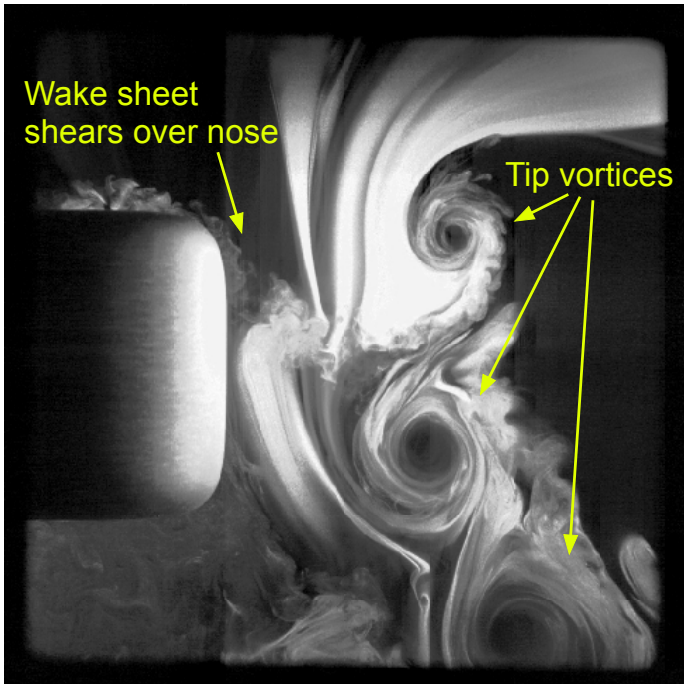

Figure 3.75: Flow visualization showing the interaction of the wake sheet with the nose of the rectangular body.

with the developing flow there in a manner similar to that seen with the isolated rotor. However, it can also be seen from Fig. 3.74 that the wake sheets from the blades did impinge on the upper surface of each body.

Further details of the fluid dynamics of this sheet impingement process are shown in Fig. 3.75 for the rectangular body shape. This interaction caused the wake sheet to distort significantly and undergo a shearing process in which the outboard portion of the wake sheet continued to convect downward, while the inboard section directly impinged on the body surface. It was noted that any vortical eddies in the sheet rapidly diffused when they impinged on the body surface, thereafter causing the downstream flow to become more turbulent.

It can also be seen from Fig. 3.74 that the flow at the tail section was more signif-

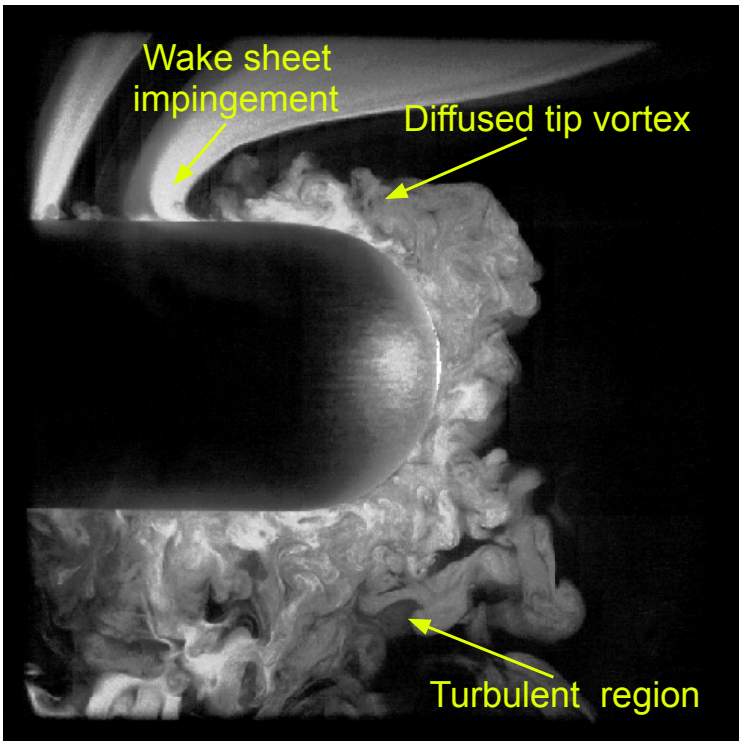

Figure 3.76: Flow visualization showing the interaction of the wake sheet and tip vortex with the tail of the circular body shape.

icantly altered by the presence of the body. In each case, the tip vortices interacted with the body at relatively young wake ages, directly impinging on the top of the body surface. In many cases, the vortices were then seen to stretch and burst, and so rapidly diffusing their vorticity. The FV, however, showed that there were still some remaining elements of the vortical flow at the ground that could be associated with the remnants of the blade tip vortices. In this case, the entire wake sheet directly impinged on the body surface and the vorticity it contained was quickly diffused.

Figure 3.76 shows more details of the interaction of the tip vortices and wake sheet with the tail section, in this case with the body with the circular cross-section. The rapid diffusion of the vorticity from the tip vortex core caused the formation of smaller eddies

that were then convected along the body surface. These eddies then followed the contour of the tail of the body, mixing with its surface boundary layer, and then combining with the large area of turbulent flow that was observed in the wake directly below the body, i.e., a bluff-body type wake. The numerous eddies observed in this region below the body were entrained into the rotor wake and were convected downstream toward the ground plane, thereby introducing a significant amount of additional turbulence into the near-wall flow region.

3.3.1.2 PIV at the Nose Region

The flows produced at the nose and tail regions of each of the bodies under the influence of the rotor wake were further examined by making time-resolved PIV measurements. Figure 3.77 shows contours of time-averaged total flow velocities near the nose region in ROI 2. These data were again ensemble averaged over 1,000 contiguous realizations of the flow. Recall that in this x-z plane, the total velocity, V_{xz}, is defined as $V_{xz} = \sqrt{u^2 + w^2}$, where u and w are the velocities in the x and z directions, respectively.

It was found that in the vicinity of the nose, all three of the bodies had relatively minor effects on the flow and little influence on the contraction or other development of the rotor wake, as can be seen by the location of the slipstream boundary for each case in Fig. 3.77. Flow separation from the surface of the circular and elliptical bodies occurred at $z/R \approx 0.7$, which was about half way down the nose of each body near the longitudinal centerline. This flow separation likely occurred because of an adverse pressure gradient that formed on the surface of the bodies near this point. For the rectangular body shape,

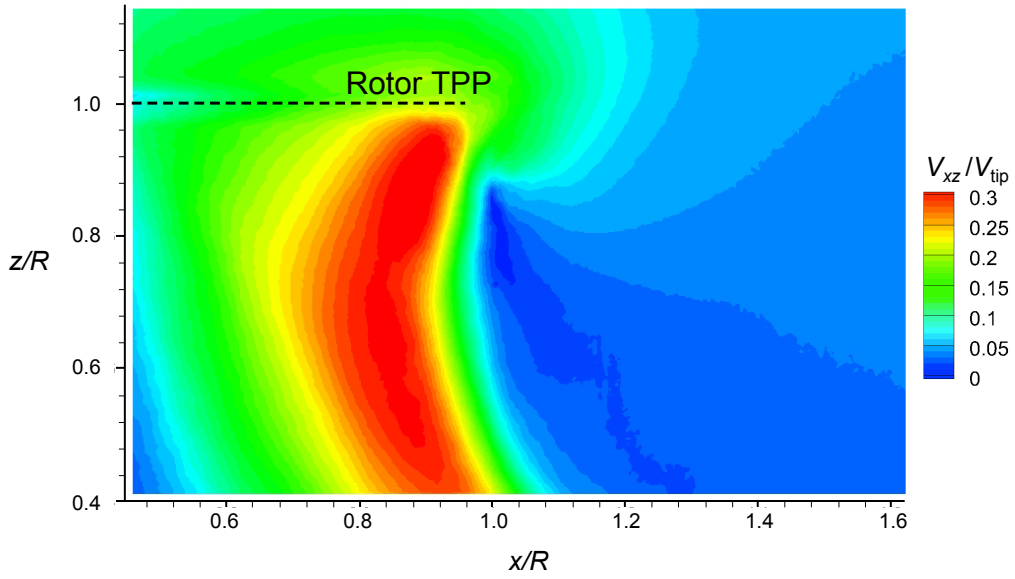

(a) Isolated rotor

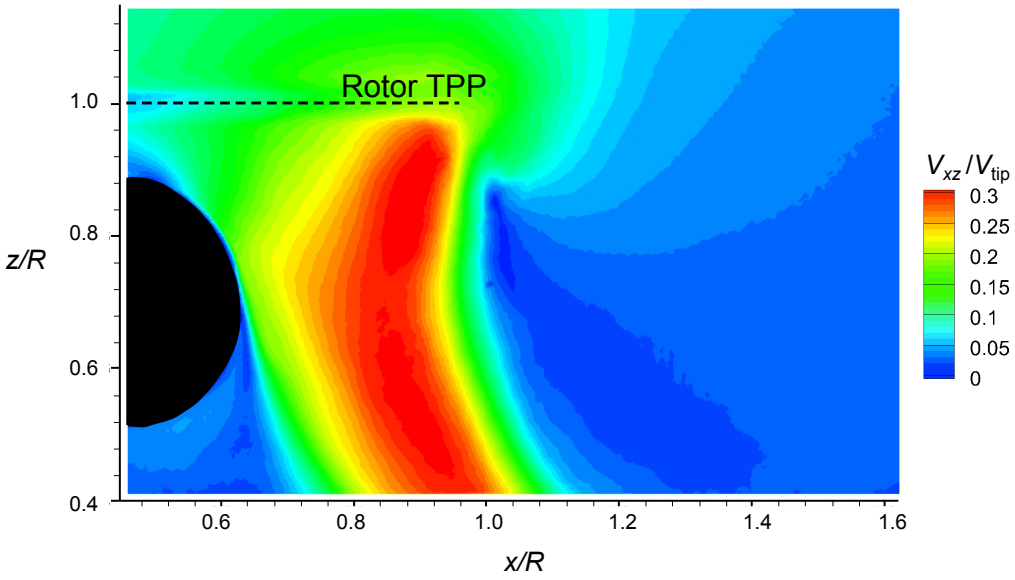

(b) Circular body

Figure 3.77: Time-averaged total velocity showing the interaction between the rotor wake development for the isolated rotor and around the nose of each body.

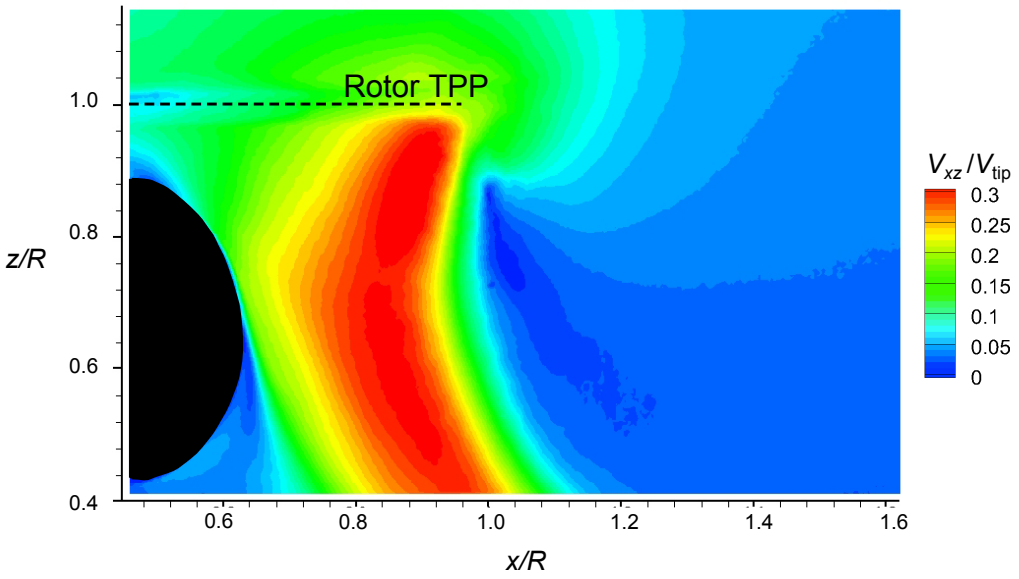

(c) Elliptical body

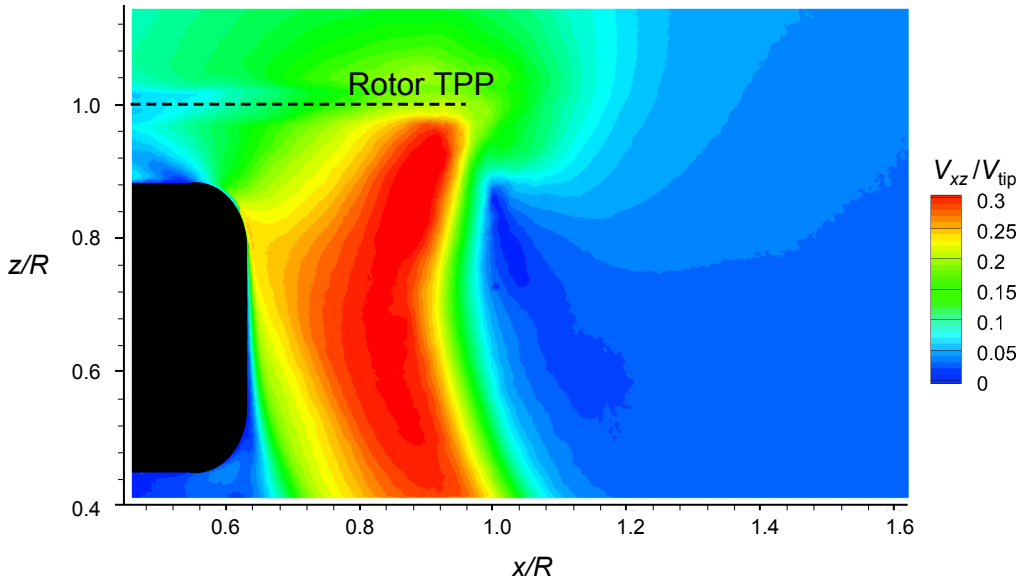

(d) Rectangular body

Figure 3.77: (Concluded) Time-averaged total velocity showing the interaction between the rotor wake development for the isolated rotor and around the nose of each body.

the flow remained attached to the surface to considerably longer downstream distances, until $z/R \approx 0.6$, i.e., almost the entire length of the nose cap.

While the time-averaged flow measurements showed the general nature of the flow as the rotor wake interacted with the body, the instantaneous PIV realizations quantified the detailed flow interactions. For example, Fig. 3.78 shows a sequence of instantaneous contours of vorticity in ROI 2 with the circular body shape; these results are representative of what was produced for all three bodies. The tip vortices, which are identified by the concentrated (red) regions of vorticity, appeared to be mostly unaffected by the body. The wake sheet (identified by the small (red/blue) pairs of counterrotating vorticity) were convected non-uniformly downward inside the rotor wake. The vorticity contained in the inboard portion of the wake sheet was seen to rapidly diffuse as it impinged upon the upper surface of the body, while most of the outboard portion was relaminarized inside the tip vortices, as detailed in Fig. 3.78b.

The boundary layer that developed on the upper surface of the body can be seen as the thin (blue) layer of vorticity shown in Fig. 3.78, in this case for the circular body shape. Notice that the boundary layer thickened during the passage of a nearby tip vortex, most likely because of the locally steeper adverse pressure gradient that the vortex flow induces on the body surface. For the circular and elliptical body shapes, the results showed that the separated boundary layer rolled up into a small, but coherent counter-rotating vortex that was then convected with the remainder of the rotor wake; this effect was not seen with the rectangular body shape. These results also showed that when the inboard portion of the wake sheet impinged on the body surface, it interacted with the boundary layer there. The outboard portions of the wake sheet that were not relaminarized by the surrounding

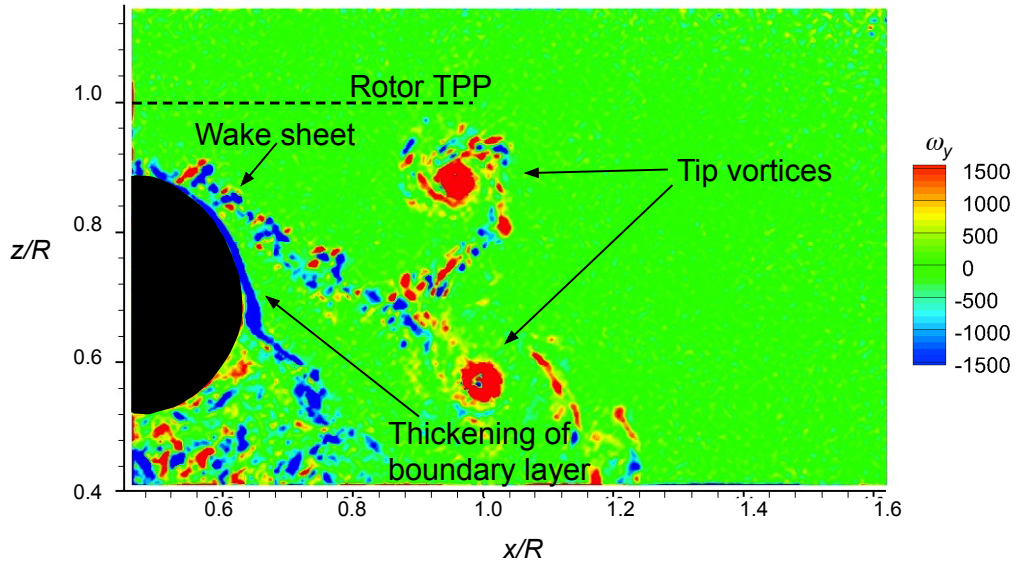

(a) PIV at time step 1, $\psi_b \approx 30°$

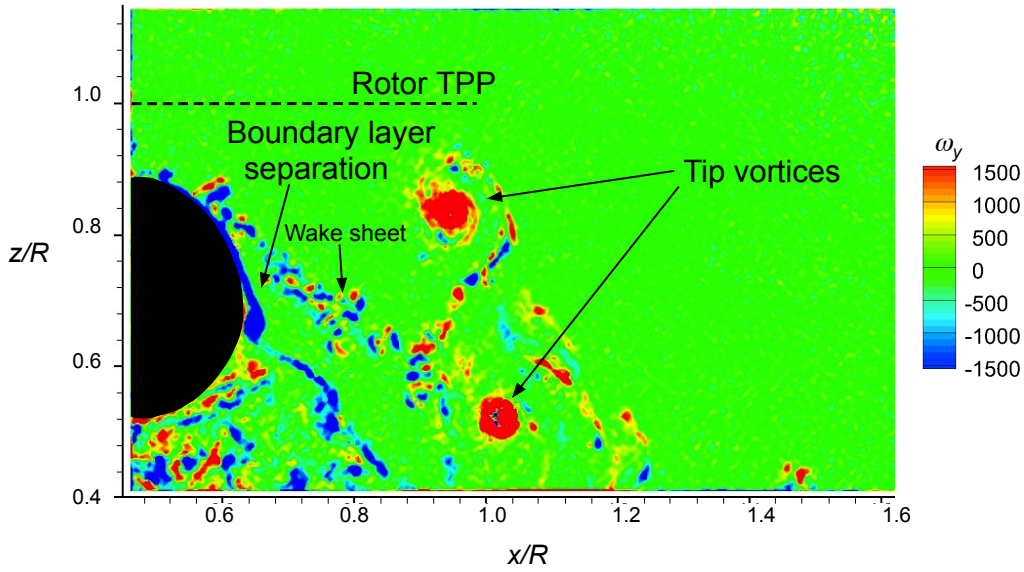

(b) PIV at time step 2, $\psi_b \approx 90°$

Figure 3.78: Instantaneous vorticity contours at the nose of the circular body showing the interaction between the boundary layer on the body and tip vortices.

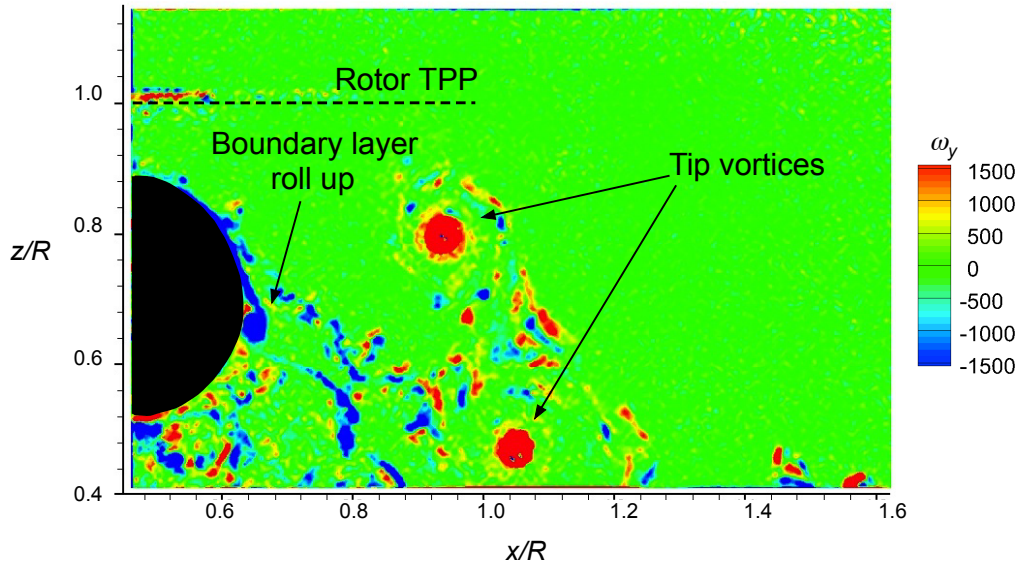

(c) PIV at time step 3, $\psi_b \approx 150°$

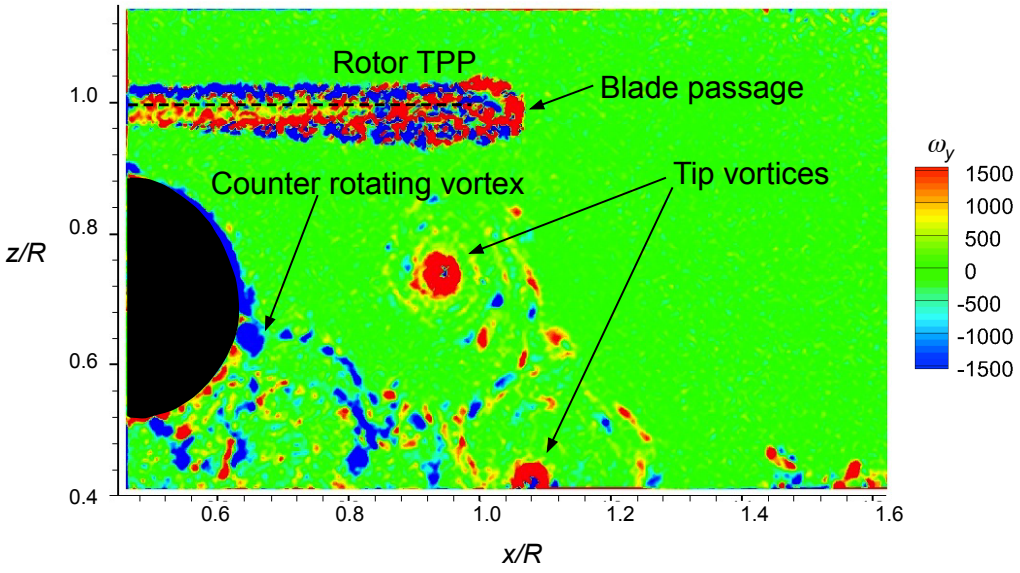

(d) PIV at time step 4, $\psi_b \approx 210°$

Figure 3.78: (Concluded) Instantaneous vorticity contours at the nose of the circular body showing the interaction between the boundary layer on the body and tip vortices.

tip vortices were then convected down toward the ground plane along with the vorticity shed from the boundary layer.

Any upstream differences caused by the bodies should also manifest as some differences in the flows in the near-wall region over the ground plane, which can also potentially affect the problem of sediment mobilization from the ground. To this end, Fig. 3.79 shows the time-averaged total velocity profiles near the ground that were produced by the isolated rotor and with the three different bodies in the rotor wake, in turn. The measurements showed that the resulting flows at the ground were relatively similar in each case. The mean flow in the wall-jet reached a peak velocity at $x/R = 1.6$ before the the wall-jet velocities began to decrease. These results showed that at the nose at least, the bodies had relatively small effects on the flow as it developed along the ground and, therefore, are likely to produce only minor differences in the resultant dust field.

3.3.1.3 PIV at the Tail Region

Compared to the nose regions, the flows produced at the tails of the bodies were found to differ more significantly from what was produced by the isolated rotor. These effects can be first illustrated by the time-averaged total velocity contours in ROI 1, which are shown in Fig. 3.80. The isolated rotor produced the highest flow velocities both near the rotor and also at the ground. With a body present, however, the rotor wake directly impinged on the upper surface of the body, thereby causing a significant decrease in the mean flow velocities. The wake then convected underneath the body towards the ground, the flow velocities there being more significantly reduced. The resultant flow at the ground

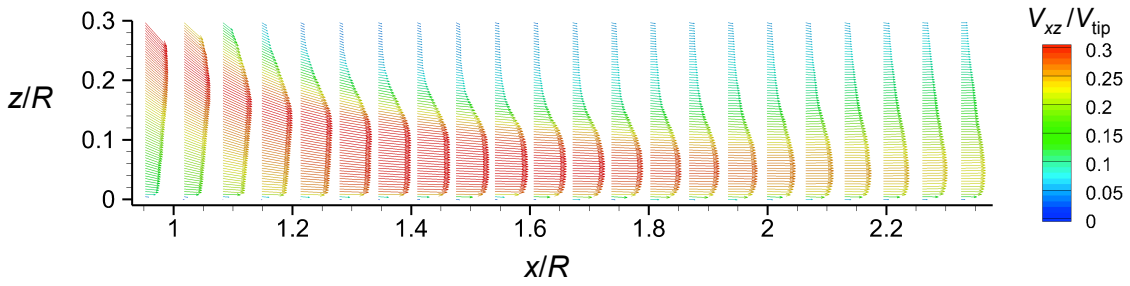

(a) Isolated rotor

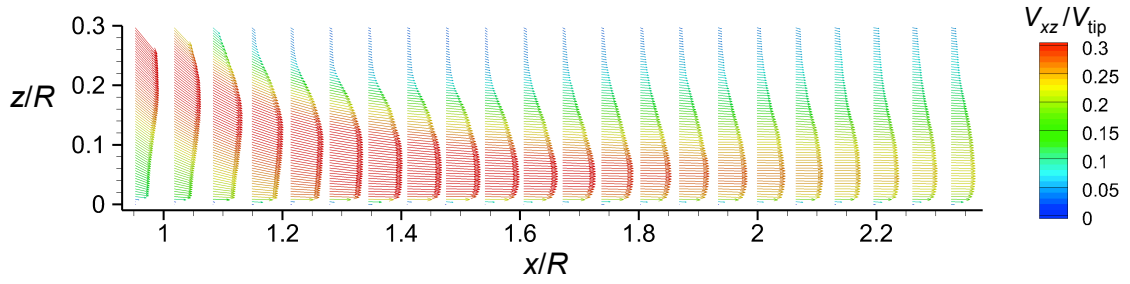

(b) Circular body

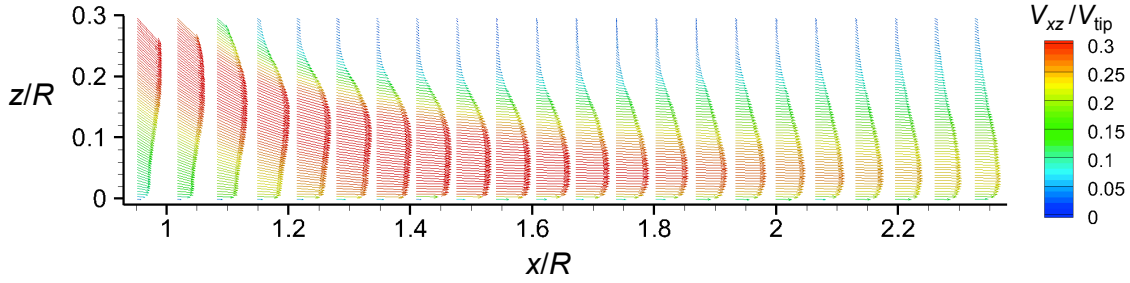

(c) Elliptical body

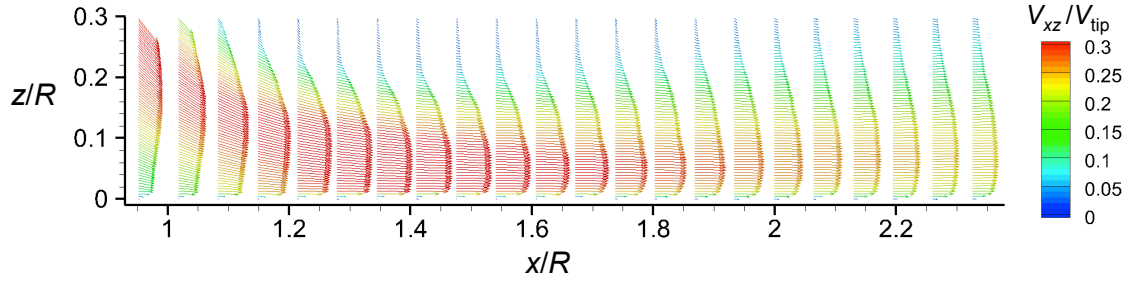

(d) Rectangular body

Figure 3.79: Time-averaged velocity profiles near the ground for the isolated rotor and below the nose of each body.

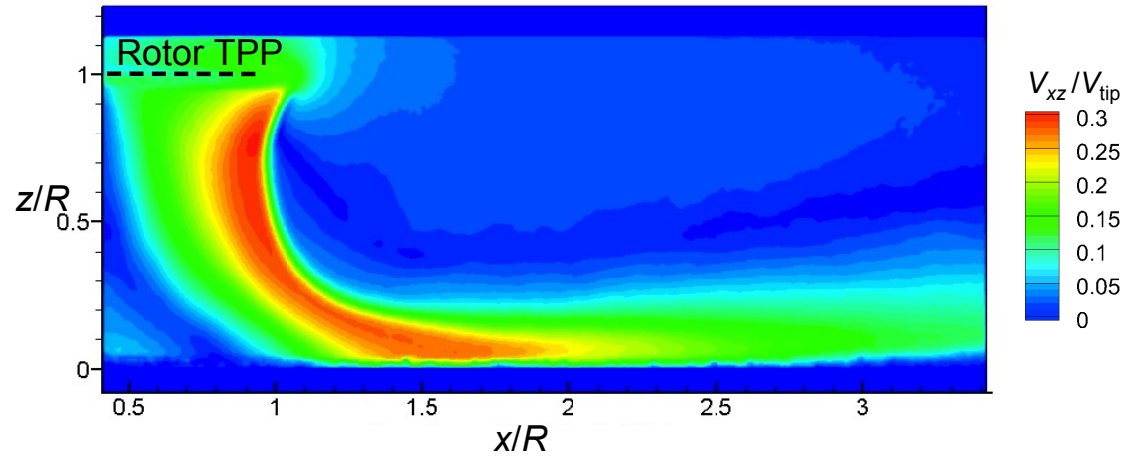

(a) Isolated rotor

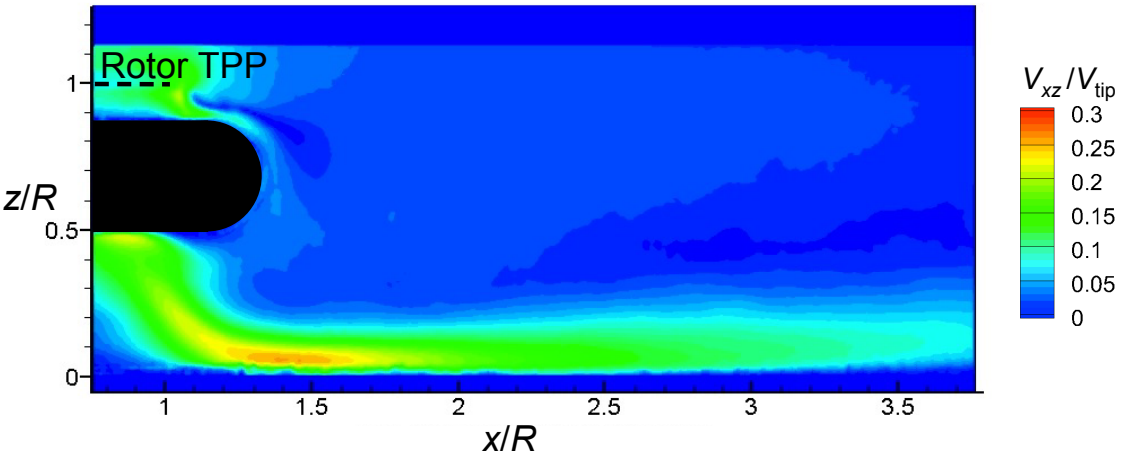

(b) Circular body

Figure 3.80: Time-averaged total velocity contours for the isolated rotor and tail region of each body.

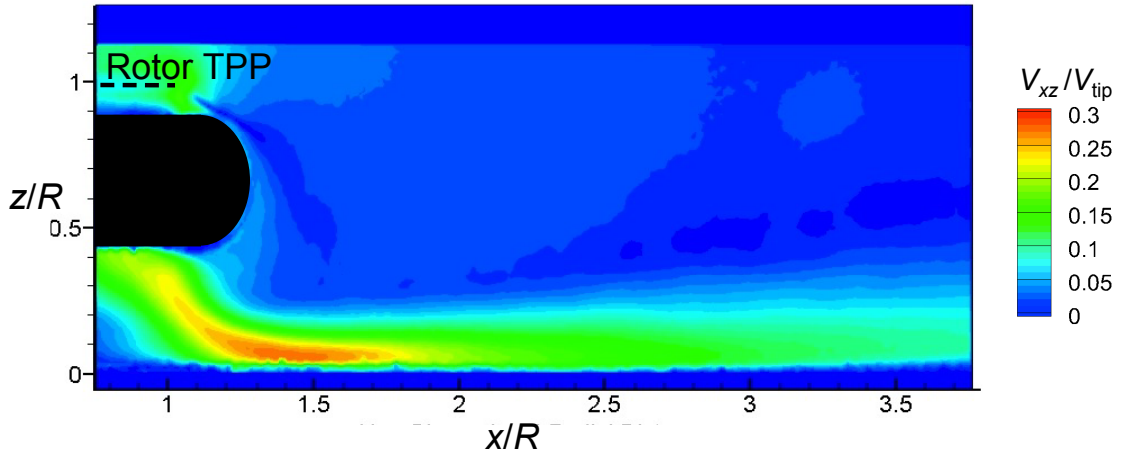

(c) Elliptical body

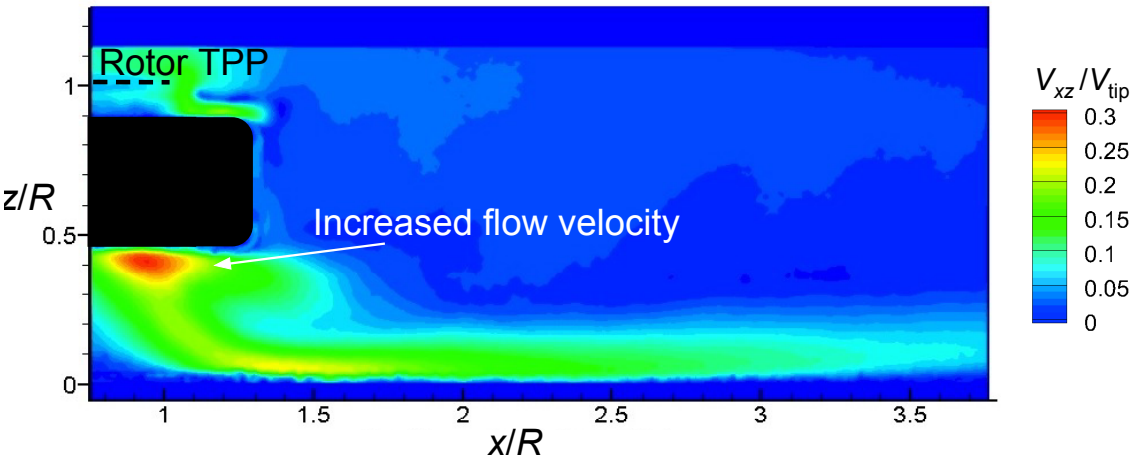

(d) Rectangular body

Figure 3.80: (Concluded) Time-averaged total velocity contours for the isolated rotor and tail region of each body.

also showed lower peak velocities when compared to those produced by the isolated rotor, and the flow was also considerably distorted compared to the corresponding flow seen at the nose region; see previously in Fig. 3.79. Notice the small localized region of increased flow velocity just below the rectangular body at $z/R = 0.4$ as shown in Fig. 3.80d, an effect that will be discussed in detail later.

Figure 3.81 shows the instantaneous vorticity contours in ROI 2 that were produced by the isolated rotor and also those produced in the presence of each of the three body shapes. The results for the isolated rotor shown in Fig. 3.81a indicated that there were two coherent vortices present in this ROI, with wake ages of $\zeta \approx 60^\circ$ and $\zeta \approx 240^\circ$, respectively, which are also marked in Fig. 3.81a. For the flows produced in the presence of the circular and elliptical body shapes, however, only the vortex at $\zeta \approx 60^\circ$ was evident in this region. In this case, an older vortex had already impinged on the tail, causing its vorticity to significantly decrease. The resulting flow then followed the body contour until the boundary layer separated at approximately half way down the height of the body and at a wake age of about $\zeta \approx 360^\circ$.

As shown in Fig. 3.81d, the interaction between the blade tip vortex and the surface of the rectangular body (at $\zeta \approx 240^\circ$) differed somewhat from that seen with the circular and elliptical bodies. Further details of this behavior are shown as a sequence of contiguous flow realizations in Fig. 3.82. It can be seen from Fig. 3.82a that the tip vortex and wake sheet were at a relatively young wake age of $\zeta \approx 30^\circ$, and were close to impinging on the upper surface of the body. By a wake age of $\zeta \approx 90^\circ$, the tip vortex had impinged on the body and also interacted with the boundary layer there, causing the boundary layer to momentarily separate from the body; see Fig 3.82b. The vorticity

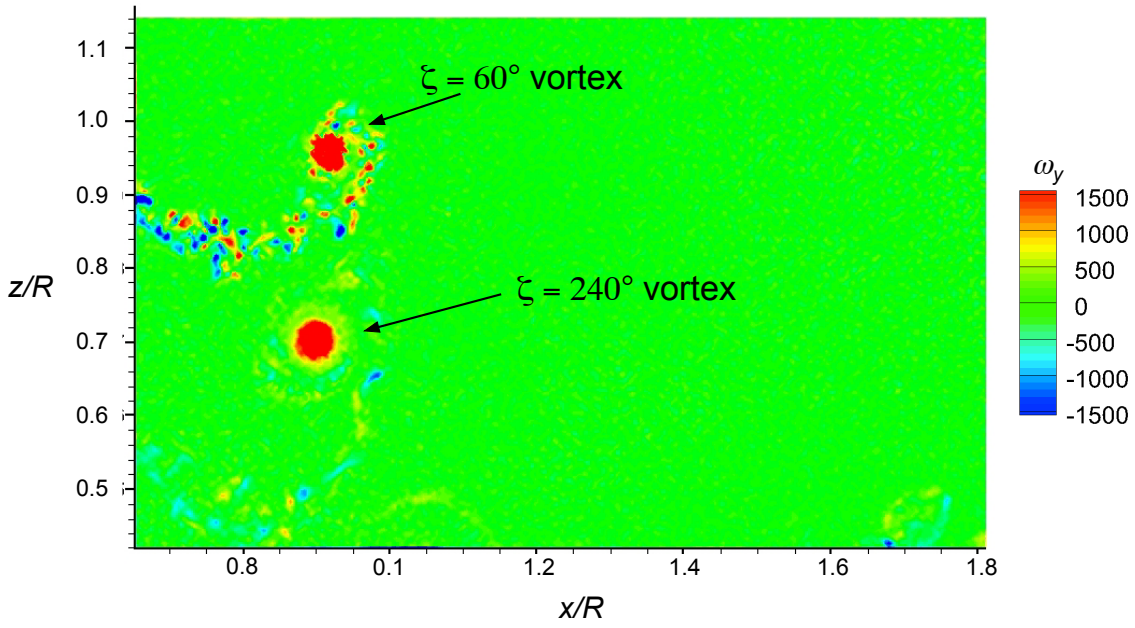

(a) Isolated rotor

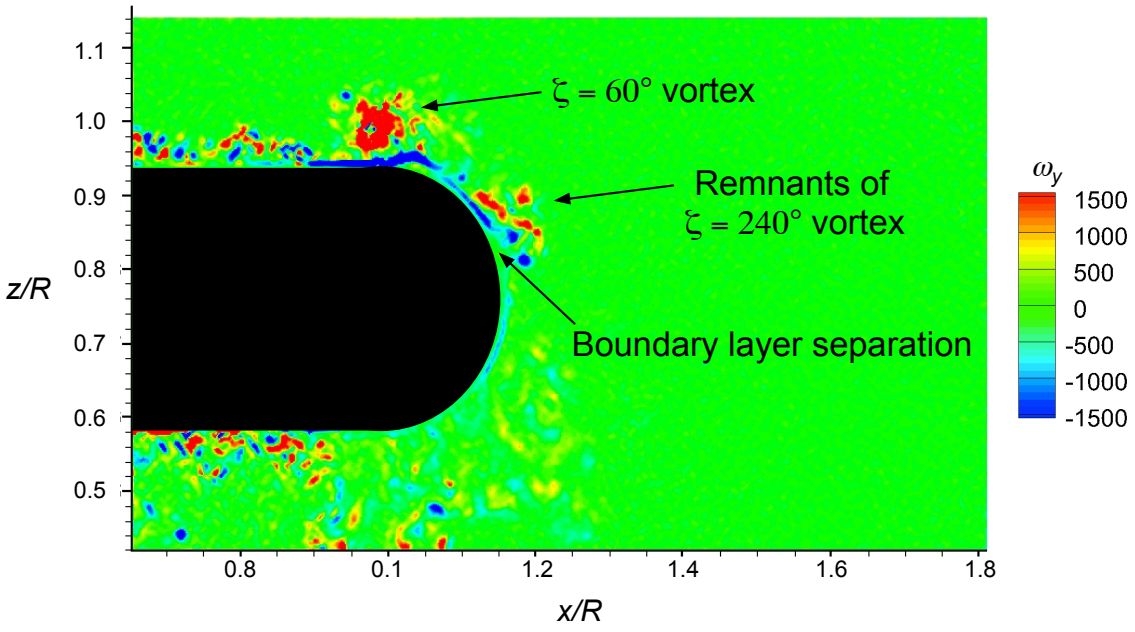

(b) Circular body

Figure 3.81: Instantaneous vorticity contours for the isolated rotor and at the tail of each body.

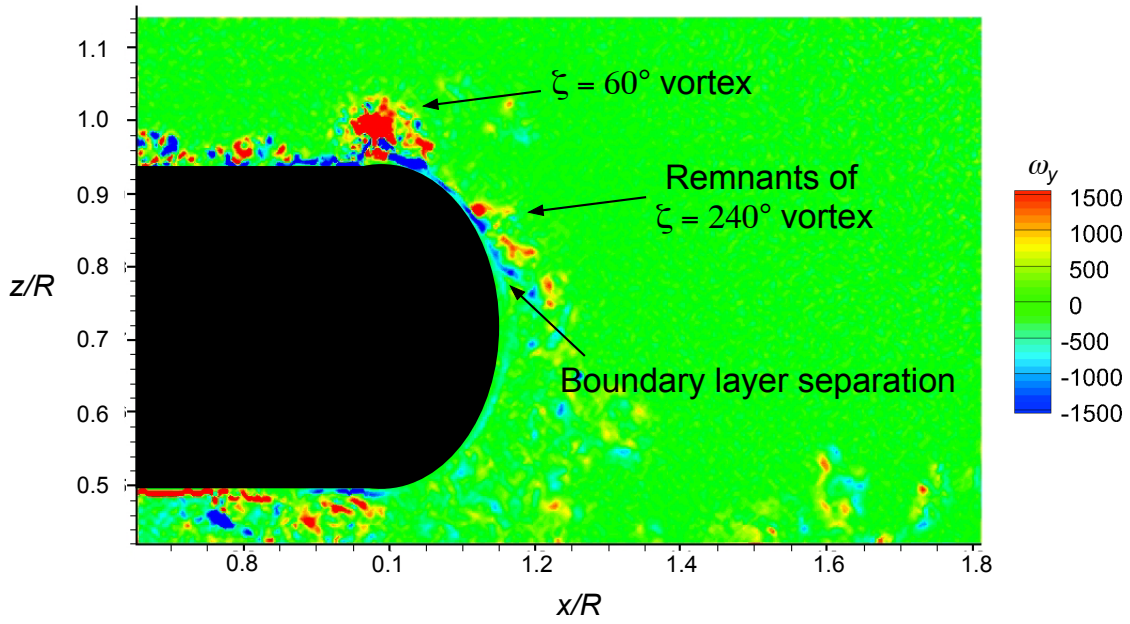

(c) Elliptical body

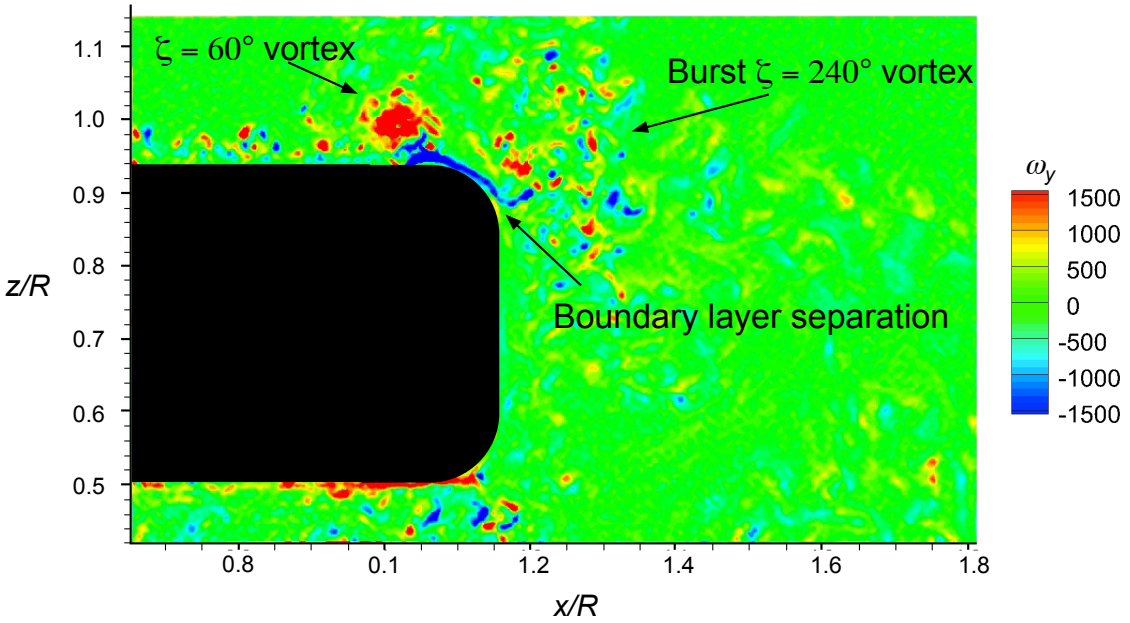

(d) Rectangular body

Figure 3.81: (Concluded) Instantaneous vorticity contours for the isolated rotor and at the tail of each body.

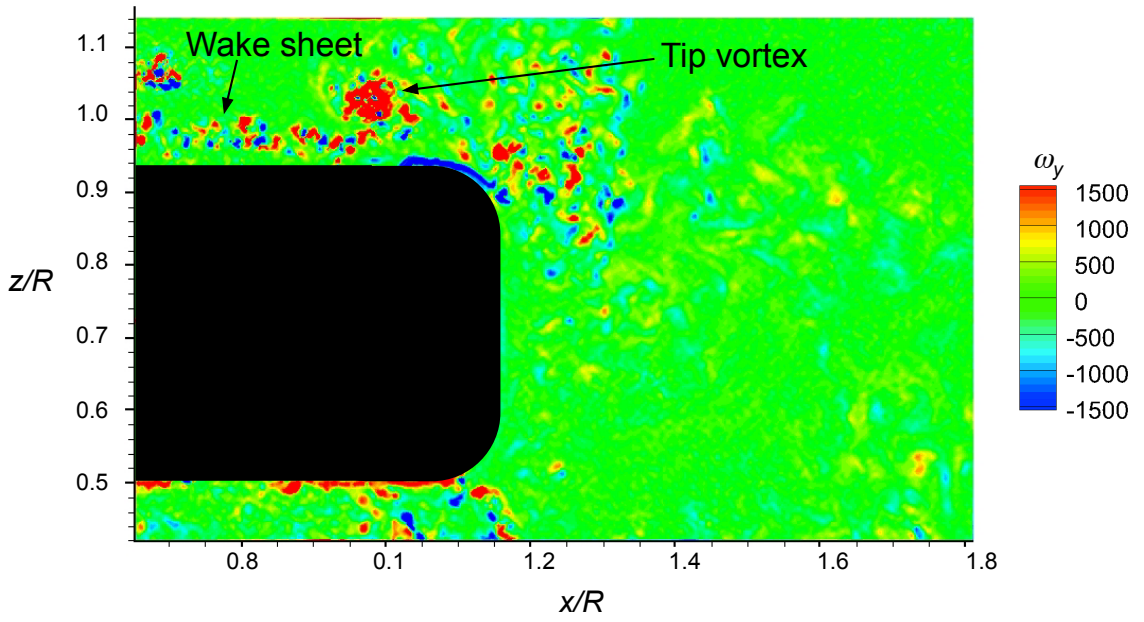

(a) PIV at time step 1, $\psi_b \approx 30°$

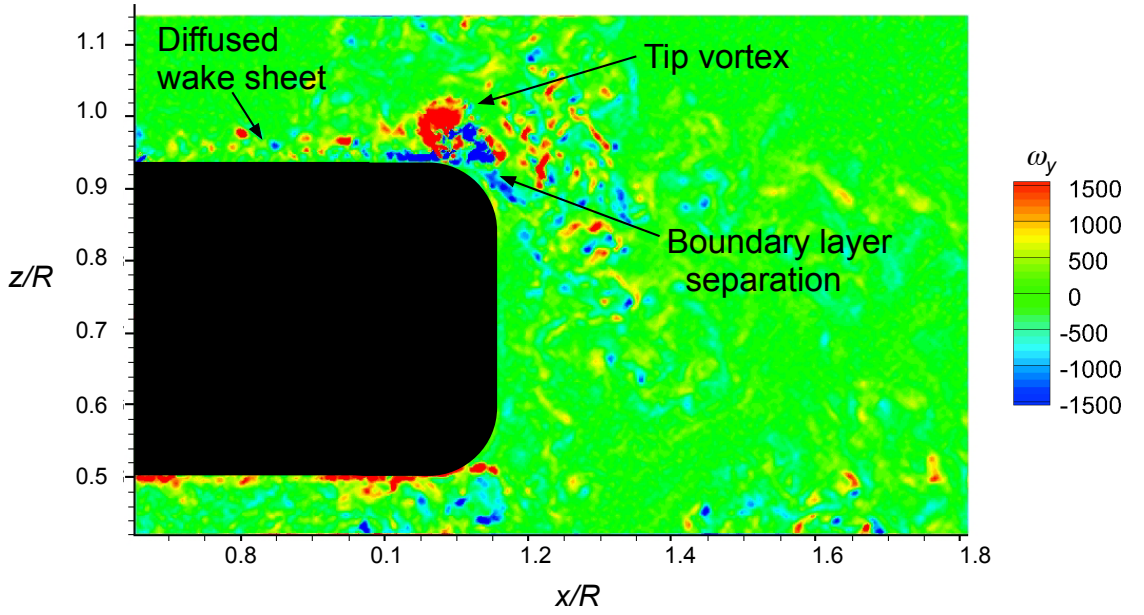

(b) PIV at time step 2, $\psi_b \approx 90°$

Figure 3.82: Instantaneous sequence of vorticity contours in the vicinity of the rectangular body showing vortex impingement on its upper surface.

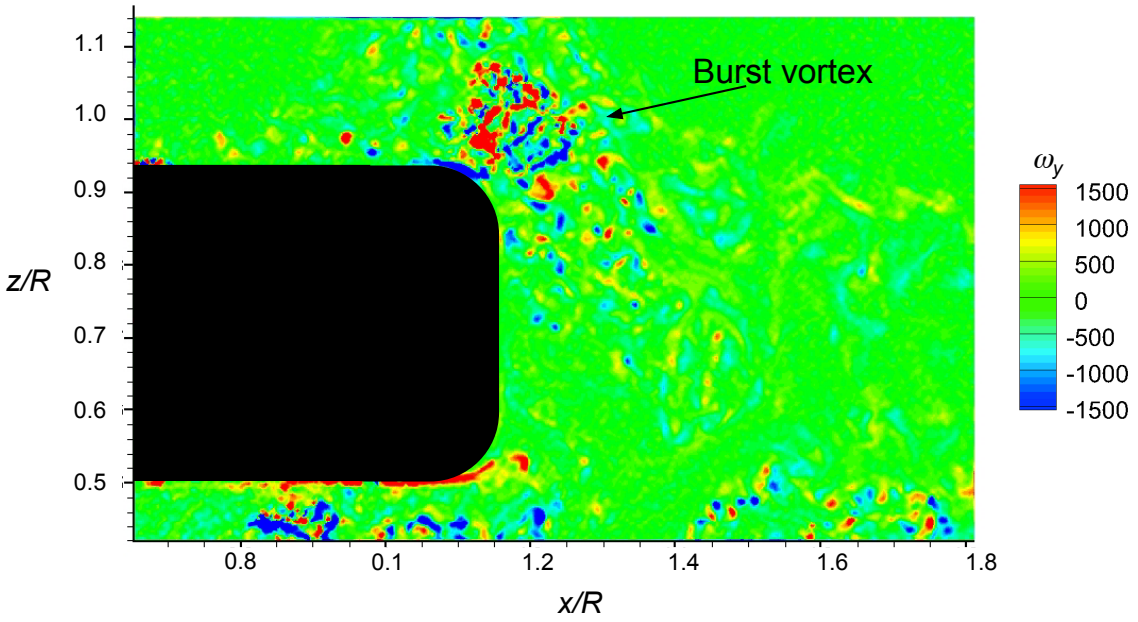

(c) PIV at time step 3, $\psi_b \approx 150^\circ$

Figure 3.82: (Concluded) Instantaneous sequence of vorticity contours in the vicinity of the rectangular body showing vortex impingement on its upper surface.

comprising the wake sheet was also significantly diffused after interacting with the body. At $\zeta \approx 150^\circ$, as shown in Fig. 3.82b, the tip vortex was observed to burst, resulting in the rapid redistribution of its vorticity and the creation of smaller eddies and turbulence. The resulting small-scale vortical flows then mixed with the separated flow from the boundary layer as it was convected downstream towards the ground.

Instantaneous realizations of vorticity at the ground (in ROI 3) for the isolated rotor and for the rotor with the three body shapes are shown in Fig. 3.83. The results confirmed that there were regions of localized vorticity that had reformed at the ground, a result previously seen in the FV; see Fig. 3.74. While the vorticity was not as concentrated compared to that shown in the isolated rotor case, the vortices were still of sufficient

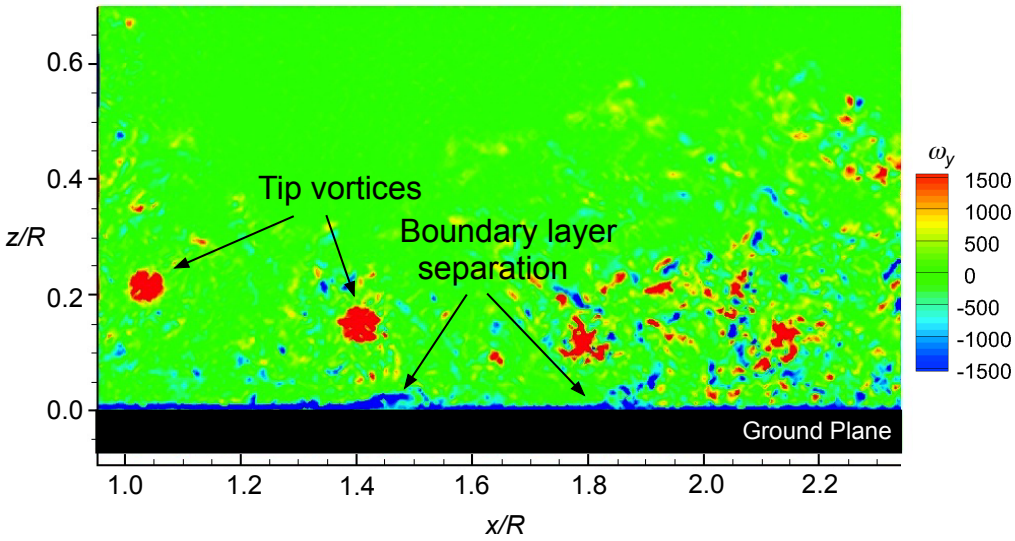

(a) Isolated rotor

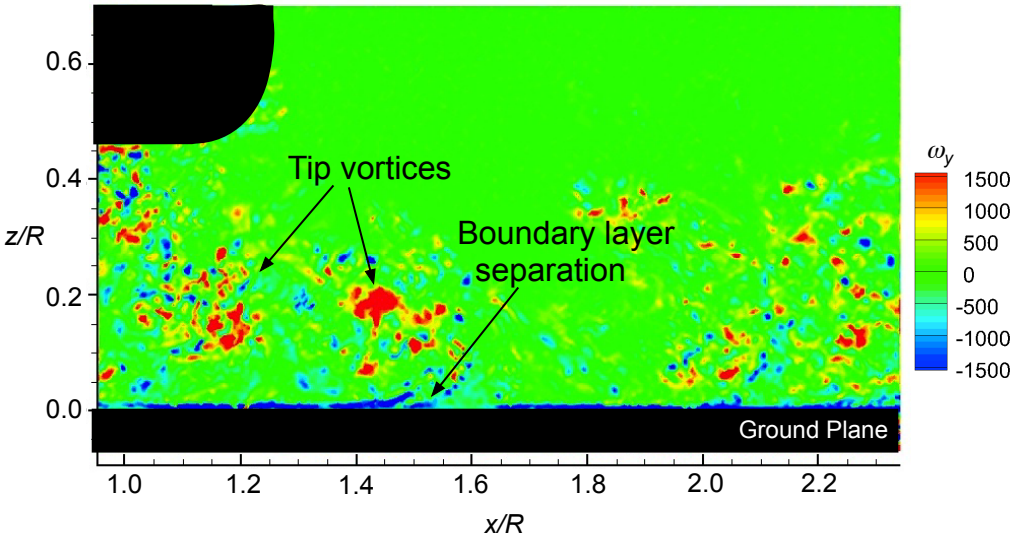

(b) Circular body

Figure 3.83: Instantaneous vorticity contours near the the ground for the isolated rotor and below the tail of each body.

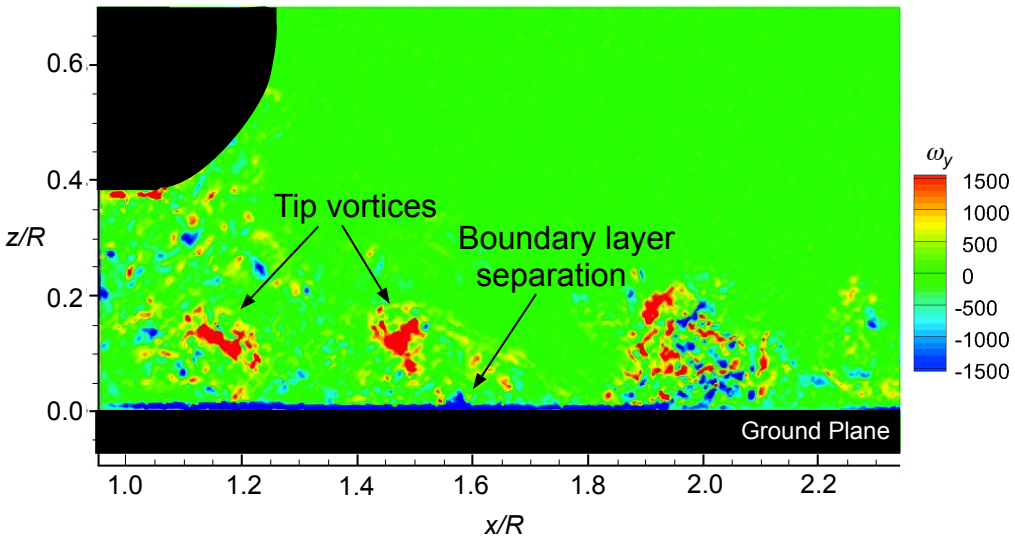

(c) Elliptical body

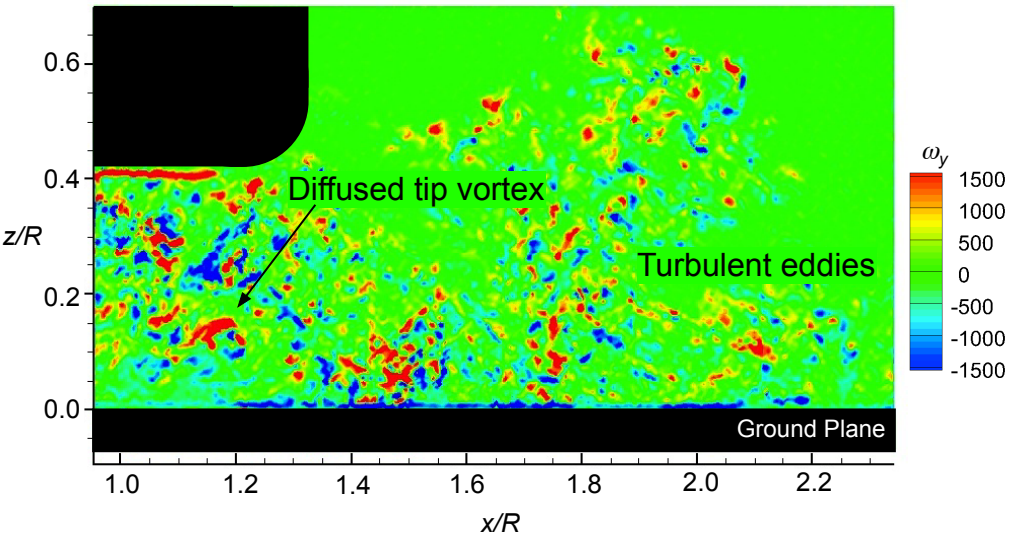

(d) Rectangular body

Figure 3.83: (Concluded) Instantaneous vorticity contours near the the ground for the isolated rotor and below the tail of each body.

strength to induce an adverse pressure gradient that caused the boundary layer to momentarily separate from the wall. The near-wall vorticity found below the rectangular body was not as concentrated as was found below the circular and elliptical body shapes; see Fig. 3.83d. The interaction between the rotor wake and the rectangular body shape produced a more turbulent and energetic near-wall flow region, as seen by the higher levels of turbulence that were present throughout the entire region.

Time-averaged profiles near the ground plane as produced by the isolated rotor and by the presence of the three body shapes are shown in Fig. 3.84. In each case, the presence of the body distorted the wake boundary and caused significantly lower peak velocities in the flow than were produced by the isolated rotor. A comparison of the near-wall flows showed that the elliptical body shape caused the highest peak velocities at the ground, which occurred at about x/R = 1.5. The circular and rectangular body shapes caused the lowest peak velocities in this region.

A more detailed comparison of the velocity profiles on the ground at downstream distances of $x/R = 1.0$ and $x/R = 2.2$ are shown in Fig. 3.85a and Fig. 3.85b, respectively. Because the wake was still in the process of turning radially outward at $x/R = 1.0$, the flows there were seen to be fairly similar in all cases. However, the isolated rotor produced a somewhat thicker wall-jet flow. In this case, the boundary layer thickness is defined as the distance from the ground plane to the location of the peak velocity in the flow. Of particular interest at this location is the significant increase in the wall-parallel velocity that was produced at $z/R = 0.4$ in the presence of the rectangular body; this increase in wall-parallel velocity was not observed for the isolated rotor flow or the flows with the other two body shapes. Further downstream, at $x/R = 2.2$, the flows that had

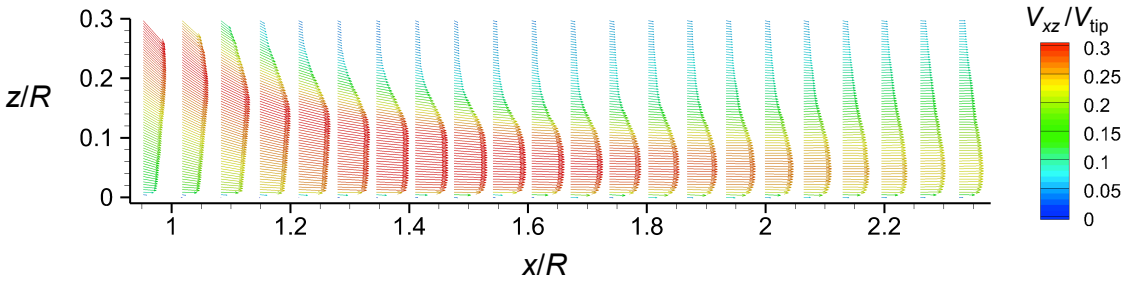

(a) Isolated rotor

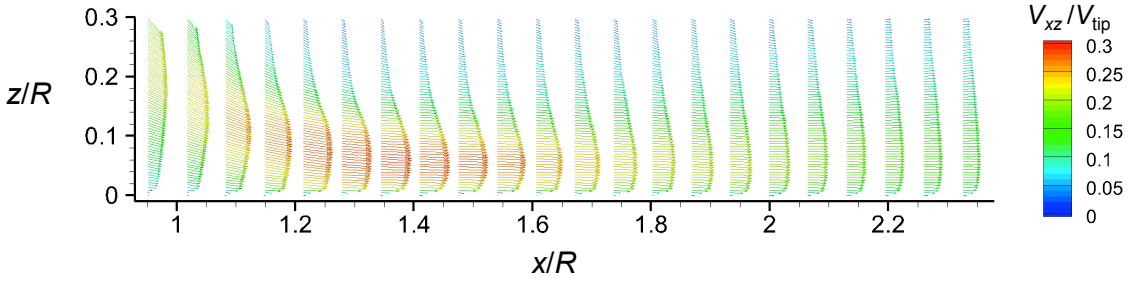

(b) Circular body

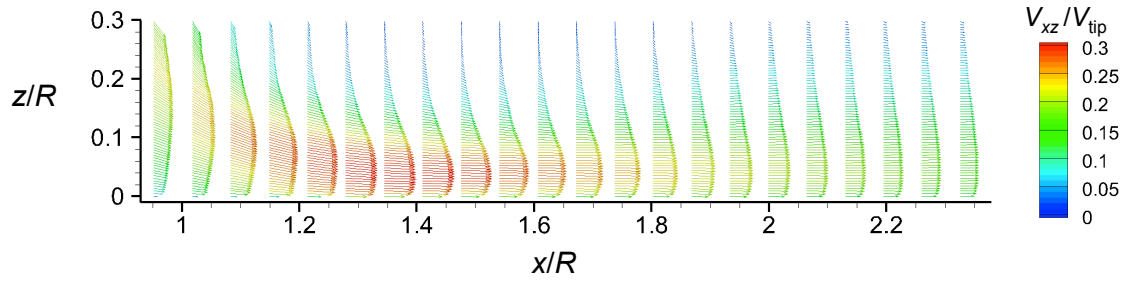

(c) Elliptical body

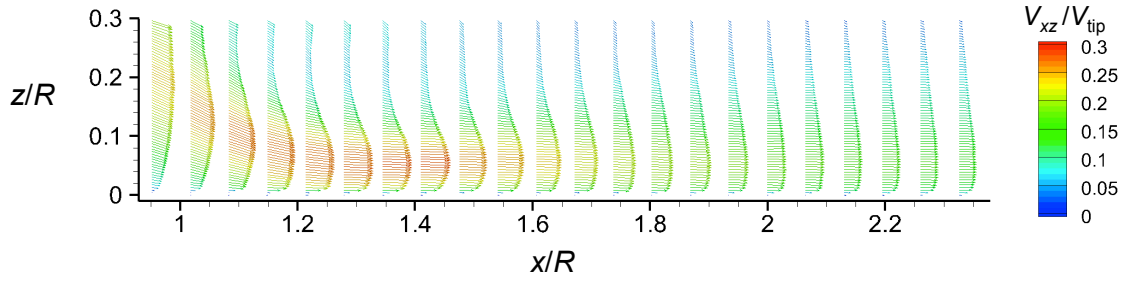

(d) Rectangular body

Figure 3.84: Time-averaged total velocity profiles near the ground for the isolated rotor and below the tail of each body.

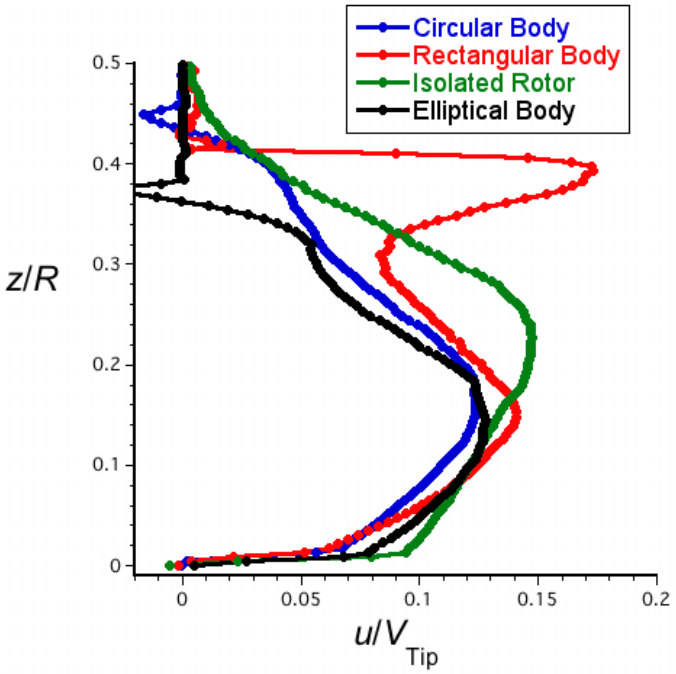

(a) $x/R = 1.0$

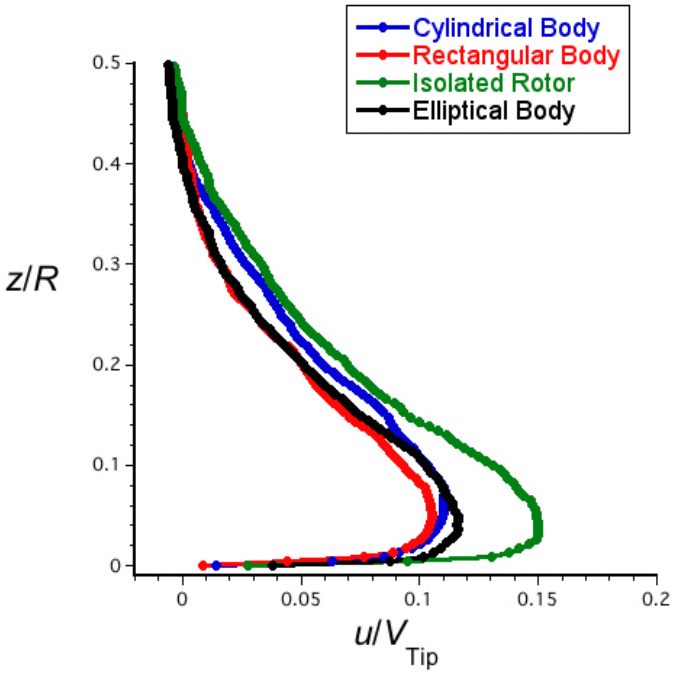

(b) $x/R = 2.2$

Figure 3.85: Time-averaged wall-parallel velocity profiles comparing the isolated rotor flow and the flow below the tail of body at two radial locations.

developed there with the bodies present had similar velocity profiles. At this radial location, however, the peak velocity in the flow was found to be slightly lower than the peak velocity produced by the isolated rotor.

3.3.1.4 Three-Dimensionality of the Flow

The measurements that were made in the vertical (x-z) plane provided considerable insight into the effects of the body shapes on the developing flow fields below the rotor and near the ground. However, the previous results that were shown for the horizontal planes (see Section 3.1.1.4) have confirmed that the rotor wake flow was inherently three-dimensional, with non-uniform variations in the flow velocities all the way to the ground plane, i.e., the flow at the ground was not radially symmetric. There is obviously an expectation that the bodies will further alter the three-dimensionality of the rotor wake as it develops over the ground.

To quantify these three-dimensional effects produced by the bodies, measurements were made in horizontal planes at the same ten different heights above the ground plane ($z/R = 0.1 - 1.0$). The time-averaged flows below the nose of the bodies at the plane $z/R = 0.1$ are shown in Fig. 3.86 as contours of total velocity in the horizontal planes, V_{xy}. While the wall-parallel velocities at the ground with the bodies present were slightly lower, the flows were not significantly different to those produced by the isolated rotor. The time-averaged flow fields in all cases showed fairly radially symmetric distributions of wall-parallel velocities. Therefore, it is reasonable to expect that the dust cloud in the nose region will not be significantly affected by the presence of a body.

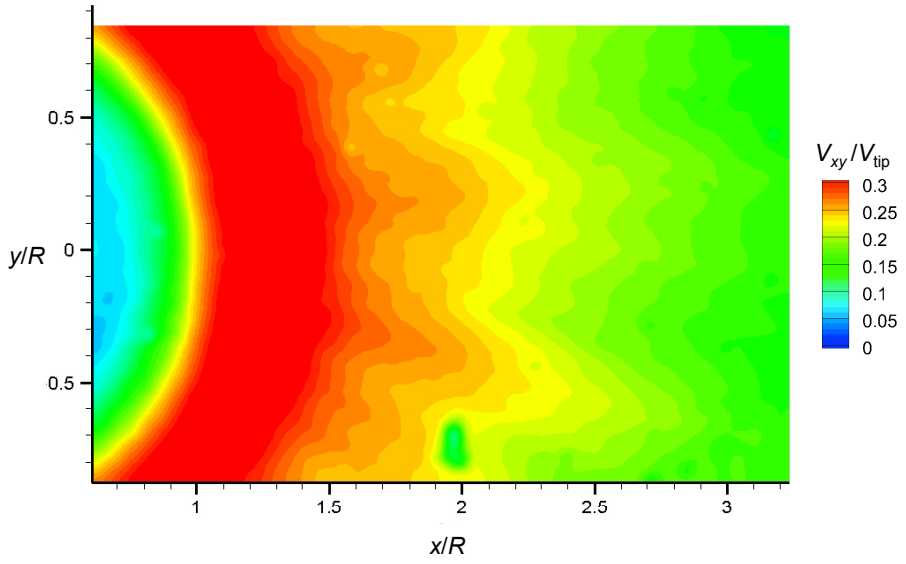

(a) Isolated rotor

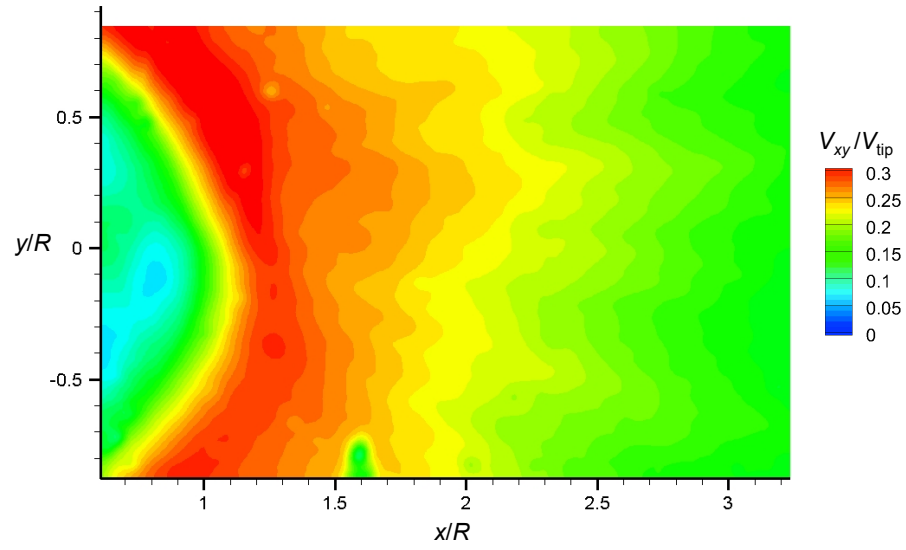

(b) Circular body

Figure 3.86: Time-averaged total velocity contours for the isolated rotor and below the nose of each body at $z/R = 0.1$.

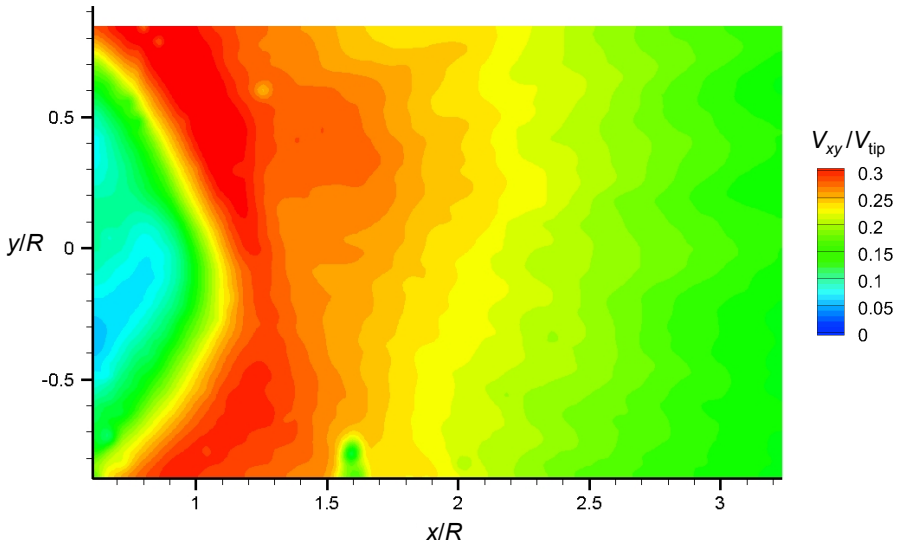

(c) Elliptical body

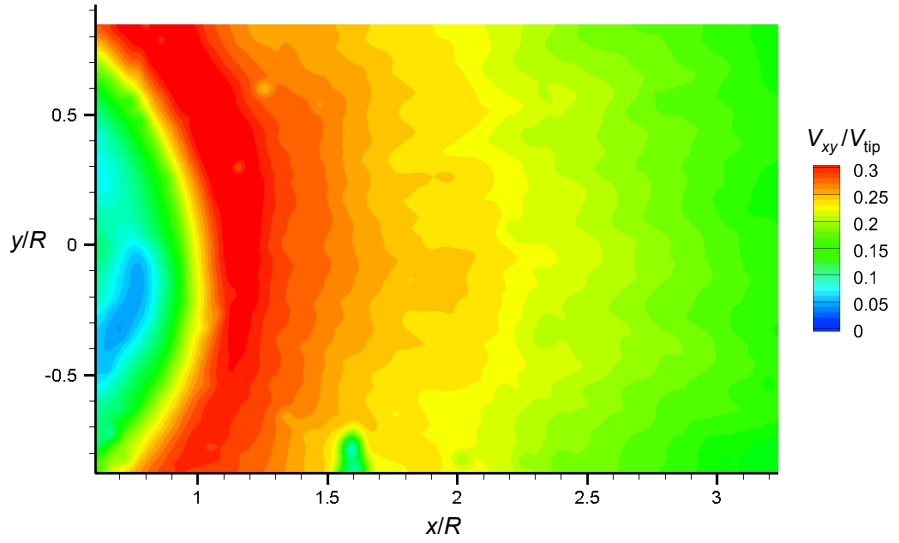

(d) Rectangular body

Figure 3.86: (Concluded) Time-averaged total velocity contours for the isolated rotor and below the nose of each body at $z/R = 0.1$.

The measurements in the vertical imaging plane, however, showed that the flow in the tail region was significantly distorted by the presence of each of the bodies; see Fig. 3.80. The flow field was measured over several x-z planes to better quantify such flow distortions. The time-averaged measurements for the isolated rotor and the circular body shape at $z/R = 0.8$ are shown in Fig. 3.87. Notice that this imaging plane was located just below the upper surface of the body.

At $z/R = 0.8$, the rotor wake that developed in the presence of the cylindrical body differed from that of the isolated rotor because the tip vortices had directly impinged on the upper surface of the body. This vortex filament was seen to wrap around the body and form a hairpin loop, stretching the filament along its length and initially intensifying its vorticity. The filament was ultimately stretched to a point where the core region thinned and burst, with the associated rapid diffusion of vorticity and the creation of turbulence. Figure 3.87b further details the interaction of the tip vortex filament with the upper surface of the body.

Time-averaged measurement made in the plane at $z/R = 0.4$ for the isolated rotor and in the presence of the three bodies are shown in Fig. 3.88. Of particular interest is that the localized region of higher flow velocity was observed in this plane. The results shown previously in Fig. 3.85a have already indicated a localized region of increased flow velocity in the vertical plane just below the tail of the rectangular body. This flow was clearly caused by the presence of the body in the rotor wake because it was not observed for the isolated rotor.

For each of the bodies, this localized flow differed in both its velocities and shape. The localized flow produced by the rectangular body was particularly interesting because

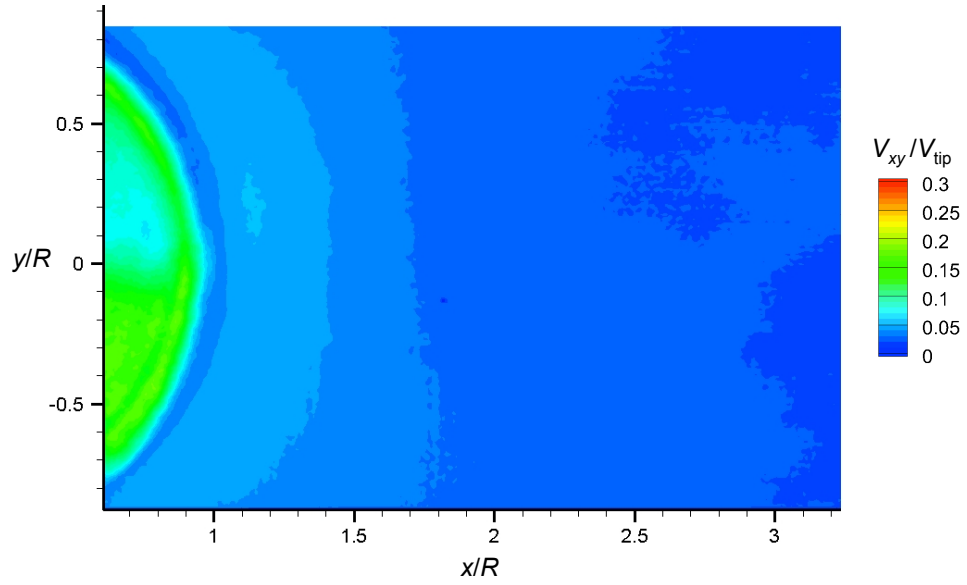

(a) Isolated rotor

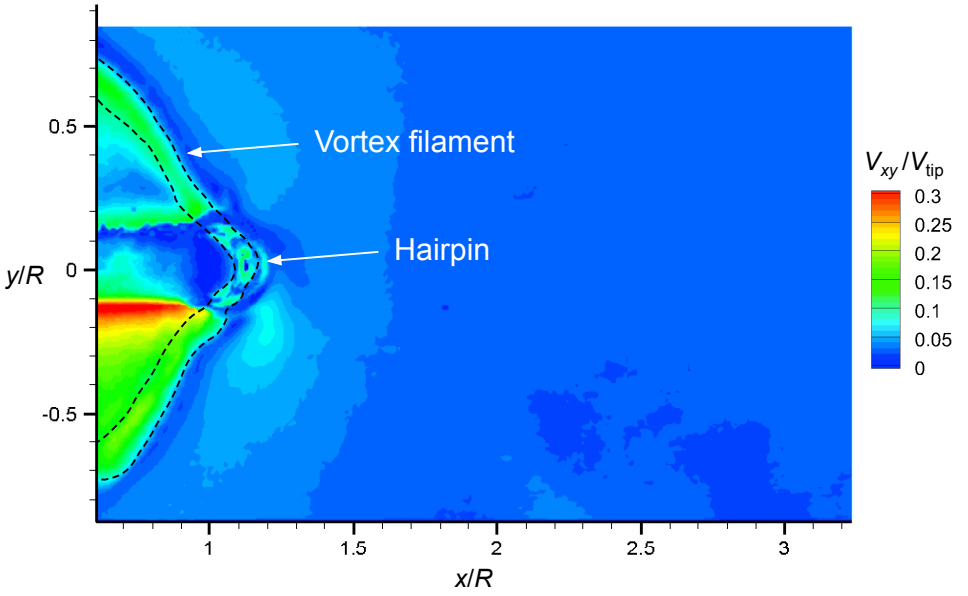

(b) Circular body

Figure 3.87: Time-averaged total velocity contours for the isolated rotor and at the tail of the circular body at $z/R = 0.8$ showing the hairpin loop of the vortex filament.

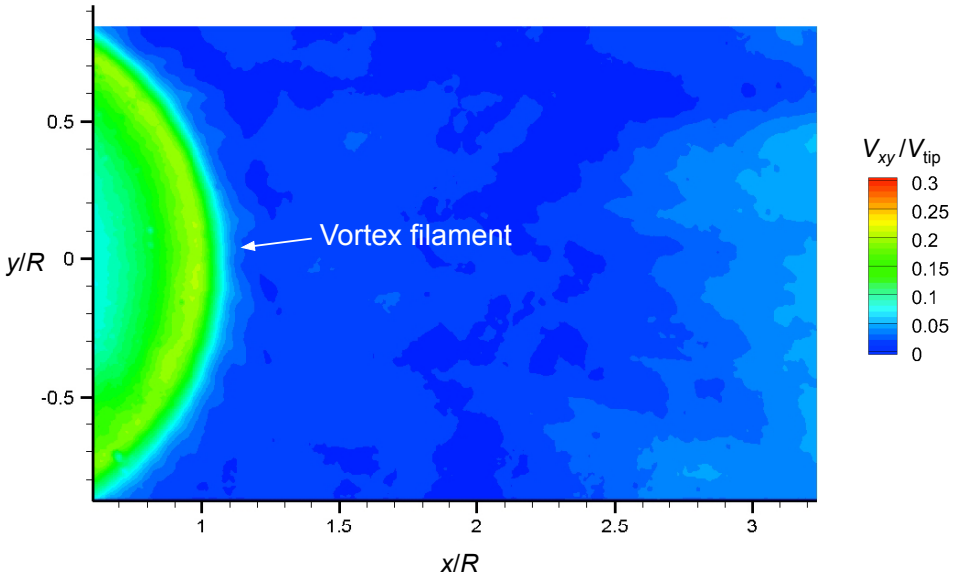

(a) Isolated rotor

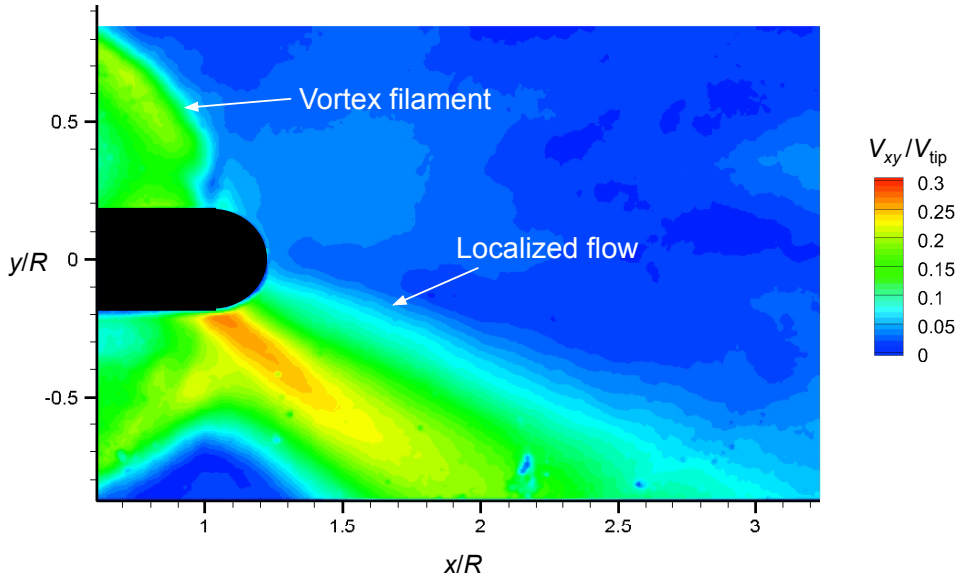

(b) Circular body

Figure 3.88: Time-averaged total velocity contours for the isolated rotor and at the tail of each body at $z/R = 0.4$.

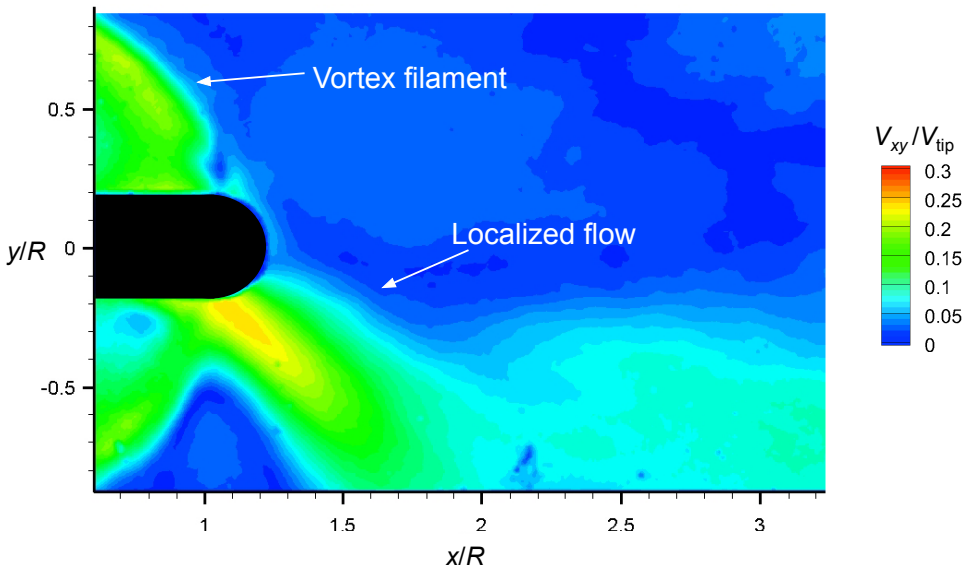

(c) Elliptical body

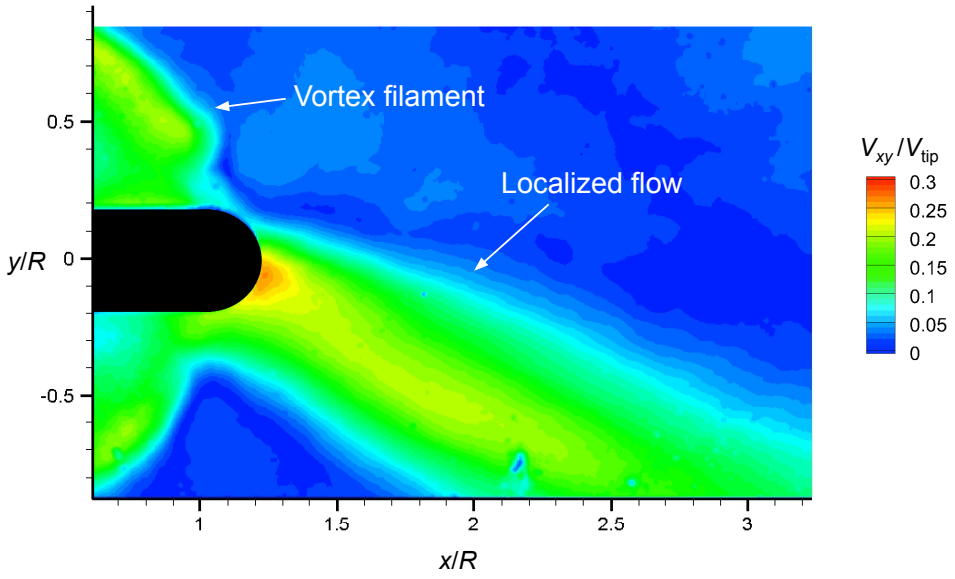

(d) Rectangular body

Figure 3.88: Time-averaged total velocity contours for the isolated rotor and at the tail of each body at $z/R = 0.4$.

it was deflected much more towards the longitudinal centerline of the body, as shown in Fig. 3.88d. Such a localized flow was also observed with the elliptical and circular bodies. However, in these cases the flow did not deflect towards the centerline of the body and was, therefore, not observed in the measurements taken in the vertical plane.

The time-averaged results for the near-wall plane at $z/R = 0.1$ are shown in Fig. 3.89. The flow in this region was found to be significantly distorted by the presence of the bodies, causing lower average flow velocities at this horizontal plane compared to those produced by the isolated rotor; see Fig. 3.89a. The impingement of the blade tip vortices on the bodies clearly affected the resulting flows near the ground, as shown by the relatively lower velocities along the extended centerline of the body. Of particular interest is that the localized flow discussed previously had convected downward and had impinged on the ground, creating there a localized region of higher flow velocities (labeled in Fig. 3.89).

To investigate the origin of this localized flow, a single vertical plane was oriented such that the flow around the cross-section of the body could be observed, i.e., a $z-y$ plane that was perpendicular to the previous vertical plane. The results for the three bodies is shown in Fig. 3.90 as contours of total velocity in this plane, V_{zy}. Recall from the results shown in Fig. 3.31 that the rotor produced a swirl velocity within the rotor wake. This swirl velocity caused the body cross-sections to be at a small angle of attack relative to the flow and they, therefore, also acted like bluff bodies in the cross-plane. Notice that on the right hand side of the bodies, there was a local flow acceleration because of the relative angle of attack of the bodies to the downwash field of the rotor. The flow around the side of the bodies ultimately detached from the surface and impinged on the ground, therefore producing this localized flow region that was seen in the horizontal planes.

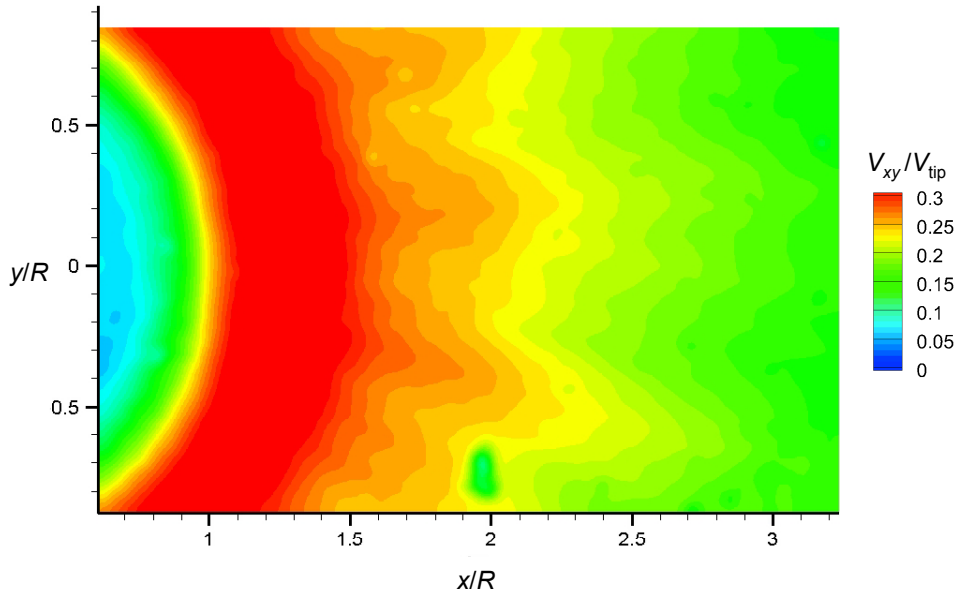

(a) Isolated rotor

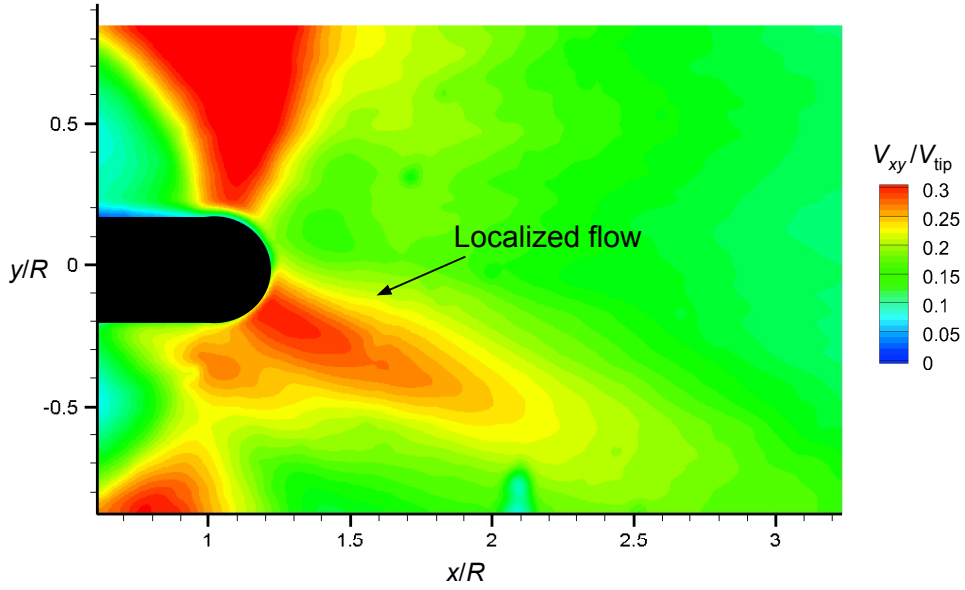

(b) Circular body

Figure 3.89: Time-averaged total velocity contours for the isolated rotor and below the tail of each body at $z/R = 0.1$.

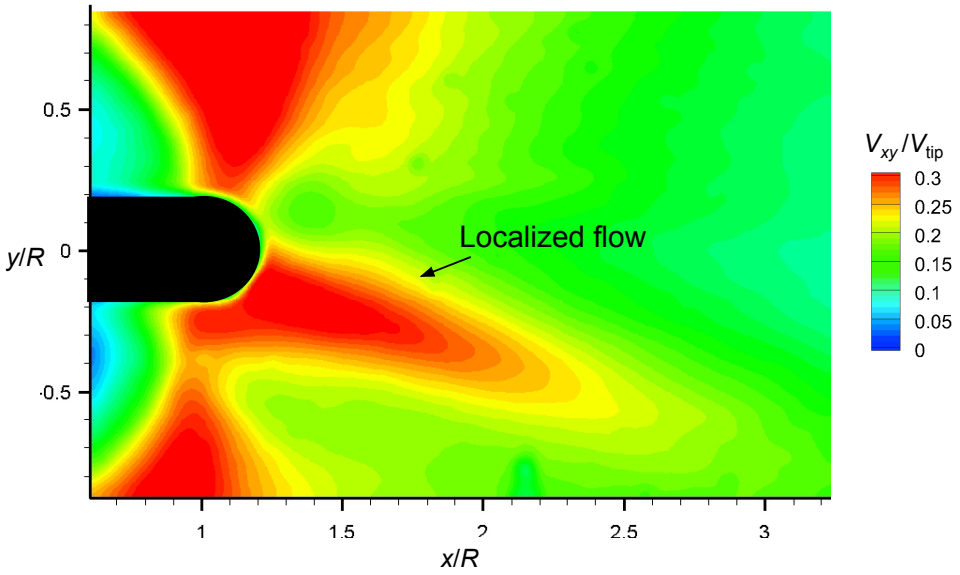

(c) Elliptical body

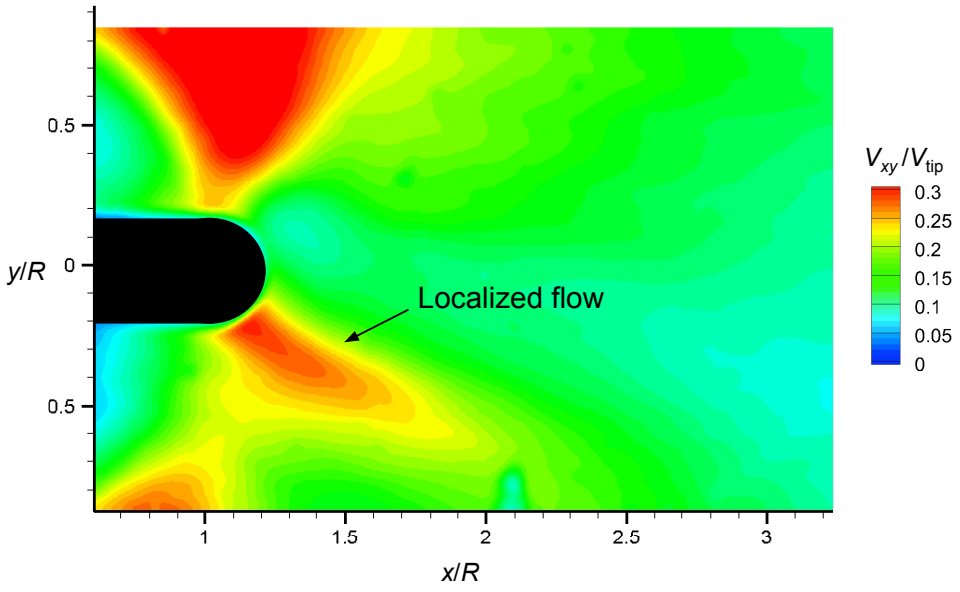

(d) Rectangular body

Figure 3.89: Time-averaged total velocity contours for the isolated rotor and below the tail of each body at $z/R = 0.1$.

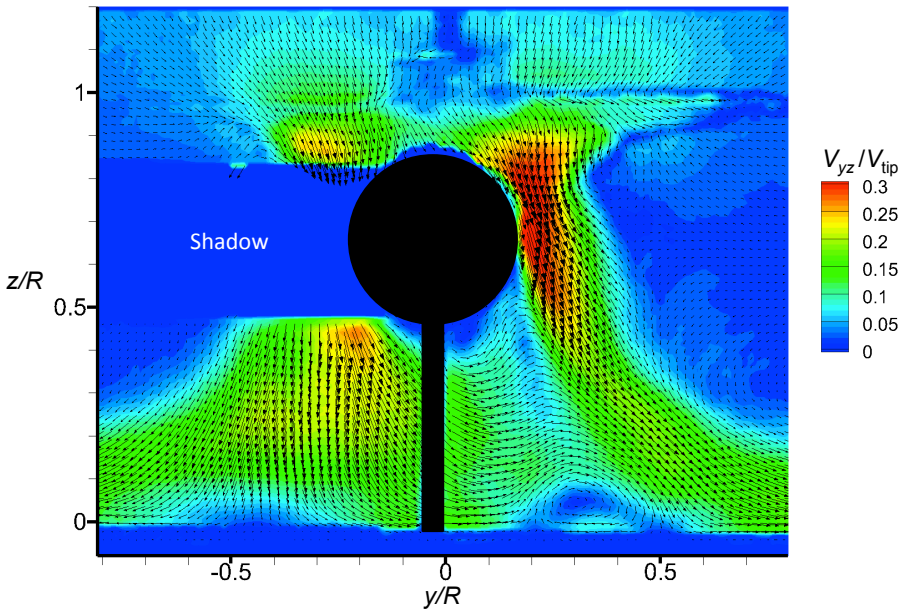

(a) Circular rotor

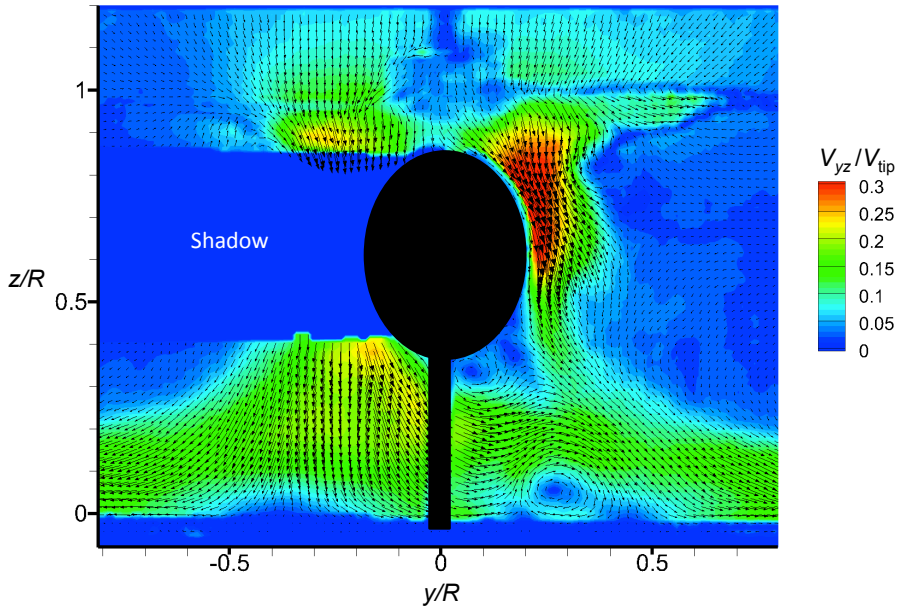

(b) Elliptical body

Figure 3.90: Time-averaged total velocity contours for the flow over the cross-section of the bodies, an $y-z$ plane.

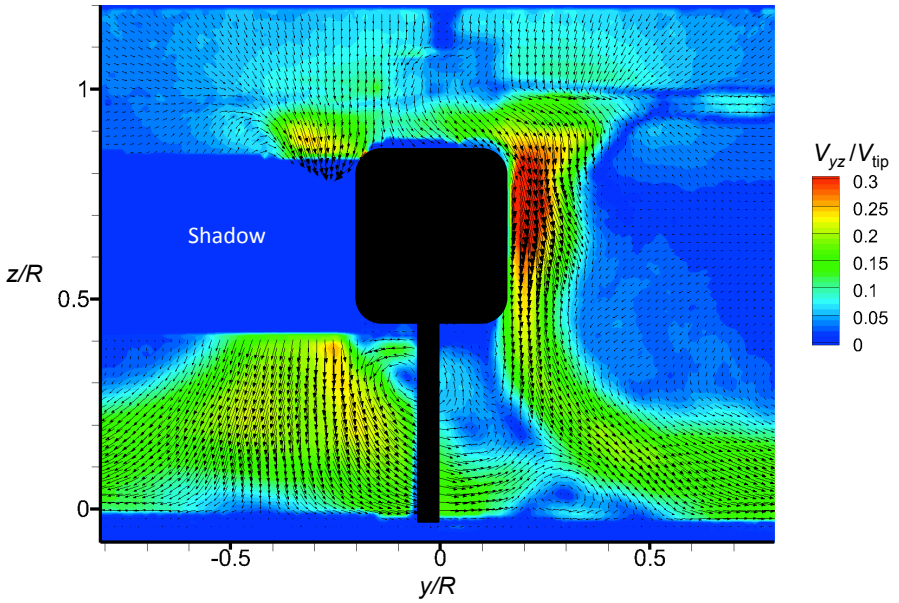

(c) Rectangular body

Figure 3.90: (Concluded) Time-averaged total velocity contours for the flow over the cross-section of the bodies, an $y-z$ plane.

3.3.2 Dual-Phase Results

Dual-phase flow experiments were also performed to measure the effects of the bodies on aspects of particle mobilization, entrainment, and uplift. Each of the bodies was placed below the rotor in turn. These experiments were also performed at the exact same rotor operating conditions as the single-phase flow experiments, but in this case the sediment bed covered the ground plane.

3.3.2.1 Results at the Nose

Figure 3.91 shows flow measurements that were made in a vertical plane (ROI 1) for the isolated rotor and when each of the bodies were placed below the rotor, in turn. The background contours are of total velocity in the vertical plane, V_{xz}, which was obtained from the PIV measurements, and the locations of each of the sediment particle determined from the PTV analysis is marked with a circle.

The results show that the isolated rotor flow mobilized the sediment particles and created a saltation layer at the ground that grew in thickness and concentration as it developed radially outward away from the rotor. In each case, the dual-phase flows with the bodies present were qualitatively similar to that produced by the isolated rotor, with some minor differences.

To further quantify the similarity between all four cases (isolated rotor flow and the corresponding flows with the three bodies), the particle concentrations of the dispersed-phase in ROI 1 for each case were averaged over 1,000 instantaneous PTV realizations, the results being shown in Fig. 3.92. The results indicated that the particle concentrations

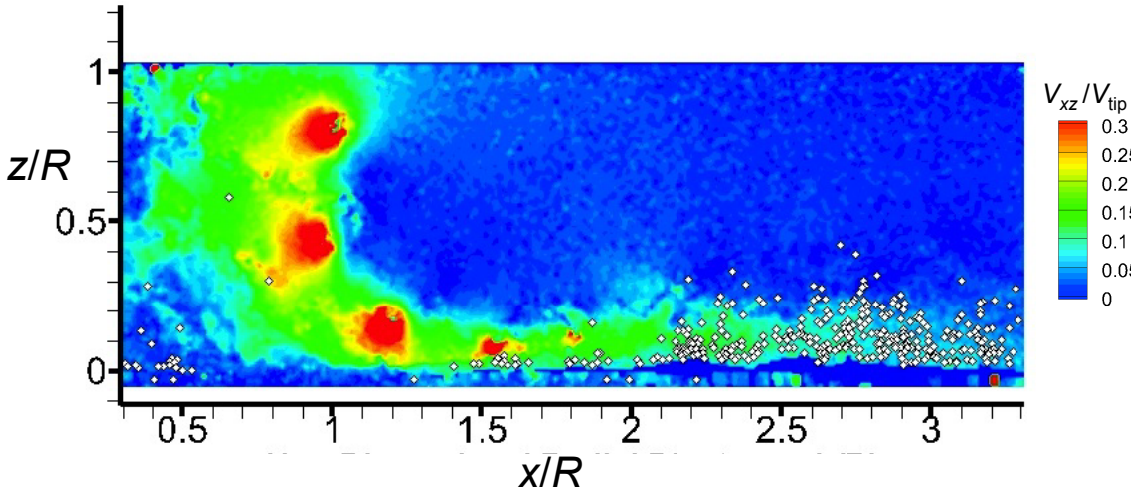

(a) Isolated rotor

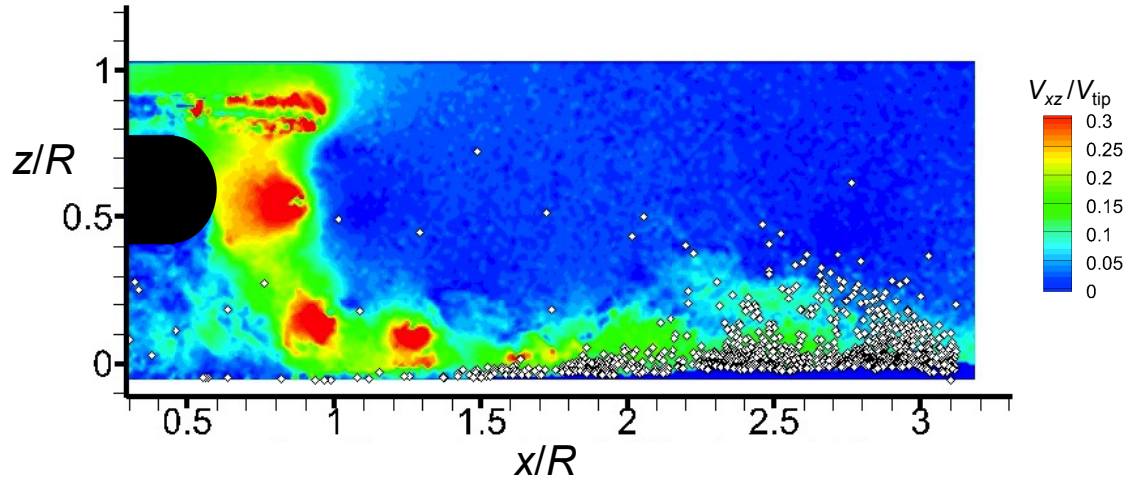

(b) Circular body

Figure 3.91: Dual-phase PIV/PTV measurements for the isolated rotor and at the nose of each body.

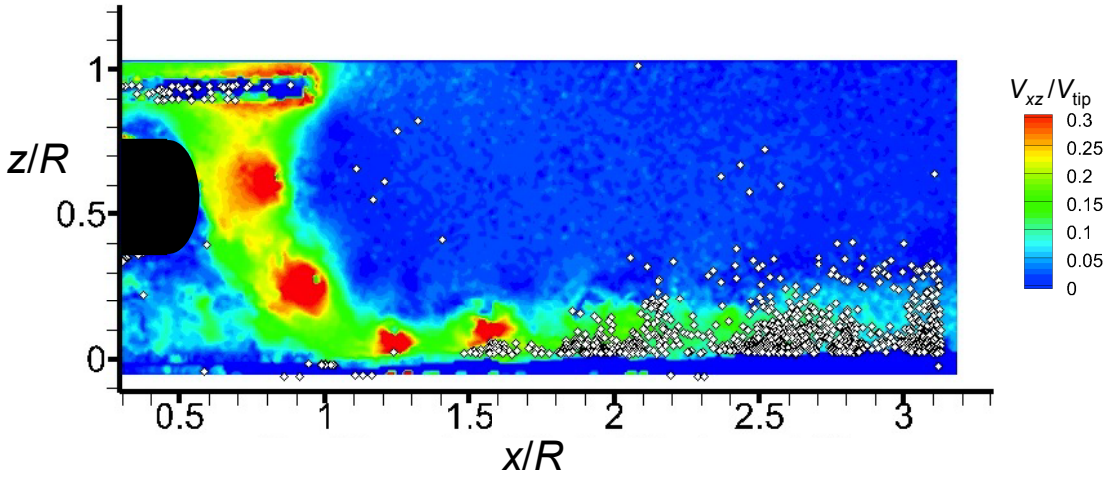

(c) Elliptical body

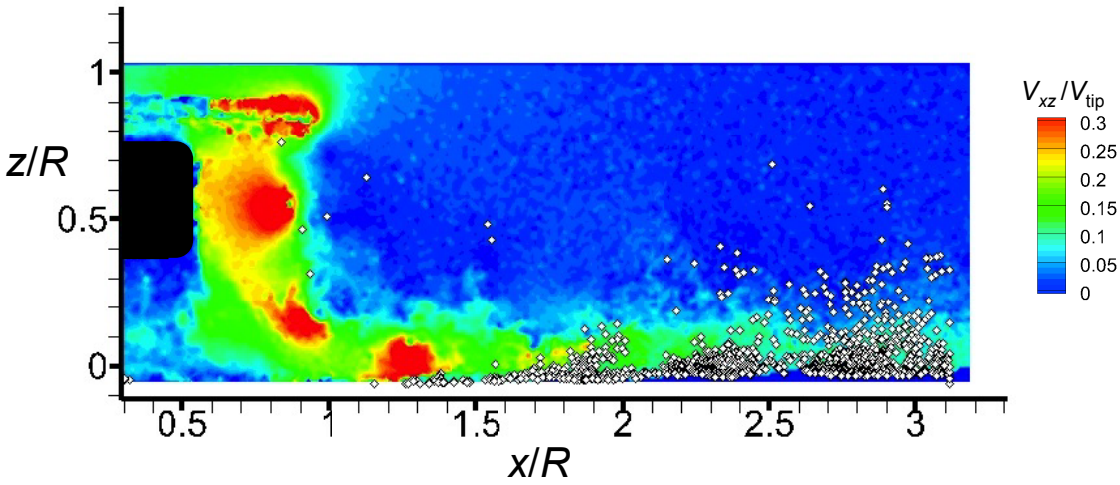

(d) Rectangular body

Figure 3.91: (Concluded) Dual-phase PIV/PTV measurements for the isolated rotor and at the nose of each body.

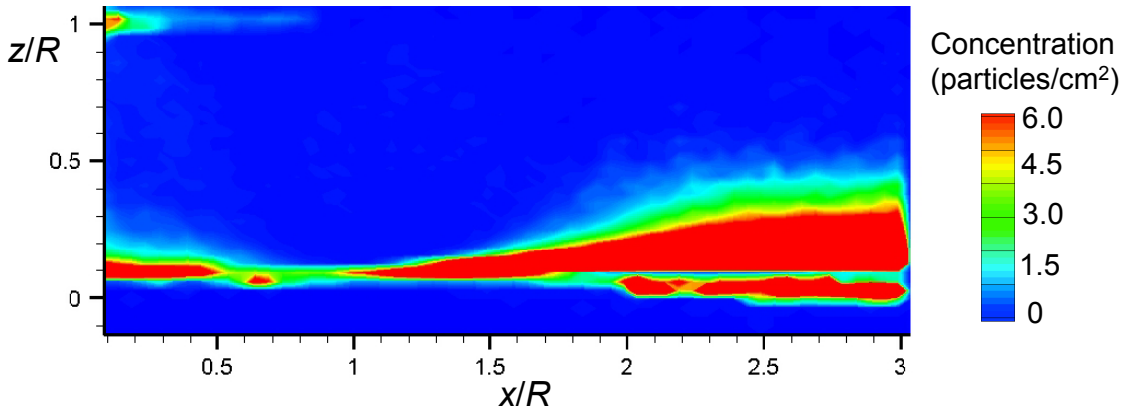

(a) Isolated rotor

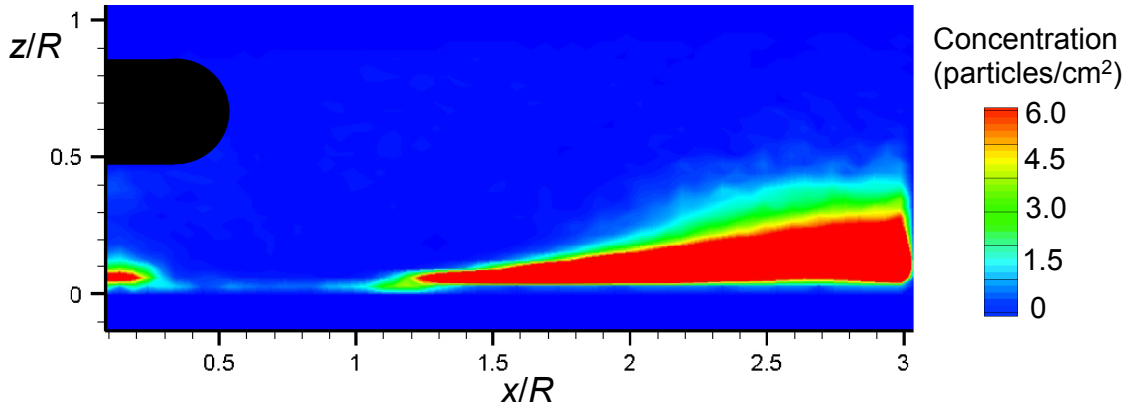

(b) Circular body

Figure 3.92: Dispersed-phase particle concentrations for the isolated rotor and at the nose of each body.

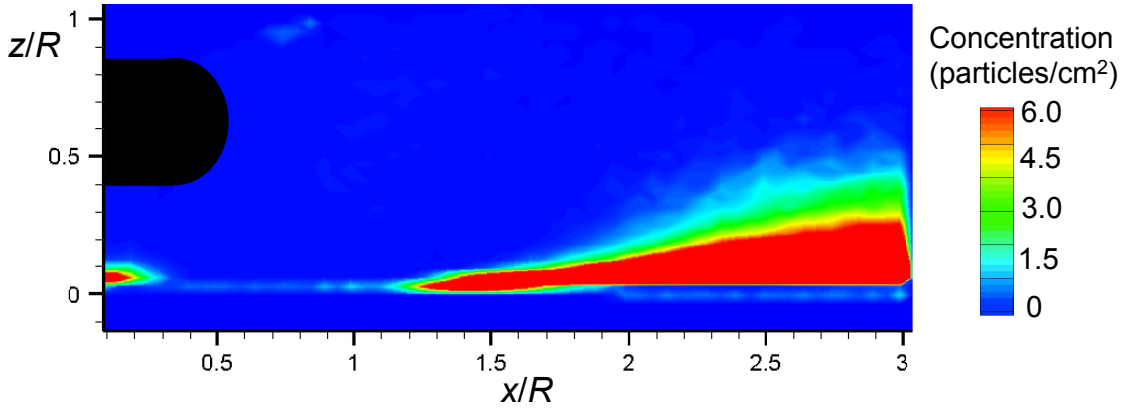

(c) Elliptical body

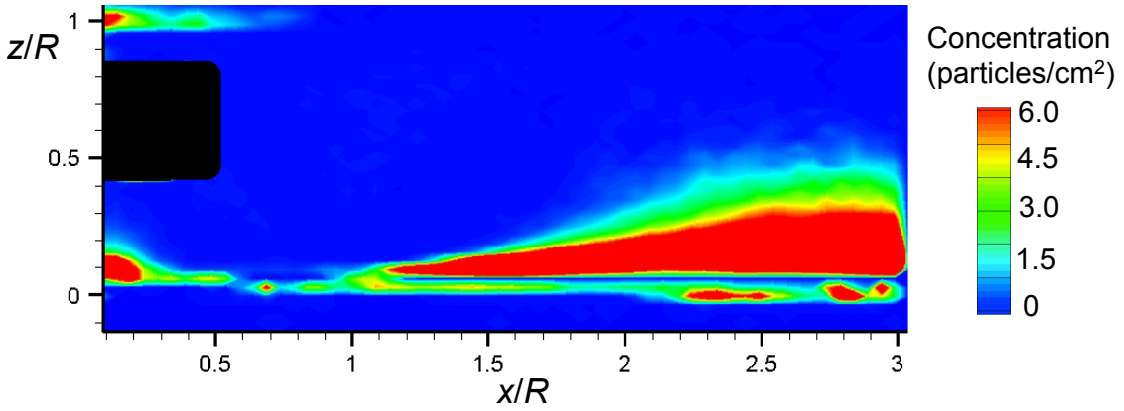

(d) Rectangular body

Figure 3.92: (Concluded) Dispersed-phase particle concentrations for the isolated rotor and at the nose of each body.

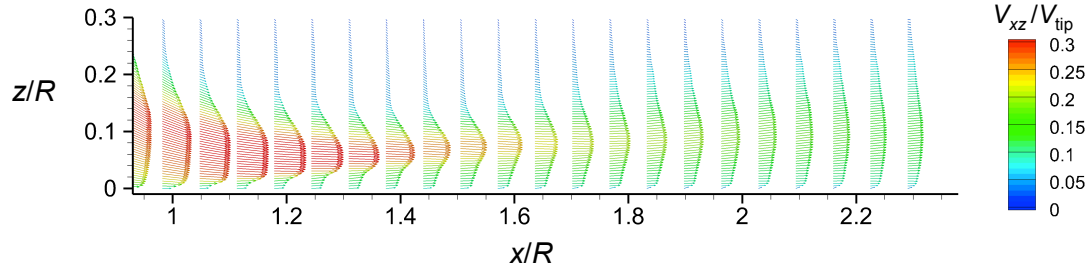

(a) Isolated rotor

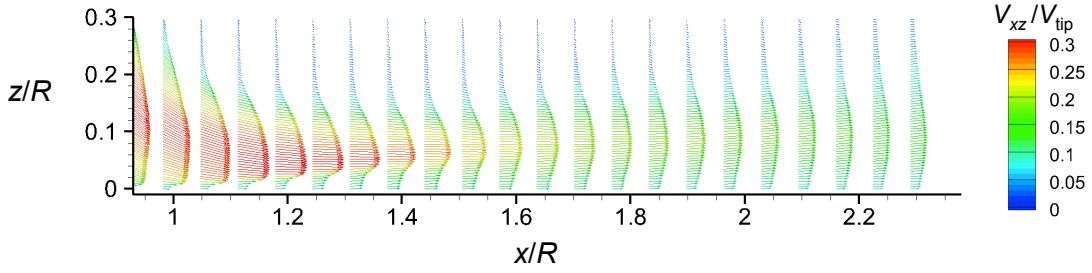

(b) Circular body

Figure 3.93: Time-averaged total velocity profiles of the carrier-phase in a near-wall region for the isolated rotor and at the nose of the circular body.

with the bodies present were clearly similar to that of the isolated rotor. Incipient motion of the particles began at a radial distance of $x/R \approx 1.0$, and the particles reached a height of up to $z/R \approx 0.5$ above the bed in this case.

The carrier-phase flow was also time-averaged over 1,000 contiguous PIV realizations, and the resulting total velocity field in the near-wall region for the isolated rotor and for the case with the circular body present is shown in Fig. 3.93. Again, the results with the circular body (which was representative of all three bodies) were similar to the isolated rotor case. As discussed previously (Section 3.1.2.1), there was a coupling between the carrier-phase and dispersed-phase of the flows, with the wall-jet flow being defected above the saltation layer.

3.3.2.2 Results at the Tail

In the tail region, the single-phase results have shown that the flows produced with the bodies present contained more significant differences to those produced by the isolated rotor (see Fig. 3.84), suggesting that differences could also be expected in the dual-phase flow environment. Figures 3.94 and 3.95 show instantaneous dual-phase flow realizations and corresponding time-averaged particle concentrations, respectively, that were produced in ROI 1 by the isolated rotor and also with the bodies present.

The results clearly show differences in all four cases. Of particular interest, is that the isolated rotor flow uplifted fewer particles into suspension than when the bodies were present. While this observation may seem unexpected, it was a consequence of the higher peak velocities that were produced at the ground by the isolated rotor, as shown in Fig. 3.96. These higher flow velocities convected the particles more radially outward before they could be picked up and suspended by the tip vortices. With the bodies present, however, the near-wall flow reached a lower peak velocity at all radial locations downstream of the rotor. While the wall-parallel velocity was still sufficiently high to mobilize the particles, the near-wall flow did not convect the entrained particles radially outward as rapidly or as far as those by the isolated rotor. Instead, the vortical flow near the wall (which contained less coherent vorticity than found with the isolated rotor) resulted in more particles being uplifted into suspension. A comparison of the results shown in Fig. 3.94 indicates that the flows caused by the presence of the rectangular body, which produced the lowest peak velocity near the wall, resulted in more particles being uplifted into suspension and these particles were also closer to the rotor. A similar result was

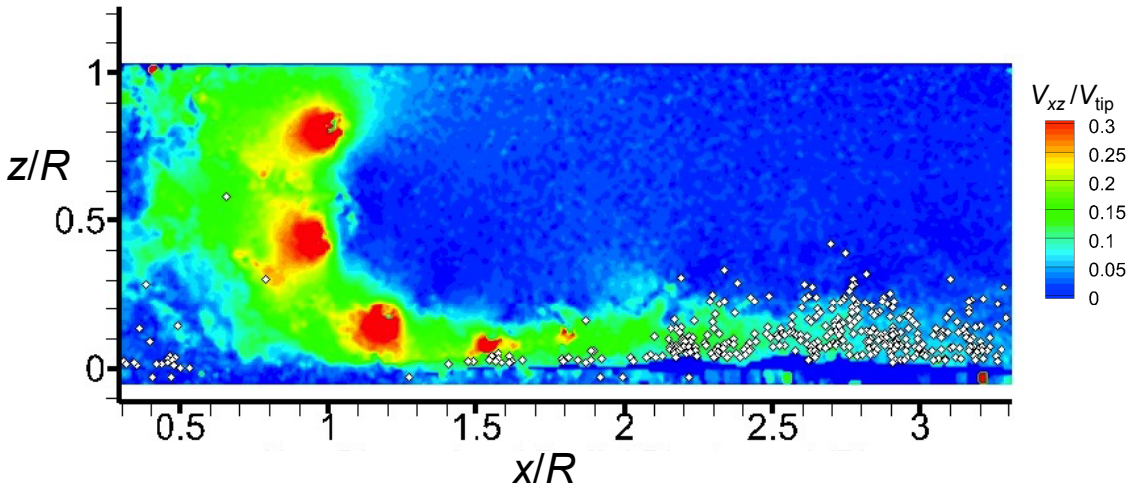

(a) PIV/PTV measurements for the isolated rotor

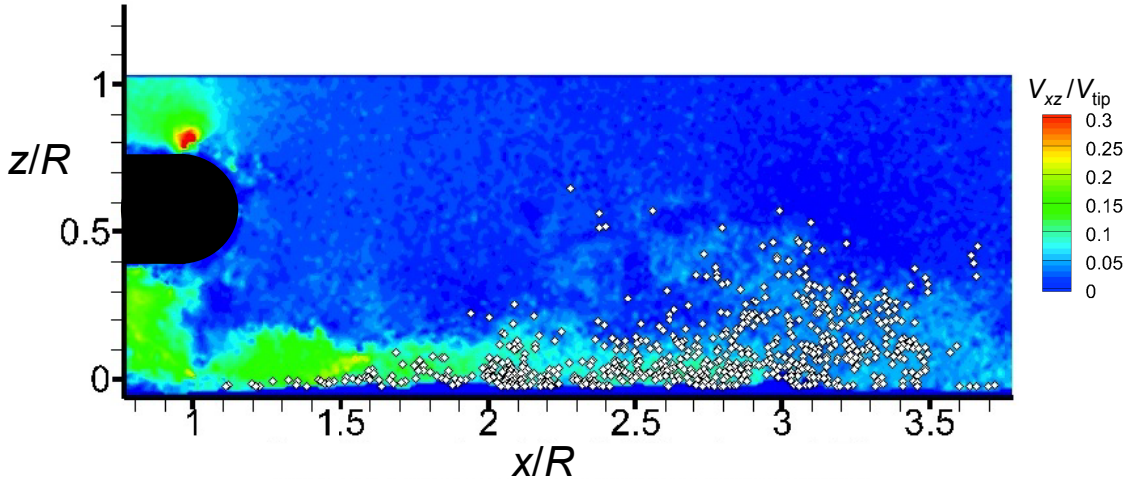

(b) PIV/PTV measurements for the circular body

Figure 3.94: Instantaneous dual-phase PIV/PTV measurements for the isolated rotor and at the tail of each body.

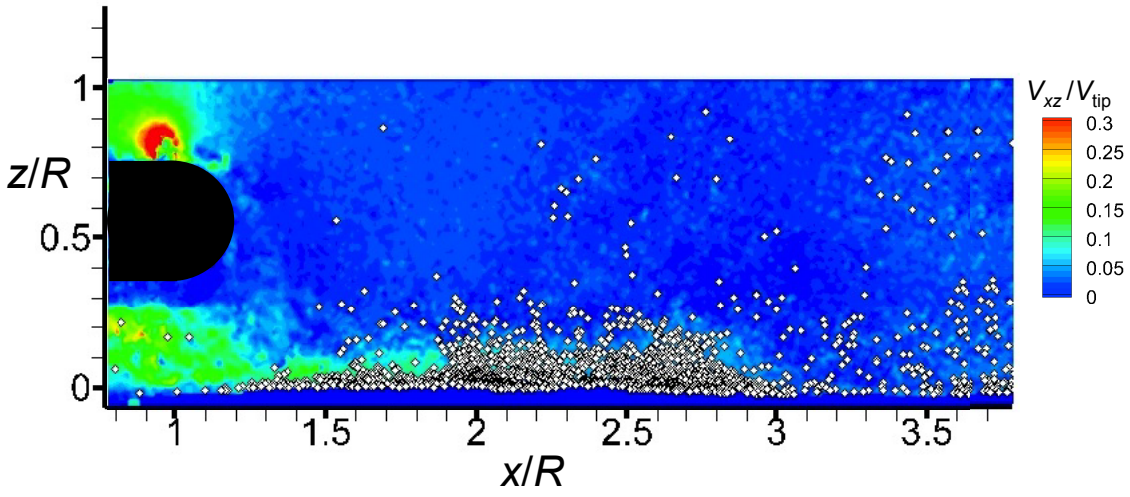

(c) PIV/PTV measurements for the elliptical body

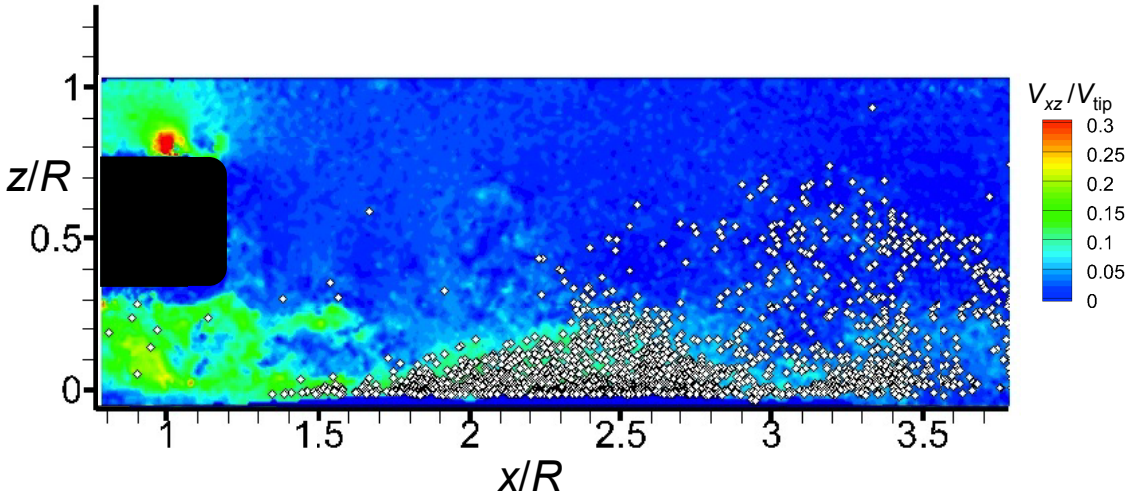

(d) PIV/PTV measurements for the rectangular body

Figure 3.94: (Concluded) Instantaneous dual-phase PIV/PTV measurements for the isolated rotor and at the tail of each body.

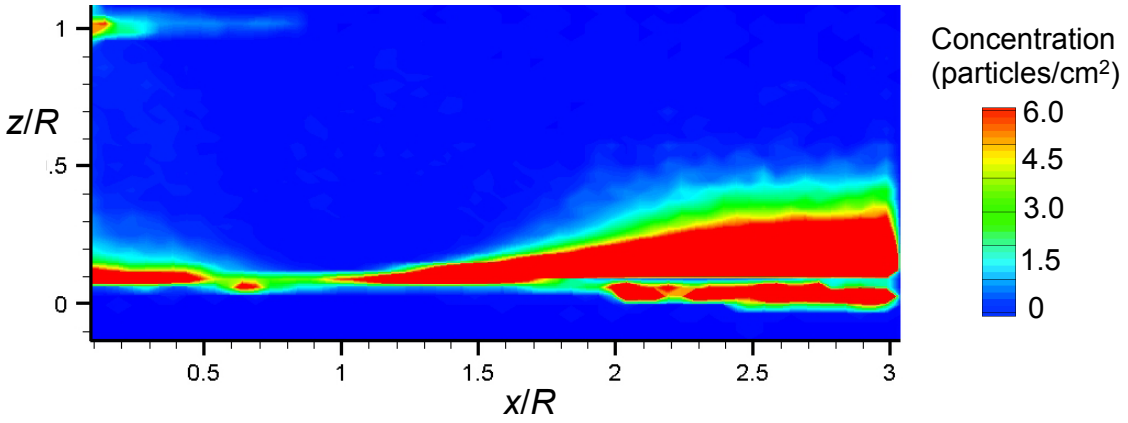

(a) Particle concentration for the isolated rotor

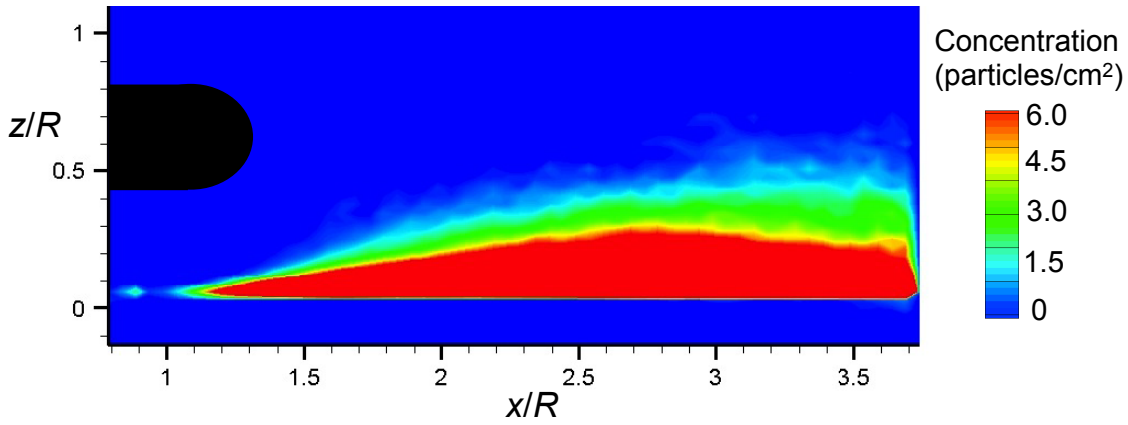

(b) Particle concentration for the circular body

Figure 3.95: Time-averaged particle concentrations for the isolated rotor and at the tail of each body.

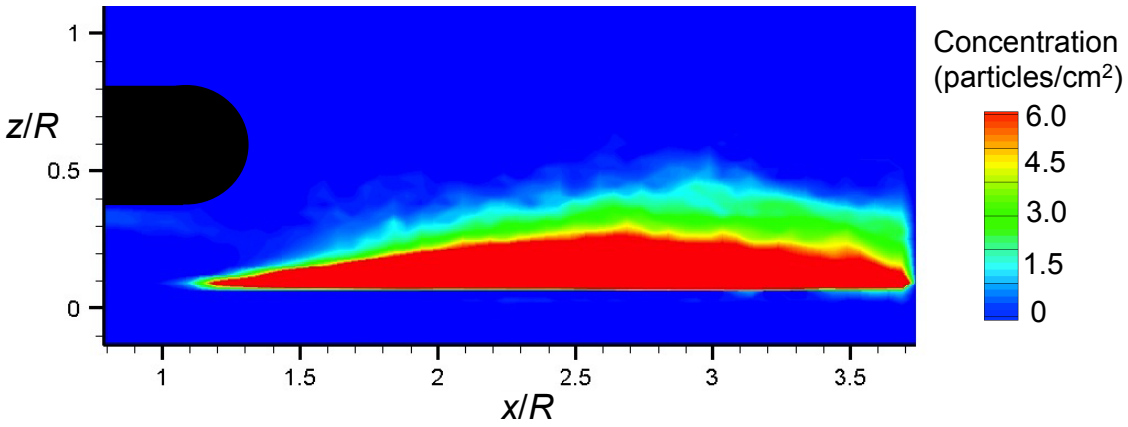

(c) Particle concentration for the elliptical body

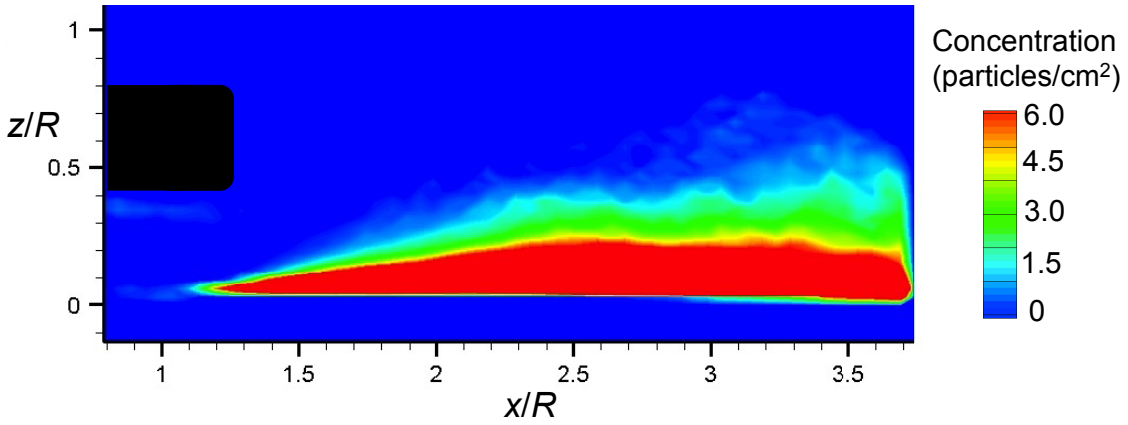

(d) Particle concentration for the rectangular body

Figure 3.95: (Concluded) Time-averaged particle concentrations for the isolated rotor and at the tail of each body.

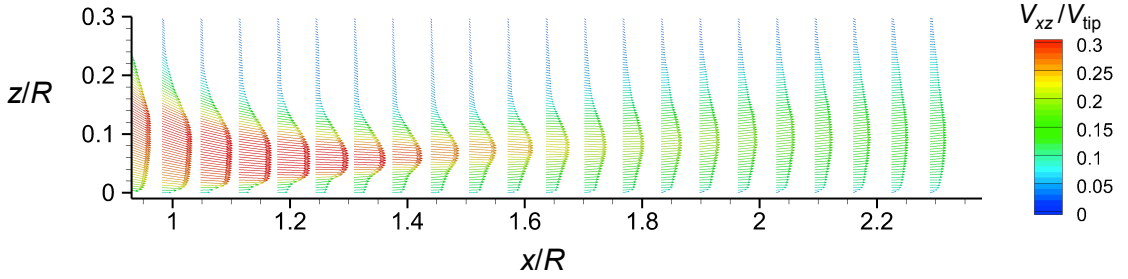

(a) Isolated rotor

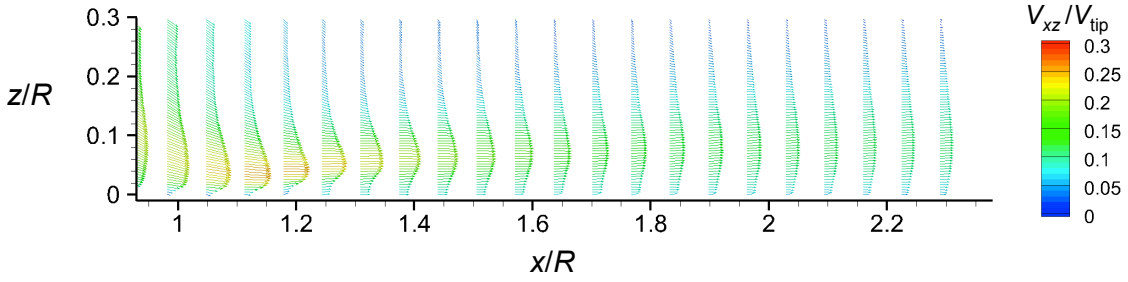

(b) Circular body

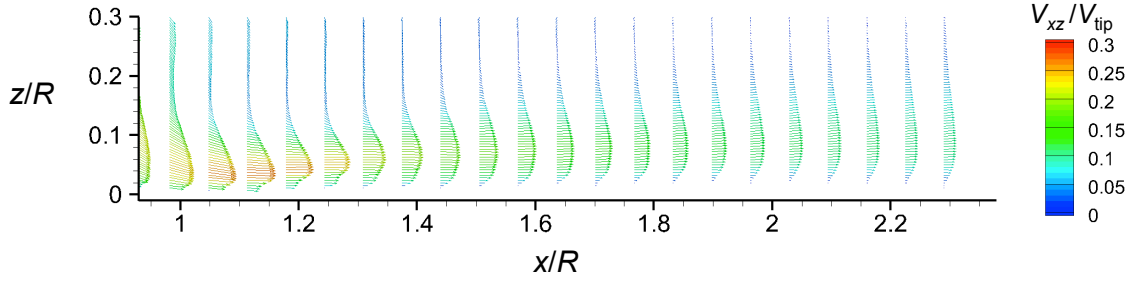

(c) Elliptical body

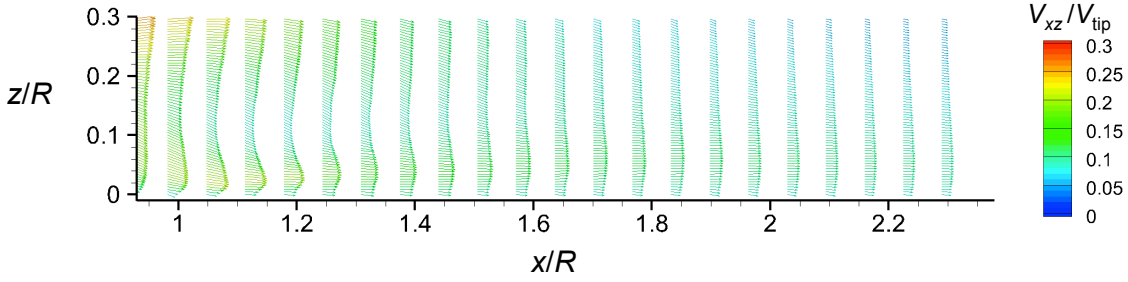

(d) Rectangular body

Figure 3.96: Time-averaged total velocity of the carrier phase in a near-wall region for the isolated rotor and at the tail of each body.

observed in Section 3.2.2, where the higher wall-jet velocities caused by higher values of disk loading convected particles radially outward before they could be uplifted.

3.3.2.3 Three-Dimensional Particle Field

Measurements made in the vertical plane showed that the particle concentrations varied between the flows produced by the isolated rotor and with the bodies in the rotor wake. However, the distinct differences seen in the flow velocities in the near-wall horizontal plane, as shown previously in Fig. 3.89, will change the boundary layer shear stress on the entire sediment bed (as shown previously in Section 3.1.1.3), and will ultimately alter the entrainment, mobilization, and uplift of the sediment particles.

For the cases with a body present in the rotor wake, dual-phase flow measurements were taken in a horizontal plane located at $z/R = 0.3$, where the previous measurements have suggested relatively high concentrations of suspended particles that were above the saltation layer (see previously in Fig. 3.52). Time-averaged particle concentration maps are shown in Fig. 3.97 for the isolated rotor and with the three bodies present in turn. The planar distribution of the dispersed-phase was clearly different between all the flows.

The particle concentrations measured with the isolated rotor indicated that particles were uplifted and suspended beginning at $x/R = 2.4$ and continuing downstream. With the bodies present, however, the particles appeared to be suspended closer to the tail region of the bodies at $x/R \approx 1.0$. Of particular interest, is that these suspended particles were in proximity to the localized flow produced near the tails of the bodies. The localized increase in velocity where the flow impinged on the bed also caused more particles to be

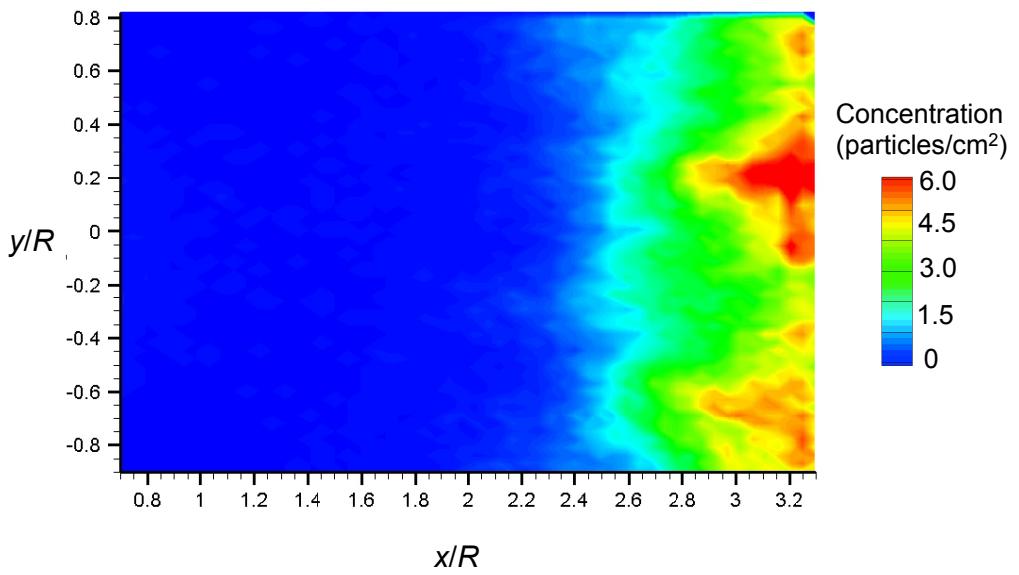

(a) Particle concentration for the isolated rotor

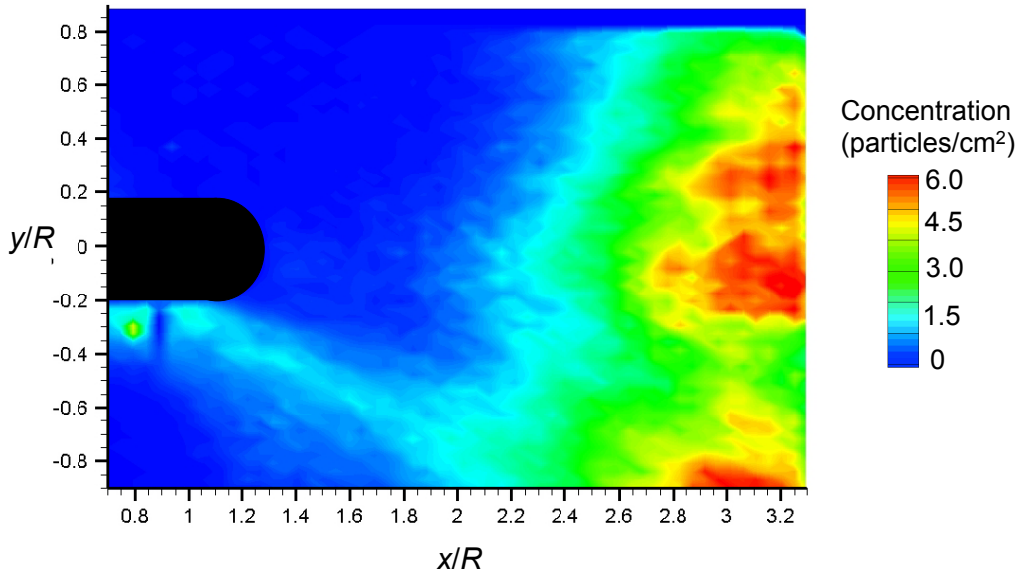

(b) Particle concentration for the circular body

Figure 3.97: Time-averaged particle concentration and instantaneous PTV measurements at $z/R = 0.3$ for the isolated rotor and at the tail of each body.

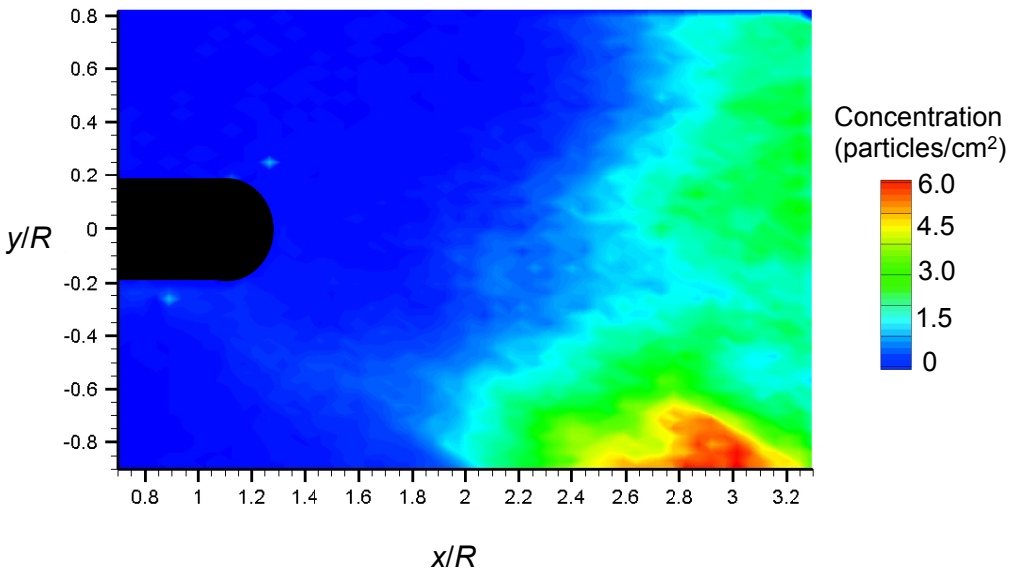

(c) Particle concentration for the elliptical body

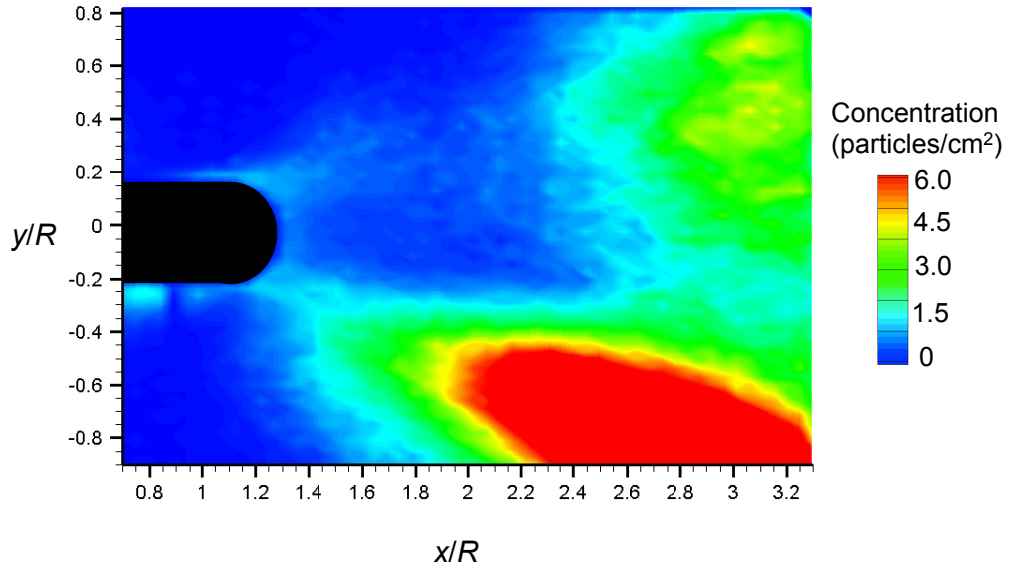

(d) Particle concentration for the rectangular body

Figure 3.97: (Concluded) Time-averaged particle concentration and instantaneous PTV measurements at $z/R = 0.3$ for the isolated rotor and at the tail of each body.

mobilized closer to the rotor. Consequently, the flow caused by the presence of the rectangular body, which had the lowest values of this localized velocity, resulted in the highest concentrations of suspended particles. In general, it was found that the flows produced with the bodies present created significantly more non-uniform particle concentrations with particles that were also uplifted closer to the rotor.

3.3.3 Summary of Body Shape Results

The foregoing results have shown that all of the bodies tested generally distorted the development of the rotor wake, which resulted in different flow velocities on the ground compared to those produced by the isolated rotor. For example, a localized flow containing relatively high velocities was observed at the tail region of each of the bodies. This localized flow was a consequence of the fluid dynamic interactions between the rotor-induced flow and the body. It was found that the isolated rotor produced a flow at the ground with a relatively high outward velocity that conveyed the sediment particles further downstream before they were uplifted by the blade tip vortices. The lower velocities produced at the ground with the bodies present resulted in some particles being uplifted closer to the rotor before they could be convected outward. As such, the rectangular body shape, which caused the lowest flow velocities at the ground, showed the highest concentration of suspended particles near the rotor.

Chapter 4

Conclusions

4.1 Summary

Time-resolved flow visualization, particle image velocimetry, and particle tracking velocimetry were performed to better understand the flows induced by a rotor that was operating over a ground plane and also over a plane covered with a mobile sediment bed, respectively. The main goal of the work was to characterize the fundamental flow physics associated with the rotor wake interactions with the ground plane and to understand how the rotor wake uplifted the sediment particles from the bed. Experiments were performed on one-bladed and two-bladed rotors operating with both matched disk loadings and also with matched blade loading coefficients, which gave different effects. The wake distortions caused by the presence of an airframe were also investigated by examining three different bodies with different cross-sectional shapes that were placed under the rotor, in turn. Dual-phase flow measurements were made in both vertical and horizontal planes to quantify the three-dimensionality of the rotor wake and induced particle field for all the different combinations of test conditions. Particular emphasis was placed on documenting the development of the blade tip vortices and how their behaviour in the flow led to the formation of a highly three-dimensional particle field.

4.2 Specific Conclusions

The following conclusions have been drawn from the research that was conducted:

4.2.1 Single-Phase and Dual-Phase Flow

1. The presence of the blade tip vortices near the wall caused the boundary layer to locally thicken and sometimes separate from the ground or bed, introducing secondary vorticity into the near-wall flow. This secondary vorticity was then entrained into the flow induced by the pairing and merging process that occurred between adjacent turns of the helicoidal vortex filaments. This complex flow environment induced by the interactions between the near-wall vortical structures was found to strongly influence the resultant particle field.

2. The near-wall flow environment near the ground was found to be highly three-dimensional. The vortex filaments impinged radially asymmetrically on the ground, with the older parts of the filament impinging first. After the impingement interactions, adjacent turns of the helical vortices were often seen to pair and merge locally along their lengths, causing significant three-dimensional variations in the local flow velocities throughout the near-wall region.

3. The blade tip vortices contributed significantly to the mobilization and uplift of sediment from the bed on the ground below the rotor. The proximity of the vortices to the wall caused a local increase in shear stress that exceeded the threshold conditions needed to mobilize the sediment particles. Furthermore, the height of the

vortex filament above the bed and the merging of adjacent vortices induced large transient fluctuations in the near-wall flow velocities. These transient fluctuations affected the quantities of particles within individual uplift events and also the height to which they were suspended.

4. Wave-like displacements were observed along the lengths of the vortex filaments; parts of the vortex filaments were found to convect closer to the ground plane or bed than other parts. The consequence of these wave-like displacements was that they induced locally higher near-wall velocities, often resulting in the discrete uplift of sediment particles into vertical or columnar plumes. These wave-like displacements, along with the structure of the tip vortices along their lengths, was found to be the primary reason for the formation of the non-uniform particle field.

5. The various particle mobilization mechanisms all significantly affected the overall three-dimensional particle field. Uplifted particles that were convected closer to the rotor disk were often reingested by the rotor and then bombarded back onto the sediment bed. These bombardments caused the ejection of many more particles into the near-wall flow region, which then rapidly expanded away from the rotor in both the azimuthal and radial directions. This latter process formed a broad, unsteady saltation layer over much of the sediment bed from which mobile particles could be readily uplifted by the induced flow of nearby sections of the vortex filaments.

4.2.2 Effects of Rotor Operating Condition

1. The disk loading and the blade loading coefficient were both found to alter the characteristics of the near-wall flow. Matching the disk loading between the two rotors caused the rotors to induce similar near-wall velocity profiles, even though the one-bladed rotor produced a relatively stronger tip vortex filaments. Matching the blade loading coefficient between the two rotors caused the vortex filaments to be of nominally the same strength, however, the two-bladed rotor still produced significantly higher near-wall flow velocities.

2. The near-wall flow velocities, tip vortex strengths, and wake shedding frequency were all found to affect the mobilization and transport of sediment particles. The higher wake shedding frequencies resulted in more frequent impingement of vortices on the sediment bed, which caused particles to be quickly convected radially outward and upward. Furthermore, stronger vortices also uplifted higher quantities of sediment. However, increasing the blade pitch to produce stronger vortices also increased the near-wall flow velocities, and so particles were convected further downstream before they could be suspended.

3. The relative quantity and concentration of particles uplifted by the one-bladed and two-bladed rotors when operating with matched values of disk loading and also with matched values of blade loading coefficient were found to be highly dependent on both the particle concentrations and overall geometry of the particle cloud. The two-bladed rotor uplifted more sediment particles, however because they were convected downstream before they were uplifted, the relatively higher levels of par-

ticle concentration occurred further away from the rotor. However, measurements with rotors with three and four bladed rotors would be needed before more definitive conclusions could be drawn on the effects of the number of blades.

4.2.3 Effects of Body Shape

1. In general, rotor wake/body interactions affected the flow at the ground. All of the bodies tested generally distorted the development of the rotor wake, resulting in different near-wall flow velocities compared to those produced by the isolated rotor. The isolated rotor produced a flow at the ground with a relatively high outward velocity that conveyed the sediment particles further downstream before they were uplifted by the blade tip vortices. The lower velocities produced at the ground with the bodies present resulted in some particles being uplifted closer to the rotor before they could be convected outward.

2. When blade tip vortices impinged on the body surface, part of the continuous helicoidal filament formed a loop around the surface, initially intensifying its local vorticity. The filament was ultimately stretched to a point where it could no longer sustain a coherent vortex core, causing bursting and the rapid diffusion of the vorticity. The resulting turbulent flow then became entrained into the rotor wake and was convected downstream towards the ground, which caused significantly high wall-normal fluctuations near the ground that were capable of uplifting sediment particles.

3. A localized flow with a relatively high velocity was observed at the tail region of

each of the bodies. This local flow appeared to be a consequence of the interaction between the rotor-induced flow in the swirl direction and the body. This local flow was found to vary somewhat in magnitude and direction for each of the three bodies. This phenomenon also affected the flow produced at the ground, causing a localized region of higher flow velocities that resulted in more particle uplift and suspension closer to the rotor.

4. The three-dimensional variations in the flow at the ground produced by the presence of the bodies manifested as non-uniform concentrations of uplifted particles. Differences in the wake distortion caused by each body shape resulted in a unique distribution of the suspended particles for each flow. The particle concentrations produced by the flow of the isolated rotor were found to be more radially symmetric, with higher particle concentrations being found farther away from the rotor.

4.3 Suggestions for Future Work

The present research has improved the understanding of the flow physics involved in the problem of rotor-induced particle motion. This research has also identified examined the effects of placing a body in the rotor wake and the interdependent effects of rotor operating condition on the development of the particle field. However, there remains several avenues of research that can provide a better understanding of rotor-induced particle motion.

The following are elements of future work on the problem that are recommended:

1. The present work has only performed an initial investigation of how the rotor disk

loading, blade loading coefficient, and wake shedding frequency have affected the mobilization and transport of sediment particles. While some general trends were noticed, more data are required to fully characterize the effects of varying these operating parameters. It is recommended that future work should include wider variations in disk loadings and blade loading coefficients, as well as examining a larger numbers of blades (e.g., three-bladed and four-bladed rotors). Field tests have shown that rotorcraft with more blades appear to produce fewer discrete structures in the resultant dust cloud, and so an investigation of varying operating conditions for three-bladed and four-bladed rotors may expose detailed flow interactions that contribute to the problem of rotor-induced particle motion.

2. This research has provided a large database of time-resolved measurements for a laboratory-scale rotor that is hovering over a ground plane and over a mobile sediment bed. Because it is impractical to perform single-phase or dual-phase flow measurements for every combination of operating conditions, CFD models should be developed and validated against the data set that has been generated in the current work. These models can then be used to extrapolate the results to more representative of full-scale rotorcraft that are operating under brownout conditions.

3. The present measurements dissected the flow field into multiple planar regions to extract the three-dimensional aspects of the flow, however, these imaging regions were not correlated in time. It would be useful to simultaneously measure the flow velocities over a volumetric region of the flow. Recent technological developments in laser-based measurement techniques are becoming available to perform these

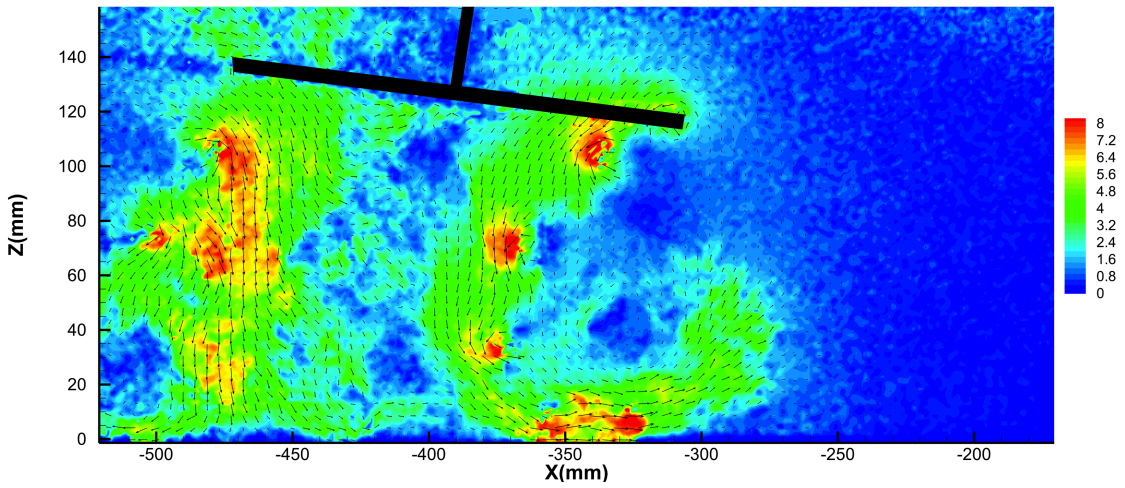

Figure 4.1: Instantaneous PIV flow realization of a rotor performing a taxi maneuver over a ground plane.

types of volumetric PIV measurements in a single-phase flow environment, and potentially in a dual-phase environment. Initial tests can be performed in a phase-resolved manner, and as the technology matures then time-resolved measurements can be made.

4. In practice, rotorcraft rarely hover directly over a sediment bed; rotorcraft are generally performing some sort of takeoff or landing maneuver near the ground. Initial experiments have been performed that have examined a laboratory-scale rotor performing vertical landing profiles and simulated taxiing maneuvers over a mobile sediment bed. For example, Figure 4.1 shows a rotor performing a simulated taxiing maneuver over a sediment bed. Notice that the vortices in front of the rotor bundle together to form a large ground vortex upstream of the rotor. This ground vortex will likely mobilize and uplift large quantities of dust, more so than for a hovering rotor. Therefore, it is recommended that a thorough investigation of the

single-phase and dual-phase environments caused by a moving rotor be thoroughly investigated in a controlled laboratory environment.

5. Rotorcraft come in a number of configurations, and rotorcraft of the future are less likely to be of the single main rotor configuration. Therefore, it would be useful to perform single-phase and dual-phase measurements of different rotorcraft configurations (e.g., tandem, coaxial, side-by-side rotors, etc.). The interaction between the multiple rotor wakes will create a complicated flow that will affect the mobilization and transport of sediment particles. Simulations have shown that different configurations produce different brownout signatures, however, the rotor wakes produced by multiple rotor configurations have not yet been investigated experimentally.

Appendix A: Sediment Particles

An X-ray sedigraph method was used to obtain the size range of the glass microspheres. This technique involves measuring the gravity induced settling rates of different size particles in a liquid with known properties. The particle size can be calculated from the measured settling velocity using Stokes's law. The inherent assumption in this measurement technique is that the particle Reynolds number while settling must be less than 0.3 (i.e., laminar flow around a spherical particle to adhere with Stokes's law). The mass frequency for the particles was measured by directing a beam of X-rays towards the settling particles in the liquid medium. The transmittance from the particles was measured and the attenuated intensity was used to calculate the mass fraction of the particles within the measurement region. In this way, the X-ray sedigraph was able to provide both the size of the particles and the mass frequency of the glass microspheres used in the present work. The particle size distribution obtained from the sedigraph is shown in Fig. A1

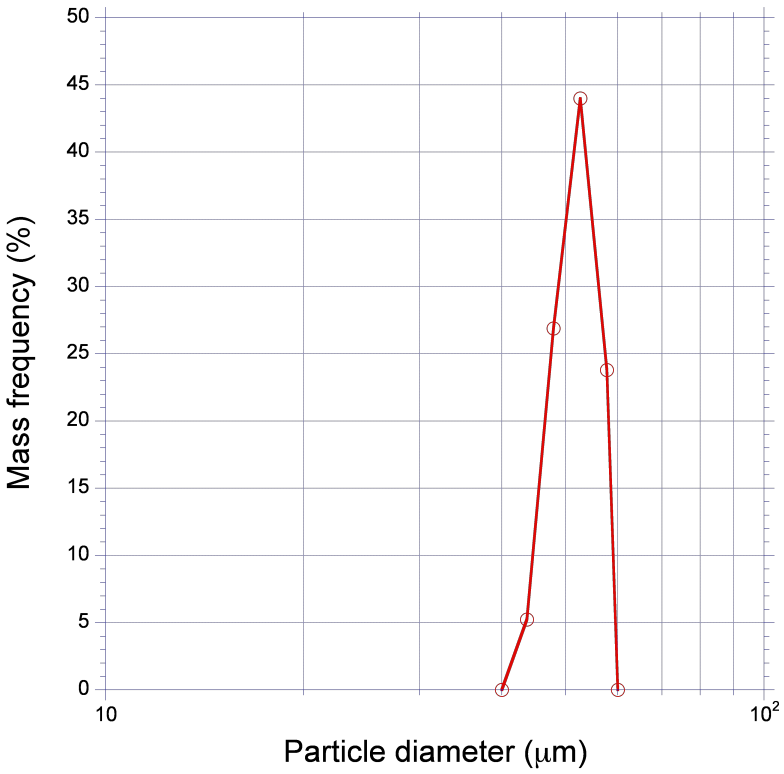

Figure A 1: Particle diameter distribution of the glass microspheres.

Appendix B: Body Shapes

Over 100 helicopters, civil and military, were examined to determine the dimensions of the fuselages and their placement under the rotor. These historical data contained measurements for helicopters over a wide range of gross weights and rotor diameters; see Fig. B2a and Fig. B2b. The dimensions of the bodies used for the present experiments were based on statistical averages of these historic data.

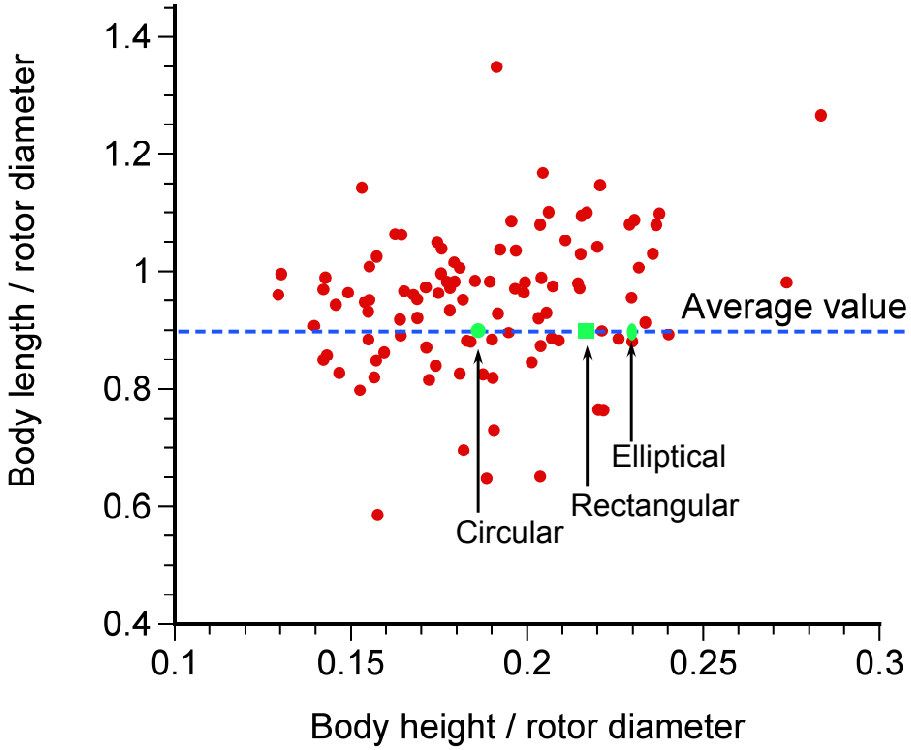

(a) Length versus height of the body

Figure B 2: Historical fuselage dimensions for helicopters and the representative dimensions of the bodies used for the current experiments.

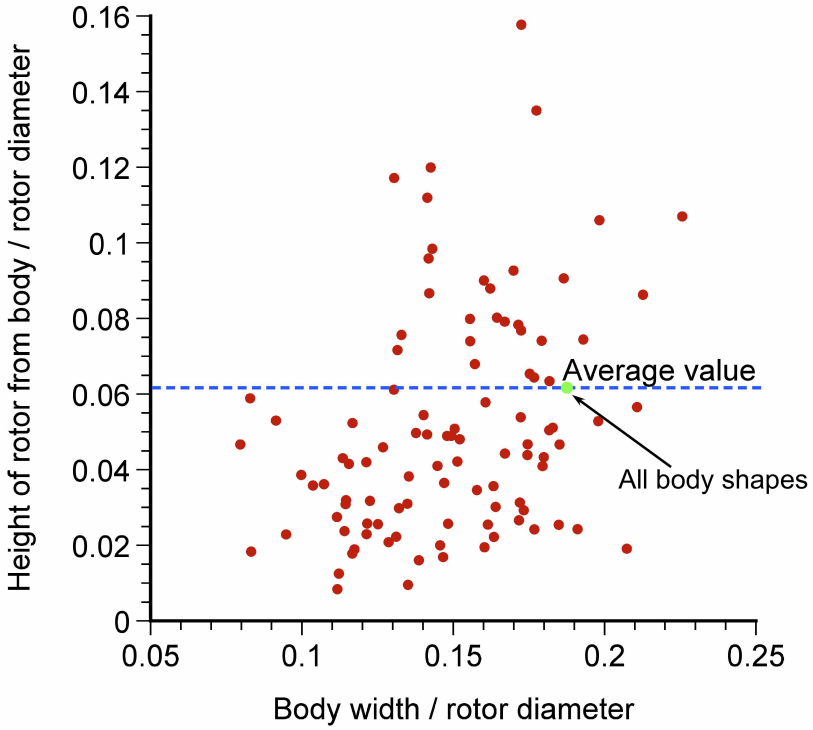

(b) Rotor/body spacing versus width of the body

Figure B 2: (Concluded) Historical fuselage dimensions for helicopters and the representative dimensions of the bodies used for the current experiments.

Appendix C: Time-Averaging

The present work has presented time-averaged quantities, including flow/particle velocities and particle concentrations. These time-averages were calculated using all the PIV/PTV measurements taken in each test case. Each run consisted of 1,000 PIV (or PIV/PTV) images that were equally spaced in time, t. Each PIV image was discretized into a two-dimensional grid, with each grid node being a measurement location denoted by the coordinate (x_i,x_j). Consider a representative flow quantity, S. This flow quantity was measured at each grid location, and so a single PIV image consisted of a two-dimensional grid with values of S at each node. As such, at a single measurement location within an instantaneous PIV image, S was a function of spatial location, (x_i,x_j), and time, t, i.e., $S(x_i,x_j,t)$. To compute the time average, $S(x_i,x_j,t)$ was averaged over the time dimension, t. Therefore, the equation for the time-average at each measurement location, $\overline{S(i,j)}$, is defined as

$$\overline{S(i,j)} = \frac{1}{1000} \sum_{t=1}^{t=1000} S(i,j,t). \tag{A0}$$

Bibliography

[1] Mapes, P., Kent, R., and Wood, R., "DoD Helicopter Mishaps FY85-05: Findings and Recommendations," Technical report, U.S. Air Force, Washington, DC, 2008.

[2] Technical report, National Transportation Safety Board, NTSB Accident Briefs: LAX01LA283, LAX01LA304, LAX04LA285, SEA05CA173.

[3] Jansen, C., Wennemers, A., and Groen, E., "FlyTact: A Tactile Display Improves a Helicopter Pilots Landing Performance in Degraded Visual Environments," *Haptics: Perception, Devices and Scenarios*, Vol. 502, (4), 2008, pp. 867–875.

[4] "Sandblaster 2 Support of See-Through Technologies for Particulate Brownout," Technical report, Task 1 Technical Report, Sponsored by Defense Advanced Research Projects Agency (DOD) Strategic Technology Office, Issued by U.S. Army Aviation and Missile Command under Contract No. W31P4Q-07-C-0215, MRI Project No. 110565, October 31, 2007.

[5] "Sandblaster 2 Support of See-Through Technologies for Particulate Brownout," Technical report, Task 5 Final Technical Report, Sponsored by Defense Advanced Research Projects Agency (DOD) Strategic Technology Office, Issued by U.S. Army Aviation and Missile Command under Contract No. W31P4Q-07-C-0215, MRI Project No. 110565, October 31, 2007.

[6] Johnson, B., Leishman, J. G., and Sydney, A., "Investigation of Sediment Entrainment in Brownout Using High-Speed Particle Image Velocimetry," American Helicopter Society 65th Annual Forum Proceedings, Grapevine, Texas, May 27–29, 2009.

[7] Sydney, A., and Leishman, J. G., "Time-Resolved Measurements of Rotor-Induced Particle Flows Produced by a Hovering Rotor," *Journal of the American Helicopter Society*, 2014 (to appear).

[8] Syal, M., and Leishman, J. G., "Modeling of Bombardment Ejections in the Rotorcraft Brownout Problem," *AIAA Journal*, Vol. 51, (4), April 2013, pp. 549–566.

[9] Knight, M., and Hefner, R. A., "Analysis of Ground Effect on the Lifting Airscrew," Technical Report 835, NACA TN, 1941.

[10] Zbrozek, J., "Ground Effect on the Lifting Rotor," Technical Report 2347, British ARC R & M, 1947.

[11] Cheeseman, I. C., and Bennett, W. E., "The Effect of the Ground on a Helicopter Rotor in Forward Flight," Technical Report 3021, ARC R M, 1955.

[12] Fradenburg, E. A., "Aerodynamic Factors Influencing Overall Hover Performance," Technical Report AGARD CP-111, 1972.

[13] Hayden, J.S., "The Effect of the Ground on Helicopter Hovering Power Required," American Helicopter Society 32th Annual National V/STOL Forum Proceedings, Washington D.C., May 10–12, 1976.

[14] Prouty, R. W., "Ground Effect and the Helicopter," AIAA Paper 85-4034, AIAA/AHS/ASEE Aircraft Design Systems and Operations Meeting, Colorado Springs, CO, October 14–16, 1985.

[15] Fradenburgh, E. A., "The Helicopter and the Ground Effect Machine," *Journal of the American Helicopter Society*, Vol. 5, (4), October 1960, pp. 26–28.

[16] Lee, T. E., Leishman, J. G., and Ramasamy, M., "Fluid Dynamics of Interacting Blade Tip Vortices With a Ground Plane," *Journal of the American Helicopter Society*, Vol. 55, (2), April 2010, pp. 1–16.

[17] Ramasamy, M., and Leishman, J. G., "Interdependence of Diffusion and Straining of Helicopter Blade Tip Vortices," *Journal of Aircraft*, Vol. 41, (5), September 2004, pp. 1014–1024.

[18] Ananthan, S., Leishman, J. G., and Ramasamy, M., "The Role of Filament Stretching in the Free-Vortex Modeling of Rotor Wakes," American Helicopter Society International 58th Annual Forum Proceedings, Montréal, Canada, June 11–13, 2002.

[19] Rauleder, J., and Leishman, J. G., "Flow Environment and Organized Turbulence Structures Near a Plane Below a Rotor," *AIAA Journal*, Vol. 52, (1), 2014, pp. 146–161.

[20] Rauleder, J., and Leishman, J. G., "Particle–Fluid Interactions in Rotor-Generated Vortex Flows," *Experiments in Fluids*, Vol. 55, (3), 2014, pp. 1–15.

[21] Bagnold, R. A., *The Physics of Blown Sand and Desert Dunes*, Dover Publications, Inc., Mineola, NY, 1941.

[22] Greeley, R., "Saltation Impact as a Means for Raising Dust on Mars," *Planetary and Space Sciences*, Vol. 50, (2), February 2002, pp. 151–155.

[23] Greeley, R., and Iversen, J. D., *Wind as a Geological Process on Earth, Mars, Venus and Titan*, Cambridge University Press, New York, NY, 1985.

[24] Greeley, R., Iversen, J. D., Marshall, J. R., and Pollack, J. B., "Aeolian Saltation Threshold: The Effect of Density Ratio," *Sedimentology*, Vol. 34, (4), 1987, pp. 699–706.

[25] Greeley, R., Balme, M. R., Iversen, J. D., Metzger, S., Mickelson, R., Phoreman, J., and White, B., "Martian Dust Devils: Laboratory Simulations of Particle Threshold," *Journal of Geophysical Research (Planets)*, Vol. 108, (E5, 5041), May 2003, pp. 1–11.

[26] Johnson, B., Leishman, J. G., and Sydney, A., "Investigation of Sediment Entrainment Using Dual-Phase, High-Speed Particle Image Velocimetry," *Journal of the American Helicopter Society*, Vol. 55, (4), 2010, pp. 1–16.

[27] Milluzzo, J., and Leishman, J. G., "Assessment of Rotorcraft Brownout Severity in Terms of Rotor Design Parameters," *Journal of the American Helicopter Society*, Vol. 55, (3), October 2010, pp. 032009–1–9.

[28] Wong, O. D., and Tanner, P. E., "Photogrammetric Measurements of an EH-60L Brownout Cloud," 67th Annual Forum Proceedings of the American Helicopter Society, May 10–13, 2010.

[29] Rodgers, S. J., "Evaluation of the Dust Cloud Generated by Helicopter Rotor Downwash," Technical Report under Contract DA 44-177-AMC-289(T), USA AV LABS Technical Report, Issued by U.S. Army Aviation Material Laboratories, Fort Eustis, VA, March 1968.

[30] Gillies, J. A., Etyemezian, V., Kuhns, H., McAlpine, J. D., King, J., Uppapalli, S., Nikolich, G., and Engelbrecht, J., "Dust Emissions Created by Low-Level Rotary-Winged Aircraft Flight Over Desert Surfaces," *Atmospheric Environment*, Vol. 44, (8), 2010, pp. 1,043–1,053.

[31] Tanner, P. E., "Photogrammetric Characterization of a Brownout Cloud," 67th Annual Forum Proceedings of the American Helicopter Society, Virginia Beach, VA, May 3–5, 2011.

[32] Haehnel, R. B., Moulton, M. A., Wenren, W., and Steinhoff, J., "A Model to Simulate Rotorcraft-Induced Brownout," American Helicopter Society 64th Annual Forum Proceedings, Montréal, Canada, April 29–May 1, 2008.

[33] Phillips, C., and Brown, R.E., "Eulerian Simulation of the Fluid Dynamics of Helicopter Brownout," *Journal of Aircraft*, Vol. 46, (4), July 2009, pp. 1416–1429.

[34] D'Andrea, A., "Numerical Analysis of Unsteady Vortical Flows Generated by a Rotorcraft Operating on Ground: A First Assessment of Helicopter Brownout," American Helicopter Society 65th Annual Forum Proceedings, Grapevine, Texas, May 27–29, 2009.

[35] D'Andrea, A., "Unsteady Numerical Simulations of Helicopters and Tiltrotors Operating in Sandy-Desert Environments," Proceedings of the American Helicopter Society Specialists Conference on Aeromechanics, San Francisco, CA, January 20–22, 2010.

[36] D'Andrea, A., "Enhanced Numerical Simulations of Helicopter Landing Maneuvers in Brownout Conditions," 66th Annual Forum Proceedings of the American Helicopter Society, Phoenix, AZ, May 11–13, 2010.

[37] D'Andrea, A., "Development and Application of a Physics-Based Computational Tool to Simulate Helicopter Brownout," Proceedings of the 37th European Rotorcraft Forum, Gallarate (VA), Italy, September 13–15, 2011.

[38] Syal, M., Govindarajan, B., and Leishman, J. G., "Mesoscale Sediment Tracking Methodology to Analyze Brownout Cloud Developments," 66th Annual Forum of the American Helicopter Society, Phoenix, AZ, May 10–13, 2010.

[39] Thomas, S., Lakshminarayan, V. K., Kalra, T. S., and Baeder, J. D., "Eulerian-Lagrangian Analysis of Cloud Evolution using CFD Coupled with a Sediment Tracking Algorithm," 67th Annual Forum Proceedings of the American Helicopter Society, Virginia Beach, VA, May 3–5, 2011.

[40] Kalra, T., Lakshminarayan, V., and Baeder, J., "CFD Validation of Micro Hovering Rotor in Ground Effect," AHS International Specialists Conference Proceedings on Aeromechanics, San Francisco, CA, January 2010.

[41] Whitehouse, G. R., Wachspress, D. A., Quackenbush, T. R., and Keller, J. D., "Exploring Aerodynamic Methods for Mitigating Brownout," American Helicopter Society 65th Annual Forum Proceedings, Grapevine, TX, May 27–29, 2009.

[42] Tritschler, J., Syal, M., Celi, R., and Leishman, J. G., "A Methodology for Rotor Design Optimization for Rotorcraft Brownout Mitigation," 66th Annual Forum Proceedings of the American Helicopter Society, Phoenix, AZ, May 10–13, 2010.

[43] Tritschler, J., Syal, M., Celi, R., and Leishman, J. G., "The Effect of Number of Blades on Optimum Rotor Design for Brownout Mitigation," Future Vertical Lift Aircraft Design Conference, San Francisco, CA, January 18–20, 2012.

[44] Morales, F. Naqvi, I., Squires, K. D., and Piomelli, U., "Euler-Lagrange Simulations of Particle Interactions with Coherent Vortices in Turbulent Boundary Layers," *Bulletin of the American Physical Society*, Vol. 54, (19), 2009.

[45] Morales, F., and Squires, K. D., "Numerical Analysis of Unsteady Vortical Flows Generated by a Rotorcraft Operating on Ground: A First Assessment of Helicopter Brownout," Proceedings of the 29th AIAA Applied Aerodynamics Conference, Honolulu, HI, June 27–30, 2011.

[46] Syal, M., *Development of a Lagrangian-Lagrangian Methodology to Predict Brownout Dust Clouds*, Doctor of philosophy, Department of Aerospace Engineering, University of Maryland, College Park, MD, 2012.

[47] Syal, M., and Leishman, J. G., "Predictions of Brownout Dust Clouds Compared to Photogrammetric Measurements," *Journal of the American Helicopter Society*, Vol. 58, (1), 2013, pp. 1–18.

[48] Lakshminarayan, V. K., "Computational Investigation of Micro-Scale Coaxial Rotor Aerodynamics in Hover," Technical report, Ph.D. dissertation, Department of Aerospace Engineering, University of Maryland at College Park, USA, 2009.

[49] Tritschler, J. K., *Contributions to the Characterization and Mitigation of Rotorcraft Brownout*, Doctor of philosophy, Department of Aerospace Engineering, University of Maryland, College Park, MD, 2012.

[50] Syal, M., Rauleder, J., Tritschler, J. K., and Leishman, J. G., "On the Possibilities of Brownout Mitigation Using a Slotted-Tip Rotor Blade," 29th AIAA Applied Aerodynamics Conference, Honolulu, Hawaii, June 27–30, 2011.

[51] Han, O. Y., and Leishman, J. G., "Experimental Investigation of Tip Vortex Alleviation Using a Slotted Tip Rotor Blade," *AIAA Journal*, Vol. 42, (4), 2004, pp. 523–535.

[52] Milluzzo, J., Sydney, A., Rauleder, J., and Leishman, J. G., "In-Ground-Effect Aerodynamics of Rotors with Different Blade Tips," 66th Annual Forum Proceedings of the American Helicopter Society, Phoenix, AZ, May 10–13, 2010.

[53] Light, J. S., and Norman, T., "Tip Vortex Geometry of a Hovering Helicopter Rotor in Ground Effect," American Helicopter Society 45th Annual Forum Proceedings, Boston, MA, May 22–24, 1989.

[54] Ramasamy, M., and Leishman, J. G., "Turbulent Tip Vortex Measurements Using Dual-Plane Stereoscopic Particle Image Velocimentry," *AIAA Journal*, Vol. 47, (8), August 2009, pp. 1826–1840.

[55] Ramasamy, M., Johnson, B., and Leishman, J. G., "Understanding the Aerodynamic Efficiency of a Hovering Micro-Rotor," *Journal of the American Helicopter Society*, Vol. 53, (4), October 2008, pp. 412–428.

[56] Reel, J. L., *Mechanisms of Vortex-Induced Particle Transport from a Mobile Bed Below a Hovering Rotor*, M.S. thesis, Department of Aerospace Engineering, University of Maryland, College Park, MD, 2014.

[57] Nathan, N. D., and Green, R. B., "Measurements of a Rotor Flow in Ground Effect and Visualisation of the Brown-out Phenomenon," American Helicopter Society 64th Annual Forum Proceedings, Montréal, Canada, April 29–May 1, 2008.

[58] Crouse, G.L., Leishman, J.G., and Bi Nai-pei, "Theoretical and Experimental Study of Unsteady Rotor/Body Aerodynamic Interactions," *Journal of the American Helicopter Society*, Vol. 37, (1), January 1992, pp. 55–65.

[59] Bi, Nai-pei, Leishman, J. G., and Crouse, G. L., "Investigation of Rotor Tip Vortex Interactions with a Body," *Journal of Aircraft*, Vol. 30, (6), Nov.–Dec. 1993, pp. 879–888.

[60] Bagai, A., and Leishman, J. G., "A Study of Rotor Wake Development and Wake/Body Interactions in Hover using Wide-Field Shadowgraphy," *Journal of the American Helicopter Society*, Vol. 37, (4), October, 1992, pp. 48–57.

[61] Hance, B. T., *Effects of Body Shapes on Rotor In-Ground-Effect Aerodynamics*, M.s. thesis, Department of Aerospace Engineering, University of Maryland, College Park, MD, 2012.

[62] Taylor, M. K., "A Balsa-Dust Technique for Air-Flow Visualization and Its Application to Flow Through Model Helicopter Rotors in Static Thrust," Technical Report 2220, NACA TN, 1950.

[63] Curtiss, H. C., Sun, M., Putman, W. F., and Hanker, E. J., "Rotor Aerodynamics in Ground Effect at Low Advance Ratios," *Journal of the American Helicopter Society*, Vol. 29, (1), 1984, pp. 48–55.

[64] Geiser, J., and Kiger, K., "A Simplified Analog for a Rotorcraft-in-Ground-Effect Flow Using a Forced Impinging Jet," 63rd Annual Meeting of the APS Division of Fluid Dynamics, Long Beach, CA, November 21–23, 2010.

[65] Geiser, S. J., *Effects of Wall Plane Topology on Vortex-Wall Interactions in a Forced Impinging Jet*, M.s. thesis, Department of Mechanical Engineering, University of Maryland, College Park, MD, 2010.

[66] Leishman, J. G., *Principles of Helicopter Aerodynamics*, Cambridge University Press, New York, NY, 2006.

[67] Shao, Y., Raupach, M. R., and Findlater, P. A., "Effect of Saltation Bombardment on the Entrainment of Dust by the Wind," *Journal of Geophysical Research*, Vol. 98, (D7), February 1993, pp. 12,719–12,726.

[68] Shao, Y., and Lu, H., "A Simple Expression for Wind Erosion Threshold Friction Velocity," *Journal of Geophysical Research*, Vol. 105, (D17), 2000, pp. 22,437–22,443.

[69] Shao, Y., "A Model for Mineral Dust Emission," *Journal of Geophysical Research*, Vol. 106, (D17), September 2001, pp. 20,239–20,254.

[70] Haehnel, R., and Dade, W. B., "Physics of Particle Entrainment Under the Influence of an Impinging Jet," Army Science Conference Proceedings, Orlando, FL, 2008.

[71] Mulinti, R., and Kiger, K., "Two-Phase PIV Measurements of Particle Suspension in a Forced Impinging Jet," 63rd Annual Meeting of the APS Division of Fluid Dynamics, Long Beach, CA, November 21–23, 2010.

[72] Baharani, A., "Investigation into the Effects of Aeolian Scaling Parameters on Sediment Mobilization Below a Hovering Rotor", M.S. Thesis, Department of Aerospace Engineering, University of Maryland, College Park, MD, 2011.

[73] Huston, R., Morris, C., "A Wind-Tunnel Investigation of Helicopter Directional Control in Rearward Flight in Ground Effect," Technical Report TN D-6118, NASA, 1971.

[74] Sheridan, P. F., and Smith, R. P., "Interactional Aerodynamics — A New Challenge to Helicopter Technology," *Journal of the American Helicopter Society*, Vol. 25, (1), 1979, pp. 3–21.

[75] Leishman, J. G., "On Seed Particle Dynamics in Tip Vortex Flows," *Journal of Aircraft*, Vol. 33, (4), 1996, pp. 823–825.

[76] Westerweel, J, "Efficient Detection of Spurious Vectors in Particle Image Velocimetry Data Sets," *Experiments in Fluids*, Vol. 16, (1), 1994, pp. 236–247.

[77] Hall, P., "Taylor–Gortler vortices in fully developed or boundary-layer flows: linear theory," *Journal of Fluid Mechanics*, Vol. 124, (3), 1982, pp. 475–494.

[78] Ramasamy, M., Johnson, B., and Leishman, J. G., "Tip Vortex Measurements Using Dual Plane Digital Particle Image Velocimetry," American Helicopter Society 64th Annual Forum Proceedings, Montréal, Canada, April 29–May 1, 2008.

[79] Milluzzo, J., and Leishman, J. G.,, "Development of the Turbulent Vortex Sheet in the Wake of a Hovering Rotor," 69th Annual Forum Proceedings of the American Helicopter Society, May 21–23, 2013.

[80] Bradshaw, P., "The Analogy Between Streamline Curvature and Buoyancy in Turbulent Shear Flows," *Journal of Fluid Mechanics*, Vol. 36, (1), March 1969, pp. 177–191.

[81] Cotel, A. J., and Breidenthal, R. E., "Turbulence Inside a Vortex," *Physics of Fluid*, Vol. 11, (10), 1999, pp. 3026–3029.

[82] Cotel, A. J., "Turbulence Inside a Vortex: Take Two," *Physics of Fluid*, Vol. 14, (8), 2002, pp. 2933–2934.

[83] Ramasamy, M., and Leishman, J. G., "A Generalized Model for Transitional Blade Tip Vortices," *Journal of the American Helicopter Society*, Vol. 51, (1), January 2006, pp. 92–103.

[84] Ramasamy, M., Johnson, B., Huismann, T. and Leishman, J. G., "Digital Particle Image Velocimetry Measurements of Tip Vortex Characteristics Using an Improved Aperiodicity Correction," *Journal of the American Helicopter Society*, Vol. 54, (012004), 2009, pp. 1–13.

[85] Saffman, P. G., *Vortex Dynamics*, Cambridge University Press, Cambridge, UK, 1992.